Molecular pathology – the roles of P53 in the oxidative stress and DNA damage responses in chronic liver disease and hepatocellular carcinoma

Thesis submitted to the Faculty of Medical Sciences, Newcastle University
In partial fulfilment of the requirements for the degree of Doctor of Philosophy

Ahmed Khairallah Mahdi

Supervisors:

Prof. Helen Reeves

Prof. John Lunec

Northern Institute for Cancer Research

Newcastle University

College Of Medicine
Al-Nahrain University
1987

وزارة التعليم العالي والبحث العلمي
Ministry of Higher Education & Scientific Research

April 2018

Abstract

Non-alcoholic fatty liver disease (NAFLD) has become the commonest form of chronic liver disease in western nations and is rapidly rising in the Asia-Pacific. As yet treatments are limited to diet modification and life style change, which is rarely effective. NAFLD is associated with an increasing risk of developing hepatocellular carcinoma (HCC), which is also increasing markedly and is a significant cause of death. The disease progression is difficult to study in humans as invasive procedures are needed. We have developed a mouse model reflecting the human condition to investigate mechanisms of this disease and potential therapeutic interventions. We used C3H/He mice, which develop obesity and impaired glucose tolerance with age, and explored the effect of an American lifestyle diet. The mice developed features of the metabolic syndrome and NAFLD, including non-alcoholic steatohepatitis (NASH), which was associated with an increase in DNA damage and the development of HCC. Interesting findings were observed with an anti-oxidant (bucillamine) and an FXR agonist (PX20606), but neither prevented HCC development.

As a key responder to DNA damage, *TP53* was explored in the model. In general, *TP53* mutation is reported in around 33% of HCC cases and is usually linked with aflatoxin exposure and viral hepatitis infection, but in the Western world the incidence of *TP53* mutation is lower. In our NAFLD model, all the tumours which developed were of wild-type *TP53* status. This encouraged us to explore exploiting this pathway by testing the ability of small molecule inhibitors of the MDM2-p53 binding interaction to activate p53 in a non-genotoxic manner as a potential treatment for *TP53* wild-type HCC. Promising results were obtained, with highly significant growth inhibitory effects *in vitro* and *in vivo* (NSG xenograft model) in *TP53* wild-type liver cancer cell lines through the induction of senescence. Combination studies *in vitro* also showed that the effect of MDM2-p53 binding antagonists could be potentiated by inhibition of the WIP1/PPM1D phosphatase. Our study shows that targeting the p53 pathway is worthy of further exploration for patients with liver cancer.

Declaration

I hereby declare that the work presented in this thesis is original and has not been previously submitted to any other academic institution.

Acknowledgments

I would like to express my sincerest gratitude and appreciation to my supervisors Professor Helen L. Reeves and Professor John Lunec for their tremendous help, guidance and support throughout my long PhD journey.

I would like to thank my annual progress panel Professor Nicola Curtin and Dr. Dina Tiniakos for their academic support and advice.

Special thanks to my friend Dr. Nahidh Addai who helped me from day one in this scholarship.

I would like to thank my sponsor, The Iraqi Ministry of Higher Education and Scientific Research, Al-Nahrain University / College of Medicine and my friends and guarantors Dr. Gelal Altaai, Dr. Bassam M. Hameed and Dr. Balsam Fadhil for allowing me to have this opportunity to do my PhD at Newcastle University.

I would also like to thank my colleagues for their help and support throughout the project and contribution to the work: Dr. Arman Esfandiari, Dr. Chiao-En Wu, Erhan Aptullahoglu, Dr. Catherine Willoughby, Anna Whitehead, Misti McCain, Dr. Ruchi Shukla, Dr. Stephen R. Wedge, Dr. Huw Thomas, Dr. Fiona Oakley, Dr. Caroline Wilson, and Dr. Diana Jurk.

Thank you to all my colleagues in the NICR, those who left and those who are still here fighting cancer. It has been a pleasure to work with you all and you made the last few years unforgettable.

Lastly, but by no means least, I would like to express my ultimate gratitude to the sun and moon of my life (my parents) whom without their unconditional love and support I wouldn't have been able to achieve any success in my life, and to my brothers and sisters and my friends for their love and support.

Table of Contents

Abstract ..... **i**

Declaration ..... **iii**

Acknowledgments ..... **v**

Table of Contents ..... **vii**

List of Figures ..... **xi**

List of Tables ..... **xv**

List of abbreviations ..... **xvii**

Chapter 1: Literature review **1**

1.1 Normal anatomy and histology of the Liver 2
1.2 Chronic Liver Disease (NAFLD and NASH) 3
1.2.1 Definition 3
1.2.2 Epidemiology 3
1.2.3 Pathogenesis 4
1.2.4 Grading and staging of NAFLD 11
1.2.5 Management of NAFLD 13
1.3 Hepatocellular Carcinoma (HCC) 15
1.3.1 Risk factors for HCC 15
1.3.2 Molecular mechanisms of development of HCC in NAFLD 17
1.3.3 Morphology of hepatocellular neoplasms 20
1.3.4 Staging of HCC 22
1.3.5 Treatment and prevention of HCC 23
1.3.6 Pre-clinical models of NAFLD 24
1.4 P53 pathway 26
1.4.1 Structure and function 26
1.4.2 Role of P53 in chronic liver disease 31
1.4.3 p53 in HCC 31
1.4.4 Cell cycle and p53 32
1.4.5 P53 and Senescence 34
1.4.6 P53 and apoptosis 34
1.4.7 Targeting MDM2-p53 in cancer 35
1.4.8 PPM1D /WIP1 38
1.5 Aims of the study: 39

Chapter 2: Materials and Methods **40**

2.1 General Laboratory Practice 41
2.2 Animal model design 41
2.2.1 Animal culling and tissue sampling 42
2.2.2 Tissue processing and section preparation for histopathology study 43
2.2.3 Scoring of routinely stained liver tissue sections 43
2.3 Immunohistochemistry 44
2.3.1 γ-H2AX and Ki67 manual protocol 44
2.3.2 Automated IHC protocols 45
2.3.3 Digital Imaging 46

2.4 Molecular biology methods 48
2.4.1 RNA extraction 48
2.4.2 Reverse transcription 48
2.4.3 Quantitative Real time polymerase chain reaction (qRT-PCR) 49
2.5 Cell culture methods 52
2.5.1 Tissue culture practice and authentication of cell lines 52
2.5.2 Culture of adherent cells 52
2.5.3 Counting cells 53
2.5.4 Freezing and revival of cells 53
2.5.5 Sulfrhodamine B (SRB) assay 54
2.5.6 Growth curve 54
2.5.7 Growth inhibition 54
2.5.8 Clonogenic assay 55
2.6 Drugs used in *in vitro* studies 56
2.6.1 MDM2 inhibitors 56
2.6.2 WIP1 inhibitor 57
2.7 Western blotting 58
2.7.1 Protein isolation and quantification 58
2.7.2 Immunoblotting 58
2.7.3 Immunodetection 59
2.8 Fluorescence activated cell sorting (FACS) 60
2.9 Caspase 3/7 activity assay 62
2.10 XTT assay 62
2.11 Senescence associated β-Galactosidase assay (SA-β-Gal) 63
2.12 *In vivo* xenograft study 64
2.12.1 Growth curve of HepG2-Luc in different immunocompromised mice strains 64
2.12.2 Assessing HDM201 effect on HepG2-Luc xenografts 65
2.13 Statistical analysis 65

Chapter 3: Characterisation of a dietary induced animal model of non-alcoholic fatty liver disease and hepatocellular carcinoma – a focus on p53 66

3.1 Introduction 67
3.2 Hypothesis and aims of the study 68
3.2.1 Hypotheses 68
3.2.2 Aims of the study 68
3.3 Dietary induced Obesity, NAFLD and HCC 69
3.3.1 The ALIOS diet induced obesity and hepatomegaly in C3H/He mice 69
3.3.2 The ALIOS diet induced NAFLD, NASH and Fibrosis 71
3.3.3 The ALIOS diet promoted the development of primary liver tumours 74
3.3.4 Characterising tumour development and progression in C3H/He mice 75
3.3.5 Hepatocyte DNA damage was increased in aged and ALIOS fed mice 82
3.3.6 Hepatocyte proliferation was elevated in aged C3H/He mice 86
3.4 The p53 pathway in the ALIOS diet induced NAFLD and tumours 90
3.4.1 Hepatic tissue p53 mRNA levels were elevated with age rather than with diet. 90
3.4.2 Hepatocyte p53 protein increased with age, diet and NAFLD 95
3.4.3 Hepatocyte p53 increased with liver weight and NAFLD progression 97
3.4.4 p21 immunohistochemical analysis 99
3.5 DNA damage and p53 in ALIOS diet induced hepatocarcinogenesis 102
3.5.1 DNA damage was markedly increased in HCC compared to background tissues 102

3.5.2 Proliferation was markedly increased in HCC compared to background tissues.....104
3.5.3 p53 and transcriptional target gene mRNA levels in tumour versus non-tumour regions of the liver.....105
3.5.4 p53 and transcriptional target gene protein levels in tumour versus non-tumour liver.....106
3.6 Discussion.....112
3.6.1 The impact of ALIOS diet on C3H/He mice.....112
3.6.2 Predictors of HCC development – liver size and histology.....114
3.6.3 Predictors of HCC development – a focus on γ-H2AX and Ki67.....115
3.6.4 Malignant transformation – a focus on γ-H2AX, Ki67, p53 and Ras.....116

Chapter 4: The impact of interventions in the ALIOS C3H/He mouse model of NAFLD and HCC.....118

4.1 Introduction.....119
4.2 Aims of the study in this chapter.....120
4.3 The impact of bucillamine on the dietary animal model.....121
4.3.1 Background.....121
4.3.2 The impact of bucillamine on body and liver weight.....122
4.3.3 The effect of bucillamine on the lipid profile and liver function.....123
4.3.4 The effect of bucillamine on NAFLD histopathology.....124
4.3.5 Quantification of DNA damage in the bucillamine treated group.....126
4.3.6 Proliferative status in the bucillamine treated group.....128
4.3.7 Association of bucillamine with HCC.....130
4.3.8 Quantification of p53 in the bucillamine treated group.....132
4.4 The impact of FXR agonist PX20606 on the dietary animal model.....134
4.4.1 Background.....134
4.4.2 The effect of PX20606 on body and liver weight.....136
4.4.3 The effect of PX20606 on lipid profile and liver function.....137
4.4.4 Histological assessment of the impact of PX20606.....138
4.4.5 Quantification of hepatocyte DNA damage in PX20606 treated animals.....141
4.4.6 Proliferative status in PX20606 treated animals.....143
4.4.7 The impact of PX20606 on HCC in C3H/He mice.....145
4.4.8 Quantification of hepatic p53 in the PX20606 treated animals.....147
4.5 Discussion.....149

Chapter 5: MDM2 inhibition for non-genotoxic activation of TP53 – a novel strategy for the treatment of liver cancer.....153

5.1 Introduction.....154
5.2 Aims of the study in this chapter.....155
5.3 Growth curves of different liver cancer cell lines.....155
5.4 MDM2 inhibitors repressed the proliferation and colony formation of liver cancer cell lines in a p53-dependent manner.....157
5.4.1 Growth inhibition of $p53^{WT}$ liver cancer cell lines by MDM2 inhibitors.....157
5.4.2 The effect of MDM2 inhibitors on p53 protein levels and of its downstream targets.....159
5.4.3 Inhibition of colony formation ability of p53WT cell lines by MDM2 inhibitors.....161
5.5 The effect of HDM201 on cell cycle distribution in liver cancer cell lines.....163
5.6 HDM201 inhibits growth without inducing apoptosis and does not inhibit the metabolic activity in $p53^{WT}$ liver cancer cell lines.....166
5.7 HDM201 increases the transcription of p53 downstream transcriptional targets.....168
5.8 HDM201 induced cell cycle arrest was associated with induction of senescence.....170

5.9 HDM201 inhibits the growth of liver cancer xenografts *in vivo* 174
5.9.1 HepG2-Luc responds to MDM2 inhibitors in the same pattern as HepG2 174
5.9.2 Establishing a xenograft model with HepG2-Luc in immunocompromised mice 177
5.9.3 The effect of HDM201 at a dose of 25 mg/kg/day for 7 days on HepG2-Luc xenografts . 178
5.9.4 The effect of HDM201 100 mg/kg/day for 10 days on HepG2-Luc xenografts 182
5.10 Discussion..... 185

Chapter 6: Results - The effect of WIP1 inhibitor GSK2830371 as a single agent and in combination with MDM2 inhibitors on liver cancer cell lines..... 188

6.1 Introduction 189
6.2 Aims of the study in this chapter..... 189
6.3 GSK2830371 has no or minimal effect on liver cancer cell lines when used alone at low micromolar doses..... 190
6.3.1 GSK2830371 effect on the proliferation of liver cancer cell lines..... 190
6.3.2 The effect of GSK2830371 at the protein level in $p53^{WT}$ cell lines 191
6.4 GSK2830371 potentiates the effect of MDM2 inhibitors on repressing the growth of liver cancer cell lines through the p53 pathway..... 192
6.5 The effect of GSK2830371 as a single agent and in combination with HDM201 on protein levels in $p53^{WT}$ liver cancer cell lines..... 194
6.6 The effect of GSK2830371 as a single agent and in combination with HDM201 on the clonogenic survival of liver cancer cell lines 195
6.7 The effect of GSK2830371 on cell cycle distribution when used as a single agent and in combination with HDM201..... 196
6.8 GSK2830371 as a single agent or in combination with HDM201 does not induce apoptosis and does not inhibit the metabolic activity in liver cancer cell lines..... 198
6.9 The effects of WIP1i as a single agent and in combination with HDM201 on the level of expression of p53 and its downstream transcriptional target genes in liver cancer cell lines 200
6.10 GSK2830371 potentiate the HDM201 induced senescence in $p53^{WT}$ cell lines..... 202
6.11 The effect of GSK2830371 as a single agent and in combination with HDM201 on HepG2-Luc 208
6.12 Discussion..... 210

Chapter 7: Summary, Conclusions and Future Directions..... 212

References..... 224

List of Figures

Figure 1.1: Diagram of a section of the liver showing the portal tract, central vein and the 3 acinar zones between the portal tract and central vein....2
Figure 1.2: Showing the transition through NAFLD to HCC....4
Figure 1.3: Mechanisms of pathogenesis in NAFLD elucidating the role of FFA, IR and ROS....9
Figure 1.4: Lipotoxic injury to the hepatocytes....10
Figure 1.5: Extracellular vesicles (lipotoxic-induced hepatocyte-derived) effect on liver....10
Figure 1.6: Bedossa et al algorithm for the diagnosis of NASH....13
Figure 1.7: Relation between NAFLD, metabolic syndrome and HCC....19
Figure 1.8: BCLC staging system with treatment modalities....22
Figure 1.9: p53 structure showing functional domains....26
Figure 1.10: Regulation of P53 functions by MDM2 and MDMX....27
Figure 1.11: Showing different stimuli that induce p53 function and the end result....29
Figure 1.12: Phases of the cell cycle showing the sites of cyclin and cyclin dependant kinases regulation and their inhibitory CKI....33
Figure 1.13: Three-dimensional modelling of Nutlin-3a binding to the p53-binding pocket of MDM2. 36
Figure 1.14: Direct and indirect effect of WIP1 on regulation of p53 and DNA repair....38
Figure 2.1: Dietary animal model design....42
Figure 2.2: Aperio algorithm used for scoring immunohistochemical staining....46
Figure 2.3: Chemical structure of the three MDM2 inhibitors, Nutlin-3 (216), RG7388 (237) and HDM201 (238)....57
Figure 2.4: the chemical structure of GSK2830371....57
Figure 2.5: Cell cycle analysis and gating of events using CellQuest and Cyflogic software....61
Figure 3.1 : The effect of ALIOS diet on body and liver weight....70
Figure 3.2: Histological parameters used in NAS and SAF scoring systems showing the NAFLD changes after feeding ALIOS diet in 48-week-old mouse liver....71
Figure 3.3 : Comparison of liver histological features of NAFLD in control and ALIOS diet fed mice at 48 weeks....72
Figure 3.4: NAS and SAF score comparison between the control and HF diet in 48-week-old mice…73
Figure 3.5: Tumour development in the murine dietary animal model....74
Figure 3.6: H&E stained mouse liver tissue sections showing NAFLD, HCA and HCC of different grades....76
Figure 3.7 : The association between tumour numbers and NAFLD progression in the 48-week-old mice. 77
Figure 3.8 : Tumour size association with NAFLD progression in the 48-week-old mice....78
Figure 3.9: DNA damage assessment in the 48-week-old mice....82
Figure 3.10: γ-H2AX quantification in liver tissue sections from 24- and 48-week-old mice....83
Figure 3.11 : Association of DNA damage with the progression of NAFLD in the 48-week-old mice. 84

Figure 3.12: Ki67 quantification in liver tissue sections of 24- and 48-week-old mice. 86
Figure 3.13: Ki67 expression in association with fat accumulation in the periportal zone of a 48-week-old mouse fed the ALIOS diet. 87
Figure 3.14 : Correlation of Ki67 expression with the histological parameters of NAFLD. 88
Figure 3.15: Quantification of mRNA levels for p53 pathway genes in whole liver tissue extracts from ALIOS dietary animal model mice. 91
Figure 3.16: p53 quantification in liver tissue section in 24- and 48-week-old mice. 95
Figure 3.17: p53 expression in the dietary animal model. 96
Figure 3.18: The relationship of p53 expression with the histological parameters of NAFLD in 48-week-old mice. 97
Figure 3.19 : p21 expression in dietary animal model. 99
Figure 3.20 : p53 and p21 association with NAFLD histological parameters in the 48-week-old mice. 100
Figure 3.21: γ-H2AX expression in tumours in the dietary animal model. 103
Figure 3.22 : Proliferative status in tumour samples in the dietary animal model. 104
Figure 3.23: qRT-PCR analysis of *Trp53* mRNA expression and that of its downstream transcriptional targets, in tumour versus non-tumour areas of the livers. 105
Figure 3.24 : p53 expression by immunohistochemistry in HCCs. 107
Figure 3.25: Immunohistochemical detection of p21 in HCCs. 108
Figure 3.26 : Dual expression of p53 and p21 in liver tumour samples. 109
Figure 3.27: Western blot of 48-week-old mice liver samples demonstrating increase in p21 protein levels in tumours compared to their peritumoural counterpart, in comparison to a control sample and a diethylnitrosamine (DEN) induced liver tumour sample. 109
Figure 4.1: Chemical structure of bucillamine 121
Figure 4.2: The effect of bucillamine on body and liver weight compared to the effect of ALIOS diet. 122
Figure 4.3: The effect of bucillamine on lipid profile and liver enzymes. 123
Figure 4.4: Effect of bucillamine on the histological parameters of NAFLD. 124
Figure 4.5: the effect of bucillamine on the histological scoring systems. 125
Figure 4.6: γ-H2AX immunohistochemical staining of the periportal area in the diet alone and the bucillamine treated groups 126
Figure 4.7: Ki67 immunohistochemical staining of the periportal area in the diet alone and the bucillamine treated groups 128
Figure 4.8: The effect of bucillamine treatment on tumour development in the murine dietary animal model. 130
Figure 4.9: p53 immunohistochemical staining of the periportal area in the diet alone and the bucillamine treated groups. 132
Figure 4.10: Schematic representation of FXR function. 135
Figure 4.11: chemical structure of PX20606 FXR agonist 136
Figure 4.12: The effect of PX20606 on body and liver weight compared to the effect of ALIOS diet. 136
Figure 4.13: The effect of PX20606 on lipid profile and liver enzymes. 137

Figure 4.14: Effect of PX20606 on the histological parameters of NAFLD. 138
Figure 4.15: The effect of PX20606 on the histological scoring system. 139
Figure 4.16: γ-H2AX immunohistochemical staining of the periportal area in the diet alone and the PX20606 treated groups. 141
Figure 4.17: Ki67 immunohistochemical staining of the periportal area in the diet alone and the PX20606 treated groups. 143
Figure 4.18: The effect of PX20606 treatment on tumour development in the murine dietary animal model. 145
Figure 4.19: p53 immunohistochemical staining of the periportal area in the diet alone and the PX20606 treated groups. 147
Figure 5.1: Growth curves of liver cancer cell lines with different *TP53* status. 156
Figure 5.2: The effect of three MDM2 inhibitors on the growth of liver cancer cell lines. 158
Figure 5.3: Time course treatment of $p53^{WT}$ cell lines with ~ 0.5, 1 and 2X GI_{50} doses of three different MDM2 inhibitors for 2, 6 and 24 hours. 160
Figure 5.4: Clonogenic survival of liver cancer cell lines treated with three different MDM2 inhibitors for 96 hours. 162
Figure 5.5: The effect of HDM201 on cell cycle distribution over 72 hours of treatment. 164
Figure 5.6: Cell cycle profile showing the effect of HDM201 on cell cycle distribution in liver cancer cell lines. 165
Figure 5.7: Apoptotic (caspase 3/7) activity after treatment with HDM201. 167
Figure 5.8: Metabolic activity measured by XTT assay in liver cancer cell lines after treatment with HDM201 for 96 hours. 167
Figure 5.9: qRT-PCR measurement of mRNA expression for *TP53* and downstream transcriptional targets of p53 in response to HDM201. 169
Figure 5.10: Incucyte experiment showing the effect of HDM201 on the cell morphology of $p53^{WT}$ cell lines (HepG2 and SK-Hep-1) after treatment with HDM201 for 96 hours. 171
Figure 5.11: HDM201 induces senescence in $p53^{WT}$ liver cancer cell lines. 172
Figure 5.12: Schematic summary representing the p53 pathway and the effect of MDM2 inhibition, linking p53 activation to downstream transcriptional targets that induce the dominant response of cell cycle arrest and senescence, and minimal activation of pro-apoptotic genes. 173
Figure 5.13: Growth inhibition and clonogenic survival of HepG2 and HepG2-Luc cell lines. 175
Figure 5.14: Caspase 3/7 activity and XTT assay for HepG2 and HepG2-Luc cells. 176
Figure 5.15: mRNA expression of *TP53* and p53 downstream transcriptional targets by qRT-PCR in HepG2 and HepG2-Luc in response to HDM201. 176
Figure 5.16: Growth curve of HepG2-Luc xenografts in NSG and CD1 nude mice. 177
Figure 5.17: The effect of oral 25 mg/kg/day HDM201 (single daily dose) on HepG2-Luc xenografts in NSG mice. 179
Figure 5.18: HepG2-Luc xenografts tissue sections with H&E and p21 immunohistochemical staining. 180
Figure 5.19: IVIS scan compared to the standard tumour measurement by caliper. 181
Figure 5.20: The effect of oral 100 mg/kg/day HDM201 (single daily dose) on HepG2-Luc xenografts in NSG mice. 183

Figure 5.21: the effect of oral HDM201 100 mg/kg/day (single daily dose) on HeG2-Luc xenografts in NSG mice. 184

Figure 6.1: growth inhibition assay of liver cancer cell lines with different *TP53* status with WIP1i for 96 hours (SRB assay). 190

Figure 6.2: Immunoblot of HepG2 and SK-Hep-1 cell lines treated with different concentrations of GSK2830371 WIP1i (0.07-10 µM) for 6 hours. 191

Figure 6.3: Combination effect of different MDM2 inhibitors with GSK2830371 WIP1i on liver cancer cell lines. 193

Figure 6.4: Immunoblot of HepG2 and SK-Hep-1 treated with HDM201 alone and in combination with WIP1i (GSK2830371) for 6 hours. 194

Figure 6.5: The effect of HDM201 alone and in combination with WIP1i (2.5 µM) on the cloning efficiency of liver cancer cell lines after treatment for 96 hours. 195

Figure 6.6: Cell cycle analysis showing the effect of GSK2830371 (2.5µM) WIP1i on the cell cycle distribution when combined with HDM201. 197

Figure 6.7: Caspase 3/7 activity in liver cancer cell lines after treatment with HDM201 alone and in combination with GSK2830371 (2.5µM) WIP1i. 198

Figure 6.8: XTT assay measuring the metabolic activity in liver cancer cell lines in response to HDM201 alone and in combination with GSK2830371 (2.5µM) WIP1i. 199

Figure 6.9: The expression of *TP53* and its downstream transcriptional targets by qRT-PCR in response to HDM201 alone and in combination with GSK2830371 WIP1i in liver cancer cell lines. 201

Figure 6.10: Incucyte experiment showing the effect of HDM201 alone and in combination with GSK2830371 WIP1i on HepG2 $p53^{WT}$ liver cancer cell line. 203

Figure 6.11: Incucyte experiment showing the effect of HDM201 alone and in combination with GSK2830371 WIP1i on SK-Hep-1 $p53^{WT}$ liver cancer cell line. 204

Figure 6.12: GSK2830371 WIP1i potentiates HDM201 induced senescence in HepG2 $p53^{WT}$ liver cancer cell line. 205

Figure 6.13: GSK2830371 WIP1i potentiates HDM201 induced senescence in SK-Hep-1 $p53^{WT}$ liver cancer cell lines. 206

Figure 6.14: GSK2830371 WIP1i potentiation of HDM201 induced senescence in $p53^{WT}$ liver cancer cell lines. 207

Figure 6.15: Schematic summary representing the p53 pathway and the effect of MDM2 and WIP1 inhibition. 207

Figure 6.16: Comparison of the effect of GSK2830371 WIP1i alone and in combination with HDM201 on HepG2 and HepG2-Luc. 208

Figure 6.17: Cell cycle analysis and mRNA expression of p53 transcriptional target genes in HepG2 and HepG2-Luc. 209

Figure 7.1: Hedgehog signalling pathway in NAFLD. 216

List of Tables

Table 1.1: A comparison between NAFLD scoring systems 12
Table 2.1: Aperio algorithm details used for scoring IHC stained slides. 47
Table 2.2: Reagents used for reverse transcription. 49
Table 2.3: Mouse primer sequences used for qRT-PCR. 50
Table 2.4: Human primer sequences used for qRT-PCR. 51
Table 2.5: qRT-PCR master mix constituent for each reaction 51
Table 2.6: seeding densities of liver cancer cell lines in 96 well plates 55
Table 2.7: Cloning efficiency and seeding density for clonogenic assay of liver cancer cell lines 56
Table 2.8: Antibodies used in western blotting. 60
Table 2.9: Seeding densities of HepG2 and SK-Hep-1 for SA-β-Gal assay 63
Table 3.1: dietary animal model design 68
Table 3.2: Association of HCC development with phenotypic and liver histopathology parameters. 75
Table 3.3: Incidence and histological grades of liver tumours 76
Table 3.4 : Association of tumour size with the phenotypic and liver histopathology parameters 79
Table 3.5: Binomial regression analysis of tumour development and stage in the dietary animal model. 80
Table 3.6: Association of γ-H2AX-positive hepatocyte nuclei. 85
Table 3.7: Association of Ki67-positive hepatocyte nuclei 89
Table 3.8: Correlations between *Trp53* mRNA and its downstream targets at the mRNA level. 92
Table 3.9: Hepatic genes expression associations in 48-week-old mice (bivariate analyses). 93
Table 3.10: Associations with immunohistochemistry %positive p53 hepatocytes 98
Table 3.11: Association with % positive p21 hepatocyte nuclei 101
Table 3.12: Fold change differences between tumours and non-tumour liver for mRNA expression of *Trp53*, its downstream transcriptional targets, together with alpha-fetoprotein (*Afp*) and glypican-3 (*Gpc3*) in the dietary animal model (RNAseq data) 106
Table 3.13: RNA sequence analysis data showing Ras mutation details in the animal model tumours. 111
Table 4.1: design of the interventions used in the dietary animal model. 119
Table 4.2: The impact of bucillamine on the histological parameters. 125
Table 4.3: Associations of γ-H2AX immunohistochemical staining of the periportal area with the phenotypic parameters, liver histopathology and tumours in bucillamine treated groups. 127
Table 4.4: Associations of Ki67 immunohistochemical staining of the periportal area with the phenotypic parameters, liver histopathology and γ-H2AX in bucillamine treated groups. 129
Table 4.5: Effect of bucillamine on HCC development in C3H/He mice. 131
Table 4.6: Effect of bucillamine on tumour size in C3H/He mice. 131
Table 4.7: Associations of p53 immunohistochemical staining of the periportal area with the phenotypic parameters, liver histopathology, tumours and immunohistochemical markers in the bucillamine treated groups. 133

Table 4.8: The impact of PX20606 on the histological parameters in the control treated groups (Chi^2). 139

Table 4.9: The impact of PX20606 on the histological parameters in the ALIOS (HF) treated groups (Chi^2). 140

Table 4.10: Associations of γ-H2AX immunohistochemical staining of the periportal area with the phenotypic parameters, liver histopathology and tumours in PX20606 treated groups. 142

Table 4.11: Associations of Ki67 immunohistochemical staining of the periportal area with the phenotypic parameters, liver histopathology, tumours and γ-H2AX in PX20606 treated groups. 144

Table 4.12: Effect of PX20606 on tumour development in C3H/He mice..... 146

Table 4.13: Effect of PX20606 on HCC size in C3H/He mice 146

Table 4.14: Associations of p53 immunohistochemical staining of the periportal area with the phenotypic parameters, liver histopathology, tumours and immunohistochemical markers in PX20606 treated groups. 148

Table 5.1: GI_{50} concentrations of HDM201, RG7388 and Nutlin-3 for the panel of liver cancer cell lines of varying *TP53* status..... 157

Table 5.2: The GI_{50} and LC_{50} for HepG2-Luc versus parental HepG2 cell lines for the three MDM2 inhibitors..... 175

Table 6.1: GI_{50} of MDM2 inhibitors alone and in combination with WIP1i (2.5 µM) in $p53^{WT}$ liver cancer cell lines 192

List of abbreviations

4-HNE	4-Hydroxynonenal
8-oxo-dGTP	8-oxo-7,8-dihydro-2'-deoxyguanosine 5'-triphosphate
AASLD	American Associations for Study of Liver Diseases
ABC	Avidin biotin complex
Acad11	Acyl-CoA dehydrogenase family member 11
ACC	Acetyl-CoA carboxylase
AFP	Alpha-feto protein
AIF	Apoptosis inducing factor
ALD	Alcohol liver disease
ALP	Alkaline phosphatase
ALT	Alanine aminotransferase
AST	Aspartate aminotransferase
ATCC	American Type Culture Collection
ATM	Ataxia telangiectasia mutated
ATR	Ataxia telangiectasia related
BAK1	BCL-2 antagonist killer 1
BAX	BCL-2 associated X protein
BCA	Bicinchoninic acid
BIM	Bcl-2-like protein 11
BioCOSHH	Biological Control of Substances hazardous to Health
BCLC	Barcelona Clinic Liver Cancer
BMI	Body mass index
BSA	Bovine serum albumin
BW	Body weight
CDK	Cyclin dependent kinases
CDKN1A	Cyclin-dependent kinase inhibitor 1
cDNA	Complementary DNA
CHB	Chronic hepatitis B
Chk1	Check point kinase 1
Chk2	Check point kinase 2
CHOP	CAAT/enhancer binding homologous protein
ChREBP	Carbohydrate response element binding protein
CIP/KIP	CDK interacting protein/Kinase inhibitory protein
CLD	Chronic liver disease
CLT	Cadaveric liver transplantation
c-Met	Tyrosine-protein kinase Met
COSHH	Control of Substances hazardous to Health
COSMIC	Catalogue of Somatic Mutations in Cancer
CXCL1	Chemokine (C-X-C motif) ligand 1
CYP7A1	Cholesterol 7α hydroxylase
DAB	3,3'-diaminobenzidine
DCR2	Decoy receptor 2
DDR	DNA damage response
DEB-TACE	Drug eluting beads-TACE

DMEM	Dulbecco's Modified Eagle's Medium
DMSO	Dimethyl sulphoxide
DNA	Deoxy ribonucleic acid
DSB	Double Stranded Break
EASL	European Associations for Study of Liver Diseases
ECACC	European Collection of Authenticated Cell Cultures
ECL	Enhanced ChemiLuminescence
ER	Endoplasmic reticulum
F4/80	EGF-like module-containing mucin-like hormone receptor-like 1
FACS	Fluorescence activated cell sorting
FASN	Fatty acid synthase
FDA	Food and Drug administration agency in USA
FDFT1	Farnesyl diphosphate farnesyl transferase 1
FFA	Free fatty acids
FGF19	Fibroblast growth factor 19
FOXO3	Forkhead box O3
FSC	Forward scatter
FXR	Farsenoid X receptor
G0	Gap 0
G1	Gap 1
G2	Gap 2
G6PD)	Glucose 6 phosphate dehydrogenase
GADD45	Growth arrest and DNA damage inducible 45
Gal	Galactosidase
GCKR	Glucokinase regulator
GI_{50}	50% growth inhibitory concentration
GLI	Glioma associated oncoprotein
GOI	Gene of interest
GSH	Glutathione
HB	Hepatocellular ballooning
HBV	hepatitis B virus
HBx protein	Hepatitis B X protein
HCC	Hepatocellular carcinoma
HCV	Hepatitis C virus
HDAC	Histone deacetylase
HepG2-Luc	HepG2 luciferase
HF	High Fat High Fructose
HH	Hedgehog
HPMC	HydroxyPropyl Methyl Cellulose
HRP	Horseradish peroxidase
IGF1	Insulin-like growth factor 1
IGF-1	Insulin-like growth factor
IHC	Immunohistochemistry
IL15	Interleukin 15
IL-1β	Interleukin-1 beta

IL-6	Interleukin-6
IL-8	Interleukin-8
INK4	**IN**hibitors of CD**K**4
INSR	Insulin receptor
IR	Insulin resistance
IRS-1	Insulin substrate-1
IVIS	In Vivo Image Scanning
JCRB	Japanese Collection of Research Bioresources
JNK	c-Jun NH_2-terminal kinase
Ki67	Proliferation-related Ki-67 antigen
KLF6	Krueppel-like factor 6
LC_{50}	50% clonogenic survival
LDLT	Living donor liver transplantation
LI	Lobular inflammation
LKB1	Liver kinase B1
LW	Liver weight
MAPK	Mitogen-activated protein kinase
MCP1	Monocyte chemotactic protein 1
MDM2	Murine double minute 2
MDMX	Murine double minute X
miRNAs	Micro RNAs
MKK7	MAP kinase kinase 7
MOMP	Mitochondrial outer membrane permeabilization
mRNA	Messenger RNA
mtDNA	Mitochondrial DNA
mTOR	Mammalian target of rapamycin
myc	Cellular proto-oncogene myc
NAD^+	Nicotinamide Adenine Dinucleotide
NADPH	Nicotinamide adenine dinucleotide phosphate
NAFLD	Non-alcoholic fatty liver disease
NAS	NASH activity score
NASH	Non-alcoholic steatohepatitis
NES	Nuclear export sequence
NFKB	Nuclear Factor-kappa B
NLS	Nuclear localization sequence
NOXA	Phorbol-12-myristate-13-acetate-induced gene 1 or PMAIP1
NSG	NOD SCID gamma
OCA	Obeticholic acid
OD	Optical density
OLT	Orthotopic liver transplantation
$p53^{MUT}$	*TP53* mutant
$p53^{NULL}$	*TP53* null
$p53^{WT}$	*TP53* wild type
PAI1	Plasminogen activator inhibitor 1
PAR	Poly-ADP ribose

PARG	Poly-ADP ribose glycohydrolase
PARP1	Poly-ADP ribosyl polymerase
PBS	Phosphate buffer saline
PEI	Percutaneous ethanol injection
PFT	Pifithrin -α *p*-nitro
PI	Propidium iodide
PI3K	Phosphatidylinositol-3 kinase
PIG3	p53 inducible protein 3
PNPLA3	Patatin-like phospholipase domain containing protein 3
$pp53^{Ser15}$	p53 phosphorylated at the Serine 15 site
PPARα	Peroxisome proliferator activator receptor alpha
PPARβ	Peroxisome proliferator activator receptor beta
PPARγ	Peroxisome proliferator activator receptor gamma
PPARδ	Peroxisome proliferator activator receptor delta
PPM1D	Protein phosphatase, Mg2+/Mn2+ dependent, 1D
PST	Performance status test
PTCH	Patched receptor
PUMA	p53-upregulated modulator of apoptosis
qRT-PCR	Quantitative real time polymerase chain reaction
RB	Retinoblastoma
REG	Regulatory
RF	Radiofrequency
RNA	Ribonucleic acid
RNA seq	RNA sequencing
ROS	Reactive oxygen species
RQ	Relative quantification
RT	Reverse transcription
RXR	Retinoid X receptor
S	S-phase
SAF	Steatosis activity fibrosis
SASP	Senescence associated secretory phenotype
SA-β-Gal	Senescence associated β-Galactosidase
SBRT	Stereotactic Body Radiation Therapy
SD	Standard deviation
SDS	Sodium dodecyl sulphate
SEM	Standard error of the mean
Ser	Serine
SHP	Small heterodimer partner
SIRT	Selective Internal Radiotherapy Treatment
SIRT1	Silent mating type information regulation 2 homolog 1
SMO	Smoothened
SNP	Single nucleotide polymorphism
SRB	Sulfrhodamine B
SREBP1c	Sterol regulatory element binding protein1c
SSC	Side scatter
SSDB	Single stranded DNA break

T2DM	Type 2 diabetes
TACE	Transarterial chemoembolization
TAD1	Transcriptional transactivation domain 1
TAD2	Transcriptional transactivation domain 2
TARE	Transarterial radioembolization
TBS	Tris-buffered saline
TBST	Tris-buffered saline tween
TCGA	The Cancer Genome Atlas
TET	Tetramerization
TIGAR	TP53-induced glycolysis and apoptosis regulator
TM6SF2	Transmembrane 6 superfamily 2
TNFBSF10B	Tumor necrosis factor receptor superfamily member 10B
TNF-α	Tumour necrosis factor alpha
TNM	Tumour Node Metastases
Trp53	Transformation related protein 53 (Murine gene)
WAT	White adipose tissue
WIP1	Wild type-p53 induced phosphatase 1
WIP1i	WIP1 inhibitor
WT	Wild type
YWHA/14-3-3 sigma	Tyrosine 3-Monooxygenase/Tryptophan 5-Monooxygenase Activation Protein, Sigma Polypeptide
ZMAT3	Zinc finger matrin-type 3
γ-H2AX	Phosphorylated Gamma- histone H2A variant H2AX at Ser139

Chapter 1: Literature review

1.1 Normal anatomy and histology of the Liver

The liver is one of the largest organs in the human body. It is located in the right hypochondrium and it is responsible for metabolic homeostasis. It regulates lipid, protein and carbohydrate metabolism, in addition to drug detoxification and bile secretion.

It weighs about 1400-1600 gram and receives 25% of the cardiac output from a dual blood supply (70% from the portal vein and 30% from the hepatic artery). It is divided into two lobes, right and left. Each lobe consists of multiple smaller units 1-2 mm in diameter called lobules that are hexagonal in shape. In the centre of each lobule there is a central hepatic vein, surrounded by a number of portal tracts. Within each portal tract are branches of the hepatic artery, portal vein and a bile duct. In between the central vein and the portal tracts are hepatocytes arranged in cords or trabeculae, with blood containing sinusoids in between. The sinusoids are lined by fenestrated endothelial cells which allow exchange of different materials. Adherent to the endothelial cells are Kupffer cells, which are a part of the reticuloendothelial system. In the peri-sinusoidal space lie retinol-storing stellate cells, which in time of injury transform into collagen producing myofibroblast-like cells (1, 2).

Blood entering the liver, via hepatic artery and portal vein branches, flows from the portal tracts in the lobule periphery towards the terminal hepatic vein. Defined by oxygen content of the flowing blood, the acinus is divided into three zones. Zone 1 surrounds the portal tract and gets the highest oxygen concentration, with zone three around the central vein receiving the lowest. Zone 2 sits between zones 1 and 3. These zones are of importance because they show different features related to liver injury and diseases (**Figure** 1.1) (1).

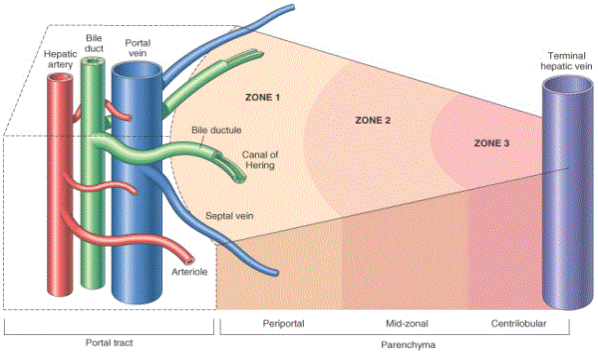

Figure 1.1: Diagram of a section of the liver showing the portal tract, central vein and the 3 acinar zones between the portal tract and central vein (1).

1.2 Chronic Liver Disease (NAFLD and NASH)

1.2.1 Definition

Steatosis, derived from the Greek word Stear - which means fat, describes the accumulation of fatty acids and lipid in hepatocytes. Non-alcoholic fatty liver disease (NAFLD) is simply defined as steatosis which occurs in the absence of intake of alcohol or consumption of <30 g of alcohol for men and 20 g for women, or the presence of another chronic liver disease (3, 4). It is the most common chronic liver disease worldwide (5).

NAFLD is a part of a larger spectrum that starts with simple steatosis, but in a minority of individuals this can progresses to a more severe form called non-alcoholic steatohepatitis (NASH). In addition to steatosis, NASH includes a variable degree of inflammation, hepatocyte injury and fibrosis. NASH is more likely to progress to cirrhosis, which eventually might lead to the development of liver failure or hepatocellular carcinoma (HCC) (5-8)

Several studies have shown a strong association between metabolic syndrome (MetS) and NAFLD. MetS is defined by the presence of three of the followings abdominal obesity with waist circumference (WC) >102 cm in men & ≥88 cm in women; elevated fasting glucose ≥ 100 mg/dL or impaired glucose tolerance test (defined as a glucose level 140 mg/dl 120 minutes after ingestion of 75 grams of glucose); elevated blood pressure (BP) ≥130/85 mmHg and Hypertriglyceridemia ≥150 mg/dL or Low serum HDL <40 mg/dl for men and <50 mg/dL. (9, 10). Statistically speaking, the presence of these conditions will increase NAFLD risk by several times (7). The presence of MetS is also associated with an increased incidence of HCC (11).

1.2.2 Epidemiology

The incidence of NAFLD is increasing all over the world. It has become the commonest form of chronic liver disease worldwide (12). In the United States and the western countries where obesity (which is defined as a body mass index BMI of > 30 kg/m^2) (13) has become extremely common; and due to the strong association between NAFLD and obesity; the increasing incidence of NAFLD represents a major health problem, affecting up to 30-40% of the population (11, 14, 15). Globally it is estimated to affect 25.28% of the world population (16). Furthermore, the incidence of obesity is increasing in eastern Asian countries like China, where it has risen from 13 to 30 % over the period from 1990 to 2008 (11, 17, 18) (**Figure** 1.2).

NAFLD is more common in males than females (8, 11, 19) and is increasingly recognised as starting in early childhood, affecting 8% of toddlers (< 2 years) and 17% of children and adolescents in the USA (20). Similar to the pattern in the general population, the obesity in childhood is increasing and so is childhood NAFLD (20, 21). NAFLD is now considered the most common cause of liver disease in the paediatric age group (22, 23). The incidence of NAFLD reportedly reaches 17% in early adulthood (24), but continues throughout life, with the highest rate in elderly age groups (>60 years in China) (25, 26).

In addition to obesity, a strong association is present between NAFLD and type II diabetes - which is closely related to obesity - and it is predicted that nearly half of the patients with type II diabetes in Europe will eventually develop NAFLD (7, 21). Given the current worldwide rate of increase in NAFLD, it is predicted to become the commonest cause of liver transplantation (5, 27).

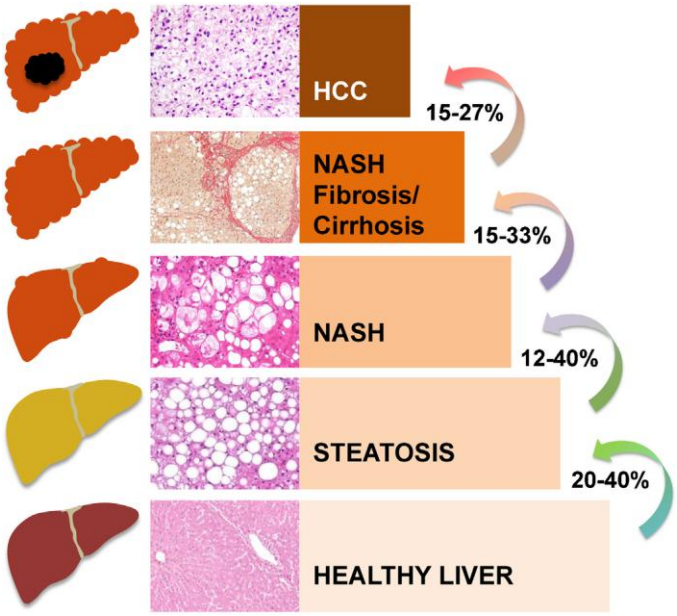

Figure 1.2: Showing the transition through NAFLD to HCC adapted from Yu et al (11).

1.2.3 Pathogenesis

Because of the changes in the style of modern life throughout the last century, individuals levels of activity have reduced and eating habits have changed - with an increase in the consumption of fast food that is rich in trans-fatty acids (processed fat), alongside with fructose-rich drinks. This dietary excess has resulted in an increased incidence of overweight and obesity, which have become major diseases that threaten communities. Their incidence has increased to worrying levels, reaching about 50% of the general population in the developed countries, with increased NAFLD incidence as a consequence (28-30). Furthermore, one of the most important

risk factors for HCC development is morbid obesity (which is defined as a body mass index BMI of > 40 kg/m^2) (13, 31).

At least two theories of NAFLD pathogenesis have been proposed. The "two-hit theory" is one, in which a first hit represented by the accumulation of fat inside hepatocytes, sensitise them to the second hit. The second hit most likely arises as a result of accumulating 'free' fatty acids (FFA), where the influx exceeds the hepatocyte ability to either store or metabolise them properly, leading to oxidative stress, death of hepatocytes and ultimately fibrosis - as part of a wound healing response (21, 32). A multi parallel hits theory has also been proposed, in which multiple factors act together to cause liver damage and inflammation (33). In the second theory the inflammatory response might occur prior to and even promote steatosis (7).

1.2.3.1 Key processes in NAFLD pathogenesis and progression

Lipid accumulation in the liver happens due to several factors, including increased fat levels due to increased dietary consumption, altered lipolysis, increased fat synthesis (lipogenesis), and possibly defective extracellular transport or excretion (33).

Excess glucose can contribute to lipid accumulation, with obesity, Insulin resistance (IR) and type II diabetes closely related. In the normal state, insulin binds to insulin receptor (INSR) and causes activation of the insulin substrate-1 (IRS-1) as well as PI3K/Akt pathway. PI3K/Akt activates glucose uptake by the cell and activates glycogen synthase leading to glycogen synthesis (34). Insulin resistance (IR) is a major player in NAFLD pathogenesis, contributing to a) increased lipolysis which leads to increased (FFA) that accumulate in the hepatocytes; b) inhibition of glycogen synthesis; c) stimulated glycolysis which leads to increase glucose levels (Hyperglycemia) that stimulate further secretion of insulin from the pancreatic β-cells.

Accumulation of FFA in hepatocytes promotes an increase in mitochondrial and peroxisomal β-oxidation, as well as activation of the transcription factor peroxisome proliferator activator receptor (PPAR-α), leading to transcription of genes involved in β-oxidation, which produces reactive oxygen species (ROS). Furthermore, the excessive β-oxidation of fat contributes to depletion of mitochondrial DNA (mtDNA) and hence disturbs mitochondrial function (**Figure** 1.3) (35).

The accumulated ROS in the presence of steatosis leads to hepatocyte lipid peroxidation, endoplasmic reticulum stress (ER stress), disturbed cell functions, cell death, stimulation of cytokine derived liver damage (TNF-α mainly) and increased cytokine secretion, all of which ultimately lead to fibrosis. ROS also induces JNK1, which inhibits the insulin activation

pathway and contributes to IR through inhibition of IRS-1 function, blocking the insulin pathway by phosphorylating IRS-1 at an inhibitory site (Ser312 in humans and 307 in mice) (**Figure** 1.3**)** (21, 36, 37).

Elevated insulin and glucose also contribute to steatosis through increased transcription of sterol regulatory element binding protein (SREBP1c) and other factors which are necessary for lipid synthesis (38). SREBP1c is negatively regulated (deacetylated and inactivated) in part by silent mating type information regulation 2 homolog 1 (SIRT1), and SIRT1 (which is a member of the histone deacetylase (HDAC) family) has a central role in fat metabolism and prevents fat accumulation in hepatocytes (39, 40). This negative regulation of SREBP1c by SIRT1 can be blocked through inhibition of SIRT1 by miRNA34a. It has been suggested that miRNA34a can bind to and inhibit the translation of SIRT1 mRNA and thus inhibit SIRT1 (21, 41). Since miRNA34a is a direct transcriptional target of p53, activation of p53 leads to inhibition of SIRT1, and consequent release of SREBP1c from the inhibitory effect of SIRT1, promoting lipid synthesis and accumulation in hepatocytes leading to steatosis, increased oxidative stress, cell injury and inflammation (7, 42-44).

Apoptosis as an important contributing factor in NAFLD pathogenesis was recently brought to our attention. With progression of the disease it was found that p53 levels increase, activating both the intrinsic (BAX, PUMA and NOXA) and extrinsic (FAS & TNF related death receptor) pathways of apoptosis, mediated by mitochondrial release of cytochrome-C and activation of caspase proteolytic cascades (45, 46). FFAs can also cause apoptosis through activation of JNK1, that causes increased p53-upregulated modulator of apoptosis (PUMA), and activation of BAX, which again lead to mitochondrial dysfunction and caspase-dependent apoptosis (**Figure** 1.3) (47). Engulfment of apoptotic bodies by stellate cells and Kupffer cells leads to generation of death ligands and Fas which promote further apoptosis (21, 37).

Lipotoxicity induced hepatocellular damage is an important factor in NAFLD pathogenesis through induction of apoptosis. It was found that due to the lipotoxic effect of FFAs DR5 is activated and can lead to hepatocellular injury through proapoptotic signalling and activation of macrophages (48). Lipotoxic injury might be lethal or sublethal to the hepatocytes (**Figure** 1.4) (49).

One of the features of sublethal lipotoxicity and hepatocellular injury is what is called hepatocellular ballooning (undead cells). This term describes hepatocytes with cellular degeneration marked by swelling of the cells and centrally located nucleus, reticulated

cytoplasm, accumulation of ubiquitinated proteins and loss of keratin 8 and 18 (49, 50). These cells are implicated in the pathogenesis and are the hallmark of NASH. Another histological feature that is linked to sublethal lipotoxic injury is the accumulation of insoluble protein inclusions in hepatocytes (Mallory-Denk bodies) that are linked to liver inflammation and fibrosis (49).

Recently it has been implicated that lipotoxicity induces intercellular signalling through extracellular vesicles (EV) release (49). EVs include exosomes (which are ~50-100 nm diameter membrane bound part of the multivesicular body (MVB)) and microvesicles (which are ~50-1000 nm and bud from the plasma membrane) (49). These EVs contain several components and mediators including proteins, RNAs, surface receptors, and lipids. EVs bind to targeted cells by interacting with surface receptors, followed by internalisation and fusion releasing their contents into the cells. Under physiological conditions EVs are released into body fluids to reach and exert their action on target cells. In NASH, lipotoxically-injured hepatocytes release EVs which contain heterogeneous compounds of which is the stress kinase mixed lineage kinase 3 (MLK3) that causes macrophages chemotaxis and activation in the liver through the potent C-X-C motif chemokine ligand 10 (CXCL10) (51). Other compounds in these EVs are miRNAs of which miRNA128-3p that regulates liver fibrosis (52), proteins inducing angiogenesis like surface protein vannin-1 (VNN1) (53), oxidised mitochondrial DNA and DAMPs that leads to inflammation (**Figure** 1.5) (54).

Another important factor is gut microbiota which plays important role in NAFLD pathogenesis. There are more than 10^4 microorganisms inside the human gastrointestinal tract that have important role in health and disease. Alteration of these commensal bacteria have a role in NAFLD development (55). Studies showed monosaccharides absorption through the intestine is increased by gut microbiota leading to increased hepatic lipogenesis through the de novo pathway and through fasting-induced adipocyte factor suppression (55, 56).

Gut microbiota causes insulin resistance through overgrowth of bacteria in the small intestine that impair intestinal epithelial cells tight junctions (that is a barrier against bacterial translocation) leading to increased intestinal permeability (57, 58). Subsequently more bacteria and lipopolysaccharides will translocate into the liver through the portal vein with increased expression of Toll-like receptor 4 (TLR4) and release of interleukin-8 stimulating inflammation of the liver. Not only that but gut microbiota converts choline (which is important in cell membrane and liver fat transport) into toxic metabolites (dimethylamine and trimethylamine)

that are further converted by the liver into more toxic compound trimethyl oxide leading to liver injury and inflammation (59, 60).

1.2.3.2 Role of Fructose

Fructose intake in large amounts and for long periods of time is closely related to IR and obesity, and hence NAFLD. It causes IR through activation of MAPKinases like MKK7(MAP2K7) and MAPK8, which inhibit hepatic glucose uptake and therefore promote glucose accumulation extracellularly (hyperglycemia), with consequent increases in insulin secretion from pancreatic cells in response to the elevated blood glucose levels (61).

Fructose also increases lipid synthesis by activation of both SREBP1c and carbohydrate response element binding protein (ChREBP), which control key enzymes like fatty acid synthase (FASN) and acetyl-CoA carboxylase (ACC) (61). At the same time fructose also causes inhibition of free fatty acid (FFAs) oxidation in the mitochondria. This is due to the fact that fructose metabolism leads to production of Acetyl CoA. If Acetyl CoA is produced in large amounts, some is converted into Malonyl CoA, which inhibits the mitochondrial oxidation of FFAs. Furthermore, some excess fructose is converted into citrate that is a substrate for lipogenesis. Thus, excess fructose leads to accumulation of FFAs and inhibits their oxidation. These FFAs will accumulate and contribute to steatosis as described above (62, 63) In addition to these effects, animal model data suggests that increased intake of fructose may be associated with greater levels of necroinflammation and fibrosis in the liver (37).

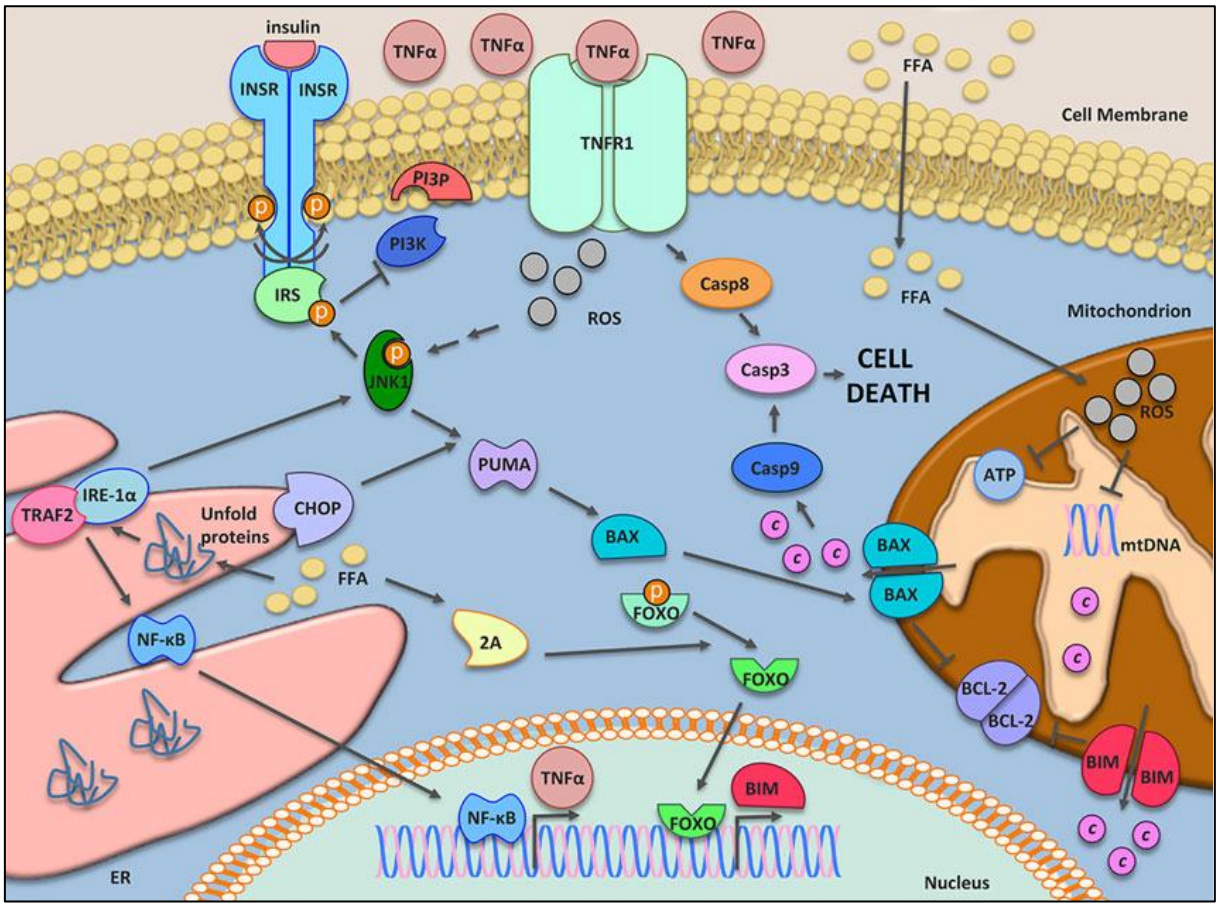

Figure 1.3: Mechanisms of pathogenesis in NAFLD elucidating the role of FFA, IR and ROS, adapted from Ferreira et al (21). Increased influx of FFAs into the hepatocytes will overwhelm mitochondrial β-oxidation causing an increase in ROS levels and depletion of mtDNA. ROS is also increased through TNF-α which is increased in NAFLD patients. FFAs also activates protein phosphatase 2A which dephosphorylate and activate the transcriptional target FOXO3. FOXO3a causes increased BIM levels, which results in apoptotic pathway activation. Endoplasmic reticulum (ER) stress is also increased in NAFLD patient liver cells, with accumulation of unfolded protein and inhibition of insulin signalling through phosphorylation of IRS-1. JNK and ER stress induced CAAT/enhancer binding homologous protein (CHOP) cause upregulation of PUMA, which activates BAX and in turn creates pores in the mitochondrial membrane releasing cytochrome c and activating apoptosis through caspase activation. ER activates NFKB pathway with more production of TNF-α, which plays a role in NASH.

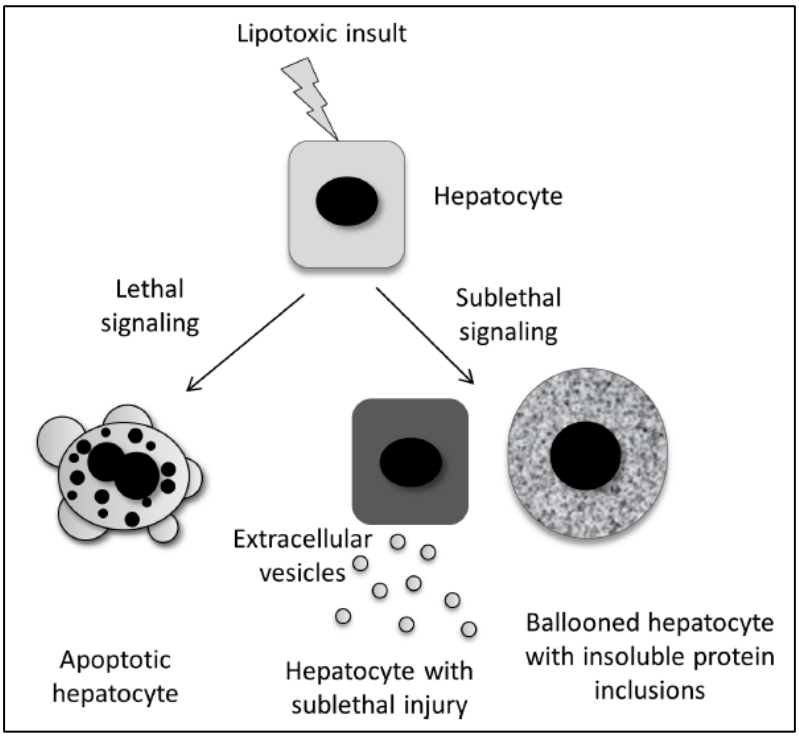

Figure 1.4: Lipotoxic injury to the hepatocytes adapted from Ibrahim et al (49). Lipid accumulation induces lethal (apoptosis) and sublethal injury of hepatocytes in the form of proapoptotic signalling with the release of extracellular vesicles and in the form of ballooning of hepatocytes.

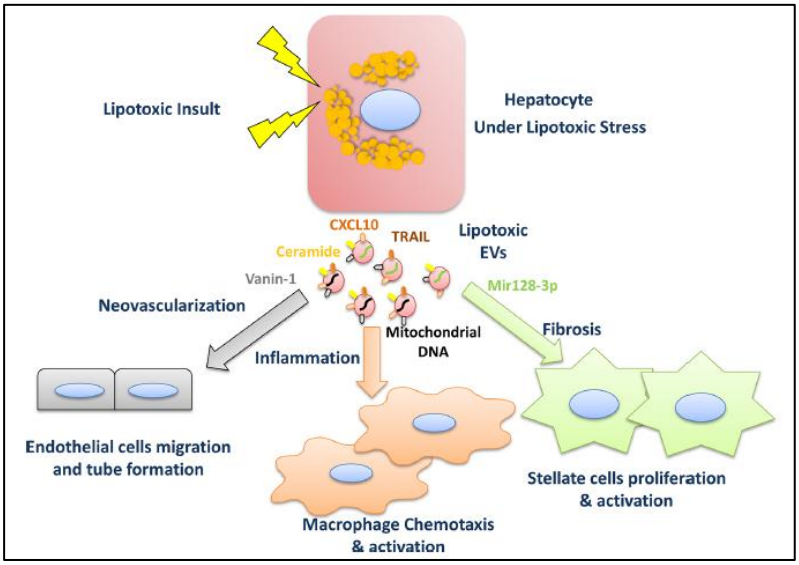

Figure 1.5: Extracellular vesicles (lipotoxic-induced hepatocyte-derived) effect on liver adapted from Ibrahim et al (49). Lipoptoxic injury induces the release of EVs from hepatocytes that contain several mediators that play important role in the pathogenesis of NASH. These mediators include miRNA128-3p that induce fibrosis through stellate cell activation. CXCL10 and ceramide, TRAIL and mitochondrial DNA vesicles induce macrophage accumulation and activation. Neovascularisation and endothelial cell migration is stimulated by VNN1.

1.2.3.3 Genetic factors

Genetic factors also play a role in the pathogenesis of NAFLD and may explain differences in the rates of progression of NASH in some patients. A single nucleotide polymorphism (SNP) in patatin-like phospholipase domain containing protein 3 (*PNPLA3*), a gene located on chromosome 22 that encodes triacylglycerol lipase enzyme, mediating hydrolysis of triacylglycerol in adipocytes, is one of the most common genetic variations associated with increased steatosis and liver fibrosis in NASH patients, as well as with HCC (64, 65). The prevalence of the variant allele of this gene, that affects PNPLA3 function, was also found to be increased in Caucasian lean NAFLD patients (66).

Other genetic variations linked to NAFLD and NASH progression through genome-wide association studies are those involved in lipid metabolism like transmembrane 6 superfamily 2 (*TM6SF2*) (a transmembrane protein found in the endoplasmic reticulum and Golgi membranes and responsible for lipid transport), farnesyl diphosphate farnesyl transferase 1 (*FDFT1*) (important in the production of cholesterol), and glucose metabolism - like glucokinase regulator (*GCKR*). GCKR is an important regulator of glucose uptake and glycolysis and affects mitochondrial β-oxidation and fat deposition (64, 65).

1.2.4 Grading and staging of NAFLD

Rather than subjective histological assessments of the severity of NAFLD, grading systems which include scores for the semi-quantitative evaluation of the morphological features of NAFLD have been proposed, with the aim of promoting consistency and reproducibility (67-69). These include the Brunt system which refers to the grades of severity of NASH (70), the NASH Clinical Research Network's NAFLD activity score (NASH CRN-NAS), and the steatosis, activity, and fibrosis (SAF) scoring system (67, 68, 71). A comparison between the three systems is summarized in **Table** 1.1(69). The NAS CRN scoring system includes several parameters which are scored separately and then a total score is calculated. It uses steatosis, lobular inflammation and ballooning as criteria for scoring NAFLD; and there is a separate stage for fibrosis. The steatosis is given a score between zero and three (0-3), according to the percentage of hepatocyte affected, in which zero means <5%, 1= 5-33%, 2= 34-66% and 3= >66%. Hepatocellular ballooning (HB) is similarly scored (0-2), with no ballooning, mild or few cells with ballooning and moderate or marked ballooning respectively. Lobular inflammation (LI) is the third parameter and is scored (0-3) depending on inflammatory foci per high power field (0=no foci, 1=<2 foci, 2=2-4 foci and 3=>4 foci). The maximum score is 8. According to this system, a score of 0-2 excludes NASH, scores of 3-4 suggest borderline

NASH, while ≥ 5 defines NASH (71). However, a score of 5 can be achieved in the absence of ballooning – thought by many to be a cardinal feature of NASH. The use of an 'activity score' centered on ballooning and lobular inflammation, was proposed as part of the SAF scoring system as a more accurate way of diagnosing NASH, assuming a grade of at least '1' for steatosis. A SAF activity score of 2, including the presence of both HB and LI, can be used for diagnosing NASH (**Figure** 1.6**)** (68).

Table 1.1: A comparison between NAFLD scoring systems, adapted from Kleiner & Makhlouf 2016 (69).

Numerical Grade or stage	Burnt system	NASH CRN-system	SAF system
		Steatosis grade	
0	None	< 5%	< 5%
1	≤ 33%	5% to 33%	5% to 33%
2	33% to 66 %	33% to 67%	33% to 67%
3	> 66%	> 67%	> 67%
		Lobular inflammation grade	
0	No foci	No foci	No foci
1	1-2 foci per 20X field	< 2 foci per 20X field	< 2 foci per 20X field
2	2-4 foci per 20X field	2-4 foci per 20X field	≥ 2 foci per 20X field
3	> 4 foci per 20X field	> 4 foci per 20X field	
		Hepatocellular ballooning grade	
0	None	None	Only normal hepatocytes
1	Mild, zone 3	Few	Few, clusters of hepatocytes with rounded shape and reticulated cytoplasm
2	Prominent, zone 3	Many	Many, enlarged hepatocytes (≥ 2X normal)
3	Marked, zone 3		
		Portal inflammation grade	
0	None	None	
1	Mild	Mild	
2	Moderate	More than mild	
3	Severe		
		Fibrosis stage	
0	None	None	None
1	Zone 3 perisinusoidal fibrosis only	Perisinusoidal or periportal fibrosis; 3 substages defined	Perisinusoidal or periportal fibrosis
2	Zone 3 perisinusoidal fibrosis and periportal fibrosis	Perisinusoidal and periportal fibrosis	Perisinusoidal and periportal fibrosis
3	Bridging fibrosis	Bridging fibrosis	Bridging fibrosis
4	Cirrhosis	Cirrhosis	Cirrhosis

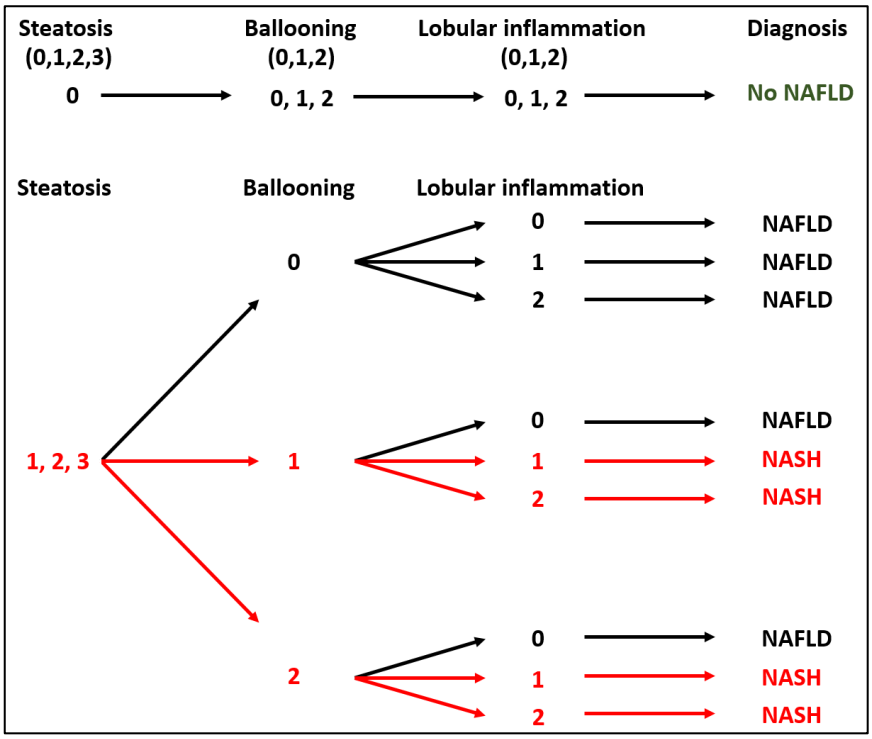

Figure 1.6: Bedossa et al algorithm for the diagnosis of NASH (68).

1.2.5 Management of NAFLD

The ideal methods to manage NAFLD that researchers have investigated centre on lifestyle modifications that include weight loss and exercise (72). Several studies reported the effect of body weight loss and healthy diet on improving the state of liver disease in patients with NAFLD and NASH - with carbohydrate restricted hypocaloric diet being very effective. A Mediterranean diet that is rich in fibres and polyunsaturated fatty acids can improve steatosis in 6 weeks in patients with NAFLD. Exercise, independently of any effect on weight loss, can improve insulin resistance (hepatic and peripheral) in patients with NAFLD, in addition to improving their cardiovascular status (72, 73). Losing 3-5% of body weight is sufficient to improve hepatic steatosis (74), and it has been shown that 40% reduction in hepatic triglyceride content can be achieved through rapid loss of body weight (4% within 2 weeks) with caloric restriction (75).

Lifestyle change is unfortunately challenging for many and difficult to maintain in the longer term. Another successful modality of treatment in morbidly obese patients is bariatric surgery, which can deliver a 25% maintained weight loss, associated with improvement in steatosis and steatohepatitis in the majority of patients receiving it (76). Benefit in terms of fibrosis is

presently less certain, being improved in some, but with some reports of no change or elevations 7-40% (77).

Patients with NASH are widely believed to be those at risk of progressing to fibrosis, cirrhosis and HCC (73). Although large number of recent studies clearly indicate that it is those patients with stage 2 fibrosis or above that are at highest risk of developing cirrhosis (73) or have a higher risk of mortality (78), recently reported and ongoing pharmacological intervention trials have and are centred on patients with NASH. The PIVENS trial compared pioglitazone, vitamin-E and placebo and was focused on adults with NASH who had a NAS score of ≥4. The TONIC trial, which compared metformin, vitamin E and placebo, was conducted in children with NAFLD and some but not all of them had NASH. Both trials reported a modest histological benefit for the antioxidant vitamin-E. In the PIVENS trial there was improvement in steatosis, lobular inflammation and liver enzymes; while the TONIC trial reported improvement in NAFLD activity score and reduction in ballooning, but was not successful in reducing liver enzymes in the treated individuals. Both trials failed to show any improvement effect on fibrosis (79, 80). Unfortunately, long term intake of vitamin E was associated with increased risk of prostatic cancer (73). Pioglitazone, which is a peroxisome proliferator- activated receptor gamma (PPAR-γ) that belongs to the thiazolidinedione family, is another drug undergoing investigation for the treatment of NAFLD. It increases the insulin sensitivity and decreases glucose levels (through decreased production and increased consumption) which was shown to improve steatosis and inflammation; in a similar but less effective way to vitamin E (81).

Obeticholic acid which is a potent FXR agonist (Farsenoid X receptor (FXR) is a nuclear receptor that is usually activated by bile acid (discussed in more details in chapter 4), is another treatment modality for NAFLD. It was found to regulate lipid and glucose metabolism and hepatic inflammation. The FLINT trial reported obeticholic acid to improve steatosis, inflammation, ballooning and fibrosis, but 20% of patients developed pruritus that was significantly associated with improvement in the histological features (82).

Pentoxifylline, which is a xanthine derivative used to treat pain and cramps and can reduce inflammation and fatty acid oxidation, is another cheap well tolerated drug under investigation and promising in the treatment of NASH (83). While several drugs are being tested for the treatment of NAFLD, liver transplantation is used as a last resort for those patients who develop liver failure or HCC (72).

1.3 Hepatocellular Carcinoma (HCC)

Hepatocellular carcinoma (HCC) is the second leading cause of cancer death worldwide (84). Owing to late stage presentation and co-existing underlying liver disease, the prognosis for the majority affected is poor, with a 5 year survival of less than 15%. Importantly, while overall cancer related deaths have been declining, deaths from HCC have been increasing over the last decade (85).

Asian countries, especially eastern and south eastern ones, have the highest incidence of HCC, with China taking the lead in accounting for half of the patients with HCC in the world. Usually HCC develops in cirrhotic patients, in those with hepatitis B or C or alcoholic liver disease. However, HCC can occur with lesser degree of fibrosis, particularly in men (86, 87).

The incidence of NAFLD related HCC has been increasing, especially in Western countries where it accounts for 4-22% of HCC cases (88). If the 15-30% of global HCC cases attributed to cryptogenic cirrhosis are considered in part NAFLD related, the contribution is even more striking. It is estimated that around 50% of cryptogenic cases are attributable to NAFLD (88).

1.3.1 Risk factors for HCC

The vast majority of HCC cases develop in chronically diseased livers, with cirrhosis being the major risk factor. Thus, any risk factor for cirrhosis is also considered as a potential risk factor for HCC, and these include alcohol intake, hepatitis B virus (HBV) infection, hepatitis C virus (HCV) infection, non-alcoholic steatohepatitis (NASH), and primary biliary cirrhosis(89, 90).

HCC can also develop in non-cirrhotic liver, being reported in pre-cirrhotic CHB, in NAFLD, in association with aflatoxin B1 exposure, and also with the hepatic iron overload which occurs in those with hemochromatosis (89, 91-93).

Viral hepatitis contributes the greatest burden overall, with Gurtsevitch et al (94) showing that nearly 50% of the global HCC were in HBV infected patients, and 25% were in HCV infected patients. Infection with HBV increases the incidence of HCC by 100 times. HBV is a DNA double-stranded virus that incorporates in the human genome contributing to mutation and chromosomal instability which explain why HBV related HCC can occur in the absence of cirrhosis. In addition, however, the consequences caused by the viral infection include an inflammatory response, necrosis, healing by scarring, in combination with regeneration. These result in cirrhosis, with additional inflammation associated DNA damage increasing mutations which disrupt the regulation of cell growth and contribute to HCC development. Specific HBV-

related genetic abnormalities are recognised, including an integration which encodes for the viral protein HBx, which stimulates transcription of NFkB and other kinases that cause increased proliferation and inhibition of apoptosis (92).

HCV on the other hand is an RNA virus that does not incorporate into the host genome. In addition to its cirrhosis related risk, however, infection reportedly stimulates oxidative stress through its core protein effects on the endoplasmic reticulum and mitochondrial outer membrane. The interaction can generate reactive oxygen species, which stimulate the NFkB and kinase pathways, affecting gene transcription and conferring additional risk. This can occur in the absence or presence of cirrhosis (95). HCV also stimulates the secretion of tumour necrosis factor alpha (TNF-α) and Interleukin-6 (IL-6), which induce IR and are involved in fibrogenesis (92).

In Sub-Saharan Africa and Southeast Asia, the ingestion of food contaminated with aflatoxin (that is a mycotoxin produced by Aspergillus fungus, due to food storage in conditions of high humidity and temperature) leads to high HCC incidence. This toxin binds to DNA in a sequence dependent manner inducing a characteristically high incidence of *TP*53 mutation at codon 249. *TP53* mutation is detected in half of the HCC cases in sub-Saharan Africa (89, 96).

Metabolic risk factors are also clearly important. The risk of HCC development is increased two-four times by type II diabetes mellitus (97-99), irrespective of the underlying etiology of chronic liver disease. In the United States, metabolic disorders had the highest contribution to the burden of HCC over the last decade (100).

Obesity and diabetes act together in a synergistic way to massively increase the incidence of HCC, which is increased by 100 times when combined with viral hepatitis B or C infection (101). In one study of the link between obesity and HCC, it was alarmingly reported that there was a 20-30% increase in the risk of liver cancer with each unit increase in the BMI (102).

Several epidemiological studies have now confirmed that NAFLD is a strong risk factor for HCC development, which might even develop in the early stages of NAFLD. In other words it doesn't need to pass through the usual route starting with steatosis, NASH, cirrhosis ending with HCC (103). Recent studies suggest that development of HCC in patients with NAFLD quite often presents without NASH or cirrhosis – with reports suggesting that this accounts for between 20 and 50% of cases (11, 93, 103, 104). Some of these reports may be affected by reporting bias – as patients without cirrhosis may have better preserved liver function and be more likely to be referred to tertiary referral centres. However, while the risk of HCC is very

much greater in patients with cirrhosis, even a relatively small – presently poorly understood – risk in obese, diabetic NAFLD patients without cirrhosis, does appear to translate into significant numbers of cases, given the prevalence of the at risk population. Common aetiologies and risk factors are summarised in greater detail below.

An additional risk factor is the deposition of iron in the liver which increases the risk of HCC development in cirrhotic patients with NASH. Iron deposition causes increased oxidative stress, which in patients with haemochromatosis raises the risk for HCC by 200 fold (11).

In developed countries, due to the improvement in controlling the risk factors for HCC (like hepatitis C and B), and due to the high and increasing incidence of obesity, the incidence of HCC due to HBV and HCV is decreasing while the incidence of NAFLD induced HCC in those countries is rising (87-89).

1.3.2 Molecular mechanisms of development of HCC in NAFLD

In chronic liver disease continuous injury to the hepatocytes will lead to cell death. Due to the regeneration capability of the liver, hepatocytes regenerate and proliferate; but unfortunately this chronic insult causes continuous division, which may be accompanied by genetic defects which contribute to HCC carcinogenesis (105). These include genetic mutations, and epigenetic changes (which involves hypo or hypermethylation that may cause activation of oncogenes or silencing of tumour suppressor genes respectively). The potential involvement of changes in miRNA expression (e.g. of miRNA 139 and 122 in HCC) have also been suggested (106). There are several pathways commonly disrupted by these kinds of changes which can contribute to carcinogenesis in HCC, including PI3K/Akt, Myc, Wnt/B-catenin, c-Met and hedghog (92, 106).

As reported above, obesity and diabetes are the major risk factors for NAFLD. Lipid deposition can lead to hepatotoxicity, increased lipid peroxidation and reactive oxidative stress. In addition to the lipotoxic effect on increasing oxidative stress, Kupffer cells when activated in NAFLD produce large amounts of reactive oxygen species that contributes to the increased oxidative stress (107). Oxidative stress is not only a major factor in NAFLD pathogenesis, but may also be a major factor in HCC carcinogenesis - through induction of DNA damage as well as mitochondrial DNA damage (107-109), associated with the induction of cell injury, apoptosis and cellular proliferation (93).

Recently it was reported that NAFLD induces selective loss of CD4+ T lymphocytes (that inhibits HCC initiation and progression) through increased ROS release (110). CD4+

lymphocytes have high ROS levels derived from their high mitochondrial mass, and the increased ROS in NAFLD lead to depletion of CD4+ lymphocytes that exerts anti-tumour activity, hence increasing the risk of tumour development due to impairment of anti-tumour surveillance (110). Additionally, it was found that CD8+ T lymphocytes function is suppressed in NAFLD through the accumulation and increased activity of IgA+ cells. This leads to decrease in the anti-tumour surveillance exerted by CD8+ lymphocytes and increase in HCC development (111).

Chronic DNA damage induced by oxidative stress induces regeneration through proliferation of hepatic progenitor cells, which are also activated by Kupffer cells in chronic liver injury (88, 112). The chronic injury of hepatocytes in NAFLD also stimulates Hedgehog signalling, leading to mobilisation of hepatic progenitor cells to replace the injured hepatocyte as part of the healing process. The continuous state of stimulation of the Hedgehog pathway can lead to aberrant proliferation and hepatocarcinogenesis (113, 114).

Abnormal lipid accumulation can also lead to a continuous state of inflammation characterised by the release of two factors implicated in the pathogenesis of HCC in NAFLD, namely tumour necrosis factor (TNF) and interleukin-6 (IL-6) (103, 115, 116). TNF activates several pro-oncogenic pathways, like Nuclear Factor-kappa B (NFkB), c-Jun NH2-terminal kinase (JNK), and the mammalian target of rapamycin (mTOR). IL-6 secreted by tumour associated macrophages plays a pivotal role through activation of the JAK/STAT3 pathway leading to stimulation of cellular proliferation and inhibition of apoptosis (103, 115, 117) (**Figure** 1.7). Additionally IL-6 is a downstream target of FGF19 which is commonly amplified in HCC and associated with poor prognosis and this appears to be through activation of JAK/STAT3 pathway (118). Lipid deposition also leads to disturbance in the levels of adipokines (119), one of which is adiponectin. Adiponectin has a strong anti-inflammatory effect and suppressive effect on oncogenic pathways. It also negatively regulates angiogenesis (93). Adiponectin suppression occurs in NAFLD and exacerbates the Kupffer cell mediated inflammatory response towards gut derived endotoxin, which leads to hepatocyte injury and proliferation (93, 120-122). The lipid related disruptions or disequilibrium between the pro-inflammatory cytokines TNF and IL-6 and the anti-inflammatory effect of adiponectin are believed to favour the development of NAFLD-HCC (11, 123).

Leptin is another important adipokine, which is elevated in NAFLD and is known to stimulate Kupffer cells and stellate cells, leading to fibrosis and a more progressive NAFLD (119, 124-

127). In addition, leptin favours immortalisation of hepatocytes through the upregulation of telomerase, also promoting HCC development (93, 128).

NAFLD associated IR and hyperinsulinemia leads to activation of insulin receptor substrate-1 (IRS-1) and elevated levels of insulin-like growth factor (IGF-1). Both insulin and IGF-1 promote cell proliferation and have also been implicated in the development of HCC (87, 93, 129-132). Hyperinsulinemia also promotes deregulation of several signalling pathways, including p53, mitogen-activated protein kinase (MAPK), phosphatidylinositol-3 kinase (PI3K/Akt), which can inhibit apoptosis and stimulate cell proliferation, further encouraging HCC development (11, 93) (**Figure** 1.7).

Recently, it was suggested that the tumour suppressor Liver kinase B1 (LKB1) might play an oncogenic role in HCC. It was found to be elevated in cirrhotic liver HCC. LKB1 regulates proliferation through the Akt pathway, as well as controlling p53 function through phosphorylation at Ser 389, preventing its movement into the nucleus and interfering with its function. This was demonstrated in an animal model and supported by studies in human tissue samples from NASH patients (133).

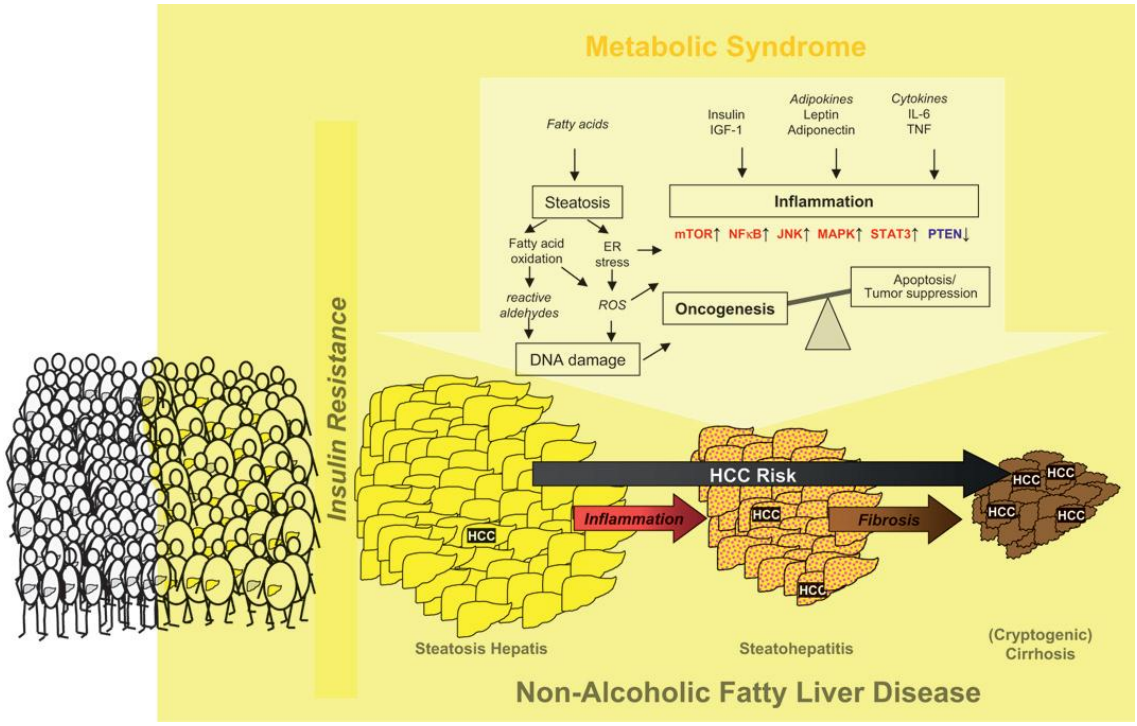

Figure 1.7: Relation between NAFLD, metabolic syndrome and HCC adapted from Stickel and Hellerbrand 2010, (134). Excess FFAs cause increased lipid peroxidation and ER stress which lead to increased ROS and DNA damage and oncogenic reactive aldehydes in addition to an inflammatory status with increased secretion of TNF and IL-6. Hyperinsulinemia, increased leptin and increased TNF and IL-6 promote inflammatory, proliferative and oncogenic pathways and suppress apoptosis. Collectively and with time there is malignant transformation and hepatocarcinogenesis.

1.3.3 Morphology of hepatocellular neoplasms

1.3.3.1 Hepatocellular adenoma (HCA)

Rare primary benign liver tumour that affects females more than males in their 30-50s and arises in non-cirrhotic liver. They are related to the use of oral contraceptives and to the use of anabolic steroids. HCA (usually solitary) are well demarcated macroscopically but do not have capsule. They are composed of benign hepatocytes that are usually larger and paler than non-neoplastic hepatocytes without nuclear pleomorphism or hyperchromasia. The neoplastic hepatocytes are arranged in 2-cell thick trabeculae and the acinar architecture is lost (135).

1.3.3.2 Hepatocellular carcinoma (HCC)

HCC usually present as a single mass but sometimes as multiple nodules (commonly in cirrhotic liver) or diffuse involvement of the liver or they are of massive type with very large size. Microscopically, the malignant tumour cells are arranged in several layers (>3 cell-thick) trabeculae, or sheets and tubules (pseudoglandular with papillary-like projections) with loss of reticulin network (135, 136). Intranuclear pseudoinclusions are often seen in the tumour cells caused by cytoplasmic invagination. The cytoplasm of the malignant cells may contain Mallory-Denk bodies, pale bodies (which are membrane-bound clusters of granular material), α-fetoprotein and α1-antitrypsin containing round hyaline globules, copper or bile pigment. The cytological and nuclear pleomorphism vary depending on the degree of differentiation of the tumour (135).

1.3.3.3 Grading of HCC:

The most commonly used system to grade HCC is the Edmondson and Steiner system that consists of 4 grades (137). Grade I, in which malignant tumour cells are small and are arranged in trabeculae with abundant cytoplasm and their nuclear irregularity is minimal with close similarity to the normal hepatocyte. Grade II, the malignant tumour cells show prominent nucleoli, hyperchromatism and their nuclei show more irregularity than grade I. Grade III, tumour cells nuclei are angulated and show more pleomorphism than that seen in grade II. Grade IV, in which the tumour cells show prominent pleomorphism and anaplastic giant cells (136).

1.3.3.4 Histological variants of HCC:

Clear cell hepatocellular carcinoma: Male predominance is prominent in this subtype in which the tumour cells have clear cytoplasm (hence the name), are arranged in trabeculae and they have cytoplasmic fat vesicles (136, 138).

Steatohepatitic HCC: This type usually arises in patients with steatohepatitis but it might also develop in patients without it. More than 5% of the tumour cells show steatosis in addition to the presence of ballooning, Mallory-Denk bodies, fibrosis and inflammatory infiltrates (136, 139).

Scirrhous HCC: This subtype shows characteristic fibrosis along the sinusoid-like blood spaces with trabecular atrophy. It can be misdiagnosed as cholangiocarcinoma or metastasis. The location of this HCC type is subcapsular and pedunculated gross appearance. It has been reported that 84% of the cases have remarkable CD8+ve lymphocytic infiltrate (136).

Sarcomatous HCC: The tumour is composed of spindle-shaped cells with bizzare anaplasia, and frequent giant cells. It is difficult to differentiate in appearance from leiomyosarcoma and fibrosarcoma (136, 140).

Fibrolamellar HCC: It is a rare type that occurs in young patients without liver cirrhosis and accounts for a minority of cases (<1%) with a better prognosis than HCC. It mimics focal nodular hyperplasia due to fibrous septae and occasional calcification in the central scared zone (138). Polygonal tumour cells form trabeculae and sheets separated by hyalinised collagenous fibres giving a lamellar appearance with frequent cytoplasmic inclusions (eg. PAS-positive cytoplasmic globules and ground glass pale bodies) with abundant immunohistochemical expression of keratin 19 and keratin 7 (136).

HCC with lymphoid stroma: This subtype has few identifiable malignant cells and a dense stromal inflammatory infiltrate, composed mainly of lymphocytes (CD3+ , CD4+ T lymphocytes and CD20+ B lymphocytes), with few macrophages, neutrophils, plasma cells and giant cells (141).

1.3.4 Staging of HCC

Staging systems are used to assess the disease status and extent of spread of the tumour in order to be able to predict the prognosis and plan an efficient treatment strategy that aims to extend patients life by weighing the benefit of the treatment against the side effects or drawbacks. Cancer staging systems - such as the widely used Tumour Node Metastases (TNM) systems – consider tumour characteristics predominantly (142). In patients with HCC, however, staging systems need to be combined with some measure of underlying liver function, as this is equally important in determining patient fitness for therapy and survival. Several combined staging system have been put forward for HCC, but due to the diversity of the disease in different parts of the world and among different patients, few have been widely applicable. The Barcelona Clinic Liver Cancer (BCLC) staging system (143, 144) is the one now most widely adopted, and takes into consideration the tumour stage, liver function and performance status. It is recommended by both the European and American Associations for Study of Liver Diseases (EASL and AASLD), being a staging system that incorporates a management algorithm to guide treatment approaches (See **Figure** 1.8). This system aids planning of treatment approaches accordingly for earlier stages with better prognosis, or in a very late stage with a poor prognosis. In those with very advanced stages, supportive care is appropriate, as intervention can shorten rather than extend life (145).

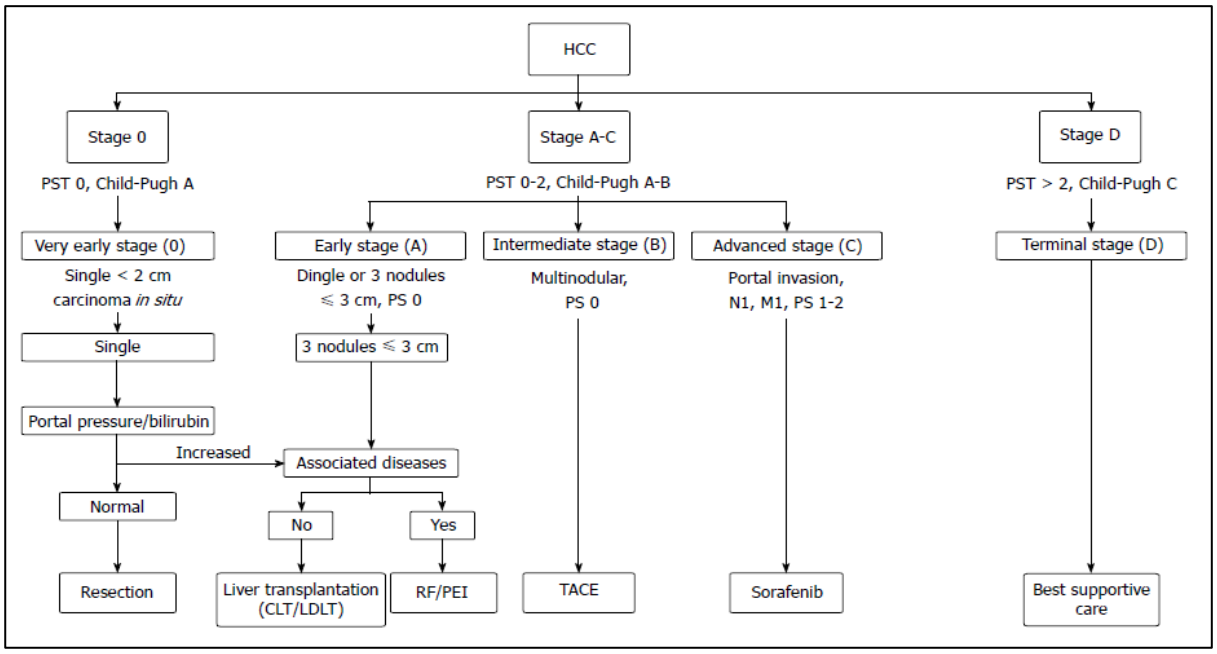

Figure 1.8: BCLC staging system with treatment modalities adapted from Tabrizian et al (145).CLT: Cadaveric liver transplantation. LDLT living donor transplantation; RF: radiofrequency; PEI: percutaneous ethanol injection; TACE: Trans arterial chemoembolization; PST: performance status test.

1.3.5 Treatment and prevention of HCC

HCC is one of the diseases with the poorest prognosis and despite the improvements in treatment modalities the mortality rate is still high because of the late diagnosis and rapid progression of the disease, with low sensitivity to chemotherapy and radiotherapy (145, 146).

Surgical intervention (excision and transplantation) appears to be the only curative treatment in early stages of the disease that succeeded in achieving a high 5 year survival rate ranging from 50 to 75%, but unfortunately it applies for a small percentage of cases and the recurrence rate is still very high – being about 70% after 5 years post tumour excision (145, 147-149).

Resection and transplantation are only applicable in early stages. Orthotopic liver transplantation (OLT) removes the diseased organ predisposing to HCC, while disease recurrence or de novo HCC are relatively common following resection. OLT, however, is a limited resource, determined by donor availability (150, 151).

Ablation (mostly thermal, which has replaced chemical ablation) is another technique used in the treatment of HCC, but is usually preferred for solitary, small lesions <2 cm and in those who are not candidates for surgery. It involves using high radiofrequency ablation (and nowadays high frequency microwaves) to induce tumour damage by heating and denaturing it. Other modalities like cryo and laser ablations are being tested (152, 153).

Transarterial chemoembolization (TACE) is used in patients with BCLC stage B HCC by injecting chemotherapeutic agent (doxorubicin) into the tumour via the hepatic artery, followed by an embolizing agent to keep the doxorubicin localised in order to increase the damage inflicted to the tumour. For carefully selected patients treated with TACE, there is a significant improvement in the 2 year survival (154-156). Drug eluting beads-TACE (DEB-TACE) and Transarterial radioembolization (TARE) with ytterium-90 microspheres are alternative locoregional treatment approaches (157, 158). Other options emerging include hepatic artery delivered Selective Internal Radiotherapy Treatment (SIRT), as well as Stereotactic Body Radiation Therapy (SBRT) (145, 159).

Systemic cytotoxic chemotherapies have traditionally been of limited use in patients with HCC, in part because of the effects on the associated diseased liver, but also because of inherent resistance to chemotherapies. Mechanisms of resistance include elevation of ABC transporters, such as p-glycoprotein, which export drugs from cancer cells, as well as cytochromes which metabolise drugs and decrease their effectiveness. Other resistance mechanisms include resistance to DNA induced damage, as well as accelerated DNA damage repair. The SHARP

trial (151), published in 2008, followed by the Asia-Pacific trial in 2009 (160), were considered a landmark in HCC patient care, as for the first time a systemic therapy was shown to have a significant survival benefit. The systemic therapy was Sorafenib, a multi-targeted tyrosine kinase inhibitor, with an inhibitory effect on the proliferative and angiogenic capability of the tumour. It remains the only first line systemic treatment approved for use in patients with HCC (156). Unfortunately, its survival benefit is modest, with a median increase in overall survival of only 10-12 weeks (151). In 2017 FDA (Food and Drug administration agency in USA) approved the use of Regorafenib as a second line treatment for patient with HCC progressing on or after sorafenib (161). Numerous first and second line trials are exploring the roles of other targeted therapies, but it is likely that – owing to tumour heterogeneity – these will be useful for subgroups of patients only, possibly in combination with other novel agents or traditional therapies.

Given the difficulties of treating HCC combined with CLD, prevention would be ideal. This has been achieved partially, by controlling HCV and HBV infection in parts of the world where those two risk factors are endemic. NAFLD treatment and prevention of its progression into HCC is the major goal of many researchers nowadays (145).

1.3.6 Pre-clinical models of NAFLD

In an attempt to understand the histopathology of NAFLD and its progression to NASH and HCC, several animal models were developed taking in consideration factors behind NAFLD pathogenesis. Each animal model succeeded in replicating certain aspects, some of which replicated the physiological while others succeeded in replicating the histopathological aspects. To achieve this different mice strains and rats and different diet types were used (162).

As the hallmark of NAFLD is steatosis related to obesity and IR. One group of animal models of NAFLD focused on feeding the animals (C57BL/6) a high fat diet (HFD) with a fat content ranging between 45-71% (163, 164). They succeeded in inducing obesity and IR and steatosis in animal livers in addition to other features of NAFLD like ballooning and MDBs (164). Others used mice models with mutations targeting leptin. Leptin regulate satiety, and so defective leptin reponbse will lead to hyperphagia, obesity, IR and diabetes. This was achieved by using *db/db* and *ob/ob* mice strains (165, 166). *db/db* had homozygous mutation in leptin receptors, while *ob/ob* mice had mutated non-functional leptin. Those two strains mimicked NAFLD but fell short of developing NASH (165, 166).

Other groups focused on mimicking NASH through induction of NASH by feeding the animals a diet deficient in choline and methionine (MCD diet). Choline deficiency (which is stored and metabolised in the liver) results in steatosis, increased oxidative stress, changes in cytokines and decrease in adipokines (60). Choline deficiency causes slight inflammation and fibrosis (60). Choline plus methionine deficiency lead to more extensive inflammation and fibrosis. Therefore MCD diet considered a good model for NASH compared to HFD, but it does not mimic the metabolic syndrome and obesity induced NAFLD as the mice fed the MCD diet do not show IR and show weight loss, with low glucose levels and leptin and triglyceride levels (167, 168).To overcome this other groups tried feeding the *db/db* or *ob/ob* mice the MCD diet (162).

Some researchers investigated the effect of fructose as a player in NAFLD progression to NASH and in fibrosis. They fed the mice high fat high fructose (HFHF) diet. HFHF diet caused more fibrosis, more inflammatory cell infiltration, more oxidative stress and more collagen compared to HFD model (169).

Most of the above mouse models failed to properly recapitulate what happens in human NAFLD progression to NASH, fibrosis and HCC development. In addition to the limitations of the C57BL/6 HFD fed animal model (failure to show NASH pathology) and MCD diet fed models (no obesity and metabolic syndrome), the number of developed tumours was very low, 2.5% in HFD and 25% in CD-HFD models (162). C3H/He mice are known to develop obesity and impaired glucose tolerance test (IGTT) and tendency for development of spontaneous HCC by one year of age (170). Selecting this strain to be fed the American life style diet (ALIOS) rich in fat and fructose was based on combining the effect of HFD and HF on exacerbation of the C3H/He phenotype. This was in a way to resemble human in the development of obesity and IGTT with age and exacerbate their tendency to develop HCC with diet. By doing this we were aiming at creating an animal model that mimics human progression from NAFLD to NASH and HCC.

1.4 P53 pathway

1.4.1 Structure and function

P53 is an important cellular protein that was first discovered in 1979. It is encoded by a gene called *TP53*, which is located on the short arm of chromosome 17 and was initially cloned in 1983 (171). It has several important functions including the transcription of genes involved in regulation of cell cycle and programmed cell death, metabolic regulation, DNA repair mechanisms, senescence and in the angiogenesis process (172).

The p53 protein is 53kDa in size and comprises 4 main domains, the N-terminal transcriptional transactivation domain, a central sequence specific DNA binding domain and carboxy terminal oligomerization (TET) and regulatory (REG) domains (**Figure** 1.9).

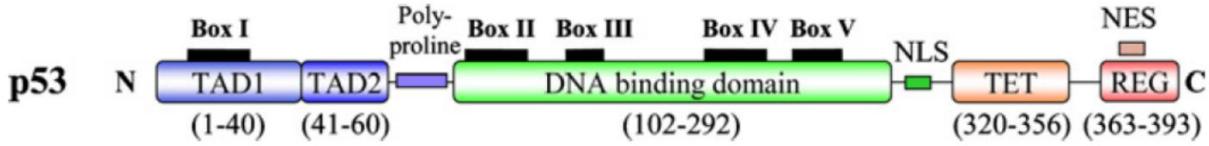

Figure 1.9: p53 structure showing functional domains. The N terminal region includes TAD1 and TAD2 transcriptional transactivation domains, there is a central DNA binding domain and a C-terminal regulatory region. The conserved regions include boxes I-V. TET is the tetramerization domain. NES is a nuclear export sequence and NLS is a nuclear localization sequence. (figure adapted from Meek, 2015) (173).

The p53 protein is stabilised and its transcriptional function activated by post-translational modifications in response to a range of cellular stresses, but particularly DNA damage. Once it is activated it forms tetramers that assemble on consensus-specific DNA binding sites in the DNA promotor regions of its target genes to induce their transcription. It either induces cell cycle arrest giving the cell enough time to repair the DNA damage or activates programmed cell death (apoptosis) to prevent the genetically damaged cell from dividing and propagating the genetic defect. This has led to it being referred to as the "guardian of the genome".

As a transcription factor it controls the transcription of a number of key genes, one of which is the murine double minute 2 (*MDM2*) gene, that was originally discovered as an amplified oncogene in a spontaneously transformed murine 3T3 fibroblast cell line. The MDM2 protein has an inhibitory effect on the function of p53 that is exerted through a) binding to the p53 transactivation domain and preventing it from binding to and transcribing its downstream targets (174, 175) and b) acting as an E3 ubiquitin ligase to target p53 for proteasomal degradation. MDM2 thus forms a negative feedback autoregulatory loop to restore p53 protein

and activity to basal turnover levels if and when the cause of the cellular stress is resolved. This feedback is vital in the regulation of p53 function and under normal conditions keeps p53 at low level (176, 177). This was demonstrated by the embryonically lethal effect of the absence of the *MDM2* gene in mice, which can be rescued by *TP53* gene deletion (178, 179). In fact MDM2 collaborates with another closely related protein called MDM4 or MDMX, which can also bind and inhibit p53, but lacks the E3 ligase activity of MDM2. MDMX forms a heterodimer with MDM2 and has been reported to enhance the ubiquitination and degradation of p53 (180) (**Figure** 1.10).

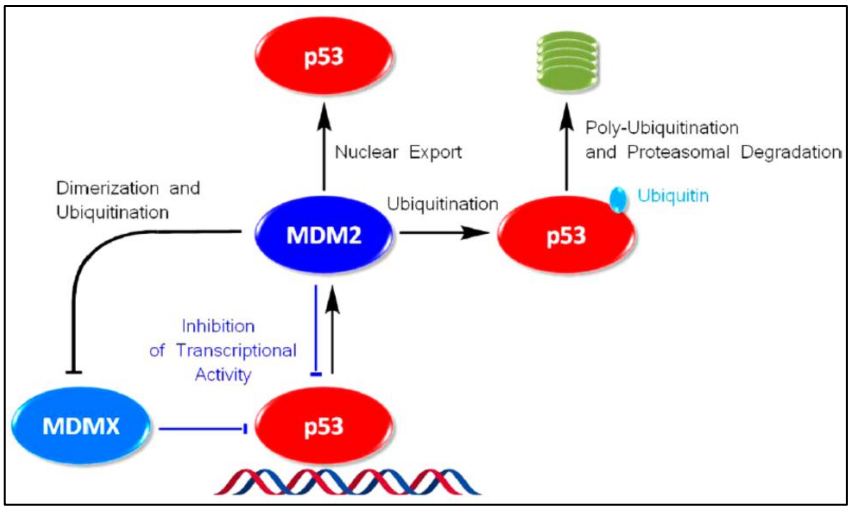

Figure 1.10: Regulation of P53 functions by MDM2 and MDMX. Adapted from Zhao et al 2015 (181). The transcriptional activity of p53 is regulated by its downstream transcriptional target (MDM2) and by MDMX. They form a complex and bind to p53. The binding by MDM2 prevents p53 from binding to DNA, as well as acting as an E3 ligase to ubiquitinate p53 and cause its proteasomal degradation, MDM2 is also reported to facilitate transport of p53 into the cytoplasm.

The activation of p53 is through several mechanisms, which includes activation by ataxia telangiectasia mutated (ATM) protein kinase that senses double stranded DNA damage to then phosphorylate and activate p53. In addition, ATM phosphorylates the CHEK2 cell cycle regulatory protein which also in turn phosphorylates and activates p53. The activation of p53 can also be mediated by other kinases such as ataxia telangiectasia and RAD3 related (ATR) and casein kinase II, or through abnormal growth signals like RAS activation, which requires a protein called p14ARF (CDKN2A). The p53 phosphorylation leads to prevention of binding to MDM2 and its consequent stabilization and accumulation in the cell as a result of the decrease in its degradation. Additional changes in the tertiary structure of p53, through additional post-translational modifications (phosphorylation, methylation, acetylation, sumoylation, or ribosylation) contribute to the regulation of p53 function. The three dimensional structure of

the inactivated p53 does not allow the DNA binding domain to bind to the DNA strands, but posttranslational modification allows the unfolding and exposure of this domain and hence allows it to carry out its transcriptional function (182).

Both cell cycle arrest and apoptosis by p53 are regulated through well-established mechanisms involving the transcriptional control of its target genes. The target genes involved in apoptosis include *BBC3* (*PUMA*), *NOXA*, *BAX*, tumour protein p53 inducible protein 3 (*PIG3*), *FAS* cell surface death receptor and others. The p53 protein is also believed to regulate apoptosis through non-transcriptional mechanisms (183). Under injurious conditions p53 translocates to the mitochondria and induces mitochondrial outer membrane permeabilization (MOMP) which leads to the release of proapoptotic factors. This is achieved by direct effect of p53 on the antiapoptotic and proapoptotic proteins, as it can bind to and inactivate antiapoptotic Bcl-2 and can bind to and activates proapoptotic proteins BAX and BAK, leading to apoptosis (184).

The regulation of cell cycle arrest in response to stress is another mechanism controlled by p53 through the transactivation of multiple genes. The *CDKN1A* gene, encoding the $p21^{WAF1}$ cyclin-dependent kinase inhibitor, is one of the main targets of p53 involved in growth arrest at the G1 and G2 phase cell cycle checkpoints, while growth arrest and DNA damage inducible 45 (*GADD45*) is another target gene involved in G2 arrest. The $p21^{WAF1}$ protein is involved in other p53 tumour suppression processes that include senescence, autophagy, regulation of cellular metabolism, antioxidant defence and microRNAs (miRNAs) (183, 185).

Other ways in which p53 functions as a tumour suppressor gene are through regulation of metabolic processes in the cell, including carbohydrate, amino acid and lipid metabolism (186, 187). It is well known that cancer cells use glucose and glycolysis for the generation of energy, and also their consumption of glutamine is increased to cover the need for nucleotide synthesis. There is also an increase in fat demand for organelle synthesis and energy production, so cancer cells synthesize fatty acids and increase their uptake. Several p53 target genes encode proteins that are key regulators of these metabolic processes. Depriving the tumours from these metabolic demands is an additional mechanism by which p53 can exert an antitumor effect. Examples of such targets that p53 regulates are: glucose 6 phosphate dehydrogenase (*G6PD*), TP53-induced glycolysis and apoptosis regulator (*TIGAR*) and glucose transporter 1, Acyl-CoA dehydrogenase family member 11 (*Acad11*) and *Lipin 1*, *SREBP-1* (187) (**Figure** 1.11).

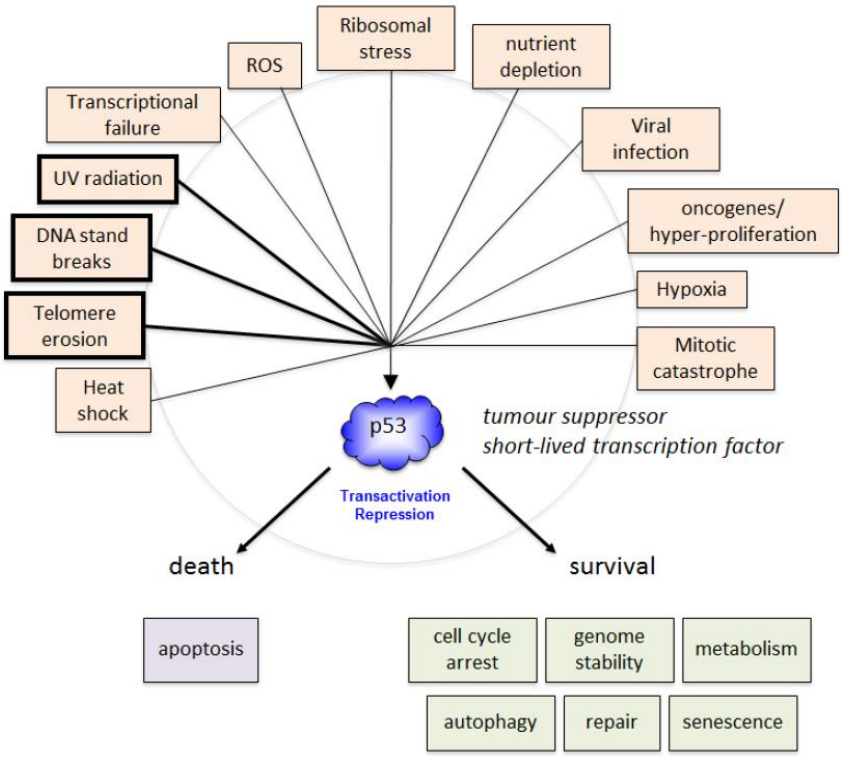

Figure 1.11: Showing different stimuli that induce p53 function and the end result, adapted from Loughery and Meek (180).

A large number of studies have shown that the *TP53* gene is mutated or absent in nearly 50% of human cancers, and this mutation leads to loss of the tumour suppressor function of p53. In the remaining 50% of cancers, *TP53* is intact but there may be inhibition of its function through other mechanisms including amplification and/or overexpression of its negative regulator MDM2 (172, 188).

Interestingly, it has been noted that when p53 is mutated, not only it loses the tumour suppressor activity, but also it acquires tumour promoting functions what is called gain of function (GOF) (189). One mechanism is through mutant p53 dominant-negative regulation of the remaining wild type p53 allele (189, 190). The mutant p53 often has a missense mutation that prevents p53 from binding to the DNA. This mutant p53 can bind to wild type p53 and forms a non-functional tetramer that prevents the remaining wild type p53 from performing its transcriptional function (189, 190).

Several mutant p53 GOF examples were illustrated in the lab and in animal models including promoting cell survival, proliferation, invasion and migration of malignant tumour cells (189). In addition to enhancing cancer metabolism through enhancing lipid metabolism and the Warburg effect. These GOF effects can be nuclear or cytoplasmic effects and can be achieved

through several mechanisms (189). Examples of nuclear effect is the regulation of transcriptional factors and cofactors leading to inhibition of tumour suppressor activities or promotion of tumour progression, like binding of mutant p53 to and inhibition of Tap63 and Tap73 (p53 family members with tumour suppressive activity) (191). Another mechanism of GOF is by regulation of expression of specific genes through regulation of chromatin structure leading to increased transcription of targeted genes associated with tumorigenesis and progression (189, 192). This was demonstrated through interaction and cooperation of mutant p53 and the chromatin remodelling complex (SWI/SNF) and through binding to Pontin (a potent helicase and AAA+ ATPase) (192, 193). Cytoplasmic GOF example is through Warburg effect stimulation (characteristic of tumour metabolism) through promoting of glucose transporter 1 translocation to plasma membrane by the mutant p53(194).

1.4.2 Role of P53 in chronic liver disease

Several factors play a role in the pathogenesis of chronic liver disease and p53 appears to be one of the important ones, in both ALD and NAFLD Multiple studies on rodent models have shown that there is upregulation of p53 and induction of apoptosis in NAFLD/NASH, and this was clearly evident at the protein level by immunohistochemical staining and western blotting showing increased levels of p53, p21 and caspase 3 (45, 195). These studies showed that p53-deficient mice had lower levels of steatosis, inflammation and fibrosis compared to wild type animals in the NAFLD animal model (45, 195). Similar results were reported for the analysis of liver samples from NAFLD patients, where p53 was shown to be upregulated immunohistochemically. The levels of p53 were higher in NASH patients than those with NAFLD, and both were higher than "normal liver" samples, although the latter were obtained from non-tumour areas of patients with colorectal metastasis to the liver (195). This was further supported by a study done by Derdak *et al* which showed that inhibition of p53 by pifithrin - α *p*-nitro (PFT) (which is a chemical compound that inhibits p53 binding to DNA) led to attenuation of steatosis in murine liver of high fat diet fed animals (196). Another suggested p53 regulated mechanism in NAFLD pathogenesis is through regulation of SIRT1 as explained before in (1.2.3.1) (40, 41, 44, 197).

1.4.3 p53 in HCC

TP53 is the commonest tumour suppressor gene that is mutated in human cancers, with the vast majority of mutations occurring in the DNA binding domain, and about 28% occurring in six so called "hot spot" residues in this domain (R175, G245, R248, R249, R273 and R282), five of which involve positively charged arginine residues (183, 198). While the Catalogue of Somatic Mutations in Cancer (COSMIC) states that 27% of HCC have a *TP53* mutation (199), other studies have reported varied percentages of *TP53* mutations ranging from 0% to 67%, depending on the geographical distribution of cases, being low in western countries and highest in sub-Saharan Africa and Southeast Asia (96).

The reason for higher incidence of *TP53* mutations in sub-Saharan Africa and Southeast Asia is the exposure to aflatoxin B1 (which causes a point mutation in codon 249Ser resulting in a G:C to T:A transversion) and HBV infection. HBx protein binds to p53 and inhibits its transcriptional function and might block p53-mediated apoptosis, leading to hepatocarcinogenesis (96, 200). Oxidative stress induced by iron and cupper deposition in the liver also causes *TP53* mutation at codon 249 and 250 (hot spot)in hemochromatosis and Wilson disease respectively (200). *TP53* mutation is usually associated with poor prognosis (96).

1.4.4 Cell cycle and p53

Eukaryotic cell division is characterised by replication of the DNA and then dividing into two new cells in a cyclical process. The cell cycle is divided into phases that include a gap phase (G1), followed by a DNA synthesis (S) phase in which the replication of DNA takes place, and then another gap (G2) phase prior to the mitosis (M) phase during which the condensed chromosomes separate and cells divide into two daughter cells. In addition there is a (G0) resting phase in which the cells have exited the cell division cycle and are non-proliferating and not-growing (201) (see **Figure** 1.12).

These phases are regulated by cellular proteins, the key regulators of the cell cycle are cyclin dependent kinases (CDK) and cyclins which form a complex together and exert their action through phosphorylation of target proteins such as retinoblastoma (RB). CDKs are a family of nine serine/ threonine protein kinases. The level of CDKs remain stable during the cell cycle but the levels of their activators, the cyclins, change. Cyclin D which has three forms (D1, D2 and D3) binds to CDK4 and CDK6 to enter into G1 phase, while cyclin E binds to CDK2 to progress from G1 to S phase. In S phase cyclin A and CDK2 are required, while cyclin A binding to CDK1 is necessary to progress from G2 into M phase which is regulated by cyclin B-CDK1 complex (201) (**Figure** 1.12).

The activity of CDKs is regulated by inhibitory proteins that inhibit the cell cycle progression, and these inhibitory proteins bind to the CDKs or to the CDK-cyclin complex and inhibit its action. These CDK inhibitory proteins (CKI) fall into two families, INK4 family which includes p15 (*CDKN2A/INK4b*), p16 (*CDKN2A/INK4a*), p18 (*CDKN2A/INK4c*), and p19 (*CDKN2A/INK4d*), and the CIP/KIP family which includes p21 (*CDKN1A/WAF1/CIP1*), p27 (*CDKN3/CIP2*) and p57 (*CDKN1C/KIP2*) (202). The INK4 family inhibits cyclin D interaction with CDK4/6 and cause G1 arrest, while CIP/KIP family causes G1 arrest through inhibition of cyclin-CDKs complexes and to a lesser extent inhibition of cyclin B-CDK1 complex to cause G2 arrest. In addition to that p21 inhibits DNA synthesis through the inhibition of proliferating nuclear cell antigen (PCNA) (201) (**Figure** 1.12).

As a guardian of the genome, and in response to cellular stress such as DNA damage, p53 can induce cell cycle arrest at the G1 or G2 phases through transactivation of downstream targets, to allow the cell to survive the stress and repair the damage and prevent its propagation during cell division. One of the downstream targets is p21 (*CDKN1A/WAF1/CIP1*) which is involved in growth arrest at the G1 and G2 phase cell cycle checkpoints (185), while GADD45 (another downstream target of p53) inhibits cyclinB-CDK1 complex and prevents the G2/M progression

leading to G2 arrest. Another way p53 causes arrest at G2 is through an additional downstream transcriptional target protein product, 14-3-3-σ (*14-3-3σ*/*YWHAS)*, which acts by removing cyclin B-CDK1 complex from the nucleus (183, 203) (**Figure** 1.12).

Ki67 is a nuclear protein found to be expressed in proliferating cells. Its level increases in all phases of the cell cycle in proliferating cells (G1, S, G2, and M) and is absent in G0 phase although it is not necessary for cell proliferation (204). The exact function of Ki67 is unknown but being expressed in only proliferating cells and the high levels of expression in cancer cells has led to its use as a proliferation marker and makes it a good diagnostic and prognostic biomarker in tumours (205).

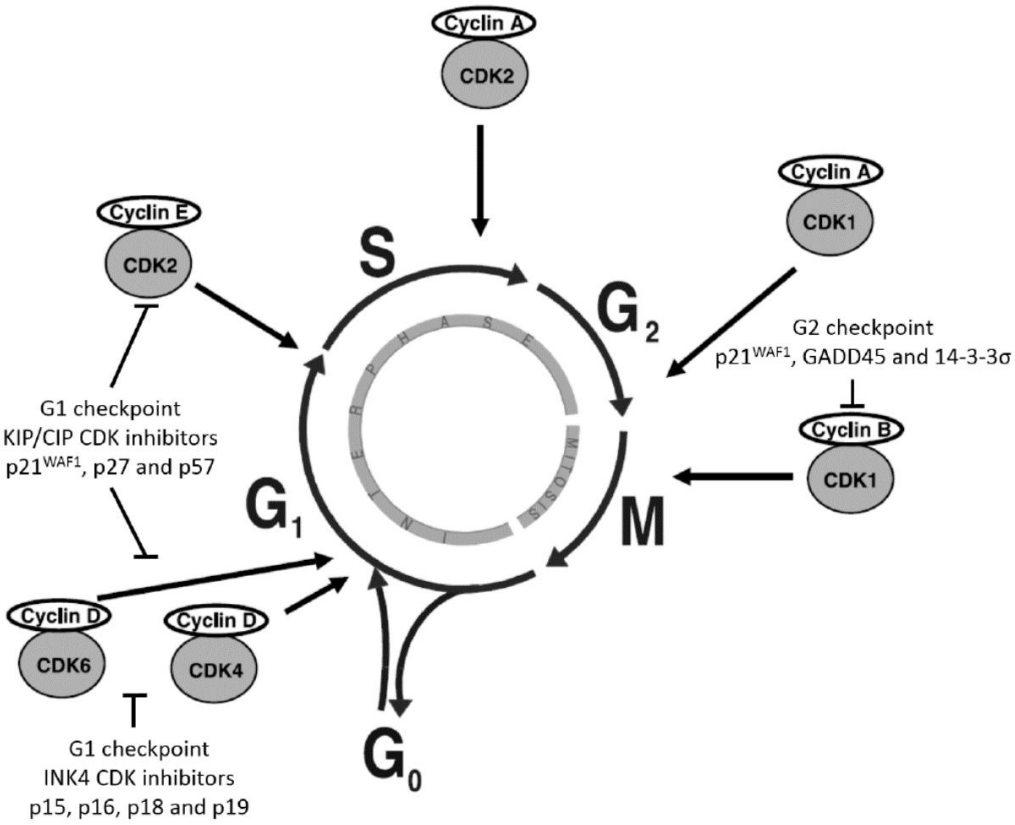

Figure 1.12: Phases of the cell cycle showing the sites of cyclin and cyclin dependant kinases regulation and their inhibitory CKI adapted from Esfandiari 2015 (201, 206).

1.4.5 P53 and Senescence

Senescence is a permanent state of growth arrest characterised by loss of proliferation ability of the cells in response to growth signals or mitogens. Additionally, senescent cell morphology changes and they become larger and flattened and express markers of senescence (p53, p21, p16, and senescence associated β-galactosidase (SA-β-Gal)), and senescence associated heterochromatic foci (207, 208).

Senescence can be triggered by several mechanisms. Replicative senescence occurs when there is shortening of the telomeres through repeated replication cycles. Oncogene induced senescence occurs as a result of persistent growth signals. Reactive oxygen species induced senescence occurs as a consequence of accumulation of oxidative DNA damage and involves p53. When DNA damage occurs, a DNA damage response (DDR) is initiated which stimulates Ataxia Telangiectasia-Mutated (ATM) phosphorylation of p53. Stabilised phosphorylated p53 leads to increased transcription of its downstream target p21, which suppresses cell growth but can also induce cell cycle arrest and senescence. Telomere shortening, if detected as a double strand break, can also activate a DDR leading to senescence. Similarly, increased DNA replication stress induced by oncogenic signalling can be associated with DNA damage generating a DDR. So, in other words, all three examples of senescence involve triggering of DNA damage repair mechanisms lead to activation of a senescence pathway. Senescence is considered as a potent tumour suppressing mechanism. Several studies have shown tumour regression after induction of senescence through activation of p53 (209, 210).

1.4.6 P53 and apoptosis

Apoptosis is a programmed cell death mechanism that occurs in normal physiological conditions (death of old cells and replacement by new cells) and in pathological conditions. It involves a series of active steps that includes condensation of chromatin and the formation of apoptotic bodies (budding of plasma membrane) that are engulfed by phagocytes. These events happen in response to intrinsic and extrinsic signals, hence the terms intrinsic and extrinsic apoptosis.

In extrinsic apoptosis the stimulation of a family of cell surface death receptors recruit adaptor molecules, which in turn activate one of the family of cysteine proteases that target aspartate residues (caspases) called the initiators. The initiators in turn activate caspases 3, 6 and 7, termed the executioners, which cause lysis of the cellular organelles through proteolytic activity

and cellular death. In Intrinsic apoptosis, the whole process is initiated by cellular signals and includes the release of mitochondrial apoptotic molecules like cytochrome c (211).

P53 activation can induce apoptosis through intrinsic and extrinsic pathways and it is known to regulate the transcription of more than 100 pro-apoptotic genes (211, 212). Of these genes that regulate the extrinsic pathway are tumour necrosis factor receptor superfamily 10A (*TNFRSF10A/DR4*), and 10B (*TNFRSF10B/DR5*), and (*TNFRSF6/FAS*). Activation of these genes leads to a sequence of events culminating in caspase activation and apoptosis.

P53 downstream transcriptional target gene products that induce intrinsic apoptosis include p53-upregulated mediator of apoptosis (PUMA), BCL-2 associated X protein (BAX) and BCL-2 antagonist killer 1 (BAK1). The transcribed proteins of these genes bind to and inhibit the anti-apoptotic function of BCL-2 family members (like BCL-2, BCL-XL). BAX and BAK form pores in the mitochondrial membrane that allow cytochrome c and other molecules to escape to the cytoplasm and activate caspases and apoptosis (213). P53 also has a direct effect on this pathway, binding to and inhibiting the function of BCL-2 family members (213).

1.4.7 Targeting MDM2-p53 in cancer

Although p53 is mutated in nearly 50% of tumours, this percentage varies from very low levels of <10% in thyroid cancer and paediatric malignancies to as high as nearly 96% in high grade serous ovarian cancers. It is clearly an important tumour suppressor and in some tumours its protein expression or function is reduced or suppressed, rather than mutated. Exploiting the p53 pathway in those wild type cases is an attractive therapeutic target (214). The negative regulators of p53 (MDM2 and MDMX) are overexpressed in tumours, ~20% of sarcoma and ~15% of breast cancer, and this means they inhibit p53 activity and behave as oncogenes. So targeting them to release p53 from their inhibitory action has been explored for cancer treatment (214).

One of the earliest attempts to exploit this pathway was in the nineties, when a small synthetic peptide homologue of p53 (IP3) was tested in cells that overexpressed MDM2. This peptide was an amino-acid substituted version of the N-terminal sequence of p53 which binds to MDM2 and shown to have a greater affinity to bind to MDM2 than the unsubstituted p53 peptide on which it was based. It was used to block MDM2-P53 interaction and stabilise p53. Introduction of this peptide into cells led to a reduction in colony formation, and cell cycle arrest and cell death in tested cell lines, through increased transcriptional activity of p53 and increased

expression of p53 downstream transcriptional targets (215). This proof of concept together with the solving of the X-ray crystal structure of a p53 peptide bound to MDM2 stimulated the search for small molecule inhibitors of the MDM2-p53 binding interaction, leading to the discovery of the Nutlin series of cis-imidazoline compounds, which bound to and blocked the small N-terminal hydrophobic pocket on MDM2 to which p53 normally binds. The consequent release of p53 from MDM2 inhibition stabilised p53 and resulted in activation of its growth inhibitory and pro-apoptotic functions (216, 217) (**Figure** 1.13). One of these compounds was Nutlin-3, a racemic mixture of two enantiomers (nutlin-3a and nutlin-3b). Nutlin-3a was found to be 150 times more potent than nutlin-3b (216). Nutlin treatment showed a dose dependent increase in p53 stabilisation and in the expression of p53 downstream targets (p21 and MDM2) selectively in p53 wild type cell lines, with cell cycle arrest, growth inhibition and apoptosis, and this was achieved both *in vitro* and *in vivo* (216). These studies supported the concept of non-genotoxic activation of p53 through small molecule inhibitors of the MDM2-p53 interaction.

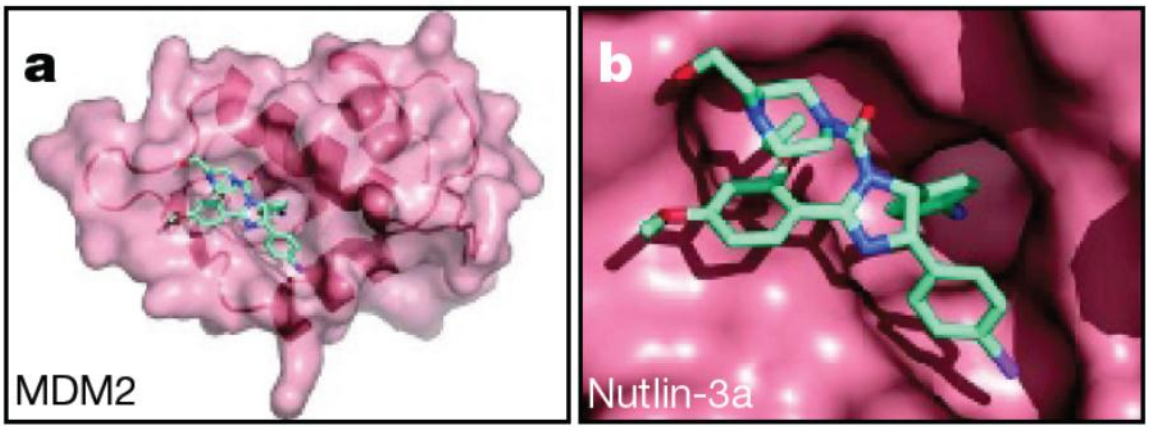

Figure 1.13: Three-dimensional modelling of Nutlin-3a binding to the p53-binding pocket of MDM2. A) MDM2 three-dimensional structure with nutlin-3a bound to it at the p53 binding pocket. B) Nutlin-3a (chemical structure) occupying the p53-binding pocket on MDM2. Adapted from Laurie et al 2006 (218).

Although Nutlin-3 was and is a useful tool compound, it does not have pharmacological properties suitable for clinical use. RG7112, which is a more potent and orally bioavailable Nutlin-based compound developed by Roche, was the first MDM2 inhibitor to be evaluated in early phase trials for solid tumours and haematological malignancies. It caused stabilisation of p53 and increased levels of p53 downstream targets (*CDKN1A, MDM2, BAX, PUMA, FAS, TNRSF10B, TP53INP1, ZMAT3 and FDXR*). Some patients with haematological malignancies achieved complete remission after treatment with this compound (217). It was relatively well tolerated, but gastrointestinal symptoms and haematological side effects (neutropenia and

thrombocytopenia) were observed, attributed possibly to the role of MDM2 in the survival of hematopoietic stem cells (219) and inhibition of megakaryocyte and hematopoietic cells through activation of p53 (220). In an attempt to reduce the side effects associated with the use of high doses, further development of the small molecule inhibitors led to the emergence of more potent compounds with better pharmacological properties, one of which is the Roche second generation MDM2 inhibitor RG7388 (Idasanutlin). HDM201, an imidazopyrrolidinone developed by Novartis, is one of the most recent and potent MDM2 inhibitors, with high selectivity for wild-type p53 cells (221). Encouraging results have been reported in xenograft tumour models, and it is already being tested in several ongoing clinical trials (222). Again side effects have been reported, with grade 3/4 haematological side effects (anaemia, neutropenia and thrombocytopenia that were regimen dependent and of late onset), although gastrointestinal side effects may be less severe (217, 221). Several small molecule inhibitors of MDM2 have been and are currently undergoing clinical trials - including RG7388, SAR405838, MK-8242, AMG232, DS-3032b, HDM201 and CGM097 (217, 221).

Another modality in exploiting p53 is through gene therapy by transducing cancer cells with wild type p53 (223). This can be achieved by replacing the E1 region (of a recombinant human serotype 5 adenovirus) by a wild type p53 expression cassette (rAd-p53) and used as a drug called Gendicine (223). Gendicine has been authorised as the first licenced gene therapy by the China Food and Drug Administration (CFDA) in 2003 (224). Introducing exogenous p53 expression in tumour cells induces cell death through apoptosis. This was shown in a phase I clinical trial involving arterial administration of Gendicine to metastatic colorectal carcinoma (225). In HCC this modality has also been tested in a pilot phase II clinical trial in unresectable HCC through multiple arterial injections of Gendicine (226), or through transcatheter bronchial arterial infusion of gendicine into pulmonary metastatic HCC (227).Recently it has been tested in BCLC stage B HCC patient through transarterial chemoembolization combined with gendicine gene therapy (TAGE) (223). This gene therapy with wild type p53 is promising and the side effects developed with TAGE were of low grade and no special intervention was required to treat them (223).

1.4.8 PPM1D /WIP1

Wild type-p53 induced phosphatase 1 (WIP1) is the protein encoded by the *PPM1D* gene. It is a member of the serine/threonine protein phosphatase 2C (PP2C) family. It is one of the downstream targets of p53 and forms an additional negative auto regulatory loop by dephosphorylating p53 at serine 15 site and inhibiting its function. The gene is amplified and activated by mutation in some cancers and it has oncogenic properties (228, 229). Additionally, WIP1 dephosphorylates other upstream p53 pathway proteins - including ATM, p38 MAPK and γ-H2AX - abolishing cell cycle checkpoints, inhibiting DNA repair and inhibiting apoptosis and senescence (230). WIP1 was also reported to dephosphorylate the negative regulators of p53 (MDM2 and MDMX), stabilising them and hence leading to downregulation of p53 see (**Figure** 1.14) (206, 231).

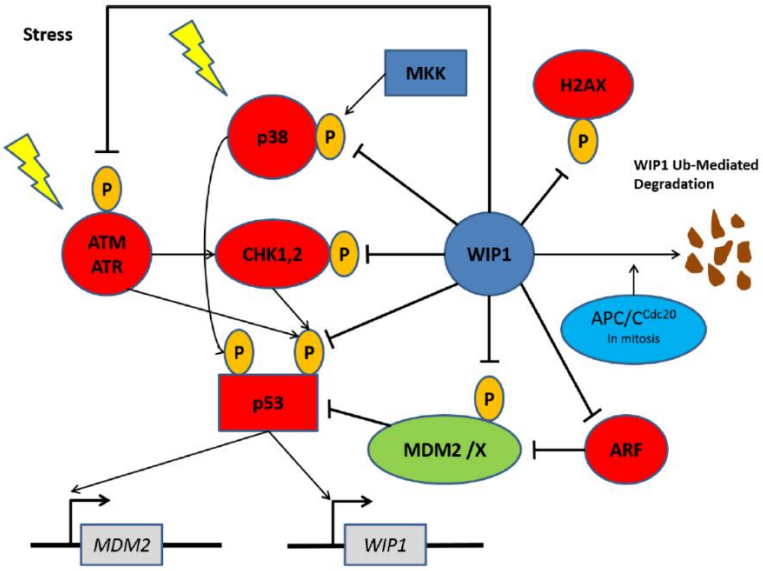

Figure 1.14: Direct and indirect effect of WIP1 on regulation of p53 and DNA repair adapted from Esfandiari 2015 (206).

Several studies have shown that *PPM1D/WIP1* is amplified and overexpressed in several solid tumours like breast, ovarian, neuroblastoma, medulloblastoma, gastric and pancreatic adenocarcinoma. Overexpression of WIP1 at both the mRNA and protein level was found to be associated with poor prognosis and shorter patient survival for these tumours (229). In HCC, several studies reported that WIP1 was overexpressed in 59% of cases at the protein level and 65% of cases at the mRNA level; and was found to be associated with larger tumour size, advanced stage, recurrence of tumour and shorter survival (228, 229, 232). Si-RNA knockdown of WIP1 in HCC cell lines showed inhibition of growth, invasion and migration of HCC cell lines. WIP1 has been proposed as a potential target for the treatment of liver cancer, as well as a prognostic marker (229).

1.5 Aims of the study:

1. Explore the effect of diet on the development of HCC in a relevant murine model.
2. Explore NAFLD progression and HCC grade in association with DNA damage and p53 expression.
3. Explore *TP53* status in HCC in the dietary murine model.
4. Explore the impact of dietary interventions on NAFLD, NAFLD stage and HCC development in the dietary animal model.
5. Explore the effect of non-genotoxic activation of p53 through MDM2 inhibition by small molecule inhibitors in liver cancer cell lines and a xenograft model.
6. Explore the effect of chemical inhibition of WIP1 on liver cancer cell lines.
7. Explore the effect of chemical inhibition of WIP1 on the sensitivity of liver cancer cell lines to MDM2 inhibition.

Chapter 2: Materials and Methods

2.1 General Laboratory Practice

Every experiment and procedure undertaken in the NICR or in the Medical School laboratories were performed following the standards set by Newcastle University to ensure safe working with biological and chemical substances in laboratories, which comply with the Control of Substances hazardous to Health Regulations 2002 (COSHH) and Biological COSHH (BioCOSHH).

2.2 Animal model design

An animal model was designed to study fatty liver disease and the risk of HCC development. C3H/He male mice were purchased from (Harlan, USA) and 4 mice were allocated in each cage. They were divided into two groups, the control (C) and the American Life Style group (ALIOS).

The control group (n=47) were fed a control diet (TD.110196, Harlan Laboratories, Wisconsin, USA) a normal fat diet (6% Soybean oil) with no trans-fat), while the ALIOS group (n=48) was fed (TD.110201, Harlan Laboratories, Wisconsin, USA), a high trans-fat diet with a high fructose corn syrup equivalent water (42g/L; 45% glucose, 55% fructose) to mimic what is served in fast food restaurant chains. Both groups were followed till they were 48-week-old and they were culled at 4 time-points (12, 24, 36 and 48 weeks).

In parallel to the above study we had an intervention study aimed at exploring the impact of two different interventions on NAFLD progression into NASH and/or HCC development. Each intervention consisted of two groups (C) and (ALIOS) and both received the intervention under study. The first intervention was the antioxidant (Bucillamine) (Santen Pharmaceutical, UK) at a dose of 10 mg/kg/day (n=22). The second intervention was Farsenoid X-Receptor (FXR) agonist (PX20606) (Phenex pharmaceutical, Heidelberg, Germany), for which two doses were used: 1 mg/k/day (n=24) and 5 mg/kg/day (n=16). The study design is shown in **Figure** 2.1.

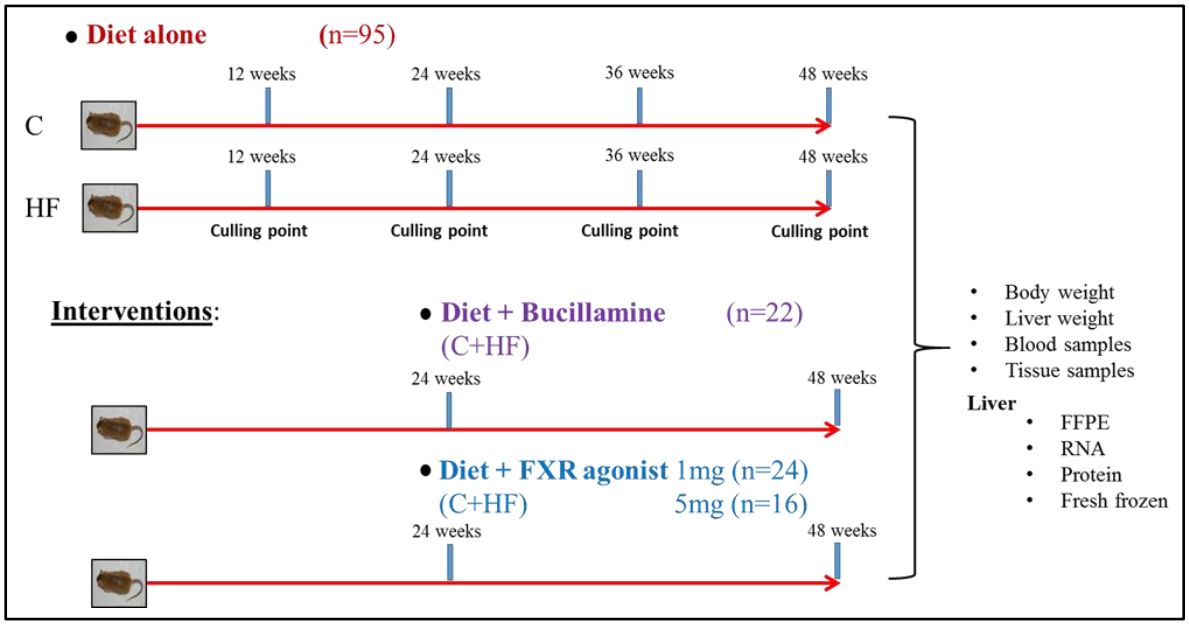

Figure 2.1: Dietary animal model design. C refers to control and HF refers to High Fat High Fructose diet (the ALIOS diet), n=number of mice, FFPE=Formalin Fixed Paraffin Embedded.

2.2.1 Animal culling and tissue sampling

Mice were culled at four specified time points, namely 12, 24, 36 and 48 weeks, where liver samples were taken. The samples were divided into three groups, including formalin fixed (samples put in tubes containing 10% formaldehyde to fix the tissue for paraffin embedded tissue blocks preparation), fresh frozen in liquid nitrogen and another set of samples was put in Eppendorf tubes containing RNA later solution to fix the tissue and preserve RNA from degradation. Then the formalin fixed and RNA later samples were placed in the refrigerator for 24 hours to allow penetration of the samples, while the fresh frozen were stored at -80 °C. The RNA later preserved samples were subsequently transferred into the -80 °C freezers for long term storage, while the formalin fixed samples were processed into paraffin-embedded tissue blocks.

Blood sample was collected from each animal through tail bleed before and after treatment. This was achieved through putting the animal in a hot chamber to induce peripheral vasodilatation and facilitate blood collection from the tail. This sample was sent to the chemistry lab to assess the liver function and lipid profile (MRC Harwell, Oxfordshire, UK).

2.2.2 Tissue processing and section preparation for histopathology study

After fixing, each sample was processed using the histology lab automatic tissue processor to ensure optimal dehydration and replacement of the water in the tissue with paraffin wax in paraffin block molds, in order to facilitate 3-5 microns microtome sectioning. This was achieved by passing them into jars containing ascending concentrations of ethanol (70, 95 and absolute) for 2 hours each; and then passing through xylene jars, with the final step being through melted liquid paraffin wax. Then the samples were embedded into paraffin blocks.

Ten sections (5 μM) were prepared from each case, from which one was stained with Hematoxylin and eosin according to a standardized protocol, for histological examination and assessment and scoring of the liver disease by a specialist liver pathologist. Another section was stained with Sirius red, a special stain used to stain fibrous tissue and to enable the histopathologist to assess and score the fibrosis stage. Other slides were used for immunohistochemical staining.

2.2.3 Scoring of routinely stained liver tissue sections

Each H&E and Sirius red stained slide was examined under the microscope and NAS and SAF scoring systems were used to score fatty liver disease and tumour grade (if present). The scoring was done by two independent people, a specialized liver pathologist Dr. Dina Tiniakos and Dr. Helen Reeves.

After examining the liver tissue sections and diagnosing NAFLD/NASH based on the pattern of injury and histological features, the disease status was given a score according to the NAS and SAF scoring systems of NAFLD (see 1.2.4). The NAS scoring system includes several parameters which are scored separately and then a total score was calculated. Steatosis was given a score (0-3) according to the percentage of hepatocytes affected; with 0= <5%, 1= 5-33%, 2= 34-66% and 3= >66%. Hepatocellular ballooning was scored (0-2) with no ballooning, mild or few cells with ballooning and moderate or marked ballooning respectively. Lobular inflammation is the third parameter and was scored (0-3) depending on inflammatory foci per high power field with 0=no foci, 1=<2 foci, 2=2-4 foci and 3= >4 foci. The total maximum score is 8. According to this system (0-2) score means there is no NASH, (3-4) indicates borderline NASH while ≥ 5 supports the presence of NASH (71). Due to this overlap, the use of the activity score (ballooning and lobular inflammation) in the SAF scoring system was more accurate in scoring NASH by using a cut off value of 2 for NASH (71).

2.3 Immunohistochemistry

Immunohistochemical staining of the liver sections was done to detect several markers of interest in our dietary animal model liver tissue sections; these were: phosphorylated Gamma-histone H2A variant H2AX (γ-H2AX), which is one of the sensitive early markers of DNA damage and repair (233); Ki67 as a marker of proliferation; the tumour suppressor p53, as well as the protein product of its downstream transcriptional target, *Cdkn1a*, referred to as p21.

The antibodies used were against γ-H2AX at the Ser139 site at a concentration of 1:100 (9718S, Cell signalling), Ki67 at 1:1000 (ab16667 (SP6), abcam), p53 CM5P at 1:400 (Novocastra), and p21 at a concentration of 1:50 (ab7960, abcam).

IHC staining was performed by either a manual protocol or with an automated Ventana processor (Roche).

2.3.1 γ-H2AX and Ki67 manual protocol

A two-day manual protocol was used for γ-H2AX and Ki67. Day one included dewaxing and rehydration of the tissue sections by passing through Xylene and descending concentrations of ethanol, eventually to water, followed by blocking of endogenous peroxidase using 3% H2O2 in methanol for 15 minutes. Slides were then washed once in PBS for 5 minutes at room temperature.

Antigen retrieval was also on day 1, in EDTA 1mM, microwaved for 15 minutes (power 80). Subsequently 300 ml of water was added, and the slides left to cool for 20 minutes at room temperature. Slides were then washed in PBS solution for 5 minutes at room temperature on a shaker. The tissue was encircled with a wax pen to promote coverage of tissues with the minimum of reagents. Avidin activity was blocked with 3 drops of a blocking solution per slide for 20 minutes at room temperature (Avidin/Biotin Blocking Kit, reference number SP-2001, Vector laboratories), followed by washing in PBS solution 3 times for 5 minutes at room temperature. Biotin was similarly blocked with the same kit. Antigenic sites were then blocked with 20% swine serum (diluted in PBS) for 30 minutes at room temperature, prior to adding the primary antibody and incubating the slides overnight at 4^0C.

On day two, slides were taken out of the refrigerator or the cold room and left to warm up and then washed in PBS 3 times for 5 minutes at room temperature. Swine anti rabbit biotinylated secondary antibodies were added (polyclonal swine anti-rabbit immunoglobulin, reference

number E0353 Dako), (1:200 dilution in PBS), and left for 60 minutes at room temperature, followed by wash in PBS 3 times for 5 minutes at room temperature.

Three drops of vector Avidin Biotin Complex (ABC) reagent were added per slide (Vector ABC tertiary, reference number PK 7100 Vector labs), and left for 45 minutes at room temperature to intensify the signal. Slides were then washed 3 times in PBS solution for 5 minutes at room temperature.

Then detection of the immunoreaction was done by adding 100 µl DAB mix (reference number SK 4100, Vector labs) which was prepared with 5 ml H_2O, 2 drops buffer, 4 drops DAB, 2 drops H_2O_2. The development reaction was monitored under the microscope until positive brown immunoperoxidase staining was seen. Then the reaction was stopped by adding PBS or washing in PBS.

Then the slides were counter-stained with Haematoxylin for 20 second, followed by washing the slides with tap water for 1 minute and dehydration in ascending concentrations of Ethanol, in steps of 50%, 70%, 90%, absolute, for 4 minutes in each. This was followed by clearing in xylol, twice for 5minutes each time. Slides were mounted with DPX and left to dry. Different buffers (PBS, TBS 1X and TBS tween 1X) were tested for the wash and dilution of antibodies with no difference in the results, but using TBS-tween facilitated uniform spread of the reagents over the tissues.

2.3.2 Automated IHC protocols

Automated IHC staining was performed using an automated system (Ventana machine, Roche) with different numbered Ventana protocols. For p53 IHC, protocol number 32 was used, which included a mild antigen retrieval. For p21 IHC, different protocols and four different antibodies from Abcam and Santa Cruz Biotechnologies companies were tested (ab7960, ab80633, sc-397, sc-756) using manual and automated staining techniques but they failed to produce convincing staining quality and after 3 months of optimization, anti-p21 antibody (ab7960, Abcam) (which gave the best results compared to the rest of the tested antibodies) was chosen and protocol 38 was used, which included an extended antigen retrieval and a blocking step. Antigen retrieval was heat-based as the slides were placed on heat-plates in the Ventana. Further details about the reagents and protocols are not disclosed by the manufacturer. After IHC, the slides were similarly mounted and left to dry.

2.3.3 Digital Imaging

The immunostained slides were scanned using an Aperio Digital Imaging system (AperioCS2, Leica Biosystems); which is a slide scanning system to capture interactive digital images of the slides (20X and 40X magnifications) and store high quality images of the scanned slides onto a server that can be accessed and analysed through the internet.

On the digital images, for each tissue section 30 selected areas were demarcated using Aperio Imagescope software. These included 10 periportal (around the portal tracts), 10 centrilobular (around the central vein) and 10 intermediate areas (in between the two). The specified areas were analysed using a designed algorithm using Aperio software (Spectrum Version 11.1.0.751 © Copyright 2006-2011 Aperio Technologies) to calculate the percentage of positively stained hepatocytes (**Figure** 2.2). Details of the algorithm are summarised in **Table** 2.1. There was a negative and positive control slide in each run. The negative control included processing the slides through all the immunohistochemical staining steps without adding the primary antibody to detect any non-specific binding of the secondary antibodies. The positive control slides were prepared from tissue micro array (TMA) of mouse tissue (liver, kidney and spleen) with parp+/+ and parp -/- status treated with doxorubicin.

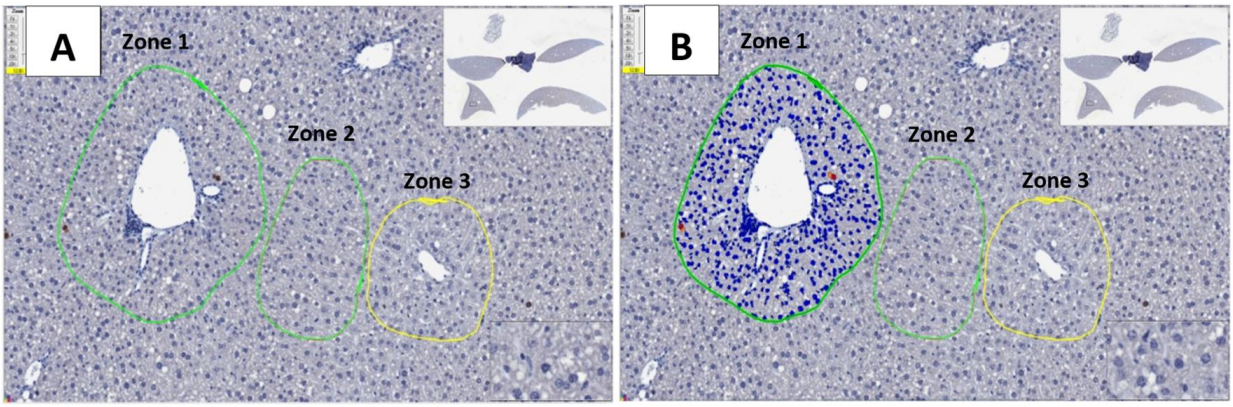

Figure 2.2: Aperio algorithm used for scoring immunohistochemical staining. (A) Demarcation of liver zones using Aperio tools. (B) Aperio algorithm applied for a γ-H2AX stained slide showing the detection of hepatocyte nuclei in the periportal area, with negatively stained nuclei bluish in colour and positively stained nuclei in brown (strong positive) and orange (moderately positive).

Table 2.1: Aperio algorithm details used for scoring IHC stained slides.

Aperio algorith parameters	Value
Version	9.1
View Width	1000
View Height	1000
Overlap Size	100
Pixel Size (um)	0.504
Averaging Radius (um)	1
Averaging Radius (Pixels)	2
Curvature Threshold	2.5
Segmentation Type	2
Threshold Type	1
Lower Intensity Threshold	0
Upper Intensity Threshold	200
Min Nuclear Size (um^2)	20
Min Nuclear Size (Pixels)	79
Max Nuclear Size (um^2)	1.00E+06
Max Nuclear Size (Pixels)	3.94E+06
Min Roundness	0.249
Min Compactness	0.25
Min Elongation	0.249
Remove Light Objects	0
Weak(1+) Threshold	210
Moderate(2+) Threshold	188
Strong(3+) Threshold	162
Black Threshold	0
Edge Trim	Weighted
Markup Image Type	Analysis
Nuclear Red OD	0.696858
Nuclear Green OD	0.643073
Nuclear Blue OD	0.317563
Positive Red OD	0.244583
Positive Green OD	0.509334
Positive Blue OD	0.825081
Clear Area Intensity	240
Use Mode	Analysis/Tuning
Classifier Type	IHC Nuclear

2.4 Molecular biology methods

2.4.1 RNA extraction

Ribonucleic acid (RNA) was extracted from murine tissue samples as well as from liver cancer cell lines.

The RNA later stored murine liver samples were thawed on ice and RNA was extracted using an RNeasy Mini Kit (Qiagen) according to the manufacturer's protocol. A DNase treatment step was included during the extraction to ensure the removal of any DNA, using on-column digestion with a RNase-free DNase kit (Qiagen), also according to the manufacturer's protocol. The RNA concentration was determined by measuring the optical density (O.D.) at 260 nm with a Nanodrop ND-1000 micro-spectrophotometer (labtech, International). The eluted RNA samples (30 µl) were stored at -80 ^{0}C.

For cell line work, cells were seeded at a density of 2.5-3 x 10^5 cells/well in a 6 well plate for 24 hours and then treated with the compound of interest for 6- and 24-hour time points. At time of harvest, the medium was removed and cells were washed with phosphate buffer saline (PBS) and cells were trypsinized and collected in Eppendorf tubes. Cell pellets were stored in -80°C freezers. RNA was extracted from the pellets using an RNeasy Mini Kit (Qiagen) according to the manufacturer's protocol. A DNAse treatment step with on-column digestion was carried out using the RNase-free DNase kit (Qiagen). The RNA concentration was determined by measuring the optical density (O.D.) at 260 nm by Nanodrop.

2.4.2 Reverse transcription

Reverse transcription system (RT) (Cat. No. A3500, Promega) was used to reverse transcribe RNA to generate cDNA from the extracted RNA samples, according to the manufacturer's protocol. 500 ng of RNA was added to a 10 µl reaction mixture, which consisted of 2 µl of 25 mM $MgCl_2$, 1 µl of RT 10X buffer, 1 µl of 10 mM dNTP mixture, 0.25 µl of Ribonuclease Inhibitor, 0.3 µl (15 units) of reverse transcriptase, 0.5 µl of oligo-dT 15 primer, made up to a final volume of 10 µl with nuclease-free water (**Table** 2.2). The samples were incubated at 42°C for 1 hour and at 95°C for 5 minutes and then kept at 4°C until storage at -20 ^{o}C.

Table 2.2: Reagents used for reverse transcription.

Reagent	Volume in µl
$MgCl_2$ magnesium chloride	2
Reverse Transcription 10X Buffer	1
dNTP mix 10 mM	1
Recombinant RNasin® Ribonuclease Inhibitor	0.25
AMV Reverse Transcriptase (HC)	0.3
$Oligo(dT)_{15}$ Primer	0.5

2.4.3 Quantitative Real time polymerase chain reaction (qRT-PCR)

Specific primers sequences were designed or taken from the Harvard Medical School primer bank web site and purchased from Invitrogen (Invitrogen, ThermoFisher scientific). The purchased primers were diluted in a ratio of 1:10 from 100 µM stocks to a working concentration of 10 µM. The primer sets were validated using the absolute quantification method with an ABI 7900 sequence detection system and GAPDH was used as a housekeeping reference gene. The validated primers were used in a semi-quantitaive real time polymerase chain reaction (qRT-PCR) and fold changes relative to a reference sample was calculated using RQ manager software (Applied Biosystem, version 1.2, Foster city, USA) and the formula $2^{-\Delta\Delta Ct}$, where Ct is the cycle number threshold to reach a given level of product detection. In this method a calibrator and a normalizer are used. The calibrator is the control or untreated sample while the normalizer is the housekeeping gene. To calculate the fold difference in expression of the gene of interest (GOI), the cycle threshold of that GOI is adjusted to the housekeeping gene in each of the samples and the calibrator as shown in the equation below (from life technologies Real-time PCR handbook):

$$\textbf{Fold difference} = 2^{-\Delta\Delta Ct}$$

$$\Delta\Delta Ct = \Delta Ct_{\text{ Sample}} - \Delta Ct_{\text{ Calibrator}}$$

$$\Delta Ct_{\text{ Sample}} = \Delta Ct_{\text{ GOI of Sample}} - \Delta Ct_{\text{ Normalizer (housekeeping gene) of Sample}}$$

$$\Delta Ct_{\text{ Calibrator}} = \Delta Ct_{\text{ GOI Calibrator}} - \Delta Ct_{\text{ Normalizer (housekeeping gene) of Calibrator}}$$

Prior to qRT-PCR, cDNA was thawed on ice and further diluted with 90µl of nuclease-free deionised water to ensure a final concentration of 5 nanogram per microliter. A master mix was prepared for each set of primers, which consisted of the following components for each 10 µl single reaction: 5 µl Platinum SYBR Green qPCR SuperMix-UDG with ROX (Invitrogen), 0.2

µl (10 µM) of each primer (forward and reverse) and 2.6 µl of nuclease-free H_2O. Two microliters of diluted cDNA (10 ngm) was added to each single reaction well, with 8 µl of master mix, to get a total volume of 10µl in each well. The samples were loaded in triplicates onto a 384-well reaction plate (MicroAmp optical plate, Applied Biosystems) and the qRT-PCR reaction was performed using the 7900HT Fast Real-Time PCR System (Applied Biosystems, Foster city, CA) with the standard thermal cycle steps (50^0C for 2 min, 95^0C for 10 min followed by 40 cycles of 95^0C for 15 sec and 60^0C for 1 min). Triplicate results were analyzed with SDS 2.3 software by calculating the relative expression of targeted genes in relation to the housekeeping gene (GAPDH) and a calibrator sample. In the dietary animal model study, the calibrator was one of the 12 weeks mice in the control group. For the cell line work, the calibrator was the control sample for the treatment condition. The mouse primer sequences that were used for the dietary animal model are listed in **Table** 2.3, while the primer sets used for the human liver cancer cell line work are listed in **Table** 2.4.

Table 2.3: Mouse primer sequences used for qRT-PCR.

The Genes	Primers Sequence (5' -> 3')		length
mTrp53	Forward	GCGTAAACGCTTCGAGATGTT	21
	Reverse	TTTTTATGGCGGGAAGTAGACTG	23
mMDM2	Forward	TAAAGTCCGTTGGAGCGCAAA	21
	Reverse	CTGCTGCTTCTCGTCATATAACC	23
mMDM4	Forward	TTCGGAACAAATTAGTCAGGTGC	23
(MDMX)	Reverse	GTGCATTACCTCTTTCATGGTGA	23
mP21	Forward	CAGATCCACAGCGATATCCAGACA	21
(CDKN1A)	Reverse	GAAGAGACAACGGCACACTTTGCT	20
mSIRT1	Forward	TGATTGGCACCGATCCTCG	19
	Reverse	CCACAGCGTCATATCATCCAG	21
mPARP1	Forward	GGTCTTTAAGAGCGACGCTTAT	22
	Reverse	TTCTGTGTCTTGACCATGCAC	21
mGadd45a	Forward	CCGAAAGGATGGACACGGTG	20
	Reverse	TTATCGGGGTCTACGTTGAGC	21
mNudt1	Forward	ACCTCCAGGCTTTATACCCTTG	22
	Reverse	CTTAGCCCCATCCTCAATGGT	21
mGAPDH	Forward	GGTGCTGAGTATGTCGTGGAGTCTA	25
	Reverse	GGGCGGAGATGATGACCCTTT	21

Table 2.4: Human primer sequences used for qRT-PCR.

The Genes	Primers Sequence (5' -> 3')		length
TP53	Forward	CAGCACATGACGGAGGTTGT	20
	Reverse	TCATCCAAATACTCCACACGC	21
MDM2	Forward	AGTAGCAGTGAATCTACAGGGA	22
	Reverse	CTGATCCAACCAATCACCTGAAT	23
P21	Forward	TGTCCGTCAGAACCCATGC	19
(CDKN1A)	Reverse	AAAGTCGAAGTTCCATCGCTC	21
GADD45A	Forward	GAGAGCAGAAGACCGAAAGGA	21
	Reverse	CAGTGATCGTGCGCTGACT	19
BAX	Forward	CCCGAGAGGTCTTTTTCCGAG	21
	Reverse	CCAGCCCATGATGGTTCTGAT	21
PUMA	Forward	ACCTCAACGCACAGTACGA	19
(BBC3)	Reverse	CTGGGTAAGGGCAGGAGTC	19
FAS	Forward	AGATTGTGTGATGAAGGACATGG	23
	Reverse	TGTTGCTGGTGAGTGTGCATT	21
TNFRSF10B	Forward	ATGGAACAACGGGGACAGAAC	21
	Reverse	CTGCTGGGGAGCTAGGTCT	19
PPM1D	Forward	TTTCTCGCTTGTCACCTTGC	20
(WIP1)	Reverse	TTCCAAGAACCACCCCTGAG	20
GAPDH	Forward	CAATGACCCCTTCATTGACC	20
	Reverse	GATCTCGCTCCTGGAAGAT	19

Table 2.5: qRT-PCR master mix constituent for each reaction.

Reagent	Volume in µl
SYBR green	5
Primer Forward	0.2
Primer Reverse	0.2
Nuclease free deionized water	2.6

2.5 Cell culture methods

A panel of liver cancer cell lines with different *TP53* status was used. These included *TP53* wild type ($p53^{WT}$) HepG2 and SK-Hep-1, *TP53* mutant ($p53^{MUT}$) Huh-7, Huh-1, SNU475 and SNU182, and *TP53* null ($p53^{NULL}$) Hep3B. SNU475, SNU182 and SK-Hep-1 were from the European Collection of Authenticated Cell Cultures (ECACC). HepG2, HuH7 and Hep3B from our authenticated Northern Institute for Cancer research cell line bank (see below) were originally from the American Type Culture Collection (ATCC). Huh-1 cells were obtained from the Japanese Collection of Research Bioresources (JCRB) cell bank (JCRB0199, JCRB). Bioware® Brite HepG2-Red-Fluc (HepG2-Luc) cells were purchased from (BW134280, Perkin Elmer, USA).

2.5.1 Tissue culture practice and authentication of cell lines

All cell line work was done in class II biological safety sterile cabinets, (Biomat, Medair Technologies, MA, USA). To minimise the risk of cross contamination and infection, the cell line handling was carried out in accordance with good practice criteria (234). All cell lines were authenticated using short tandem repeat DNA profiling (LGC Standards, UK), which uses human hypervariable DNA microsatellite regions that consist of a core sequence of 1-6 base pair long repeated DNA motifs, to detect cell line unique molecular fingerprints to ensure the avoidance of cross contamination and/or genomic instability in the used cell lines (235).

All cell lines were confirmed mycoplasma infection free on a 3 months basis (LT07-318, MycoAlert Mycoplasma Detection Kit, Lonza, UK). All experiments were performed on cell lines less than 30 passages from purchase or authentication and this was achieved by preservation of early post-authentication passages of several vials cryogenically.

2.5.2 Culture of adherent cells

All cells were maintained in either Dulbecco's Modified Eagle's Medium (DMEM) or Ham's F-12 (D6421, Sigma Aldrich, Dorset, UK), apart from SNU475 and SNU 182, which were maintained in RPMI-1640 medium (R8758, Sigma Aldrich, Dorset, UK). The media were supplemented with final concentrations of 10% heat-treated foetal bovine serum and L-Glutamine (2mM). All the cells were grown at 37°C and 5% CO_2 in air humidified atmosphere in Sanyo CO_2 incubators.

When cells were ~70% confluent, the medium was removed, the cells washed with PBS and then trypsin-EDTA solution (0.5 gm trypsin / L and 0.2 gm EDTA/L in sterile distilled water)

was added to the cell monolayers, followed by incubation for 3-5 minutes at 37^0C in the incubator to detach the cells. To stop the trypsinisation, full growth medium containing serum was added and then the cells were re-suspended, diluted and transferred to new flasks or experimental plates.

2.5.3 Counting cells

Cell densities were estimated using a Neubauer haemocytometer (Hawksley, Sussex, UK). After re-suspension of the trypsinized cells, 10 µl was added to each side of the haemocytometer cover slip. The volume of each grid equals 0.1 mm^3; ten grids were counted (5 on each side) and the average was multiplied by 10^4 to give us the estimate of cell number in 1 ml, thereby allowing appropriate cell densities to be prepared and seeded.

2.5.4 Freezing and revival of cells

Cells to be frozen for storage were ensured to be growing in the exponential phase (~70% confluent). After being tryspsinized and collected they were centrifuged at 350 rcf for 5 minutes (Mistral 3000i, DJB Labcare). Cell pellets were re-suspended in freezing medium, composed of complete growth medium, into which an additional 10% FBS and 10% dimethyl sulfoxide (DMSO) (#276855, Sigma) was added. The cell density for freezing was > 10^6/ml, and 1ml of re-suspended cells was divided into aliquots in cryogenic vials (NUNCTM, Rochester, NY, USA) and transferred into a cryochamber filled with isopropyl alcohol (Cryo 1ºC freezing container, Nalgene) to achieve an approximate -1°C/min rate of cooling when placed at -80˚C. For long term storage, vials were transferred into liquid nitrogen (Biosystem, Cryostor). The vials were labelled with (cell line name, date, passage number and the operator name).

To revive the cells, stored vials were thawed quickly and diluted with fresh medium slowly, and then centrifuged at 350 rcf for 5 minutes and the supernatant aspirated. Then the cell pellet was re-suspended in fresh medium and transferred into flasks. The medium was removed after 24 hours together with any dead floating cells and replaced with fresh medium.

2.5.5 Sulfrhodamine B (SRB) assay

This assay was developed by Skehan *et al* (236) to estimate cell density in multi-well plates. It is based on binding of the SRB dye to amino acids in proteins under mild acidic conditions and indirectly reflects the number of cells in the well through estimating the protein contents of the well. Cells were seeded in 96 well plates and grown for the specific time points. Cells were then fixed with Carnoy's fixative (3 parts methanol and 1 part acetic acid) (20 µl added to each 100 µl in each well) and kept at 4°C for up to two weeks. Plates were washed 5 times with distilled water (dH2O) and left to dry overnight. Then the wells were stained by adding 100 µl/well of 0.4% SRB in 1% acetic acid and left for 30 minutes. Unbound SRB was discarded and the plates were washed 5 times with 1% acetic acid and left to dry. Protein-bound SRB was then dissolved by adding 100 µl/well of 10mM Tris-HCL (pH10.5) solution with mild shaking for 20 minutes with a vibrating platform shaker (Titramax 1000, Heidolph), to ensure all the SRB dissolved. The optical density was measured at 570nM with FLUO star Omega plate reader.

2.5.6 Growth curve

Cells were seeded in a 96 well plate with different seeding densities (500, 1000, 2000, 3000, 4000 and 5000 cells /well) with 5-10 intra experimental replicates. Seven plates were seeded (a plate was seeded for each day of the week) and a plate was fixed every 24 hours with Carnoy's fixative (20 µl per well) and kept in the fridge. SRB staining was done as described in 2.5.5. The doubling time was calculated using Graphpad prism 6 software.

2.5.7 Growth inhibition

Cells were seeded in 96 well plates at the optimum seeding density chosen depending on cell line growth curve (seeding densities summarized in **Table** 2.6) in a 100 µl/well of media. After 24 hours they were treated by adding 100 µl/well of each concentration of the compound under study with a range of concentrations and 3-5 intra-experimental replicates for each concentration. A DMSO control with a final concentration of 0.2% was included in each plate. After 96 hours of treatment cells were fixed with Carnoy's fixative and stained with SRB as mentioned in 2.5.5. Mean, standard deviation (SD) and standard error of the mean (SEM) was calculated using the optical densities of the intra-experimental replicates. The data was normalized to the control (DMSO/solvent) and expressed as percentage of growth inhibition. Graphpad prism 6 software was used to calculate the 50% growth inhibitory concentration (GI_{50}) using (Lowess/spline fit) function and the mean±SEM of GI_{50} of 3 or more independent experiments was calculated.

Table 2.6: seeding densities of liver cancer cell lines in 96 well plates

Cell line	Seeding density per well in 96 well plate
HepG2	2000
SK-Hep-1	1000
Huh-7	3000
Hep3B	3000
Huh-1	3000
SNU475	3000
SNU182	3000
HepG2-Luc	2000

2.5.8 Clonogenic assay

Cells were seeded in a 6 well plate (seeding densities in **Table** 2.7) and were allowed to adhere for 24 hours and then treated with a solvent control and a range of drug concentrations for 96 hours in a final concentration of 0.2% DMSO. Then the media containing the drug was gently removed and replaced with fresh medium and the cells left to grow to form colonies for 21 days. At time of harvest, the media was removed gently and the colonies were fixed with Carnoy's fixative for 5 minutes and the fixative was removed and the plates were left to dry. Subsequently they were stained with 0.4% crystal violet dissolved in dH2O for 30 minutes and thereafter the plates were washed with gently flowing tap water and left to dry overnight. Visible purple stained colonies were counted in each well and the cloning efficiency was calculated using the following formula:

Cloning efficiency= (counted colonies / number of seeded cells) x 100

The data was normalized to the DMSO control and the concentration of the drug that reduced the colony formation by 50% (LC_{50}) was determined using (Lowess/spline fit) function in Graphpad prism 6 software. The mean of ≥ 3 repeats was calculated ± SEM and clonogenic survival curve was plotted.

Table 2.7: Cloning efficiency and seeding density for clonogenic assay of liver cancer cell lines

Cell line	Seeding density per well in a 6 well plate	Cloning efficiency
HepG2	500	20-25 %
SK-Hep-1	300	26-30 %
Huh-7	1500	8-10 %
Hep3B	120	60-70 %

2.6 Drugs used in *in vitro* studies

2.6.1 MDM2 inhibitors

Three MDM2 inhibitors were used during the course of our study (**Figure** 2.3). Nutlin-3 ($C_{30}H_{30}Cl_2N_4O_4$) was purchased from NewChem (#548472-68-0,Newcastle, UK) in powder form with a molecular weight of 581.5 gm/mol with >98% purity and dissolved in DMSO (276855, Sigma) to a final concentration of 10mM and aliquoted and stored at -20 °C. Another two potent MDM2 inhibitors were sourced by custom synthesis with the help of Newcastle University/Astex Pharmaceuticals Alliance. Idasanutlin, also known as RG7388 or RO5503781 ($C_{31}H_{29}Cl_2F_2N_3O_4$), is a second generation MDM2 inhibitor that is already in phase III clinical trials. This compound was developed by Roche through optimisation of Nutlin. Its molecular weight is 615.15 gm/mol. It was dissolved in DMSO to a final concentration of 1mM and stored in -20 °C. HDM201 ($C_{26}H_{24}Cl_2N_6O_4$) is an imidazolopyrrolidinone analogue that was developed by Novartis is already in phase I clinical trial. It has a molecular weight of 555.41 gm/mol. It was dissolved in DMSO to a final concentration of 20mM, from which aliquots of lower concentrations were prepared and stored at -20°C.

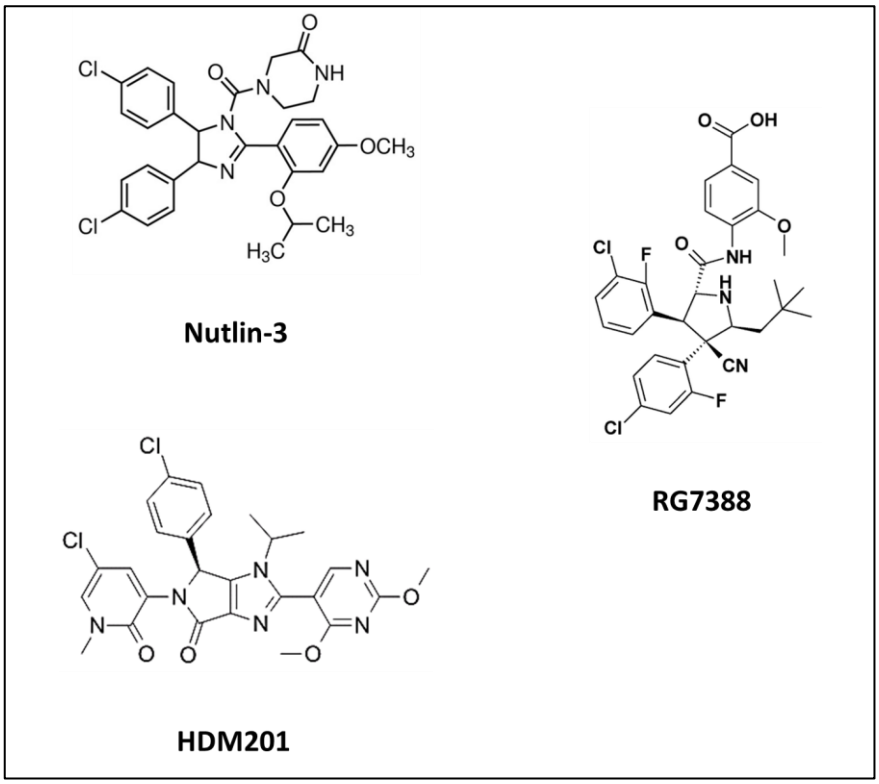

Figure 2.3: Chemical structure of the three MDM2 inhibitors, Nutlin-3 (216), RG7388 (237) and HDM201 (238).

2.6.2 WIP1 inhibitor

GSK2830371 ($C_{23}H_{29}ClN_4O_2S$) is a selective WIP1 inhibitor, the chemical structure of which is shown in **Figure** 2.4. It has a molecular weight (461.02). It was purchased from Tocris (#5140). It was dissolved in DMSO in 10mM aliquots and stored in -20°C.

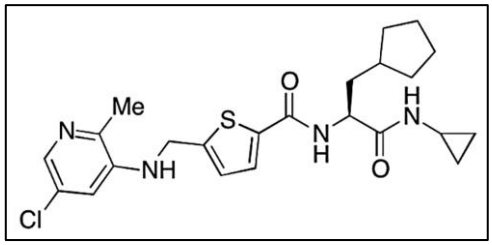

Figure 2.4: the chemical structure of GSK2830371(239).

2.7 Western blotting

2.7.1 Protein isolation and quantification

Cells were seeded in a 6 well plate at 2.5 x 10^5 cells / well for 48 hours and then treated with compound of interest at the specified concentration for different time points. Medium was removed and cells were washed with 1X PBS. Then 50 µl of SDS lysis buffer (0.0625M Tris-HCl pH 6.8, 2% SDS (Sigma), 10% Glycerol (Sigma)) was added per well and cells were detached with a cell scraper and the lysates collected and transferred into Eppendorf tubes and spun down. Samples were then heated for 10 minutes at 100°C and spun down. Sonication of each sample was performed at an amplitude 6 for 10 seconds (Soniprep 150 plus) to fragment the DNA and reduce the viscosity of the sample. This was repeated three times for each sample. Lysates were then centrifuged at maximum speed for 5 minutes at 4°C and the supernatant stored at -20°C until use.

Protein estimation and quantitation was done using a bicinchoninic acid (BCA) assay kit (Pierce BCA protein assay, Thermo scientific Fisher). This assay uses a colorimetric detection system based on the reduction of cupric ions Cu^{+2} to cuprous ions Cu^{+1} through the effect of reagent B in an alkaline medium (biuret reaction). This is followed by detection of the cuprous ions by reagent A in the kit, a purple colour is formed, the intensity of which is proportionate to the protein concentration in the sample. To perform this assay a standard range of protein concentrations 0.2-1.2 mg/ml was prepared from bovine serum albumin (BSA). Protein samples were diluted at a ratio of 1:10 and loaded into a 96 well plate in a quadruplicate; water was added into the blank wells. A mixture of reagent A and reagent B at a ratio of 50:1 was prepared and 190 µl was added into each well. The plate was incubated on a shaker for 1 minute to ensure proper mixture of the reagents, and then incubated at 37°C for 30 minutes. The absorbance at 570 nM was subsequently determined using a FLUOstar Omega plate reader (BMG Labtech). A standard curve was plotted for the control samples using the plate reader analysis software and the concentration of protein in each well was calculated accordingly.

2.7.2 Immunoblotting

A 20-25 µg aliquot of each sample was mixed with loading buffer in a microfuge tube and heated for 10 minutes at 100°C in a dry heating block. After centrifugation and gentle resuspension, the samples were loaded into the wells of a Sodium dodecyl sulphate (SDS) polyacrylamide gel (Mini-protean TGX 4-20% gradient pre-cast gel, Bio-Rad) immersed in a vertical gel electrophoresis tank filled with electrophoresis buffer (1:10 dilution of the stock buffer of 144 g Glycine (Sigma G8898), 30 g Tris base (Fisher 10667243) and 10 g SDS (Sigma

L3771). A ladder of protein molecular weight markers was loaded instead of a sample in two wells on each side of the gel. All the protein targets studied were less than 100 kDa, therefore the See Blue pre-stained low molecular weight protein standard (#LC5625, Life Technologies) was used. After electrophoretic separation of the samples for 45 minutes at 180 volts, the separated proteins underwent a transfer step. A nitrocellulose 0.45-micron membrane was used (#RPN203C, Hybond-C Amersham). For each gel, 2 filter papers and 2 blotting pads and 1 nitrocellulose membrane were soaked in transfer buffer. Thereafter they were layered with the gel in the following sequence from the Cathode probe (black) to the anode probe (transparent): 1 blotting pad, 1 filter paper, the gel, the membrane, filter paper and blotting pad. Before transferring the proteins, air bubbles were removed by passing a roller over the layers. Then the transfer of proteins was carried out at 100 Volt for 30 minutes in a tank completely filled with the transfer buffer (70.7 g Glycine (Sigma G8898), 15.15 g Tris base (Fisher 10667243), one litre methanol 99.9% (Fisher Bioreagents) and distilled water to a final volume of 5 litres). After completing the transfer, membranes were blocked with 5% milk in Tris-Buffer Saline solution with 1% tween 20 (TBS= 80 g NaCl (Sigma S7653), 24.2 g Tris base (Fisher 10667243), and distilled water up to one litre final volume with adjusted PH of 7.6) for 1 hour on a shaker.

The whole membrane or cut membrane was then incubated with the primary antibody of interest for the specified time. This was followed by a washing step in TBST for 5 minutes and then the membrane was incubated for 1 hour at room temperature with a secondary antibody, which could be goat anti-Mouse or anti-Rabbit (according to the primary antibody type) and conjugated with horseradish peroxidase (HRP) at a dilution of 1:1000 (Cat No.: P0447/P0448Dakocytomation) (**Table** 2.8). All dilutions were prepared using 5% non-fat milk or BSA in 1X TBST solution.

2.7.3 Immunodetection

The membrane was washed with TBST three times for 10 minutes each before visualising the protein locations with an Enhanced ChemiLuminescence (ECL) system (GE Healthcare Life Sciences). ECL contains a chemiluminescence substrate and an oxidising agent mixed at a ratio of 1:1 and incubated with the membrane for 1 minute before exposing the membrane to an x-ray film (Fujifilm) in the dark. Under the effect of the HRP conjugated to the secondary antibodies, triplet carbonyl is formed from the substrate and the decay of this triplet to singlet emits light that is detected by the x-ray film and the detected signal is proportionate to the

amount of the secondary antibody that in turn is proportionate to the target protein content in the sample. The x-ray films were then scanned and the results analysed.

Table 2.8: Antibodies used in western blotting.

Antibody	Species	Cat. #, Company	Dilution	Molecular weight kDa
p53	Mouse	M7001, Dako	1:3000	53
Phosphorylated p53 at serine 15	Rabbit	9284, Cell signalling	1:1000	53
Acetylated p53 at lysine 382	Rabbit	#2525, Cell Signalling	1:500	53
MDM2	Mouse	OP40, Merck Millipore	1:1000	90
p21	Mouse	OP64, Calbiochem	1:100	18
WIP1	Mouse	#sc-376257, Santa Cruz	1:200	85
PARP	Mouse	C2-10, Trevigen	1:1000	114 (cleaved PARP 85)
BAX	Rabbit	2772S, Cell Signalling	1:1000	21
GAPDH	Rabbit	2118, Cell signalling	1:1000	35.8
B-Actin	Mouse	A4700, Sigma	1:3000	42

2.8 Fluorescence activated cell sorting (FACS)

Cells seeded at 250 000 cells per well in 6-well plates were treated after 24 hours, to allow recovery and attachment, with 24, 48 or 72 hours drug exposures, after which floating and adherent cells were collected together and centrifuged at 500g for 5 minutes. Pellets were then fixed with 70% ethanol and stored at 4°C. Cells were then centrifuged at 500g for 5 minutes and washed with 1mL PBS, followed by further centrifugation at 500g for 5 minutes, re-suspension in 250 µl of phosphate buffered saline (PBS) and incubation with 40 µg/mL propidium iodide (PI) (Sigma-Aldrich) and 20 µg/mL Ribonuclease A (RNase A) (Sigma-Aldrich) for 20 minutes in the dark at room temperature. PI is a fluorescent dye that binds to double stranded DNA and RNA. RNase A was used to cleave the P-O^5 bond in RNA, releasing the PI. The retained fluorescent signal is thus from the DNA only and proportionate to the DNA content of the cells.

Samples were processed using a FACS calibur flow cytometer (BD biosciences) after being stained with PI. In this machine single cells pass through a tube and intersect with a laser beam (488nM). Some of the incident light passes through the cells and is recorded by a sensor. This is called forward scatter (FSC) and it reflects the cell volume. Some light gets more broadly scattered and is called side scatter (SSC). This reflects granularity of the cell. The fluorescent

signal from the PI (excitation wavelength of 535/617nm) when passed through argon laser beam of 488 nm is also detected and recorded. The analyses are described later.

Before analysing the treated samples, adjusting the settings of the instrument was necessary to ensure that the collected signal was from the cells and not from other particles. Therefore untreated cells were passed through the machine and the settings were adjusted using CellQuest Pro software (Becton Dickinson, Oxford, UK). G1/G0 phase signal intensity was adjusted in the region of 200, to allow the recording of events at lower intensity than the G1, namely sub-G1. 25000 events were recorded per sample (**Figure** 2.5).

To analyse cell cycle changes, Cyflogic (1.2.1) (CyFlo Ltd, Turku, Finland) software was used to calculate the percentage of cells (events) in each of the three cell cycle phases, G1/G0, S, and G2/M, based on the signal collected that reflects the DNA content of the cells in each phase (**Figure** 2.5). In addition, sub-G1 signals were recorded. In normal dividing cells there are 3 phases, G1/G0 phase in which the cells have a single copy of the diploid genome (2N); followed by the synthesis phase (S) that will lead to doubling the DNA content (4N) in the G2/M phase. Events with signal intensity below the G1/G0 (2N) were considered sub-G1 and reflect dying disintegrated (apoptotic) cells. Analysing the cell cycle allows identification of any changes in the number of cells in each phase, allowing interpretation of the effects of conditions or compounds used on the cell cycle distribution. The analysed data was plotted using GraphPad Prism 6 software.

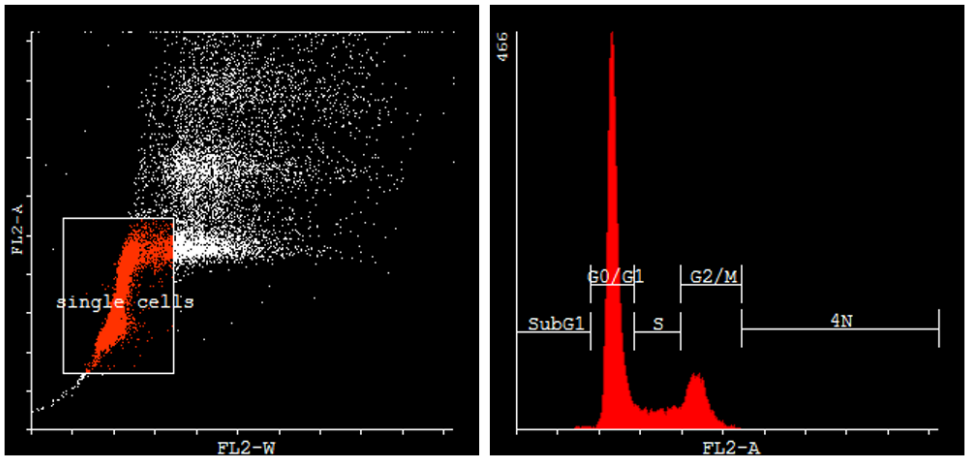

Figure 2.5: Cell cycle analysis and gating of events using CellQuest and Cyflogic software. X-axis represent DNA content (signal intensity-major ticks =100) and Y-axis represents the frequency or number of events (number of cells) to generate a histogram of the distribution of cells in different phases of the cell cycle.

2.9 Caspase 3/7 activity assay

Cells were seeded at 8000 cells/well in a white opaque 96 well plates. After 24 hours they were treated with the compound of interest for another 24 hours, prior to the addition of the caspase 3/7 Glo reagent (Promega) in a 1:1 ratio and incubation for 30 minutes at room temperature. The luminescence was measured with a FLUOstar Omega plate reader (BMG Labtech). This technique is based on the generation of luminescence through the cleavage of a substrate in the assay reagent in the presence of active caspase 3/7 in the wells. The measured luminescence is then normalised to the solvent control and the mean of three independent repeats was plotted as a relative luminescence ± SEM.

2.10 XTT assay

XTT is a colorimetric assay that assesses cellular proliferation, viability and cytotoxicity. It is based on the cleavage of a tetrazolium salt (water soluble) into a formazan salt in the presence of an electron coupling agent, and this process occurs in live cells only and is dependent on NAD(P)H production through glycolysis. The cleavage of tetrazolium salts is performed by the succinate-tetrazolium reductase system (EC 1.3.99.1), which is part of the respiratory chain in the mitochondria. The formed formazan salt is water soluble and gives an orange colour. The absorbance of light at 450 nM is measured and reflects the number of viable cells in the well.

Cells were seeded at $5x10^3$ cell / well in 100 µl per well, in 96 well plates in triplicate for each condition. Five plates were seeded and after 24 hour all of the plates, apart from the untreated control plate, were treated with cell line specific doses of GI_{50}, 10X GI_{50} (calculated according to the SRB assay) and 1µM of HDM201 alone and in combination with WIP1i (2.5µM). The drug solvent was DMSO arranged to be at a final concentration of 0.2% to have minimal effect and control samples were treated with this concentration alone. Every 24 hours a plate was taken out of the incubator and 50 µl of XTT assay mix (that is a mixture of a 5ml XTT salt and a 0.1 ml electron coupling agent) was added per well, prior to incubation for 4 hours. In each plate, a triplicate of media-only control was added as a background control. Light absorbance was measured at 450 nM wavelength using a FLUOstar Omega plate reader. The blank background absorbance was subtracted and data was plotted using GraphPad Prism 6 software.

2.11 Senescence associated β-Galactosidase assay (SA-β-Gal)

β-Galactosidase activity is usually detected at an acidic pH 4.5, using the substrate X-Gal. In senescent cells which accumulate β-Galactosidase in their lysosomes, activity can be detected at a suboptimal pH 6.0. The development of a blue-green stain results from cleavage of the chromogenic X-Gal substrate by the β-galactosidase enzyme (240). This method can be used for the indirect detection of senescent cells.

Cells were seeded in 12 well plates (Corning) and in Nunc chambered coverglass system slides (155360, Lab Tek I chambered #1.5 German coverglass system, ThermoFisher scientific, USA), at the densities in (**Table** 2.9), incubated with the drug and DMSO control for 96 hours, prior to fixing and staining with an SA-β-Gal kit (CS0030, Sigma) according to the manufacturer's protocol. After development of positive staining, the reagent was removed and replaced by PBS, or 70% glycerol for long term storage. Images were captured using the EVOS XL cell imaging system (ThermoFisher scientific). Ten high power field images were analysed and the percentage of positively stained cells was calculated. The mean of three independent repeats was plotted together with the standard error of the mean.

Table 2.9: Seeding densities of HepG2 and SK-Hep-1 for SA-β-Gal assay

	Cell seeding density per well in a 12 well plate		Cell seeding density per chambered slide	
	HepG2	**SK-Hep-1**	**HepG2**	**SK-Hep-1**
DMSO control	7000	5000	20000	10000
WIP1i	7000	5000	-	-
MDM2 inhibitor				
0.5 GI_{50}	10000	10000	-	-
GI_{50}	20000	20000	40000	40000
10X GI_{50}	80000	40000	200000	80000

2.12 *In vivo* xenograft study

All of the *in vivo* experiments were performed according to the Guidelines for the Welfare of Animals in Experimental Neoplasia (Second Edition), set by the United Kingdom Coordinating Committee on Cancer Research and national law (241) and after being reviewed and approved by the local institutional animal welfare committee.

2.12.1 Growth curve of HepG2-Luc in different immunocompromised mice strains

The ability of HepG2-Luc to form xenografts was tested in two different immunocompromised mice strains, NOD SCID gamma (NSG) (Bred in house - Comparative Biology Center, Medical School, Newcastle University) and CD1 nude mice (Charles River, UK). NSG mice lack B and T lymphocytes and lack natural killer cells, while CD1 nude mice lack the Thymus and T cells. 8-10 weeks old female mice were allocated into two groups with 5 mice/group of each strain. A 50 µl suspension of 10^7 HepG2-Luc cells in a cocktail of 50% matrigel (BD Biosciences) and 50% DMEM medium were injected subcutaneously into the right flank of each mouse (after removal of hair for NSG mice with a clipper and hair removal cream). They were left to grow with close monitoring of the tumour growth by digital Vernier calliper measurements of the largest dimensions of the detectable tumours three times a week. The collected data were plotted using GraphPad Prism 6 software to generate a growth curve.

In parallel to tumour size measurements using the standard Vernier calliper method, and because the HepG2-Luc cells have luciferase activity, In Vivo Image Scanning (IVIS) was performed once a week by injecting the mice with 100µl per mouse of D-luciferin (3gm/mL) intraperitoneally (IP) 10 minutes before scanning the mice. The mice were anaesthetised by isoflurane inhalational using a controlled flow anaesthesia machine while IVIS imaging was performed. After IP injection, D-luciferin is absorbed into the blood. In HepG2-Luc cell xenografts, dependent on the vasculature and substrate delivery, D-luciferin should be oxidised under the catalytic effect of luciferase enzyme to generate a light signal. The IVIS scanning system detects any photons emitted from the animal and the bioluminescence data can be plotted.

The HepG2-Luc line reportedly had improved luciferase brightness. A new codon-optimized luciferase from *Luciola Italica* (RedLuc) was developed by Perkin Elmer, with a red-shifted emission peak wavelength of 617 nm, and approximately 100-fold higher signal intensity compared to other firefly luciferases.

When the tumours reached a dimension of 10x10 mm, or one of the dimensions exceed 15 mm, euthanasia was carried out to comply with ethical standards.

2.12.2 Assessing HDM201 effect on HepG2-Luc xenografts

8-10 weeks old female NOD SCID mice were allocated into 4 cages with 5 mice per cage. A 50µl volume of 10^7 HepG2-Luc cells in suspension were injected in a cocktail of 50% matrigel and 50% DMEM medium subcutaneously into the right flank of each mouse after hair removal. When the tumours were palpable (approximately 5x5 mm), the animals were randomised and divided into two groups to receive a single daily dose of either the HDM201 or the control vehicle (5% ethanol alcohol in 1% HydroxyPropyl Methyl Cellulose) through oral gavage.

In the first xenograft study, treated mice received a single daily dose of 25 mg/kg /day for 7 days. In the follow-up study, mice received 100 mg /kg/day for 10 days. Standard tumour measurement with a Vernier calliper and recording of body weight was performed three times weekly. To ensure that the measurements were non-biased, the person measuring the tumour size and body weight was blinded to the treatment and control groups. When the tumours reached a dimension of 10x10 mm or one of the dimensions exceed 15 mm, the animals were euthanised. Subcutaneous xenografts were recovered by dissection and divided into two parts, one kept in formalin at 4°C for processing into FFPE blocks and the other fresh frozen in liquid nitrogen and stored at -80°C.

2.13 Statistical analysis

All data were presented as the Mean ± standard error of the mean (SEM) unless otherwise specified. The p-value was calculated using Microsoft Office, IBM SPSS 22 and GraphPad Prism 6 software with a p-value of < 0.05 considered statistically significant at the 95% confidence level. Paired and unpaired t-tests and one-way ANOVA with multiple hypotheses correction were used as appropriate for the comparison data type unless otherwise specified.

Chapter 3: Characterisation of a dietary induced animal model of non-alcoholic fatty liver disease and hepatocellular carcinoma – a focus on p53

3.1 Introduction

Non-alcoholic fatty liver disease (NAFLD) is the most common chronic liver disease in the western world and is part of a spectrum that involves steatosis and non-alcoholic steatohepatitis (NASH), with inflammation and fibrosis leading to cirrhosis in some cases (16, 67). On a background of dietary excess and relative inactivity, with dramatically rising levels of the metabolic syndrome (obesity, type 2 diabetes (T2DM), and cardiovascular complications), NAFLD affects up to 25.42% of the world population (16). It is anticipated NAFLD will become the most common cause of liver transplantation in this century (5). NAFLD is also an important risk factor for the development of hepatocellular carcinoma (HCC) (5, 16). HCC is the second leading cause of cancer related death worldwide with a 5 year survival of less than 15% (84, 242).

In NAFLD the accumulation of free fatty acids (FFA) impairs mitochondrial function and causes increase in the reactive oxygen species (ROS). Oxidative stress induced cellular and DNA damage reportedly plays a central role in the progression of simple fatty liver to steatohepatitis, fibrosis and HCC (243). Lipid accumulation may also lead to a continuous state of inflammation through interleukin-6 and tumour necrosis factor and dysregulated adipokine levels (244).

Several animal models have been developed to help understand the pathophysiology of NAFLD (245) and a number of these, supported by studies in human NASH, report an upregulation of p53 in NAFLD (21, 195). The role of p53 in the development of NAFLD HCC, however, is unclear. Famed as a tumour suppressor and "guardian of the genome", its inactivation in some form might be expected. In human HCC, the incidence of *TP53* mutation is around 30%, according to the Catalogue of Somatic Mutations in Cancer (COSMIC) (199). The majority of *TP53* mutation occurs in the DNA binding domain, frequently caused by aflatoxin B1 exposure or viral hepatitis infection which are common in sub-Saharan Africa and East Asia respectively (246). The incidence of p53 mutation in NAFLD is not yet known.

In an attempt to generate an animal model better reflecting the Human condition, including progression to NASH, fibrosis and HCC rather than simple fatty liver, we fed the American life style (ALIOS (**H**igh **F**at **H**igh **F**ructose (**HF**))) diet to a strain of mice with a tendency to develop obesity and impaired glucose tolerance with age (C3H/He). Two groups of mice received control diet or ALIOS diet, with different time points of exposure, as described in detail in the methods section, but as summarised in **Table** 3.1.

Table 3.1: dietary animal model design

Age groups	Mice number	
	Control	ALIOS (HF)
12 weeks	8	8
24 weeks	8	8
36 weeks	8	8
48 weeks	23	24
Total	47	48

3.2 Hypothesis and aims of the study

3.2.1 Hypotheses

1. The development of HCC in NAFLD is associated with an inflammatory response (NASH) and the development of fibrosis.
2. The development of NASH in NAFLD is associated with oxidative stress, DNA damage and a p53 response.
3. A defective p53 response is associated with development of HCC.

3.2.2 Aims of the study

- Explore the development of HCC in the animal model of NAFLD and identify the association with the grade and stage of NAFLD.
- Explore NAFLD progression and HCC grade in association with DNA damage and p53 expression.
- Explore *TP53* status in HCC in our animal model.

3.3 Dietary induced Obesity, NAFLD and HCC

3.3.1 The ALIOS diet induced obesity and hepatomegaly in C3H/He mice

American life style diet (ALIOS (**H**igh **F**at **H**igh **F**ructose (**HF**))) fed mice showed a highly significant increase in body weight and liver weight compared to the control group fed on a normal diet. The liver to body weight ratio was higher in the ALIOS animals compared to the control (C) which was associated with more fat accumulation in the ALIOS mice livers (**Figure** 3.1).

The average body weight was (42.49±6.2g), with a range from (28.1g to 57.1g). Body weight results showed a significant increase in weight with age in both groups of mice. The body weight increased from a mean of (35.16±1.11g) in the 12 weeks age group fed ALIOS diet, to (47.25±0.92g) in the 48-weeks group ($p<0.0001$). The mean body weight in the control group increased from (32.05±0.96g) at 12 weeks to (41.31±0.82g) in the 48-weeks ($p<0.0001$) (**Figure** 3.1**; A**).

The difference in the body weight between the control and the ALIOS diet group remained significant throughout the whole study with a p value <0.05 (apart from the 12-weeks age group in which the difference between ALIOS and control groups was not significant ($p=0.054$). The largest difference was in the 48-weeks ($p<0.0001$). This shows clearly the effect of diet on weight gain.

Liver weight also increased dramatically with age, with a significantly higher increase in the ALIOS (HF) group in comparison to the control group ($p<0.0001$) (**Figure** 3.1**; B**). The average liver weight was (2.2 ±0.66 g) with a range from (1.2 to 4.7g). In the control groups the liver weight increased from (1.45±0.04g) at 12-weeks, to (1.85±0.06g) at 48-weeks, compared to the ALIOS where it increased from (1.75±0.10g) to (2.83±0.12g) at 48-weeks ($P< 0.0001$ for both groups).

The development of hepatomegaly more so than body weight was confirmed by significant increases in the liver weight (LW) to body weight (BW) ratio in aging and ALIOS diet fed mice. With advancing age, LW/BW ratios (expressed as % of body weight) increased from (4.53±0.12) at 12-weeks to (4.48±0.11) at 48-weeks, and from (4.96±0.23) to (6.04±0.2), in control and ALIOS diet groups respectively (**Figure** 3.1**; C**).

This liver weight gain correlated significantly with body weight gain, indicating that there was gain in weight associated with increase in liver weight, but highlights the liver as an organ in

which gain preferentially occurs in the presence of a high fat diet and lipid accumulation (**Figure** 3.1**; D**).

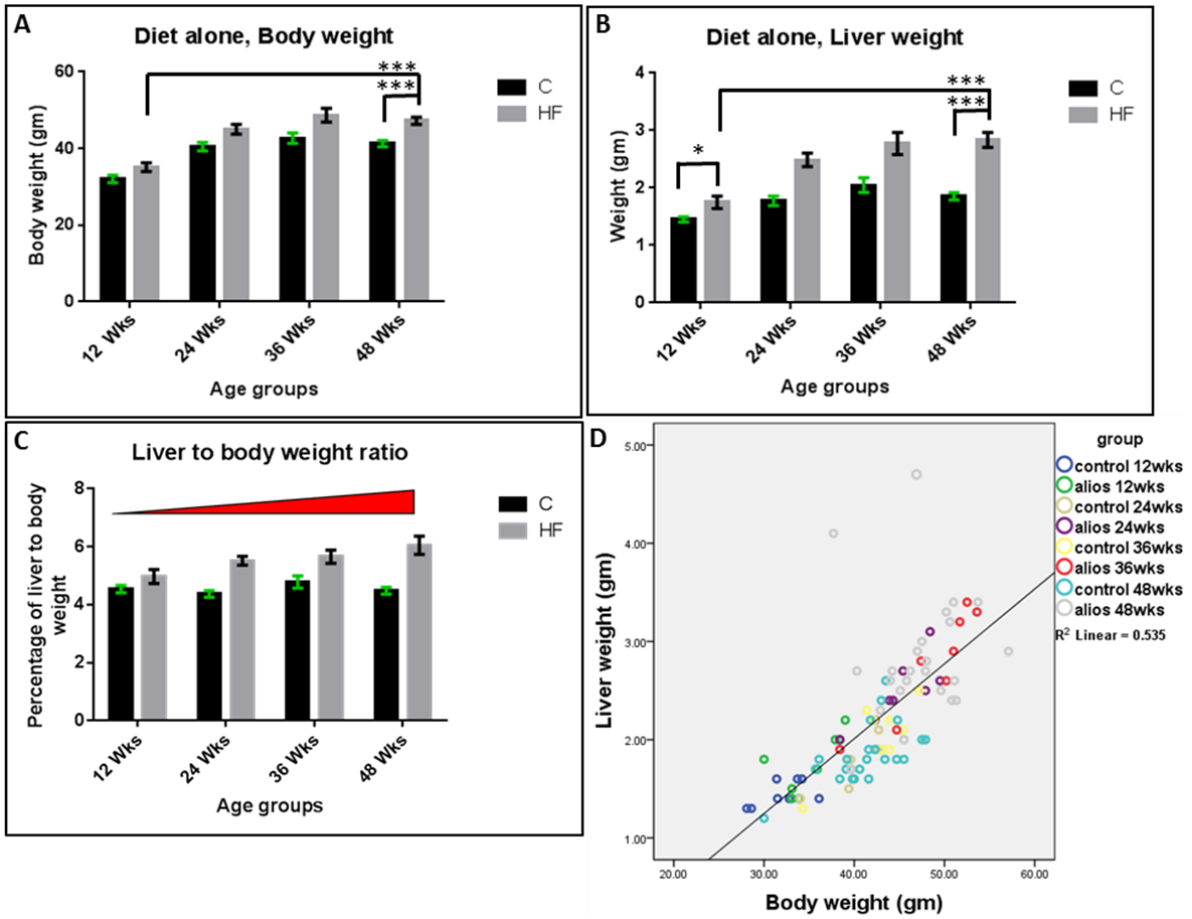

Figure 3.1 : The effect of ALIOS diet on body and liver weight. (A) Shows the increase in the body weight with age, which was higher in ALIOS (HF) fed animals compared to the control group. (B) Shows the increase in liver weight with age, again higher in ALIOS fed animals, with the greatest difference between the ALIOS and control at 48-weeks of age. (C) Liver to body weight ratio increased in ALIOS fed animals. (D) The correlation between the body and liver weight is demonstrated in the scatter plot. Y axis values represent Mean ± SE of the mean. * represent $p<0.05$, *** represents $p<0.0001$ determined by the t-test.

3.3.2 The ALIOS diet induced NAFLD, NASH and Fibrosis

Histological grading and staging of NAFLD was described in details in chapter one (**1.2.4**). The main histological parameters that are used in the scoring of NAFLD and NASH include steatosis, lobular inflammation, portal inflammation, hepatocellular ballooning and fibrosis (see 1.2.4, **Figure** 3.2).

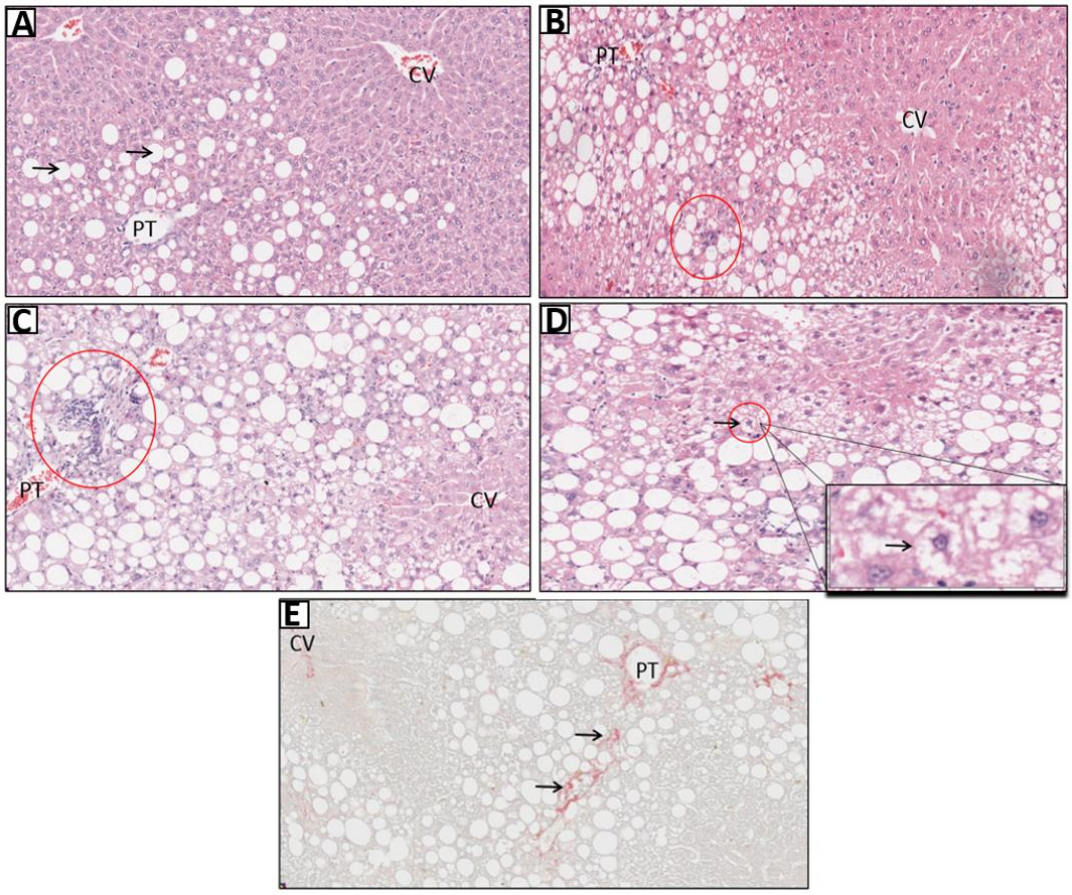

Figure 3.2: Histological parameters used in NAS and SAF scoring systems showing the NAFLD changes after feeding ALIOS diet in 48-week-old mouse liver. (A) Steatosis (arrows), (B) lobular inflammation (red circle), (C) portal inflammation (red circle), (D) ballooning (red circle and black arrow) and (E) fibrosis shown as pink stained fibrous bands (arrows). (Sirius red staining for collagen) was used to detect fibrosis in (E) while haematoxylin and eosin stain was used in all other slides. CV= central vein, PT =portal tract.

In parallel to the physical parameters that showed increased liver weight, steatosis was prominent and highly significant in the ALIOS fed group compared to the control group ($p<0.0001$) (**Figure** 3.3). In the ALIOS group all mice developed steatosis to a variable extent, with 33 cases (68.8%) graded as moderate steatosis and 7 (14.6%) cases graded as severe steatosis. In the control group the majority had either no steatosis (21.3%) or mild steatosis (36.2%). The remaining 20 cases (42.6%) had a moderate degree, with none having severe

steatosis. These data confirm that C3H/He mice develop NAFLD with age, which is more pronounced in mice fed a high fat ALIOS diet.

The dramatic effect of the ALIOS diet on other histological features of progressive NAFLD was also evident. In addition to the highly significant increases in the steatotic grade ($p<0.0001$), microvesicular steatosis ($p=0.003$), lobular inflammation ($p<0.0001$) and fibrosis stage ($p=0.009$) were also significantly increased compared to the control diet, as were Mallory Denk bodies ($p=0.018$) and pigented Kupffer cells (0.045) to a lesser degree (**Figure** 3.3). The NASH activity score (NAS) and SAF score also showed highly significant difference between the ALIOS and control groups ($p<0.0001$ in both NAS and SAF) (**Figure** 3.4).

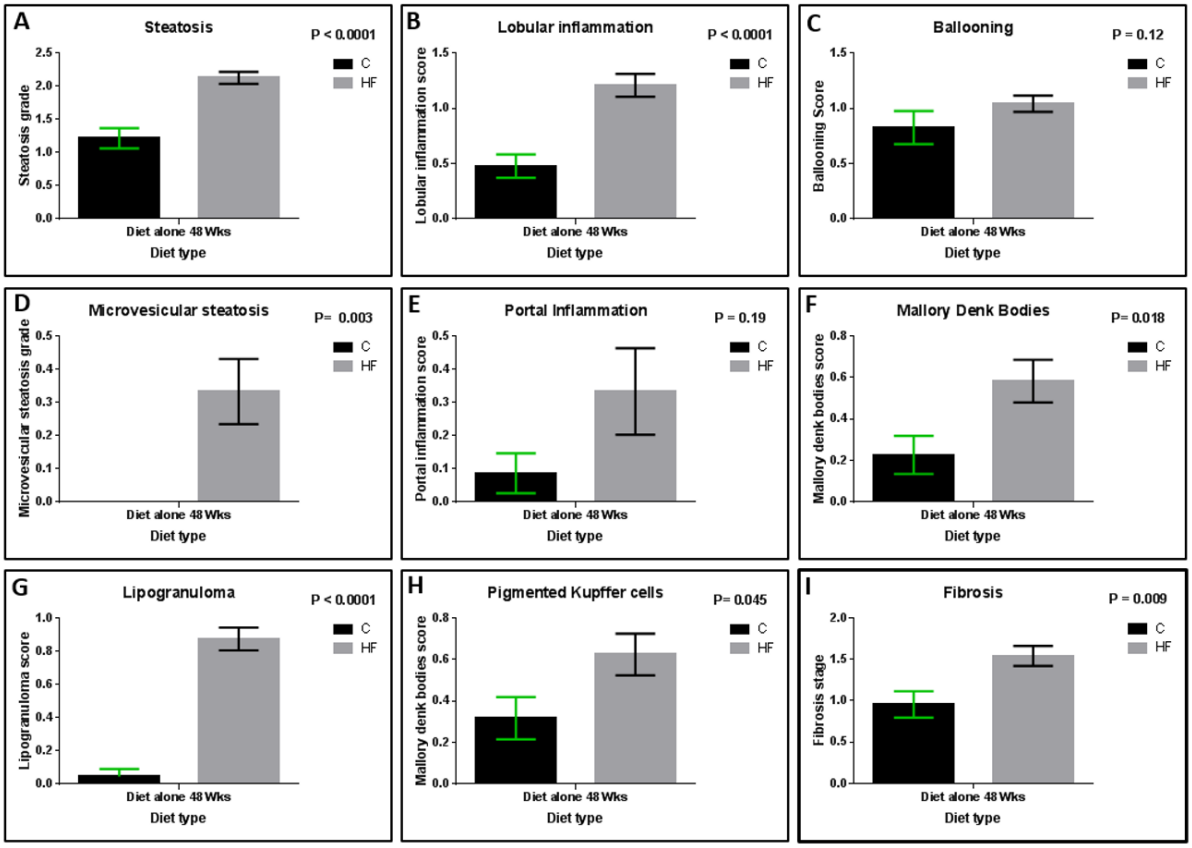

Figure 3.3 : Comparison of liver histological features of NAFLD in control and ALIOS diet fed mice at 48 weeks. Features associated with NAFLD progression were more pronounced in ALIOS (n= 23) fed mice compared to Controls (C) (n=24). Y axes values represent Mean ± SE of the mean.

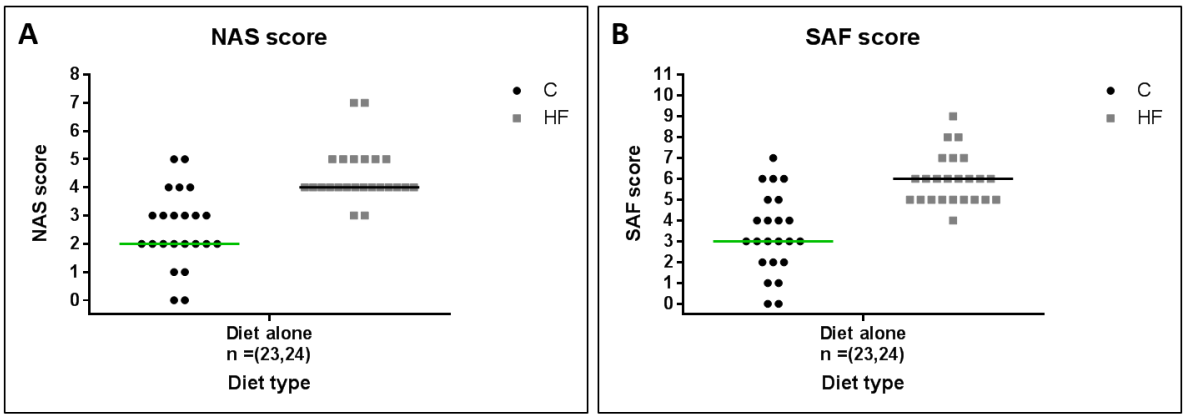

Figure 3.4: NAS and SAF score comparison between the control and HF diet in 48-week-old mice. (A) NAS and (B) SAF scoring systems showed highly significant difference between ALIOS (HF) and control (C) ($p<0.0001$). Y axes represent individual mouse scores and the horizontal line show the group median values.

3.3.3 The ALIOS diet promoted the development of primary liver tumours

Not only do C3H/He mice develop obesity and NAFLD with age, they also develop spontaneous liver tumours. In mice fed the ALIOS diet, this phenotype was dramatically exacerbated, as mice started to develop tumours at an earlier age (36 weeks), with significantly greater numbers and size of tumours by 48 weeks (**Figure** 3.5).

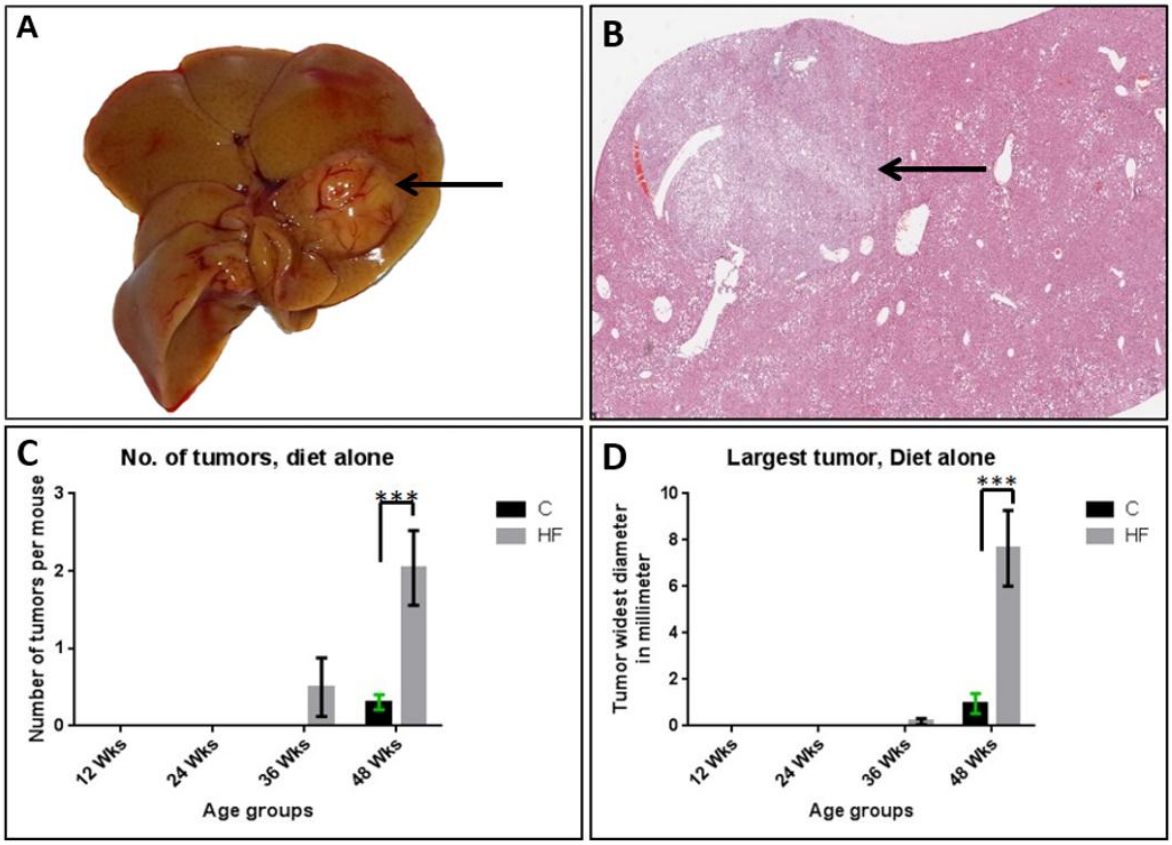

Figure 3.5: Tumour development in the murine dietary animal model. (A) Liver tumour (HCC) in a 48-week-old ALIOS (HF) fed mouse (arrow). (B) Histological section of a mouse liver stained with haematoxylin and eosin showing liver tumour (HCC) (arrow). (C)Tumours started to appear at 36 weeks of age in the ALIOS fed animals and the number of tumours was significantly higher in the ALIOS animals, despite the development of tumours by some of the 48-week-old control animals. (D) The tumour size in ALIOS (HF) mice was larger compared to those in the control animals Y axis values represent Mean ± SE of the mean. *** represents $p<0.001$ determined by t-test.

3.3.4 Characterising tumour development and progression in C3H/He mice

3.3.4.1 Tumour development associations

The combined group of 47 mice (control and ALIOS fed mice) were regarded as a single cohort for the exploration of gross and histological phenotypic associations with tumour development. Gross phenotype associations included body weight, liver weight, liver/body weight ratio and visceral adipose tissue weight. Bivariate associations with tumour number (continuous data) are shown in **Table** 3.2**.** The correlation was most marked and highly significant for liver weight, or liver/body weight ratio.

Data were similarly assessed in association with histopathology scoring of NAFLD. Associations with absence or presence of a tumour were also assessed by Chi square test for these categorical variables, as shown in **Table** 3.2. Tumours were more likely to develop in livers with more fat, but notably also in the presence of lipogranulomas and lobular inflammation. Associations with fibrosis were not as strong.

Table 3.2: Association of HCC development with phenotypic and liver histopathology parameters.

	Tumour presence			Spearman rho	
	No	Yes		Correlation	p value
Gross Phenotype Parameters					
	Mean ± SEM			Correlation	p value
Body weight (gram)	42.18±1.12	45.95 ± 0.92	-	0.381	**0.008**
Liver weight (gram)	1.93±0.11	2.67 ± 0.13	-	0.686	**<0.001**
Liver/body weight ratio	0.05±0.002	0.058±0.002	-	0.66	**<0.001**
Visceral adipose tissue weight (gram)	1.15±0.15	1.67 ± 0.16	-	0.343	**0.018**
	Tumour presence		Chi ^{2}	Spearman rho	
	No	Yes		Correlation	p value
Histological Parameters					
	Number of mice		P value	Correlation	p value
Steatosis grade (0/1/2/3)	4/7/8/1	0/4/20/3	**0.01**	0.429	**0.003**
Microvesicular Steatosis grade (0/1)	19/1	20/7	0.059	0.382	**0.008**
Hepatocellular ballooning score (B)(0/1/2)	5/12/3	4/20/3	0.579	0.058	0.699
Mallory Denk bodies (None/present)	14/6	13/13	0.172	0.305	0.1039
Megamitochondria (None/present)	16/4	17/9	0.275	0.031	0.839
Lipogranuloma (None/present)	15/5	9/17	**0.007**	0.481	**0.001**
Lobular Inflammation score (LI) (0/1/2)	9/10/1	4/18/5	0.06	0.421	**0.003**
Portal Inflammation score (0/1/2)	18/1/1	21/5/1	0.507	0.276	0.06
Pigmented Kupffer cells (None/present)	13/7	11/15	0.127	0.28	0.06
Apoptotic cells (None/present)	15/5	22/4	0.145	-0.114	0.452
Perisinusoidal fibrosis score(0/1)	6/14	1/26	**0.012**	0.361	**0.013**
Periportal fibrosis score (0/1/2)	14/6/0	15/11/1	0.636	0.253	0.086
Fibrosis stage (0/1/2/3)	6/8/6	1/14/11/1	0.064	0.355	**0.014**
NAS score (sum)	20	27		0.465	**0.001**
NAS score (<3/≥3)	14/6	6/21	**0.001**	0.477	**0.001**
SAF score (sum)	20	27		0.467	**0.001**
SAF activity (<2 either LI or B/>2 both LI & B)	11/9	6/21	**0.021**	0.351	**0.016**

Most of the tumours were of low grades (grade 1 & 2) and only two tumours were of high grade (3 and 4 respectively) (**Table** 3.3).

Table 3.3: Incidence and histological grades of liver tumours

	ALIOS diet (HF) n=24	Control diet (C) n=23
Tumours (n)	23	5
HCA	2	2
HCC Grade 1	8	0
Grade 2	11	3
Grade 3	1	0
Grade 4	1	0

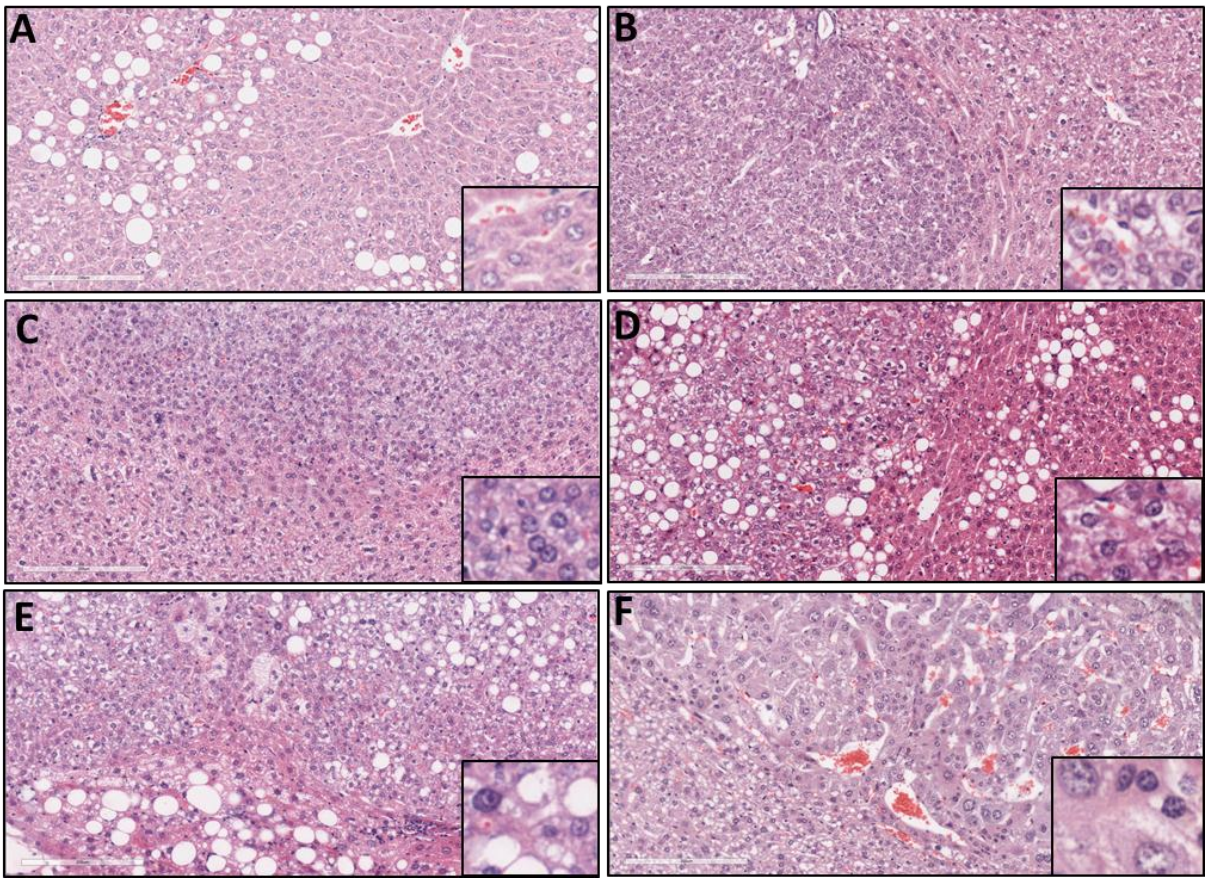

Figure 3.6: H&E stained mouse liver tissue sections showing NAFLD, HCA and HCC of different grades. (A) Liver tissue sections from a 48-week old mice fed HF diet showing steatosis. (B) HCA. Pictures (C, D, E and F) show HCC with grade I, II, III and Grade IV, respectively. On the lower right side corner of each picture there is a magnified image showing nuclear features. Magnification power 20X and the scale bar = 200 µm.

3.3.4.2 Tumour progression – associations with tumour and size

The number of liver tumours was significantly associated with histological features of more advanced NAFLD or NASH. These data are presented in **Figure** 3.7 and those histological features in which the tumour number mean value was significantly different by Kruskal Wallis test included steatosis grade (p=0.025), microvesicular steatosis (p=0.01), lobular inflammation (p=0.017), fibrosis (p=0.029), as well as highly significant association with the presence of lipogranulomas (p=0.001).

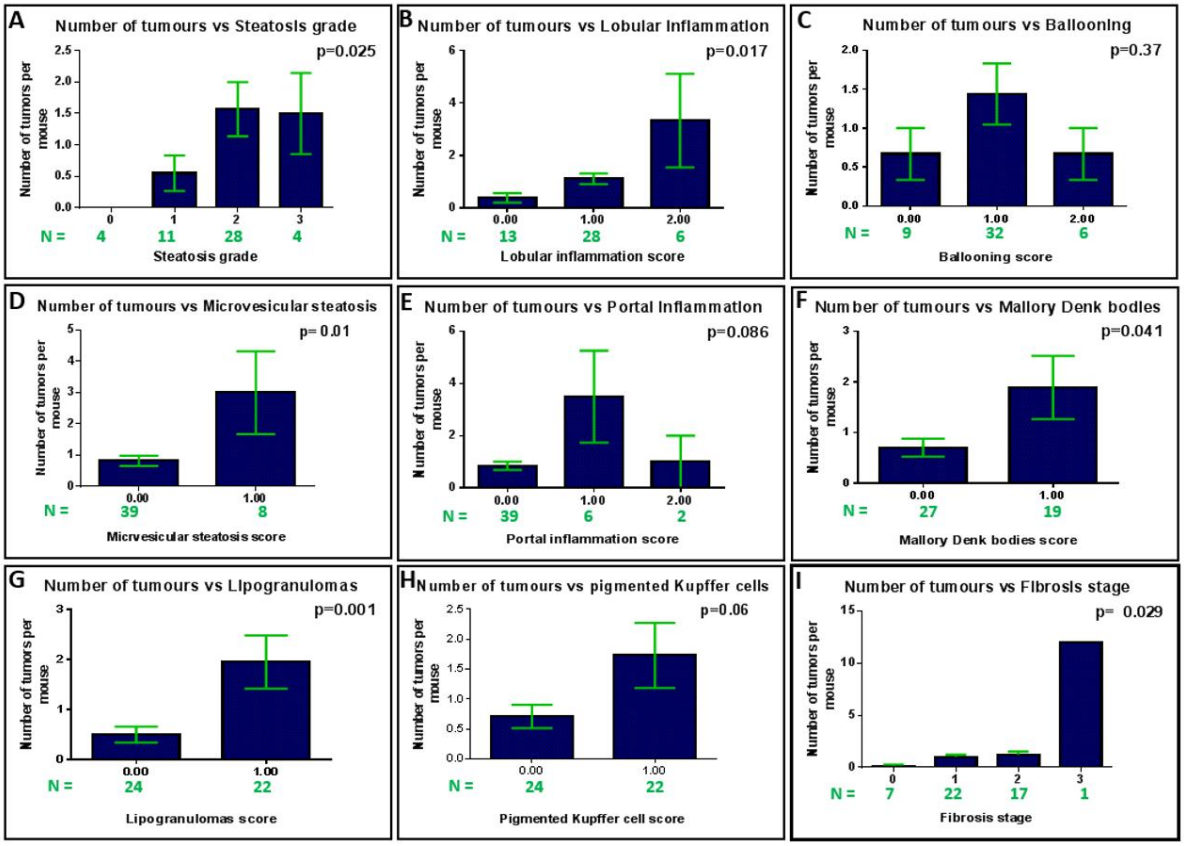

Figure 3.7 : The association between tumour numbers and NAFLD progression in the 48-week-old mice. The number of tumours associated significantly with NAFLD parameters, as indicated by significant associations with steatosis (A), lobular inflammation (B), microvesicular steatosis (D), Mallory Denk bodies (F) and fibrosis (I). The association also approaches significance with pigmented Kupffer cells (H). Y axis values represent Mean ± SE of the mean, and p values were calculated according to the Kruskal-Wallis test.

Tumours also tended to be larger (assessed here by including the largest single tumour diameter in millimetres) in cases with more advanced NAFLD (**Figure** 3.8).

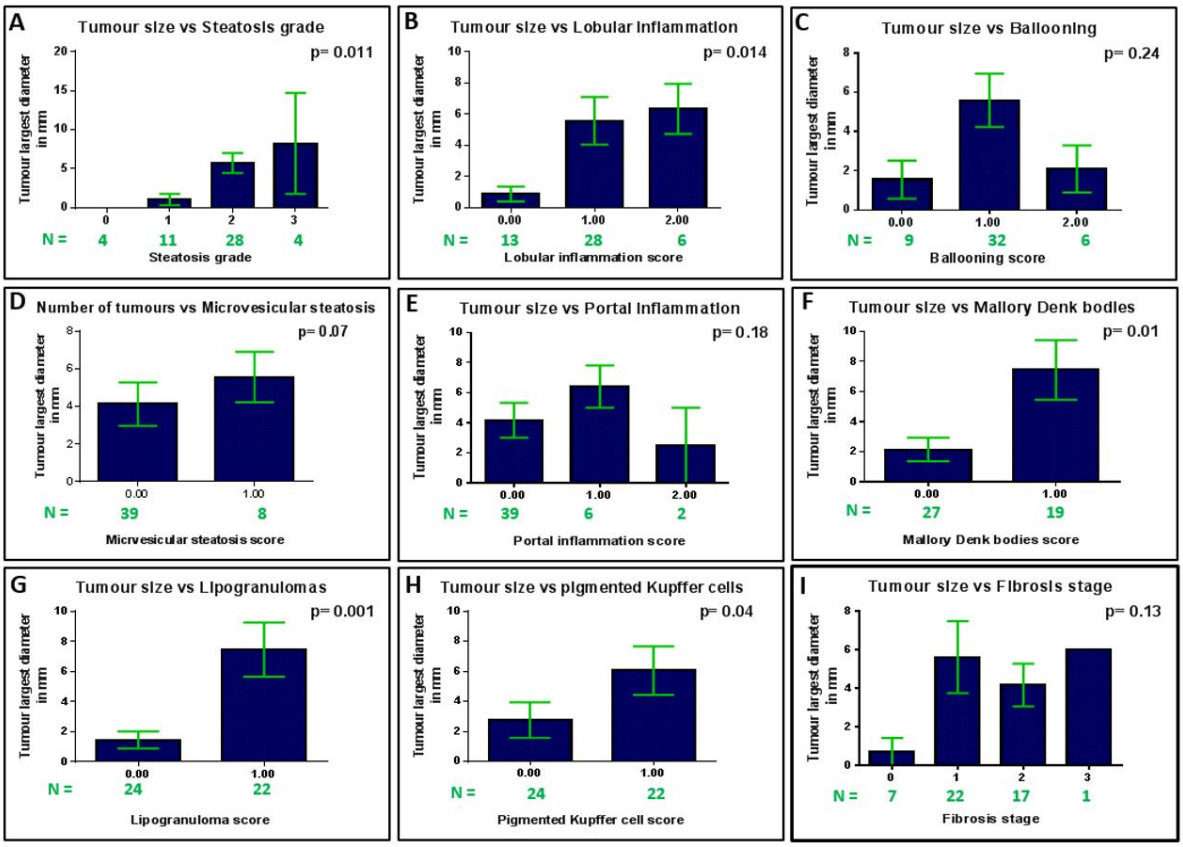

Figure 3.8 : Tumour size association with NAFLD progression in the 48-week-old mice. There was a significant association of the tumour size with steatosis (A), lobular inflammation (B), pigmented Kupffer cells (H), Mallory Denk bodies (F). The association was highly significant with lipogranulomas (G) and approaches significance with microvesicular steatosis (D). Y axis values represent Mean ± SE of the mean, and p values were calculated using the Kruskal-Wallis test.

However, including only the cases in which there were tumours, and analysing either by Chi Square for tumour size assessed as categorical data (tumours <5mm or ≥5mm), or using bivariate Spearman correlations considering tumour size as a continuous variable, these associations were less striking. Borderline significant associations with inflammatory activity were seen, brought out in the combination NAS and SAF activity scores (**Table** 3.4). The only robust association with size was the presence of Mallory-Denk bodies.

Table 3.4 : Association of tumour size with the phenotypic and liver histopathology parameters

	Tumour size			Spearman rho	
	<5mm n=11	≥5mm n=16		correlation	p value
Gross Phenotype Parameters					
	Mean ± SEM			correlation	P value
Body weight (gram)	45.56±1.39	46.22±1.25	-	0.058	0.774
Liver weight (gram)	2.4±0.17	2.86±0.17	-	0.326	0.097
Liver/body weight ratio	0.052±0.002	0.063±0.004	-	0.348	0.075
Visceral adipose tissue weight (gram)	1.89±0.27	1.51±0.19	-	-0.223	0.263
	Tumour size		Chi ^{2}	Spearman rho	
	<5mm n=11	≥5mm n=16		correlation	p value
Histological Parameters					
	Number of mice		P value	correlation	P value
Steatosis grade (0/1/2/3)	0/3/6/2	0/1/14/1	0.201	0.254	0.201
Microvesicular Steatosis grade (0/1)	9/2	11/5	0.113	0.38	0.85
Hepatocellular ballooning score (0/1/2)	2/8/1	2/12/2	0.905	0.109	0.587
Mallory Denk bodies (None/present)	9/2	4/11	**0.005**	0.581	**0.002**
Megamitochondria (None/present)	5/6	12/3	0.108	-0.335	0.094
Lipogranuloma (None/present)	5/6	4/11	0.419	0.438	**0.025**
Lobular Inflammation score (0/1/2)	3/8/0	1/10/5	**0.064**	0.349	0.074
Portal Inflammation score (0/1/2)	11/0/0	10/5/1	0.058	0.189	0.346
Pigmented Kupffer cells (None/present)	6/5	5/10	0.198	0.302	0.134
Apoptotic cells (None/present)	11/0	11/4	0.173	0.356	0.074
Perisinusoidal fibrosis score(0/1)	0/11	1/15	0.398	0.038	0.851
Periportal fibrosis score (0/1/2)	7/4/0	8/7/1	0.667	0.062	0.758
Fibrosis stage (0/1/2/3)	0/7/4/0	1/7/7/1	0.156	0.046	0.0818
NAS score (<3/≥3)	4/7	2/14	0.143	0.396	**0.041**
SAF activity (<2 either LI or B/>2 both LI & B)	4/7	2/14	**0.033**	0.395	**0.041**

3.3.4.3 Binomial Regression Analyses of tumour development and stage

As many of the factors exacerbated by diet, including obesity and NAFLD stage, were inter-related, confirming those that were the drivers of tumour development and progression was not definitively possible in this model. However, binomial regression analyses centred on either tumour development (absent or present), tumour number (1 or >1) or tumour size (<5mm or ≥5mm) were performed, as summarised in **Table** 3.5.

Table 3.5: Binomial regression analysis of tumour development and stage in the dietary animal model.

Binomial regression Table A	Tumour development	Tumour Progression	
	Tumour yes or no	Tumour number 1 or >1	Tumour size <5mm or ≥5mm
Diet	**0.001**	0.999	0.312
Mouse demographic factors			
Body weight (gram)	**0.020**	0.085	0.722
Liver weight (gram)	**0.001**	0.026	0.100
Liver to body weight ratio	**0.001**	0.050	0.109
Liver Histopathology			
Steatosis grade 0/1/2/3/4	0.249	0.547	0.190
Steatois absent/present	0.999	fat absent 4 mice, no tumours	
Microvesicular steatosis (0/1)	0.090	**0.041**	0.446
Mallory Denk Bodies absent/present	0.176	0.056	**0.010**
Ballooning degeneration	0.584	0.494	0.889
Megamitochondria absent/present	0.280	0.223	0.076
Lipogranuloma absent/present	**0.009**	0.050	0.324
Lobular Inflammation 0/1/2	0.068	0.275	0.571
Lobular Inflammation absent/present	**0.028**	0.334	0.162
Portal Inflammation 0/1/2	0.436	0.299	1.000
Pigmented Kupffer cells (0/1)	0.130	0.239	0.284
Apoptotic Bodies (0/1)	0.419	1.000	0.414
Perisinusoidal fibrosis (0/1)	**0.033**	1.000	1.000
Periportal Fibrosis (0/1/2)	0.694	0.322	0.872

Binomial regression Table B	Tumour development Tumour yes or no	
	p value	Exp (B)
Body weight (gram)	0.959	1.006
Liver weight (gram)	**0.046**	13.446
Lipogranuloma absent/present	0.851	1.210
Lobular Inflammation absent/present	0.670	1.525
Perisinusoidal fibrosis (0/1)	0.261	0.222

Binomial regression Table C	Tumour development Tumour yes or no	
	p value	Exp (B)
Diet	0.418	0.438
Liver weight (gram)	0.056	8.309

Considering histopathology features and tumour development, the presence of lipogranulomas, lobular inflammation, perisinusoidal fibrosis and grade 2 steatosis or above, were each significantly associated with tumour development in a univariate analysis (**Table** 3.5**, A**). None was independently associated with tumour development in a multivariate analysis (**Table** 3.5**, B**). This included body weight and liver weight, which in the univariate analysis was independently associated with the development of tumours, only liver weight was associated with tumour development (**Table** 3.5**, B**).

Exploration of factors potentially contributing to increasing tumour numbers, only the presence of microvesicular steatosis was significantly associated with greater than 1 tumour, although the presence of lipogranulomas and Mallory denk bodies trended towards statistical significance.

In a binomial regression analyses considering associations with larger (≥5mm) versus smaller (<5mm) tumours, including factors such as body weight, liver weight and diet, only the presence of mallory denk bodies was significantly different (p=0.01).

In these analyses, the mice were analysed as a cohort where the focus was on those variables altered by the diet in a mouse strain susceptible to obesity, impaired glucose tolerance and liver tumour development with age - rather than the diet itself (**Table** 3.5**, C**). Notably, binomial regression analysis including diet and liver weight supported the importance of liver weight rather than the diet itself driving tumour development. Analysis including diet as a variable with liver to body weight ratio reached statistical significance (p=0.05).

3.3.5 Hepatocyte DNA damage was increased in aged and ALIOS fed mice

3.3.5.1 γ-H2AX immunohistochemical analysis

To explore mechanistic biology in this model of NAFLD and tumour development, we assessed DNA damage in liver (FFPE) tissue sections, using immunohistochemical staining with anti-γ-H2AX antibodies. There were more γ-H2AX positively stained nuclei in the livers of ALIOS fed mice compared to those fed control diet at 48 weeks. This measure of DNA damage was more prominent in the periportal zones of the liver, in which the fat accumulation was also more prominent - supporting a link between fat accumulation and DNA damage (**Figure** 3.9).

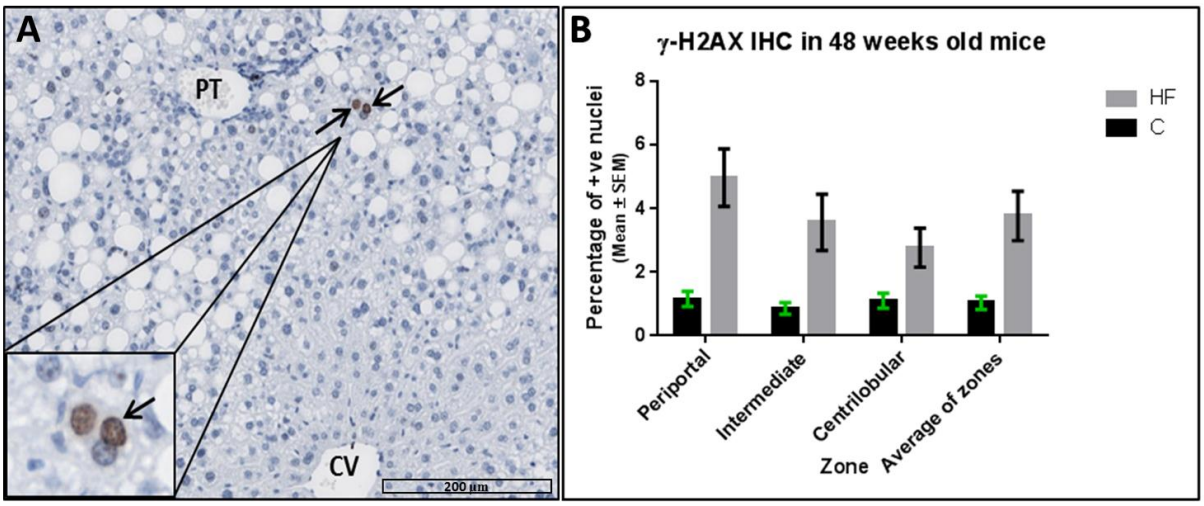

Figure 3.9: DNA damage assessment in the 48-week-old mice. (A) γ-H2AX immunohistochemical staining of mouse liver tissue sections showing positively stained hepatocyte nuclei (arrows). (B) γ-H2AX detection by IHC in liver zones of 48-week-old mice, showed a higher number of positively stained nuclei in the ALIOS fed animals compared to the control animals; and this was clear in all the different zones of the liver with the highest expression in the periportal area ($p<0.0001$, t-test). Y axis values represent Mean ± SE of the mean. The p value was calculated by t-test. Key: PT - portal tract; CV - central vein.

γ-H2AX assessed immunohistochemically in mice from earlier time points (24-week-old mice) revealed a much lower prevalence of DNA damaged hepatocytes, with no significant difference between the ALIOS diet (HF) and the control mice (**Figure** 3.10**; A**). Thus, hepatocyte DNA damage was increased in the 48-week-old mice, especially in the ALIOS fed animals (**Figure** 3.10**; B**).

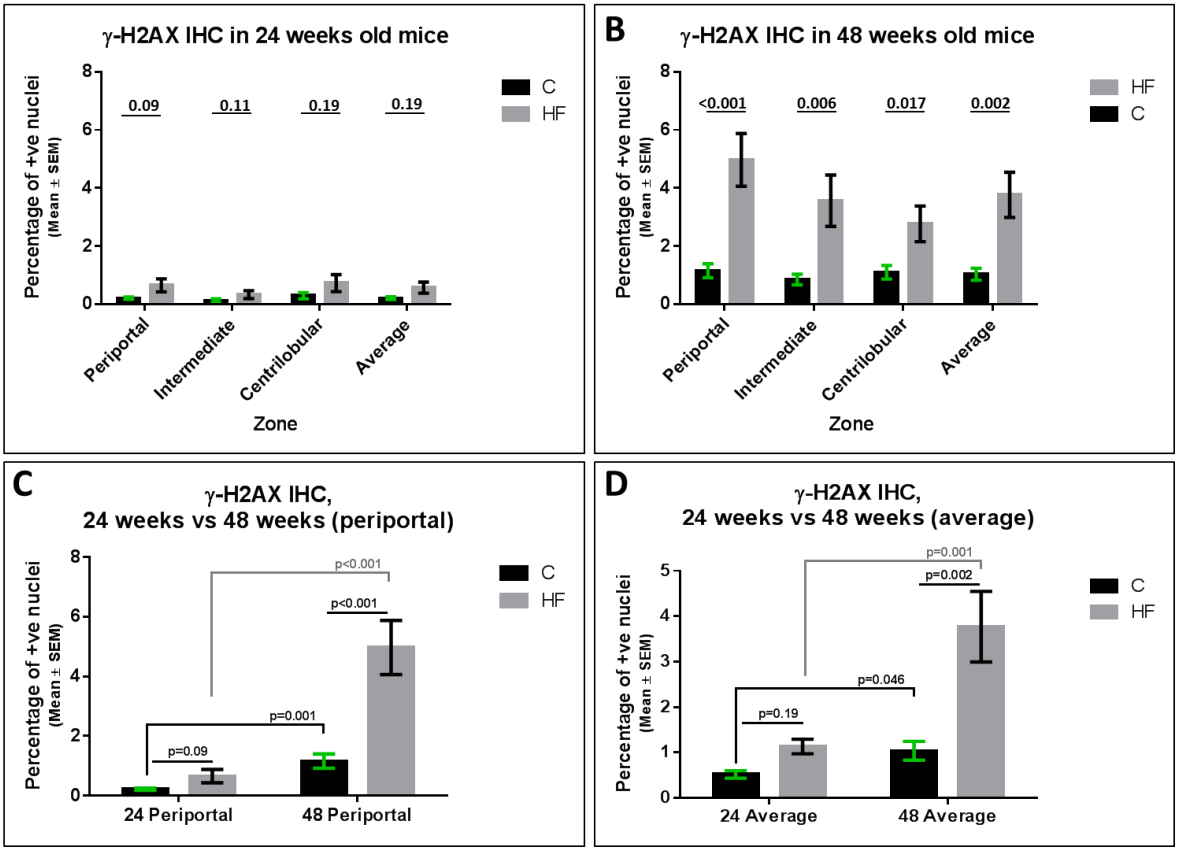

Figure 3.10: γ-H2AX quantification in liver tissue sections from 24- and 48-week-old mice. (A) γ-H2AX IHC staining in 24-week-old mice in all the three liver zones. (B) γ-H2AX IHC staining in 48-week-old mice in all the three liver zones. (C) Comparison between 24- and 48-week-old mice periportal γ-H2AX IHC staining. (D) Comparison between 24- and 48-week-old mice average γ-H2AX IHC staining of all the three liver zones. Y axis values represent Mean ± SE of the mean. The p-value was determined by t-test.

3.3.5.2 DNA damage association with NAFLD

Histological studies confirmed that DNA damage was closely associated with the progression of NAFLD (**Figure** 3.11 and **Table** 3.6). Notably, the strongest DNA damage associations were not with lobular inflammation, portal inflammation or fibrosis, but rather with steatosis grade, the presence of lipogranulomas and liver weight. Associations with the NAS and SAF scores were largely driven by the strong association with steatosis.

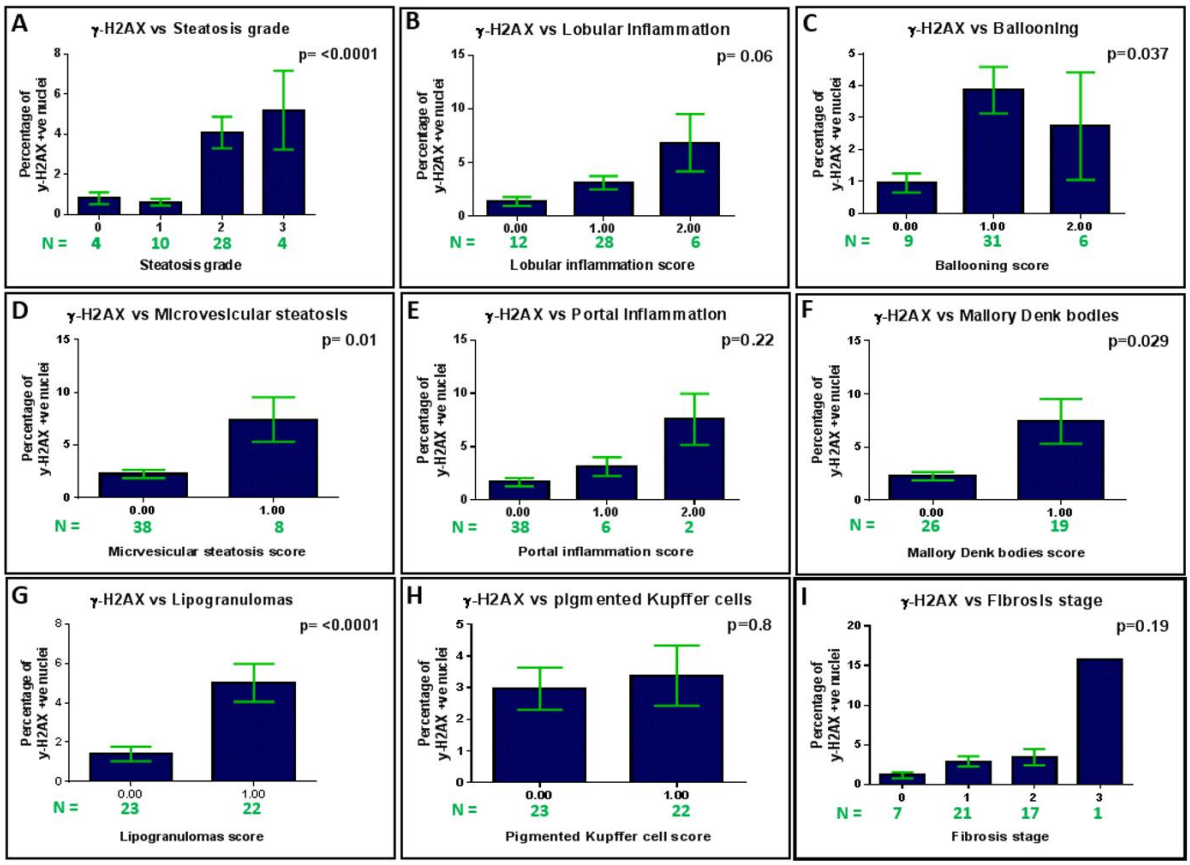

Figure 3.11 : Association of DNA damage with the progression of NAFLD in the 48-week-old mice. DNA damage was reflected and measured immunohistochemically by γ-H2AX positivity, which correlated significantly with the progression of NAFLD; as it showed significant association with steatosis (A), microvesicular steatosis (D), ballooning (C), and lipogranuloma (G). Y axis values represent Mean ± SE of the mean, and p values calculated by the Kruskal-Wallis test.

Overall, the DNA damage associations appeared to be with NAFLD progression and tumour formation, rather than tumour development per se. In a binomial regression considering absence or presence of a tumour, γ-H2AX percentage treated as a continuous variable was not significantly associated with tumour development in this model. Considering γ-H2AX as a categorical variable with only two categories (above and below the median of 1.48% positive hepatocyte nuclei), significance was reached (p=0.037). However, in an analysis combined with liver weight, only liver weight was significantly associated with tumour development (γ-H2AX p=0.888; liver weight p=0.002, Exp (B) 20.17)

Table 3.6: Association of γ-H2AX-positive hepatocyte nuclei.

	γ-H2AX IHC (% positive hepatocyte nuclei)					
					Spearman rho	
	<1%	1-2%	>2%		correlation	p value
Gross Phenotype Parameters						
	Mean ± SEM				correlation	p value
Body weight (Continuous variable) (gram)	42.61±1.35	43.47±1.19	46.43±1.14	-	0.434	**0.003**
Liver weight (Continuous variable) (gram)	1.96±0.11	2.16±0.11	2.8±0.17	-	0.597	**<0.001**
Visceral Adipose Tissue (gram)	1.18±0.18	1.31±0.29	1.74±0.16	-	0.299	**0.043**
	γ-H2AX IHC (% positive hepatocyte nuclei)					
	Chi^2				Spearman rho	
	<1%	1-2%	>2%	P value	correlation	p value
Histological Parameters						
	Number of mice			P value	correlation	p value
Steatosis grade (0/1/2/3)	2/9/6/0	2/1/9/0	0/0/13/4	**<0.001**	0.611	**<0.001**
Microvesicular steatosis grade (0/1)	16/1	11/1	11/6	**0.049**	0.384	**0.008**
Hepatocellular ballooning score (0/1/2)	6/9/2	2/7/3	1/15/1	0.107	0.194	0.197
Mallory Denk bodies (None/present)	13/4	5/6	8/9	0.141	0.329	**0.027**
Megamitochondria (None/present)	14/3	9/2	9/8	0.111	0.276	0.067
Lipogranuloma (None/present)	12/5	8/3	3/14	**0.002**	0.537	**<0.001**
Lobular Inflammation score (0/1/2)	6/9/2	4/7/1	2/12/3	0.544	0.353	**0.016**
Portal Inflammation score (0/1/2)	15/2/0	10/1/1	13/3/1	0.751	0.249	0.096
pigmented Kupffer cells (None/present)	8/9	7/4	8/9	0.633	-0.38	0.806
Apoptotic cells (None/present)	12/5	11/0	13/4	0.148	0.03	0.82
Perisinusoidal fibrosis score(0/1)	4/13	2/10	1/16	0.354	0.212	0.157
Periportal fibrosis score (0/1/2)	12/4/1	6/6/0	10/7/0	0.451	0.125	0.409
Fibrosis stage (0/1/2/3)	4/8/5/0	2/4/6/0	1/9/6/1	0.557	0.226	0.409
NAS score (<3, ≥3)	11/6	6/6	2/15	**0.006**	0.506	**<0.001**
SAF activity (<2 either LI or B/>2 both LI & B)	9/8	5/7	2/15	**0.035**	0.449	**0.002**
Tumour development, progression and grade						
Tumour (absent/present)	11/6	5/7	4/13	0.053	0.353	**0.016**
Tumour number (continuous, n=46 cases)					0.399	**0.006**
Tumour Number (1/ >1; 26 cases)	4/2	4/3	5/8	0.472	0.333	0.096
Tumour size (continuous, n=26 cases)					0.353	**0.016**
Tumour size (<5mm/≥5mm; 26 cases)	2/4	2/5	6/7	0.711	0.3011	0.959
Tumour grade (1/2/3/4; 20 cases)	0/3/0/0	3/4/0/0	2/6/1/1	0.621	0.225	0.341

3.3.6 Hepatocyte proliferation was elevated in aged C3H/He mice

The increase in liver weight in C3H/He aged mice may simply have been a result of fat accumulation in hepatocytes. However, given the strong association between liver weight and tumour development, we explored proliferation in these murine livers. To measure this, Ki67 (as a marker of proliferation detecting all phases of cell cycle) was assessed immunohistochemically, expressed as the percentage of positively stained hepatocyte nuclei. Counts were compared in periportal, intermediate and centrilobular zones, in mice culled at either 24- or 48-weeks of age, fed either control or ALIOS diets.

The data are summarised in **Figure** 3.12. The first observation was that the percentage of proliferating hepatocytes more than doubled with age in the control mice, from an average of about 0.49% in 24-week-old mice, to 1.23% in 48-week-old mice. The second observation was that the percentage of positive hepatocytes was significantly higher in ALIOS fed mice, at both time points. In the younger mice with less severe NAFLD, there was no difference in the liver zone distribution. The most striking increase in the older mice was in the periportal zones of mice fed the ALIOS diet, indicating a relationship between the level of fat accumulation and associated changes in that zone (**Figure** 3.12). An example is shown in **Figure** 3.13.

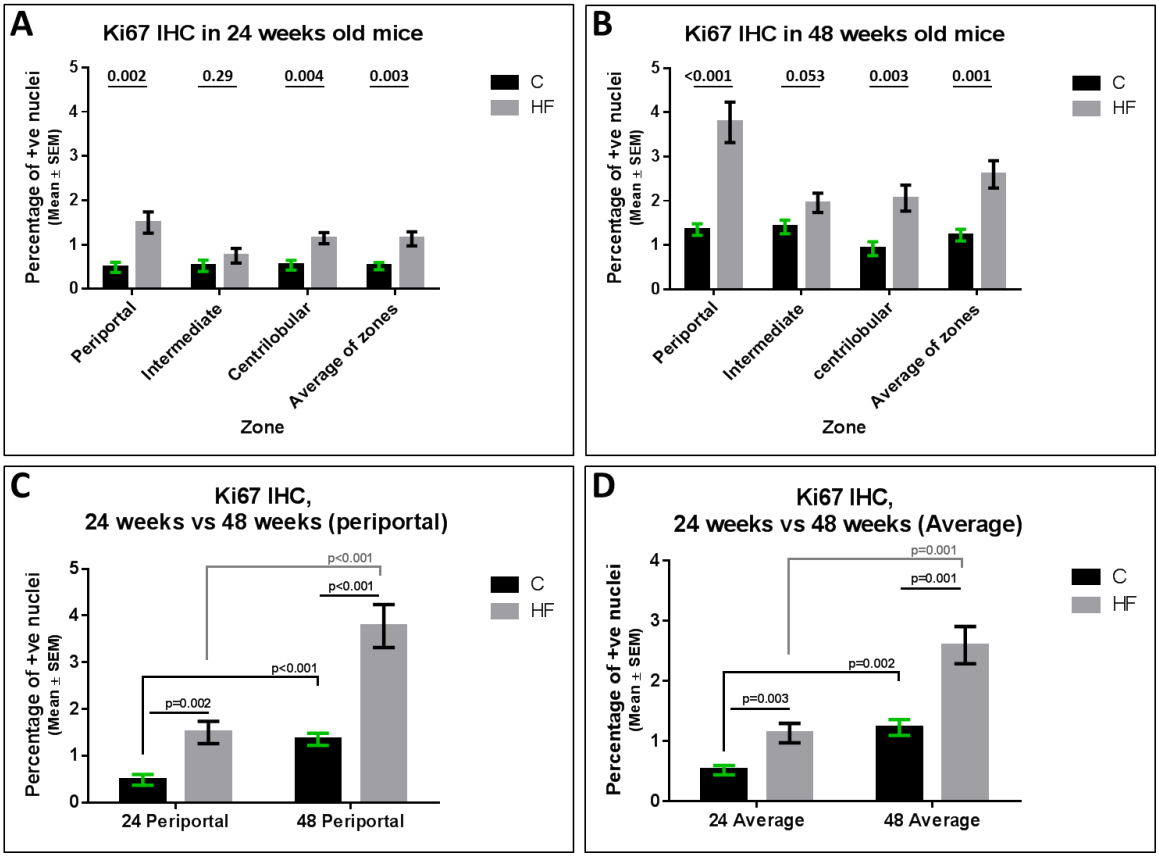

Figure 3.12: Ki67 quantification in liver tissue sections of 24- and 48-week-old mice. (A) Ki67 IHC staining in 24-week-old mice in all the three liver zones. (B) Ki67 IHC staining in

48-week-old mice in all the three liver zones. (C) Comparison between 24- and 48-week-old mice periportal Ki67 IHC staining. (D) Comparison between 24- and 48-week-old mice average Ki67 IHC staining of all the three liver zones. Y axis values represent Mean ± SE of the mean. The p-value was determined by t-test.

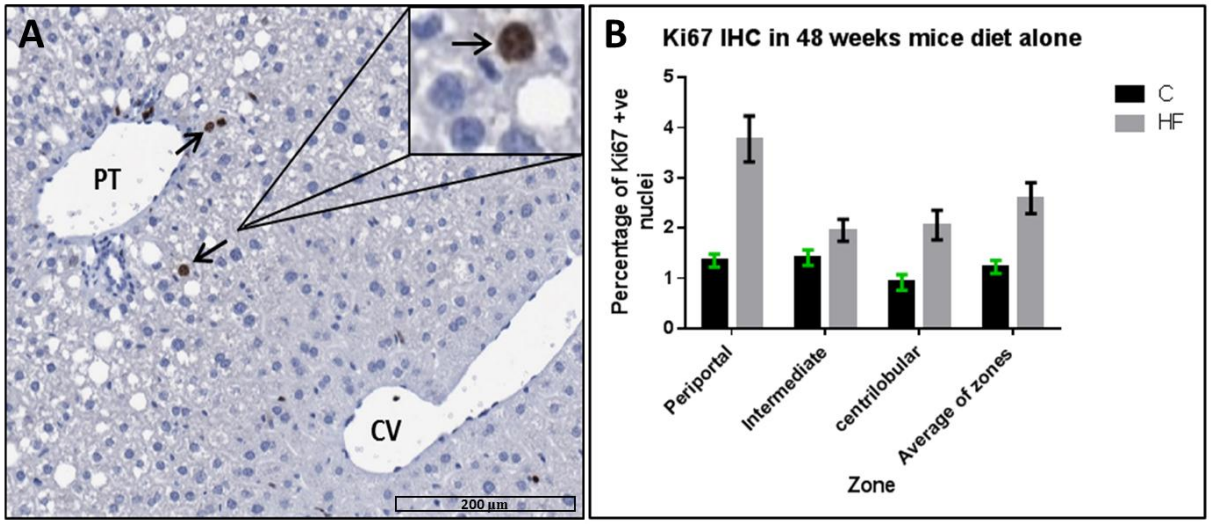

Figure 3.13: Ki67 expression in association with fat accumulation in the periportal zone of a 48-week-old mouse fed the ALIOS diet. Ki67 assessment by immunohistochemical staining showed positively stained nuclei (arrows) around the portal tract. Key: PT - portal tract; CV - central vein.

Several studies investigated the effect of lipid accumulation on liver regenerative capability (247). Some of which showed no effect of mild steatosis on liver regeneration (248, 249), while several others showed a decrease in liver regeneration in animal models of chronic steatosis (250-252). The mechanism by which steatosis impairs liver regeneration remains unclear (247). In our dietary animal we showed an interesting increase in proliferation of hepatocytes (reflected by Ki67 positively stained hepatocyte nuclei) in areas of lipid accumulation which contradicts these studies and the mechanism needs further exploration but it might be induced in part through activation of the Hedgehog signalling pathway in chronically injured hepatocyte in NAFLD that induces proliferation (113) (detailed explanation in chapter 7).

The associations between Ki67 expression and other parameters was also explored. Ki67 correlated highly significantly with body and liver weight, as well as with some of the histological features of progressive NAFLD – including steatosis, lobular inflammation and presence of lipogranulomas (**Figure** 3.14). Currently this data is limited by smaller numbers than the others (only 24 of 47 cases analysed). Of note, there was a highly significant association between Ki67 and γ-H2AX positive cells in the cases studied. Despite smaller numbers, the

associations between Ki67 positive perpiportal hepatocyte nuclei and tumour development and progression, were much more striking than those with γ-H2AX (**Table** 3.7).

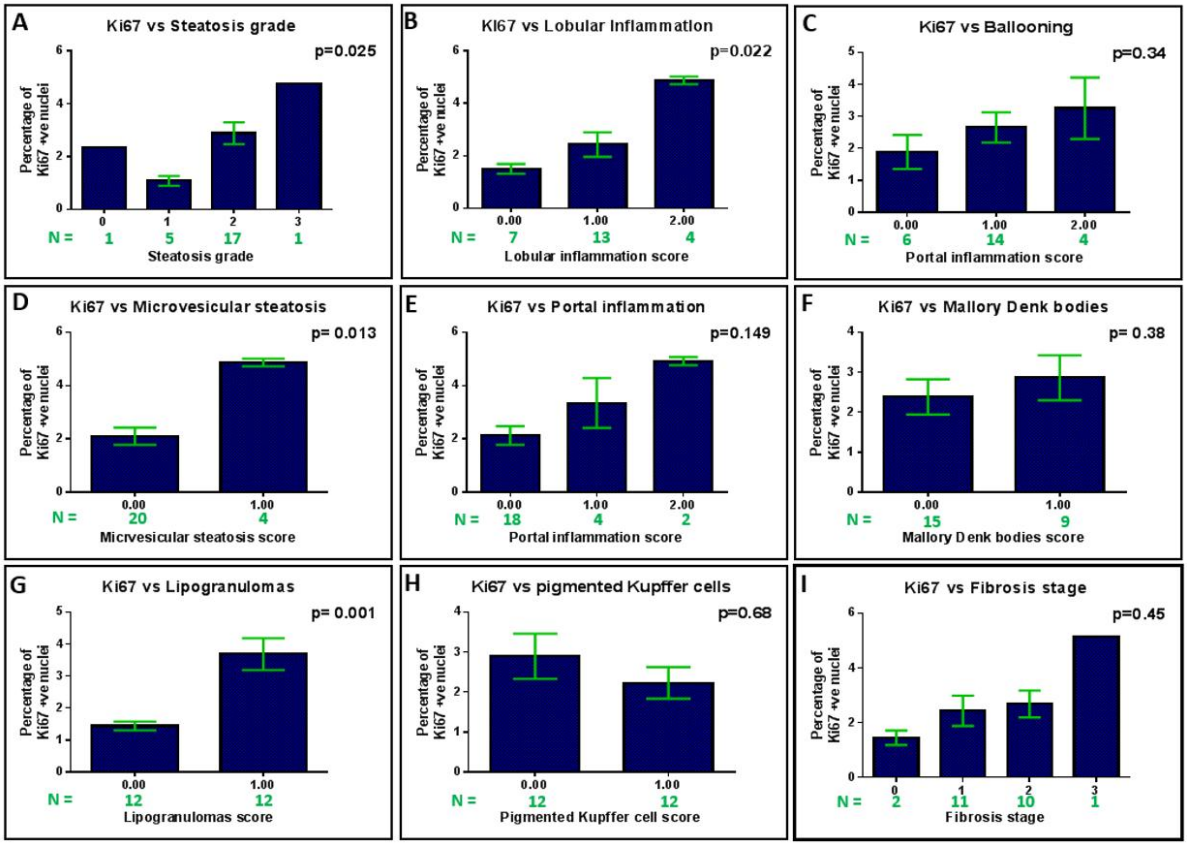

Figure 3.14 : Correlation of Ki67 expression with the histological parameters of NAFLD. Ki67 expression assessed by immunohistochemistry correlated significantly with steatosis grade (A), lobular inflammation (B), microvesicular steatosis (D) and highly significant association with lipogranulomas (G) indicating more proliferation with advancing disease. Y axis values represent Mean ± SE of the mean, and p values were measured by Kruskal-Wallis test.

Table 3.7: Association of Ki67-positive hepatocyte nuclei

(24 cases only)	Ki67 (% positive hepatocyte nuclei)(periportal)				
				Spearman rho	
	<1.71%	≥1.71%		correlation	p value
Gross Phenotype Parameters					
	Mean ± SEM			correlation	p value
Body weight (Continuous variable) (gram)	41.3±0.56	47.4±1.57	-	0.648	**0.001**
Liver weight (Continuous variable) (gram)	1.8±0.05	2.88±0.2	-	0.78	**<0.001**
Visceral Adipose Tissue (gram)	1.27±0.17	1.72±0.16	-	0.341	0.103
(24 cases only)	Ki67 (% positive hepatocyte nuclei)(periportal)				
		Chi^2		Spearman rho	
	<1.71%	≥1.71%	P value	correlation	p value
Histological Parameters					
	Number of mice		P value	correlation	p value
Steatosis grade (0/1/2/3)	0/5/6/0	1/0/11/1	**0.018**	0.533	**0.007**
Microvesicular Steatosis grade (0/1)	11/0	9/4	0.098	0.517	**0.01**
Hepatocellular ballooning score (0/1/2)	4/5/2	2/9/2	0.63	0.295	0.162
Mallory Denk bodies (None/present)	8/3	7/6	0.423	0.18	0.399
Megamitochondria (None/present)	8/3	7/6	0.423	0.367	0.078
Lipogranuloma (None/present)	9/2	3/10	**0.012**	0.674	**<0.001**
Lobular Inflammation score (0/1/2)	5/6/0	2/7/4	0.093	0.547	**0.006**
Portal Inflammation score (0/1/2)	10/1/0	8/3/2	0.337	0.383	0.064
Pigmented Kupffer cells (None/present)	5/6	7/6	1	-0.084	0.695
Apoptotic cells (None/present)	8/3	11/2	0.63	-0.2	0.349
Perisinusoidal fibrosis score(0/1)	1/10	1/12	1	0.174	0.416
Periportal fibrosis score (0/1/2)	6/5/0	7/5/1	1	0.212	0.32
Fibrosis stage (0/1/2/3)	1/5/6/0	1/6/5/1	1	0.255	0.23
NAS score (<3, ≥3)	8/3	3/10	**0.038**	0.707	**<0.001**
SAF activity (<2 either LI or B/>2 both LI & B)	7/4	3/10	0.095	0.585	**0.003**
Tumour development, progression and grade					
Tumour (absent/present)	9/2	3/10	**0.012**	0.506	**0.012**
Tumour number (continuous, n=46 cases)				0.54	**0.006**
Tumour Number (none/1/ >1)	9/2/0	3/3/7	**0.003**	0.534	**0.007**
Tumour size (continuous)				0.546	**0.006**
Tumour size (none/<5mm/≥5mm)	9/2/0	3/4/6	**0.011**	0.522	**0.009**
Tumour grade (1/2/3/4; 20 cases)	1/1/0	2/6/1	1	-0.128	0.708
Immunohistochemical markers					
γ-H2AX % positive (above/below median)	9/2	2/11	**0.001**	0.709	**<0.001**

3.4 The p53 pathway in the ALIOS diet induced NAFLD and tumours

The p53 tumour suppressor protein is often referred to as the 'gatekeeper' or "guardian" of the genome, as it is part of the normal DNA damage response. It has a role in the suppression of proliferation and programmed cell death. In NAFLD p53 upregulation has been previously reported and p53 is believed to play a role in the pathogenesis of the disease (see 1.4.2) (45, 195). Given the evidence of an elevation in hepatocyte DNA damage, as well as an apparent proliferative state associated with age and enhanced by the ALIOS diet, we explored the expression of p53 and some of its key target genes in the liver tissues of these mice. This was investigated for whole tissues at the RNA level, as well as for protein expression and distribution by immunohistochemistry.

3.4.1 Hepatic tissue p53 mRNA levels were elevated with age rather than with diet.

In the C3H/He ALIOS diet model, the relative expression of *Trp53* mRNA in whole liver tissues was significantly upregulated with advancing age (Control diet: $p<0.001$; ALIOS diet $p<0.001$, t-test, **Figure** 3.15). The elevations occurred in association with the rising liver weight and steatosis, which also occurred with age. However, there was in fact no significant difference in *Trp53* whole liver mRNA expression between the ALIOS and control fed groups at any age studied.

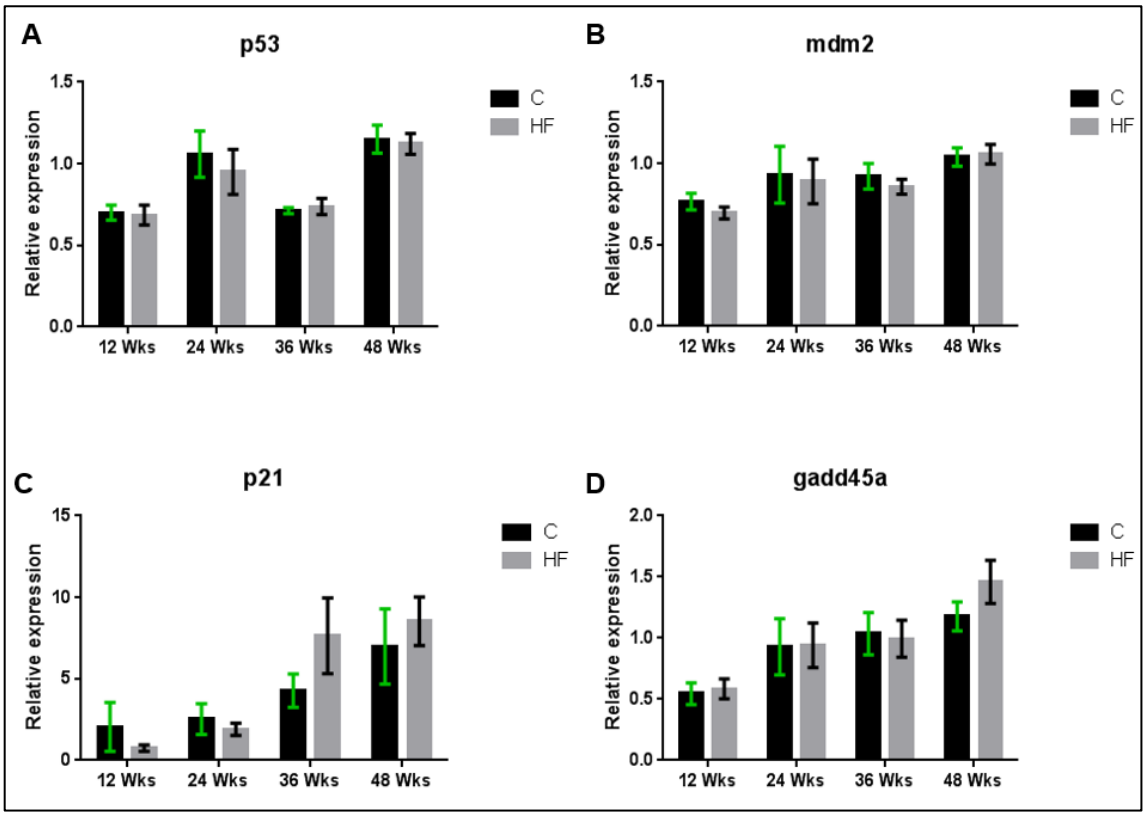

Figure 3.15: Quantification of mRNA levels for p53 pathway genes in whole liver tissue extracts from ALIOS dietary animal model mice. qRT-PCR assessment of the expression of *Trp53* (A) and its downstream targets *Mdm2* (B), *Cdkn1a* (*p21*) (C) and *Gadd45a* (D) in the dietary animal model in the four age groups (12,24,36, and 48 weeks). There was a significant difference in *Trp53* and its downstream transcriptional targets expression with age ($p<0.001$) but not with the diet. No significant difference in *Trp53* expression with diet at any age group ($p= 0.43, 0.40, 0.40, 0.95$) for the (12, 24, 36 and 48 weeks) age groups respectively. *Gapdh* was used as the house keeping reference gene and a 12-week-old control diet sample as the calibrator. Y axis values represent mean ± SEM.

The upregulation of p53-downstream genes *Mdm2*, *Cdkn1a (p21)*, and *Gadd45a* correlated significantly with rising *Trp53* **(Figure** 3.15**; Table** 3.8**),** but again, this was predominantly with advancing age rather than with a specific dietary condition (**Figure** 3.15). With the exception of an elevation of *Cdkn1a* (*p21)* mRNA in whole liver tissue of ALIOS fed mice at 48 weeks of age ($p=0.002$), none of the studied genes showed a significant whole tissues mRNA change associated with diet either.

Of note, the correlation between *Trp53* and its target *Cdkn1a (p21)* was not as striking or significant as that observed with its transcriptionally regulated negative modulator *Mdm2*, or *Gadd45*. The relationship between *Trp53* mRNA and its targets was more closely assessed within the age and dietary categories. The relationship between *Trp53* and its negative regulator, *Mdm2*, persisted with age and different dietary groups. A strong and significant relationship with *Cdkn1a (p21)* was present in young mice, up to 24 weeks, in both control and

ALIOS dietary groups. At 48 weeks this association was less striking in control diet mice and was lost in ALIOS diet mice. The relationship with *Gadd45a* was less robust and was only evident in larger groups, rather than appearing to be affected by age or diet.

Table 3.8: Correlations between *Trp53* mRNA and its downstream targets at the mRNA level.

Spearman Rho Correlations	All ages (n=95)		Up to 24 weeks (n=32)		48 weeks only (n=47)	
	correlation	p value	correlation	p value	correlation	p value
P21 mRNA	0.348	**0.001**	0.569	**<0.001**	0.229	0.122
Mdm2 mRNA	0.633	**<0.001**	0.529	**0.002**	0.546	**<0.001**
Gadd45a mRNA	0.459	**<0.001**	0.291	0.106	0.187	0.208
CONTROL ONLY						
	All ages (n=47)		Up to 24 weeks (n=16)		48 weeks only (n=23)	
P21 mRNA	0.392	**0.008**	0.543	**0.045**	0.442	**0.035**
Mdm2 mRNA	0.572	**<0.001**	0.482	0.058	0.497	**0.016**
Gadd45a mRNA	0.38	**0.008**	0.435	0.092	0.156	0.478
ALIOS DIET ONLY						
	All ages (n=48)		Up to 24 weeks (n=16)		48 weeks only (n=24)	
P21 mRNA	0.351	**0.014**	0.653	**0.006**	0.079	0.713
Mdm2 mRNA	0.718	**<0.001**	0.635	**0.008**	0.561	**0.004**
Gadd45a mRNA	0.574	**<0.001**	0.162	0.549	0.171	0.425

These data suggest that *Trp53* post translational functional status is maintained throughout, as the relationship with *Mdm2* is never lost. However, the data also indicate that transcriptional regulation of other targets is either reliant on more than p53, or p53 transcriptional control is altered. In the case of *Cdkn1a* (*p21*) transcriptional control, this appears to change in the livers of mice fed the ALIOS diet.

Levels of hepatic *Trp53* mRNA in the livers of mice at 48 weeks of age were explored in association with other liver related phenotypic changes **(Table** 3.9). There was little of note, with a similar lack of associations between liver *Mdm2* mRNA and liver associated features.

In sharp contrast, there were significant positive associations between *Cdkn1a (p21)* mRNA and both the presence of γ-H2AX and Ki67 positive nuclei. The average positive nuclei counts were considered for this association as they were most likely to associate with whole liver mRNA gene expression changes. Notably, there were more striking and highly significant associations with liver phenotype - including with liver weight; steatosis grade, lobular inflammation and the presence of either lipogranuloma or perisinusoidal fibrosis. Furthermore, there were significant associations with tumour number and tumour size.

Table 3.9: Hepatic genes expression associations in 48-week-old mice (bivariate analyses). Benjamini–Hochberg procedure with a false discovery rate of 0.25 was used.

Associations explored at 48 weeks (n=47)	P53		MDM2		P21		PARP	
Cor: correlation; p: p-value	Cor.	p	Cor.	p	Cor.	p	Cor.	p
Gross Phenotype Parameters								
Liver weight (continuous)	-0.253	0.087	-0.231	0.119	0.479	**0.001**	**-0.492**	**0.001**
Histopathology Parameters								
Steatosis grade (0/1/2/3)	-0.185	0.214	0.092	0.537	0.386	**0.007**	-0.298	**0.042**
Microvesicular Steatosis (0/1)	0.046	0.759	-0.144	0.334	0.146	0.327	-0.063	0.676
Ballooning (0/1/2)	0.035	0.817	-0.183	0.218	0.365	**0.012**	-0.306	**0.036**
Mallory Denk bodies (0/1)	-0.007	0.965	-0.185	0.219	0.304	**0.04**	-0.226	0.131
Megamitochondria (0/1)	-0.207	0.167	0.018	0.905	0.147	0.329	-0.3	**0.043**
Lipogranuloma (0/1)	-0.066	0.665	-0.133	0.379	0.397	**0.006**	**-0.334**	**0.023**
Lobular Inflammation (0/1/2)	0.197	0.185	0.028	0.853	0.442	**0.002**	-0.199	0.18
Portal Inflammation (0/1/2)	-0.071	0.634	**-0.344**	**0.022**	0.159	0.286	-0.207	0.162
Pigmented Kupffer cells (0/1)	0.192	0.202	0.033	0.829	0.22	0.142	0.044	0.77
Apoptotic cells (0/1)	-0.068	0.653	-0.159	0.291	-0.175	0.244	-0.103	0.495
Perisinusoidal fibrosis (0/1)	0.004	0.977	0.189	0.202	0.414	**0.004**	-0.24	0.104
Periportal fibrosis (0/1/2)	0.08	0.592	-0.201	0.175	0.188	0.205	-0.145	0.332
Fibrosis stage (0/1/2/3)	0.057	0.702	-0.089	0.553	0.318	**0.02**	0.221	0.135
NAS score (<3, ≥3)	0.033	0.824	0.04	0.791	0.533	**<0.001**	-0.279	0.057
SAF score (NAFLD, NASH)	0.085	0.571	0.038	0.802	0.549	**<0.001**	-0.359	**0.013**
Immunohistochemical markers								
γ-H2AX (average)	-0.207	0.167	-0.96	0.526	0.316	**0.032**	-0.337	**0.022**
Ki67 (average)	-0.047	0.826	-0.232	0.275	0.495	**0.014**	-0.423	**0.039**
Tumour development and progression								
Tumour (No/Yes)	-0.06	0.687	0.151	0.312	0.412	**0.004**	-0.2	0.178
Tumour number	-0.11	0.461	-0.007	0.963	0.39	**0.007**	-0.204	0.169
Tumour size	-0.029	0.846	0.081	0.591	0.465	**0.001**	-0.274	0.063
Tumour grade	0.041	0.864	-0.027	0.911	0.23	0.329	0.075	0.754

In the 48 week mice livers we considered a role for an alternative *Cdkn1a (p21)* transcriptional regulator, the zinc finger tumour suppressor *Klf6*, which is reported to play a role in NAFLD progression (253). However, this was not associated (Spearman correlation 0.153; p=0.326).

We explored *Cdkn1a (p21)* mRNA associations with a number of other genes. In all age groups of mice irrespective of diet, the strongest positive association was with *Nudt1* expression – the gene that encodes Nudix hydrolase 1, or 7,8-dihydro-8-oxoguanine triphosphatase (Spearman correlation 0.613; p<0.001). Misincorporation of oxidized nucleoside triphosphates into DNA and/or RNA during replication and transcription can cause mutations that may result in carcinogenesis. Nudt1 is an enzyme that hydrolyzes oxidized purine nucleoside triphosphates, to monophosphates, thereby preventing misincorporation.

A 48-week age specific negative association of *Cdkn1a* (*p21*) was noted with mRNA expression of poly ADP ribose polymerase 1 (*Parp1*) (Spearman correlation -0.345; p=0.018). Parp1 binds to single strand breaks in DNA and initiates repair. Of interest, this gene was negatively associated with increasing liver weight.

While these changes in *Cdkn1a (p21)* mRNA indicate altered p53 transcriptional control in ageing obese mice, the associations with liver phenotypes and other genes are hard to interpret in isolation. As expression of p21 protein is typically associated with growth suppression, positive associations with Ki67, liver weight and tumour formation are interesting but may be bystander changes associated with a key, as yet, unidentified mechanistic process, rather than ones that are functionally relevant. For further interpretation, exploration at the protein level would be essential.

3.4.2 Hepatocyte p53 protein increased with age, diet and NAFLD

The protein level of an expressed gene does not necessarily reflect the RNA level and we went on to perform p53 immunohistochemistry on FFPE liver tissue sections. IHC also enables the study of expression more specifically in individual cell types, which whole tissue RNA studies do not.

Considering first the relationship with age, there were quite marked differences in p53 IHC. In the livers of mice at 24 weeks, p53 was hardly detectable – again with little difference between ALIOS versus control diet fed mice (**Figure** 3.16**; A**). However, the number of p53 positive hepatocyte nuclei was significantly elevated in 48 week old mice, and was associated with the presence of γ-H2AX positive nuclei (**Figure** 3.16**, B**).

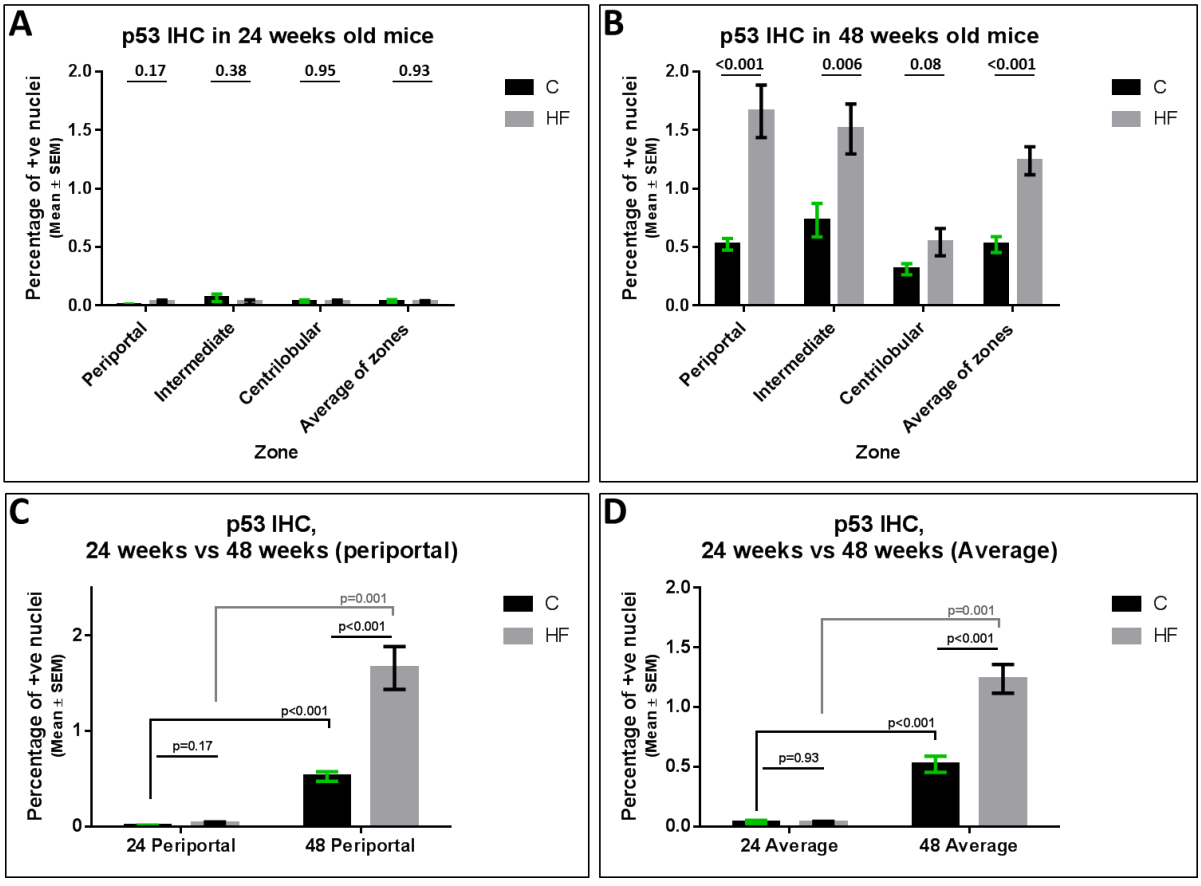

Figure 3.16: p53 quantification in liver tissue section in 24- and 48-week-old mice. (A) p53 IHC staining in 24-week-old mice in all the three liver zones. (B) p53 IHC staining in 48-week-old mice in all the three liver zones. (C) Comparison between 24- and 48-week-old mice periportal p53 IHC staining. (D) Comparison between 24- and 48-week-old mice average p53 IHC staining of all the three liver zones. Y axis values represent Mean ± SE of the mean. The p-value was determined by t-test.

These age-related changes in the frequency of p53 positive hepatocyte complemented the *Trp53* whole liver mRNA data, although there was no significant correlation between the two considering all cases and heterogeneous groups. The numbers of cases within each group assessed by IHC was smaller than for RNA, but in the ALIOS fed 48-week animals, the association between the *Trp53* mRNA and p53 protein trended towards significance (Spearman correlation 0.559; p=0.059, n=12)

In contrast to the whole tissues RNA expression data, there were differences in p53 IHC staining between ALIOS diet versus control diet fed mice. In fact, the level of p53 positive nuclei was elevated in all the liver zones of the ALIOS fed animals compared to the control group. The highest level of p53 positive nuclei was seen in the periportal area (**Figure** 3.17) which coincides with the areas of fat deposition and DNA damage reflected by the γ-H2AX positivity in this area. Thus, there was a spatial correlation between p53 and γ-H2AX positivity (**Figure** 3.9).

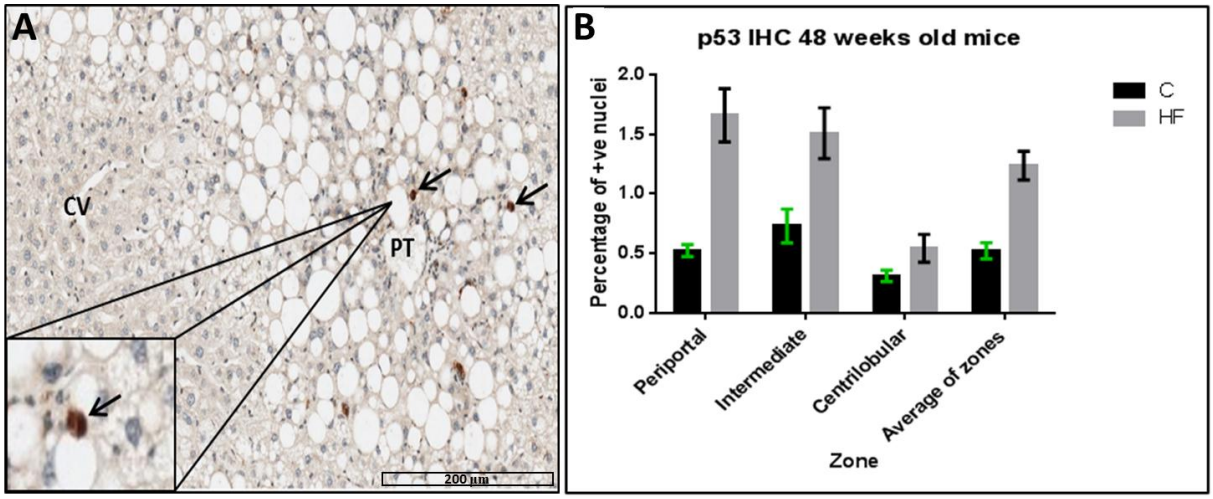

Figure 3.17: p53 expression in the dietary animal model. Assessment of p53 expression by immunohistochemical staining showing positively stained hepatocyte nuclei in the periportal area in conjunction of high levels of steatosis (arrows-picture). The graph (right) shows significantly higher level of p53 in the livers of ALIOS fed mice compared to the control diet and the highest level was detected in the periportal area of the liver in the ALIOS fed animals ($p<0.0001$, t-test, n=12 in each dietary group). Y axis values represent mean ± SEM. Key: PT - portal tract; CV - central vein.

3.4.3 Hepatocyte p53 increased with liver weight and NAFLD progression

The p53 levels showed an increase with features of NAFLD progression to NASH. Mean data are presented graphically in **Figure** 3.18, with Chi^2 and bivariate associations on categorical and continuous datasets respectively shown in **Table** 3.10.

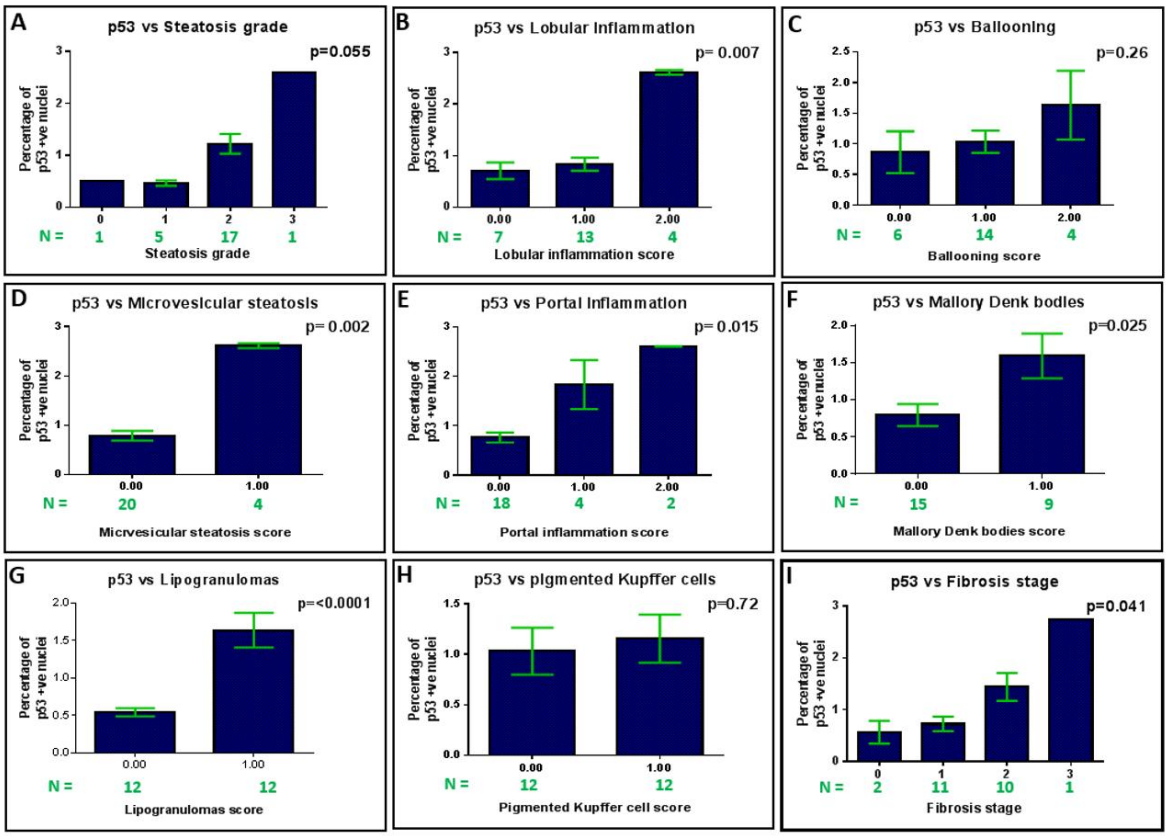

Figure 3.18: The relationship of p53 expression with the histological parameters of NAFLD in 48-week-old mice. Expression of p53 assessed by immunohistochemistry showed a significant association with lobular inflammation (B), portal inflammation (E) microvesicular steatosis (D) fibrosis stage (I) and Mallory Denk bodies (F) and a very highly significant association with lipogranulomas (G). Y axis values represent Mean ± SE of the mean, and p values were calculated by the Kruskal Wallis test.

Table 3.10: Associations with immunohistochemistry %positive p53 hepatocytes.

(24 cases only)	p53 IHC % positive nuclei				
				Spearman rho	
	<0.78	≥0.78		correlation	P value
Gross Phenotype Parameters					
	Mean ± SEM			correlation	P value
Body weight (Continuous variable) (gram)	41.71 ± 1.14	46.6 ± 1.39	-	0.648	**0.001**
Liver weight (Continuous variable) (gram)	1.93 ± 0.15	2.68 ± 0.21	-	0.745	**<0.001**
(24 cases only)	p53 IHC % positive nuclei				
	Chi2			Spearman rho	
	<0.78	≥0.78	P value	correlation	P value
Histological Parameters					
	Number of mice		P value	correlation	P value
Steatosis grade (0/1/2/3)	1/5/5/0	0/0/12/1	**0.005**	0.576	**0.004**
Microvesicular Steatosis grade (0/1)	11/0	9/4	0.098	0.646	**0.001**
Hepatocellular ballooning score (0/1/2)	3/6/2	3/8/2	1	0.339	0.105
Mallory Denk bodies (None/present)	8/3	7/6	0.423	0.466	**0.022**
Megamitochondria (None/present)	8/3	7/6	0.423	0.193	0.367
Lipogranuloma (None/present)	9/2	3/10	**0.012**	0.758	**<0.001**
Lobular Inflammation score (0/1/2)	4/7/0	3/6/4	0.172	0.555	**0.005**
Portal Inflammation score (0/1/2)	10/1/0	8/3/2	0.337	0.599	**0.002**
Pigmented Kupffer cells (None/present)	5/6	7/6	1	0.072	0.737
Apoptotic cells (None/present)	8/3	11/2	0.63	-0.096	0.654
Perisinusoidal fibrosis score(0/1)	1/10	1/12	1	0.218	0.3077
Periportal fibrosis score (0/1/2)	8/3/0	5/7/1	0.225	0.565	**0.004**
Fibrosis stage (0/1/2/3)	1/7/3/0	1/4/7/1	0.494	0.578	**0.003**
NAS score (<3, ≥3)	8/3	3/10	**0.038**	0.67	**<0.001**
SAF activity (<2 either LI or B/>2 both LI & B)	6/5	4/9	0.408	0.415	**0.044**
Immunohistochemical markers					
γ-H2AX IHC periportal (median, <&≥1.48)	9/2	2/11	**0.003**	0.61	**0.002**
γ-H2AX IHC periportal (continuous)				0.522	**0.009**
Ki67 IHC periportal (median, <&≥1.71)	9/2	2/11	**0.003**	0.719	**<0.001**
Ki67 IHC periportal (continuous)				0.737	**<0.001**
Tumour development and progression					
Tumour (no,yes)	9/2	3/10	**0.012**	0.666	**<0.001**
Tumour size (<5mm, ≥5mm)	2/0	4/6	0.455	0.702	**0.011**

There were also significant associations with γ-H2AX positive hepatocytes. In combination, these data support an increase in p53 – possibly as a result of post-translational changes, given the lack of diet associated changes at an mRNA level - in response to injury. However, the growth and tumour suppressor functions of p53 were not evident, given significant positive associations with Ki67 positive proliferating hepatocytes and tumour development (**Table** 3.10). This suggest an additional layer of p53 dysfunction.

3.4.4 p21 immunohistochemical analysis

The level of p21 protein as a downstream target of p53 and a regulator of cell cycle was assessed. The percentage of p21 positively stained nuclei was higher in all liver zones in the ALIOS mice at 48 weeks compared to the control but the difference failed to reach statistical significance (**Figure** 3.19). The pattern of p21 positive nuclei increased in the livers of 48-week-old mice fed the high fat diet with NAFLD was similar to that of p53, but again not significant (**Figure** 3.20).

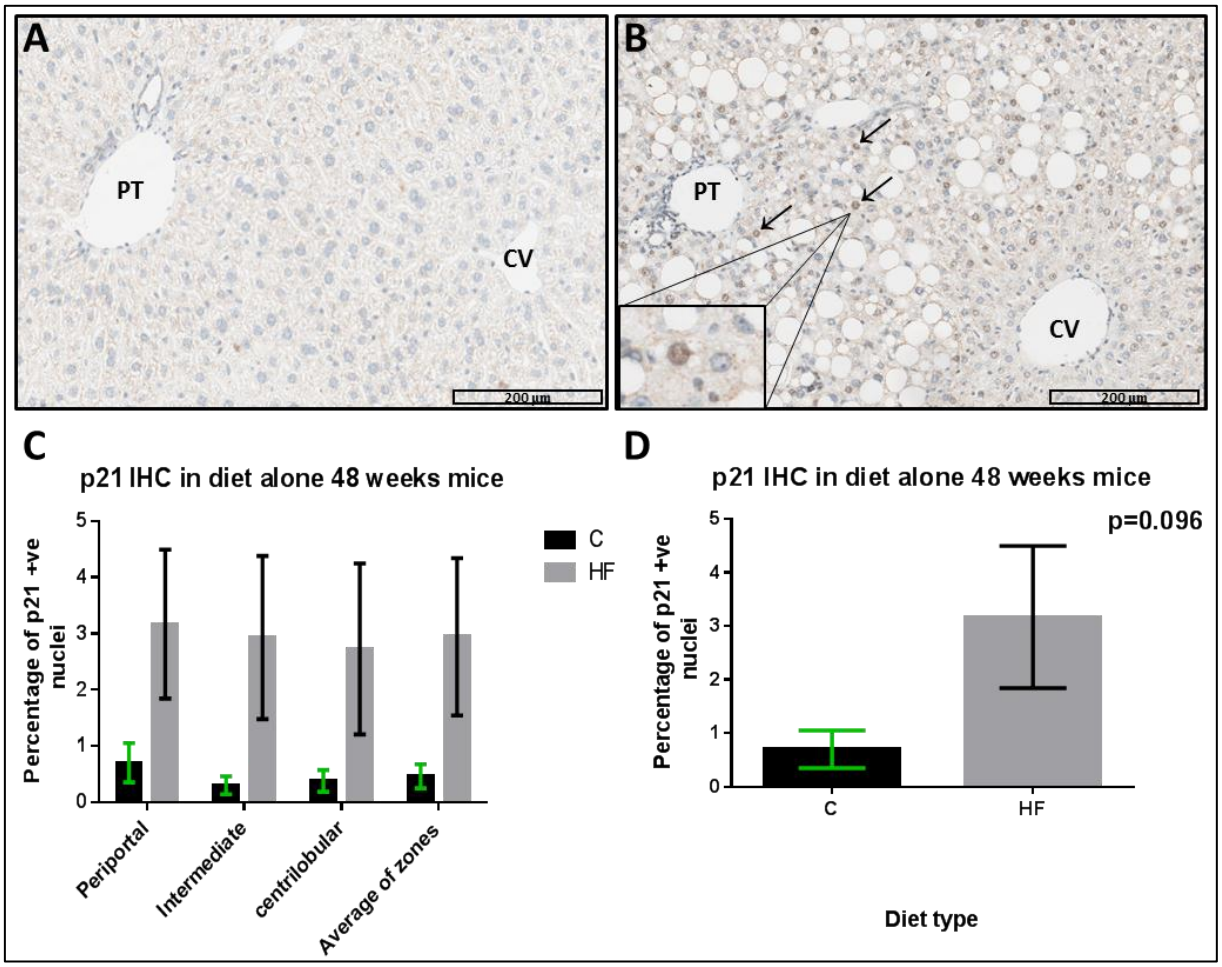

Figure 3.19 : p21 expression in dietary animal model. (A) 48-week-old control animal liver tissue section with very low expression of p21 and nearly all the hepatocyte nuclei in the section were negative. (B) 48-week-old ALIOS mouse liver tissue sections showing high number of p21 positive nuclei especially around the portal tract (Arrows). Power 20X. (C) P21 expression in liver zones in the dietary groups. (D) Periportal p21 expression in the ALIOS (HF) group compared to the control. Y axis values represent Mean ± SEM of the mean. The p-value was calculated by t-test. Key: PT - portal tract; CV - central vein.

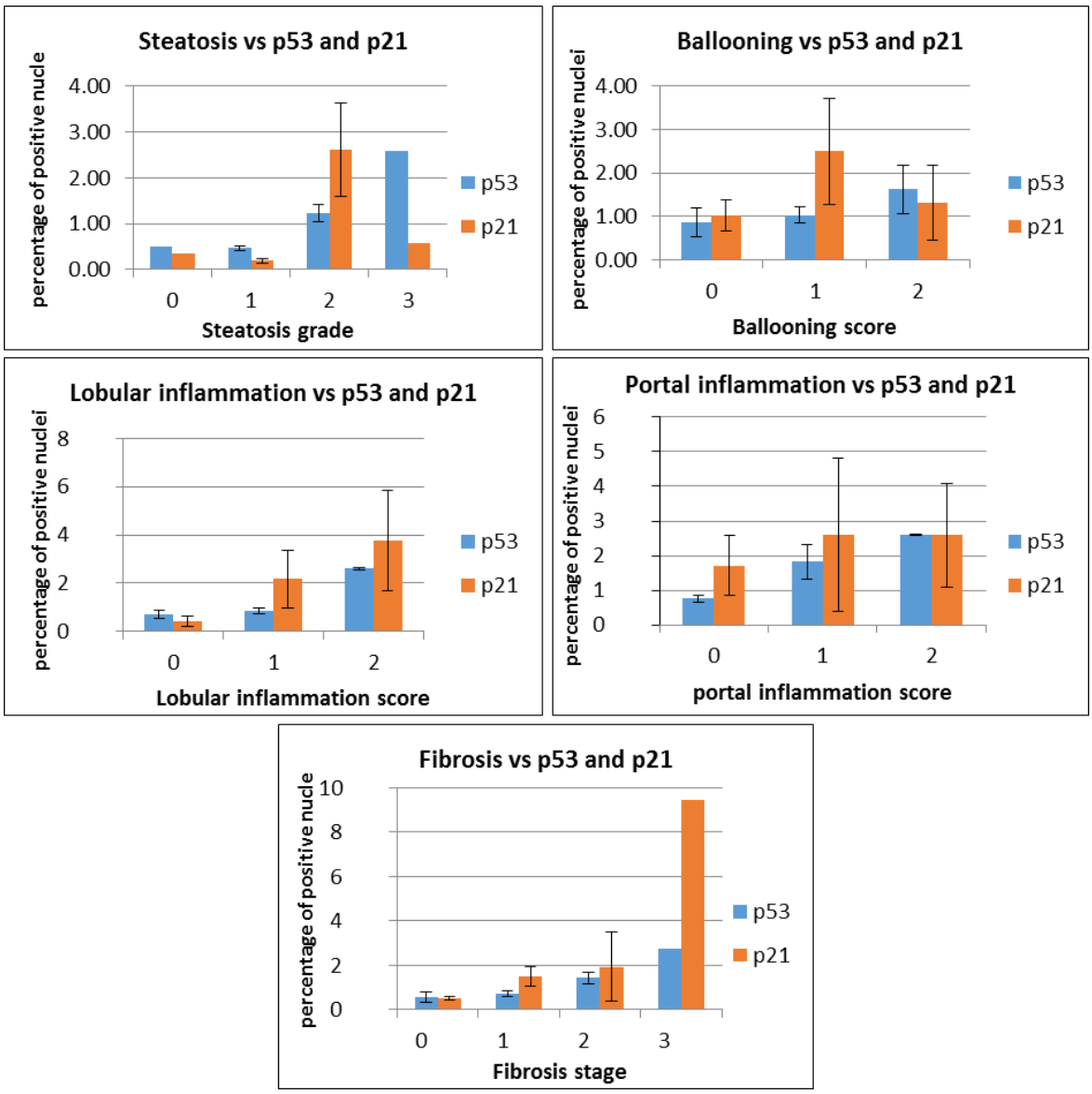

Figure 3.20 : p53 and p21 association with NAFLD histological parameters in the 48-week-old mice. Immunohistochemical staining for p53 and p21 plotted against the histological parameters. The expression of p21 followed similar patterns as to p53, although the associations were not statistically significant. (Y axis values represent Mean ± SE of the mean).

It was important to try to clarify the relationships of *Trp53* mRNA and protein to those of p21 detected by IHC. As noted previously, the association between *Trp53* mRNA and *Cdkn1a (p21)* mRNA was lost in ALIOS fed mice at 48 weeks and the relationship between *Trp53* mRNA and p53 protein was not robust. However, a strong and significant association was evident between the % of p53 positive nuclei (average of all zones) and whole liver *Cdkn1a (p21)* mRNA (Pearson correlation 0.631; p=0.001, n=24 :12 control diet and 12 ALIOS diet mice at 48 weeks). This data suggests that when present, p53 protein upregulated *Cdkn1a* (*p21)* transcription appropriately. What was lacking was any correlation between *Cdkn1a* (*p21)* mRNA and p21 protein (Spearman correlation -0.062; p=0.773, n=24).

Generally, p21 protein was detected in very few hepatocytes by IHC. In 4 cases, it was undetectable and in an additional 13/24 cases it was present in <1% of hepatocyte nuclei. In 7 cases it was clearly detected in >1% of hepatocyte nuclei, with the highest % positivity being 13%. Associations were explored, as summarised in **Table** 3.11. There appeared to be a positive association with the presence of γ-H2AX positive nuclei. There were no clear associations with liver weight, NAFLD histopathology or presence, or numbers of liver tumours.

Table 3.11: Association with % positive p21 hepatocyte nuclei

(24 cases only)	p21 in hepatocyte nuclei (% positive)				
				Spearman rho	
	<0.5%	≥0.5%		correlation	p value
Gross Phenotype Parameters					
	Mean ± SEM			correlation	p value
Body weight (Continuous variable) (gram)	43.83 ±1.32	45.1 ±1.59	-	0.193	0.365
Liver weight (Continuous variable) (gram)	2.32 ±0.21	2.43±0.22	-	-0.022	0.919
(24 cases only)	p21 in hepatocyte nuclei (% positive)				
	Chi^2			Spearman rho	
	<0.5%	≥0.5%	p value	correlation	p value
Histological Parameters					
	Number of mice		p value	correlation	p value
Steatosis grade (0/1/2/3)	0/5/9/0	0/0/8/1	0.093	0.301	0.153
Microvesicular Steatosis grade (0/1)	13/2	7/2	1	0.195	0.362
Hepatocellular ballooning score (0/1/2)	4/9/2	2/6/1	1	0.064	0.766
Mallory Denk bodies (None/present)	11/4	4/5	0.212	0.206	0.334
Megamitochondria (None/present)	11/4	5/4	0.657	-0.026	0.905
Lipogranuloma (None/present)	8/7	5/5	1	0.073	0.736
Lobular Inflammation score (0/1/2)	4/9/2	3/5/1	1	0.049	0.82
Portal Inflammation score (0/1/2)	12/3/0	6/2/1	0.593	0.186	0.384
Pigmented Kupffer cells (None/present)	6/9	5/4	0.675	-0.079	0.714
Apoptotic cells (None/present)	13/2	5/4	0.15	0.363	0.081
Perisinusoidal fibrosis score(0/1)	1/14	1/8	1	-0.044	0.839
Periportal fibrosis score (0/1/2)	8/6/1	5/4/0	1	-0.081	0.708
Fibrosis stage (0/1/2/3)	1/7/6/1	1/4/4/0	1	-0.04	0.852
NAS score (<3, ≥3)	7/8	4/5	1	-0.091	0.672
SAF activity (<2 either LI or B/>2 both LI & B)	6/9	4/5	1	0.061	0.776
Immunohistochemical markers					
γ-H2AX IHC periportal	10/5	1/8	**0.013**	0.423	**0.04**
Ki67 periportal	9/6	2/6	0.193	0.099	0.652
Tumour development and progression					
Tumour (no,yes)	9/6	3/6	0.4	-0.024	0.911
Tumour number (continuous)				-0.03	0.889
Tumour size (<5mm, ≥5mm)	3/3	3/3	1	-0.023	0.916
Tumour size (continuous)				-0.002	0.991

3.5 DNA damage and p53 in ALIOS diet induced hepatocarcinogenesis

The mouse tumour tissues were graded histologically on H&E sections as previously described and the FFPE tissues were also available for additional immunohistochemistry to assess γ-H2AX, Ki67 and p53. As described in the methods, tissues for RNA extraction were saved for some of the larger tumours. A small number of qRT-PCR analyses were performed on these tissues. Some of the tumours and those of a parallel experiment were saved for later RNA-Seq analysis, which has recently been performed. Analyses are ongoing and not a substantial aspect of this thesis. Some reference to these data will be included, largely in the context of interpretation of the p53 data.

3.5.1 DNA damage was markedly increased in HCC compared to background tissues

γ-H2AX assessment in tumour sections showed variable levels of detection but it was significantly higher in the tumours compared to the peritumoural areas ($p<0.001$), supporting the presence of more DNA damage in the tumour cells than the normal hepatocytes (**Figure** 3.21).

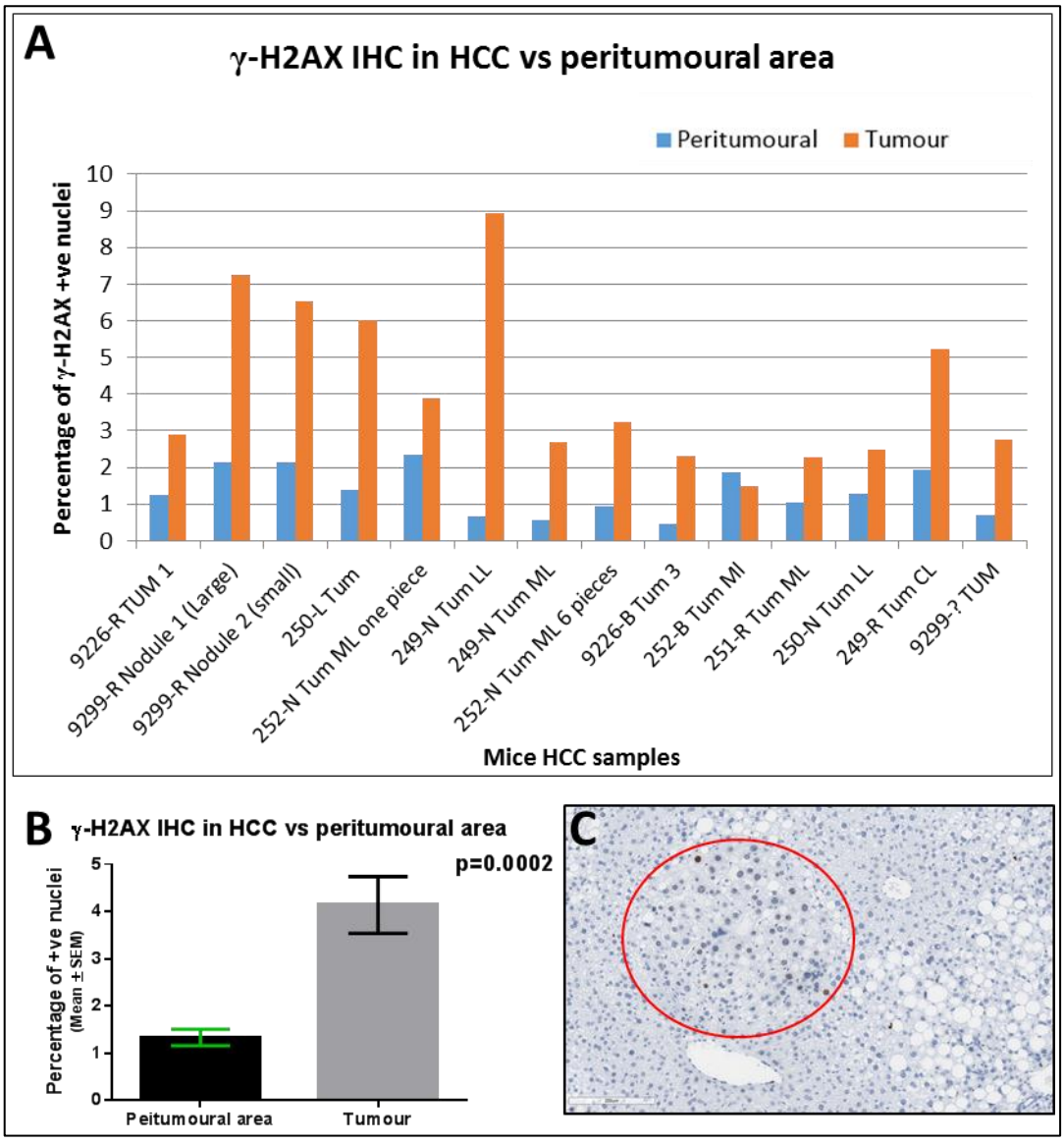

Figure 3.21: γ-H2AX expression in tumours in the dietary animal model. (A) Expression of γ-H2AX in liver tumours individually and in their normal peritumoural periportal area. (B) Highly significant difference ($p<0.0001$) between the mean percentage of γ-H2AX positive nuclei in tumours versus the mean value in normal peritumoural areas. The p-value was calculated by Wilcoxon test. (C) Representative image of mouse liver tissue section from a HF fed 48-week-old mouse showing high number of γ-H2AX positively stained nuclei in the tumour (red circle) compared to the background liver.

3.5.2 Proliferation was markedly increased in HCC compared to background tissues

All of the tumours showed high levels of proliferation compared to the peritumoural area, reflected by the high percentage of Ki67 positive nuclei, which was significantly higher in the tumours than in the peritumoural area ($p<0.001$) (**Figure** 3.22).

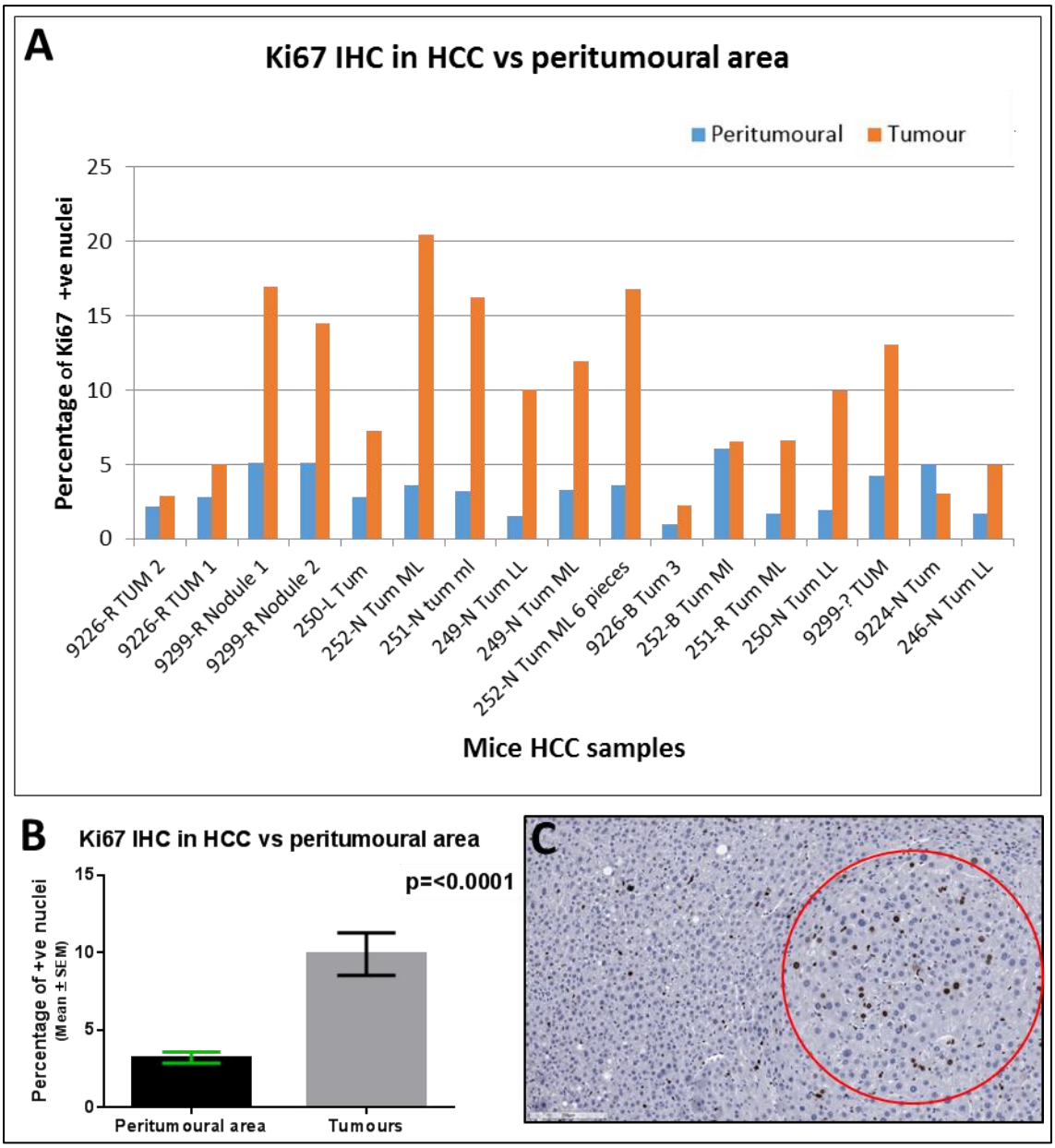

Figure 3.22 : Proliferative status in tumour samples in the dietary animal model. Different tumours showed different levels of expression of Ki67 as shown in (A), and the level of expression in the tumours was higher than the peritumoural areas (B). Values represent Mean ± SE of the mean; p-value was determined by Wilcoxon test. (C) Representative image of mouse liver tissue section from a HF fed 48-week-old mouse showing high number of Ki67 positively stained nuclei in the tumour (red circle) compared to the background liver.

3.5.3 p53 and transcriptional target gene mRNA levels in tumour versus non-tumour regions of the liver

In a small number (n=4) of the larger tumours, RNA was extracted and expression levels and associations of *Trp53* and its target genes were explored by qRT-PCR. There was an increase in the *Trp53* mRNA and that of its downstream transcriptional target genes, in tumours compared to non-tumour tissues. These changes included a 2.2 fold increase for *Trp53*, a 3.34 fold increase in *Mdm2* and 1.6 fold increase in *Gadd45a*. The most dramatic increase was that of *Cdkn1a (p21)*, with a 22.27 fold higher level in the tumours (**Figure** 3.23).

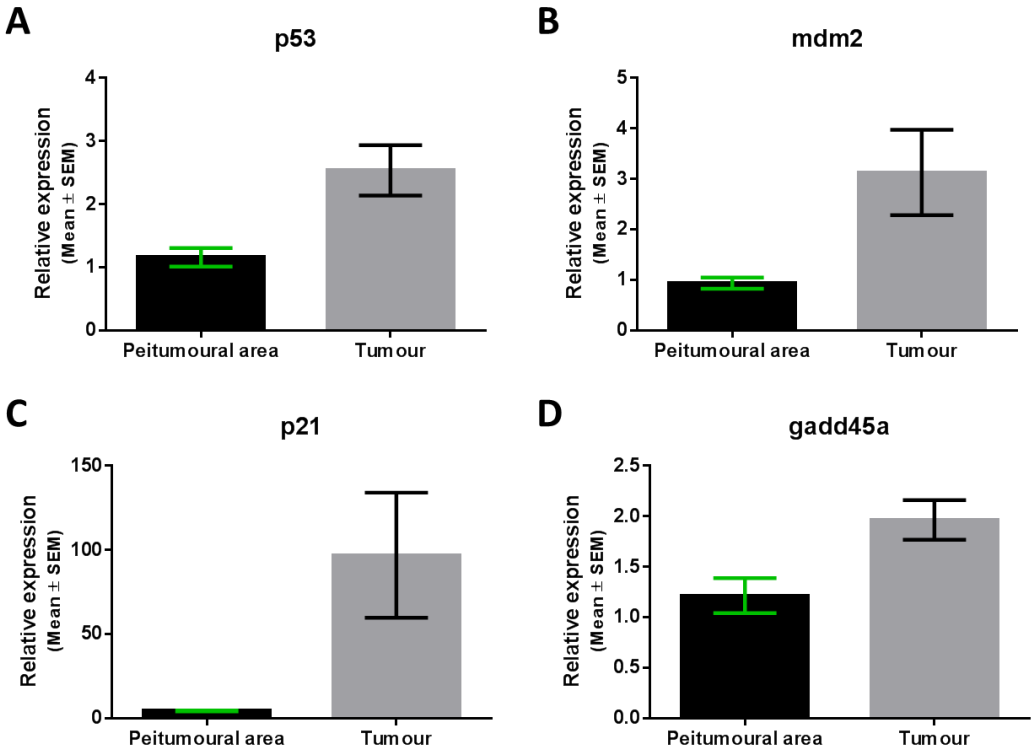

Figure 3.23: qRT-PCR analysis of *Trp53* mRNA expression and that of its downstream transcriptional targets, in tumour versus non-tumour areas of the livers.

RNASeq analyses were performed in 23 non-tumour and 8 tumour samples. With a focus on p53 and p21 expression, similar changes were observed (**Table** 3.12). Sequence analyses on RNAseq data confirmed that all tumours were p53 wild type, without any evidence of p53 mutation.

Table 3.12: Fold change differences between tumours and non-tumour liver for mRNA expression of *Trp53*, its downstream transcriptional targets, together with alpha-fetoprotein (*Afp*) and glypican-3 (*Gpc3*) in the dietary animal model (RNAseq data).

Gene name	Non-Tumours (Normalised log2 values)	Tumours (Normalised log2 values)	Difference between tumours and non-tumours	Fold difference between tumours and non-tumours	p value (t-test)	Adjusted p value
Trp53	9.1	9.8	0.8	1.7	1.09*E-12	4.99*E-08
Cdkn1a	6.8	10.6	3.8	13.6	2*E-07	0.009
Mdm2	9.5	10.7	1.3	2.4	9.5*E-06	0.435
Gadd45a	8.0	8.1	-0.1	1.0	0.9	41213.7
Ppm1D	7.1	7.3	0.2	1.1	0.01	457.93
Afp	5.1	13.0	8.0	292.8	5.4*E-20	2.47*E-15
Gpc3	4.9	12.4	7.6	190.8	1.5*E-15	6.87*E-11

3.5.4 p53 and transcriptional target gene protein levels in tumour versus non-tumour liver

Levels of p53 protein were assessed by IHC in 22 pairs of tumour versus non-tumour tissues. Staining for p53 was typically detected in less than 2-3 % of hepatocytes in non-tumour tissues. In about one third of cancers, p53 was either undetected or present at very low levels. In the majority of the 22 tumours assessed (14/22; 64%) p53 was detectable. In 9/22 (41%) it was present in at least 5% of tumour cells, while in 4/22 (18%) it was present in over 7.5% of tumour cells. In one tumour, p53 expression was present in greater than 20% of nuclei (**Figure** 3.24). An increase in p53 is consistent with the observation of elevated DNA damage – as suggested by increased detection of γ-H2AX positive nuclei in the tumours. However, this was not associated with a suppression of proliferation, which would suggest that the increased p53 was either insufficient or ineffective for suppressing proliferation and growth of the tumours. To explore this further, p21 at the protein level was assessed in tumours using (IHC and western blot analysis).

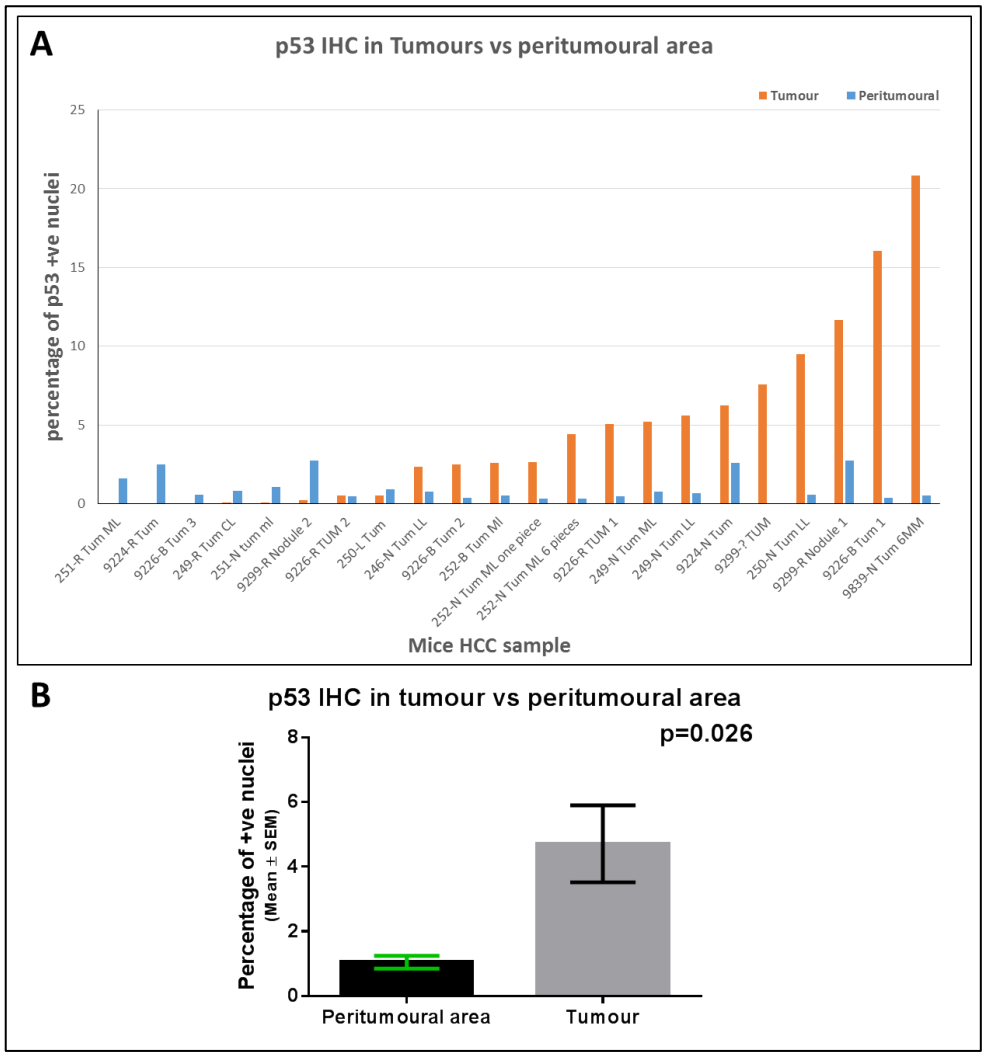

Figure 3.24 : p53 expression by immunohistochemistry in HCCs. (A) Different tumours showed different levels of expression of p53 protein. The percentage of p53 positive nuclei was significantly higher in the tumours than the normal peritumoural areas (p=0.026). (B) Shows the mean percentage positivity values. The p-value was calculated by the Wilcoxon test.

Despite the markedly elevated expression of *Cdkn1a (p21)* mRNA in the tumours analysed, the majority (82 %) had very low levels of p21 protein detectable by IHC. In 50 % of cases, the levels of p21 detected by IHC was higher than in non-tumour tissues, and modest increases were noted in a small number of the tumours large enough for protein extraction and western blot (**Figure** 3.27). Overall, however, there was no significant difference between the percentage of p21 positive cells in the tumours and the peritumoural areas, for all the cases analysed by IHC (**Figure** 3.25**)**. Similar to the non-tumour tissues, there was no correlation between p53 and p21 protein detection (**Figure** 3.26, **Table** 3.11). Of the 10 tumours with >2.5% p53 positive nuclei, 7 had little or no detected expression of p21.

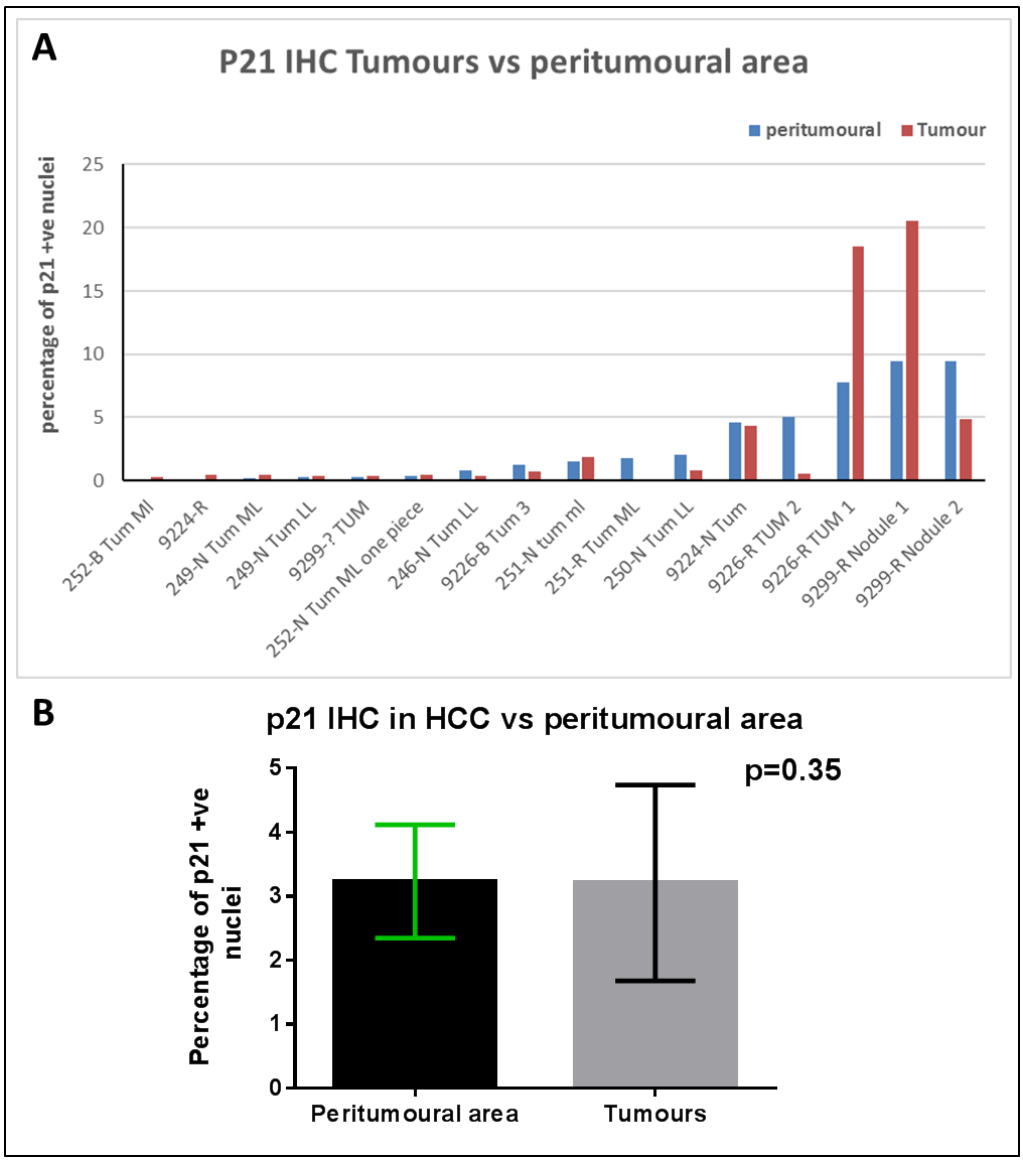

Figure 3.25: Immunohistochemical detection of p21 in HCCs. (A) The individual cases showing percentage p21 positive nuclei in tumour versus its peritumoural counterpart. (B) Comparison of mean levels of p21 expression between tumours and the peritumoural areas, showing there was no significant difference; p-value was determined by Wilcoxon test.

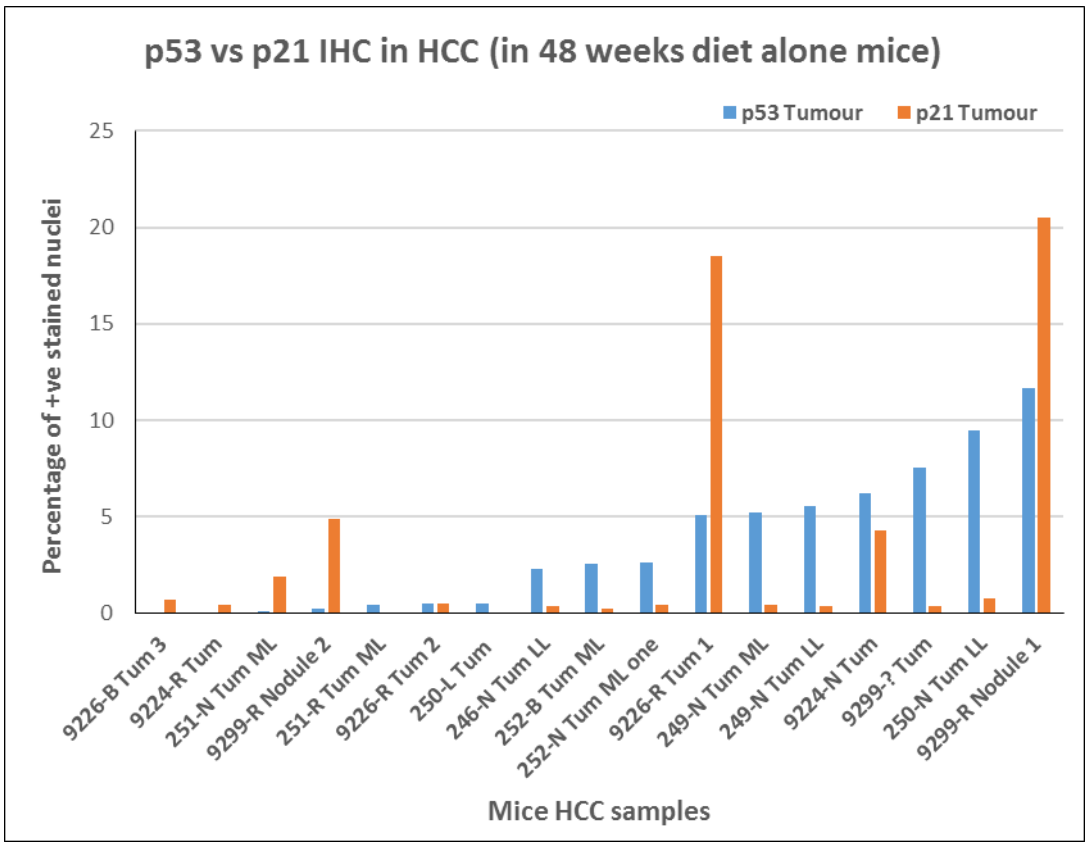

Figure 3.26 : Dual expression of p53 and p21 in liver tumour samples. shows the variable levels of expression of p53 in liver tumour samples and in the same samples this was generally not reflected by concomitant expression of p21; despite the latter being a downstream target of p53 it was expressed in a very low percentage of cells even in the tumours that showed high percentage of p53 positive staining.

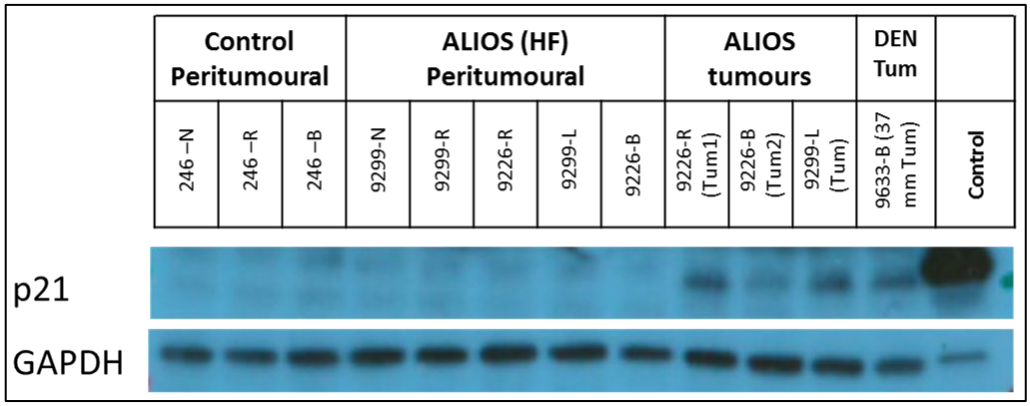

Figure 3.27: Western blot of 48-week-old mice liver samples demonstrating increase in p21 protein levels in tumours compared to their peritumoural counterpart, in comparison to a control sample and a diethylnitrosamine (DEN) induced liver tumour sample. GAPDH was used as a loading control reference protein. The control was a mouse embryonic fibroblast cell line (NIH3T3) treated with an MDM2 inhibitor.

3.5.4.1 Tumour summary

In all of the tumours analysed by RNASeq, *Trp53* mRNA expression levels were elevated relative to non tumour tissues. IHC analyses indicate that in up to one third, the elevated mRNA does not translate into increased levels of p53 protein positive tumour cells. Irrespective of this, the vast majority of tumours appeared to have markedly elevated levels of *Cdkn1a(p21)* mRNA. However, the mRNA increase only occasionally translated into higher levels of p21 protein detection by IHC (**Figure** 3.25), although the Western blot analysis appeared to show a more consistent increase in p21 protein levels in the tumour samples compared with non-tumour liver (**Figure** 3.27). In summary, these data suggest that a p53 DNA damage response was evident in the tumours, with increased *p53* mRNA and protein expression in the majority of cases, together with increases in p53 transcriptional target gene mRNA, including dramatic elevations in *Cdkn1a (p21)*, with some evidence of increased p21 protein detection by Western blot analysis of a limited sample of larger ALIOS tumours. However, these increases in p21 expression were clearly unable or insufficient to prevent the proliferation of tumour cells and growth of the tumours.

In addition to the γ-H2AX evidence of elevated DNA damage in the tumours, was the additionally notable evidence of high levels of Ki67 positive proliferating tumour cells. While the lack of an effective inhibition of proliferation despite the p53 response is likely to be a key factor, the specific driver of proliferation in the tumours remains to be established. Preliminary analysis of the tumour RNASeq data indicated that 74% of tumours had acquired mutations in either *Hras* (59%) or *Kras* (15%) as one of the likely candidates involved (**Table** 3.13).

Table 3.13: RNA sequence analysis data showing Ras mutation details in the animal model tumours.

Tumour ID	VarID (chr:loc:ref:alt)	Protein_ position	Gene _Symbol	Amino_acids	Codons	Reads AD	Reads DP
T3	chr7:141192551:G:T	61	Hras	Q/K	Caa/Aaa	111,27	138
T4	chr6:145234355:T:G	61	Kras	Q/H	caA/caC	61,42	103
T5	chr7:141192230:C:A	117	Hras	K/N	aaG/aaT	164,57	221
T7	chr7:141192551:G:T	61	Hras	Q/K	Caa/Aaa	115,56	171
T8	chr6:145234341:G:A	66	Kras	A/V	gCa/gTa	23,12	35
T9	chr7:141192551:G:T	61	Hras	Q/K	Caa/Aaa	84,66	150
T11	chr7:141192551:G:T	61	Hras	Q/K	Caa/Aaa	97,81	178
T12	chr7:141192550:T:A	61	Hras	Q/L	cAa/cTa	127,86	213
T13	chr7:141192551:G:T	61	Hras	Q/K	Caa/Aaa	87,66	153
T14	chr7:141192230:C:G	117	Hras	K/N	aaG/aaC	118,101	219
T15	chr7:141192550:T:A	61	Hras	Q/L	cAa/cTa	101,93	194
T16	chr7:141192550:T:C	61	Hras	Q/R	cAa/cGa	105,87	192
T17	chr7:141192551:G:T	61	Hras	Q/K	Caa/Aaa	79,70	149
T18	chr7:141192550:T:A	61	Hras	Q/L	cAa/cTa	96,74	170
T19	chr7:141192551:G:T	61	Hras	Q/K	Caa/Aaa	139,65	204
T20	chr7:141192550:T:A	61	Hras	Q/L	cAa/cTa	107,78	185
T21	chr6:145246772:C:G	12	Kras	G/R	Ggt/Cgt	29,17	46
T24	chr7:141192551:G:T	61	Hras	Q/K	Caa/Aaa	234,175	409
T26	chr7:141192551:G:T	61	Hras	Q/K	Caa/Aaa	100,69	169
T27	chr6:145234355:T:G	61	Kras	Q/H	caA/caC	57,50	107

3.6 Discussion

3.6.1 The impact of ALIOS diet on C3H/He mice

NAFLD has emerged in the last few years as a major global health challenge, particularly in more affluent developed countries. It is closely connected with obesity and type II diabetes (11, 13). As these have increased, with obesity affecting nearly 25% of the global population, so has the incidence of NAFLD (16). NAFLD doesn't spare race or age group. In many, simple steatosis persists without progression to more advanced disease. If there is progression, it is usually a slow process that takes place over many years. Ultimately, however, it can progress to cirrhosis and promote the development of HCC (5).

Due to the alarming increase in incidence of NAFLD in the population, understanding its pathogenesis and why the disease progresses in some but not in others, has become a priority in the field of liver disease research. In humans, due to the slow progression and long course of the disease, as well as the ethical obstacles associated with repeated liver biopsy, studying the temporal relationships with the disease is challenging. The study of the disease in animal models which mimic what happens in human body, but over a shorter period of time, can aid the understanding of key mechanisms and also permit their manipulation to test causality.

In our model we tried to recapitulate what happens in human disease, by exposing mice with a predisposition to developing obesity and impaired glucose tolerance to high fat and fructose containing diet, imitating the Western lifestyle diet represented by the high fat fast food and fructose-sweetened beverages. The goal was to define a relevant model and explore key demographic and histopathological features associated with NAFLD-HCC development, as well as to explore further the contribution of p53.

The impact of the ALIOS diet on the liver was first explored by Tetri *et al* 2008 (254), with a similar diet assessed by Charlton *et al* 2011 (255). Both groups of researchers showed that the diet resulted in a prominent gain of body and liver weight, with steatosis. Our data recapitulated these findings. Our histological assessment confirmed a pattern of steatosis typical of animal models and paediatric NAFLD (256), with distribution of more marked steatosis in the periportal (zone 1) hepatocytes, extending to zones 2 and 3 as the disease progressed. In human adult NAFLD, more prominent steatosis is usually evident around the central vein (Zone 3), involving zones 2 and 1 as disease progresses. The explanation for this difference is presently unknown (257).

The index study by Tetri *et al*, was relatively short term (16 weeks only) and while there was some evidence of 'NASH', there was little evidence of progression to portal inflammation or fibrosis. The Charlton *et al* model was accompanied by a higher degree of inflammation and ballooning degeneration. The Newsome Group were the first to publish the effect of a more prolonged diet (12 months), describing a more progressive disease and the development of small 1-2 mm liver tumours (258). Ganz et al (259) have also reported a Male C57Bl/6 mouse model fed high fat high fructose diet for 49 weeks, in which 41% of their mice developed tumours, but these were histologically adenomas rather than HCCs.

Our model takes these studies further by using a different mouse strain – the C3H/He strain – whose profile reflects that of humans, in that the mice develop obesity and impaired glucose tolerance with age. These mice are also reported to develop 1-2mm liver tumours at 1 year of age. In our model, the introduction of the ALIOS diet exacerbated this phenotype, with liver tumours evident from 36 weeks of age. By 1 year, over 80% of the mice fed the ALIOs diet had tumours, many of which were over 5mm in size.

Characterisation of the tumours histologically confirmed that two of the smaller tumours were adenomas, but the majority were HCC. At a molecular level, a pilot study performed by our group prior to this one had confirmed marked increases in expression of the tumour markers AFP and Glypican-3 using RT-PCR (260). RNASeq data from the tumours characterised in this model confirmed very dramatic increases in expression of these marker genes. The histological phenotype was described as a steatohepatitic one – in keeping with the steatohepatitic-HCC (SH-HCC) phenotype that has been described more commonly in patients with HCC arising on the background of the metabolic syndrome (261). There is the possibility that these HCC arise from the malignant transformation of benign adenomas (262). The model created should enable us to define the malignant transformation process of these tumours in more detail. Our major aim, however, was to create a model in which we could assess the environment promoting the development and progression of HCC on a background of NAFLD and the metabolic syndrome. Notably these mice do develop more tumours in association with progressive NAFLD, but none of the mice had advanced fibrosis compatible with cirrhosis. While cirrhosis remains the key risk factor for development of HCC in chronic liver disease, the development in the absence of cirrhosis in individuals with the metabolic syndrome is increasingly reported (93, 263). Our model may facilitate the understanding of HCC development in the absence of cirrhosis in obese individuals.

3.6.2 Predictors of HCC development – liver size and histology

While hard to dissociate all of the inter-related features associated with HCC development, the tendency to develop HCC was already there, associated with age, and exacerbated by the ALIOS diet. Combining the dietary groups of mice gave a range of phenotypic changes as seen in human individuals and enabled us to study histological and mechanistic associations with HCC development, number of HCC and HCC. While age and diet were clearly a risk factors for tumour development, binomial regression indicated that liver weight itself was particularly important. Within the histopathological assessments which are related to each other, it appeared that steatosis grade was important. While lobular inflammation was related to the development and progression of HCC size, it was notable that it was the presence of lipogranulomas that was the most consistent and highly significant histopathological feature associated with both HCC development and progression.

Lipogranulomas can be histologically "defined as a space-occupying, compact collections of macrophages, including lipophages, surrounding a single or multiple fat droplets" (264), which are present in a number of different conditions including fatty liver disease (265). In addition to these histologically defined accumulations of macrophages – possibly recruited from the circulation (266), increases in pigmented Kupffer cells, which are resident macrophages, were also documented, but less consistently. Associations with elevations in macrophages have been reported in other mouse models of liver disease (259, 267) and macrophages have been proposed by some as the real accomplice or determinant of NAFLD pathogenesis and progression (67, 268). Activated macrophages produce different cytokines (e.g. IL-1β, IL-6 , IL-8 and TNF) that induce inflammation and fibrosis in the liver – both factors associated with the risk of development of HCC (269). Macrophages are now known to exist in a continuous spectrum of phenotypes which can be either anti- or pro-tumour development, although they are usually referred to by the simplified nomenclature of M1 (classically activated, anti-tumour) and M2 (alternatively activated, pro-tumour) macrophages (270). The transition between pro- and anti-tumour phenotypes is thought to be flexible, adapting to or dependent on signals from the local microenvironment, with profound effects on tumoural immunity via production of pro/anti-inflammatory mediators and expression of inhibitory molecules against T cells and NK cells (271).

Our data raises the profile of lipogranulomas or macrophages as worthy of further characterisation in human NAFLD and HCC. Although 'lobular inflammation' and 'portal inflammation' were less robustly associated with tumour development in our model, activated

$CD8^+$ T lymphocytes and natural killer cells reportedly play important roles in NASH and HCC development in other models. Selective loss of chronic inflammatory cells such as $CD4^+$ T lymphocytes induced by NAFLD through increased ROS production, or even recruitment and activation of acute inflammatory cells such as neutrophils may be key (110, 272, 273). A role for the cytokine IL-17 has also recently been proposed as a critical link (274). The contributions of these immune cells and regulatory cytokines in our own model will be worthy of further study, possibly with the opportunity to assess a regulatory component linked back to macrophages within lipogranulomas.

3.6.3 Predictors of HCC development – a focus on γ-H2AX and Ki67

Wang et al 2009 (275) and several other researchers have previously shown an increase in the positive nuclear immunohistochemical staining for γ-H2AX in mouse liver tissue sections with advancing age, around central veins in particular rather than periportal areas. Our model showed similar results in aged mice on the control diet, although at the 48-week time point studied the increases in the percentage of positively stained nuclei were similar in all regions. In the ALIOS fed mice, the percentage of positive nuclei was markedly increased, with the highest level of γ-H2AX around the portal tracts – the areas with the highest degree of steatosis, linking fat accumulation to DNA damage. This is not the region of NASH associated 'lobular inflammation' and suggests that increased steatosis itself may be causally linked with DNA damage. An excess of FFAs in hepatocytes can impair mitochondrial function and release of ROS, which can in turn cause DNA damage, potentially mediated and amplified through autocatalytic chain reactions of lipid peroxidation (276). Exploration of other markers of oxidative stress and damage related to oxidative stress were attempted (4HNE, PAR and 8-oxoguanosine), but failed technically. The antibodies used were mouse monoclonal antibodies and non-specific binding to mouse liver tissues persisted despite the use of kits to block endogenous mouse IgG. Alternative rabbit polyclonal antibodies were also explored but their specificity was poor.

An increase in hepatocyte p53 protein levels with progressive NAFLD in this model was in concordance with a previous report in high fat fed animals' livers (259). A positive correlation between the degree of steatosis and the level of p53 expression in human liver has also been documented (195), and an indirect role for p53 in the regulation of lipid metabolism via induction of miRNA34a and inhibition of SIRT1 has been proposed (21, 196). Using γ-H2AX positive nuclei as a marker defining DNA damage, we have shown an association with a concomitant highly significant increase of p53 positive nuclei in periportal areas with fat

accumulation, in keeping with a DNA damage induced p53 response. Of note, γ-H2AX positive nuclei and p53 were detected in the areas of highest fat accumulation, associated with the presence of lipogranulomata and not necessarily lobular or portal tract inflammation. In combination, the data suggests that increasing steatosis, presumably associated with elevated levels of FFA accumulation and oxidative stress associated DNA damage, were associated with stabilisation of p53 protein and elevated expression of its target gene *Cdkn1a(p21)* – in non-tumour liver. Why increased expression of this negative growth regulator nevertheless appeared to be associated with a proliferative response, as reflected by high Ki67 levels, was less clear.

3.6.4 Malignant transformation – a focus on γ-H2AX, Ki67, p53 and Ras

Although elevations in the order of 2-5-fold of γ-H2AX, Ki-67 and p53 in non-tumour tissues were each associated with HCC development and progression, the changes comparing non-tumour and tumour liver were much more dramatic. Ki67 positive nuclei reached 15-20% in some tumours, with a mean value of 10% in the tumours studied. The percentage of γ-H2AX positive nuclei was also elevated in tumours, frequently in the order of 10-fold. On this background, the p53 data needs careful consideration. In the 22 HCC studied with IHC, p53 (despite high levels at the RNA level) was either not detected or detected at low levels by IHC, in 8/22 (36%) of cases. In these, p21 was absent or very low in 6 and present in 2-3% of nuclei in the other two. However, markedly elevated levels of *Cdkn1a(p21)* mRNA in all the tumours regardless of p53 protein detected by IHC suggest either an intact relationship between p53 and *Cdkn1a(p21)* mRNA beyond the sensitivity of p53 detection by IHC, or other factors promoting transcriptional increases in *Cdkn1a(p21)*. Furthermore, whether p53 positive nuclei were present or not in tumours had little impact in general on p21 protein, which was barely detected in 7/10 (70%) of these cases. Thus, irrespective of p53 expression or not, p21 protein was not detected. RNAseq analysis confirmed the wild type status of the *Trp53* transcripts expressed in the tumours. These data suggest that the *Trp53* sequence was normal, but that its downstream negative growth regulatory functions – in terms of induction of stable p21 and growth suppression - were ineffective. This may be in keeping with recent evidence that p21 is not an effector of the tumour suppressor properties of p53 (118).

Although further analyses are ongoing, our preliminary assessment, including RNAseq data, suggest evasion of the inhibitory effects of p53 and p21 as a consequence of upregulated proliferative responses. These were evident in non-tumour tissues in association with liver weight, steatosis and inflammation (largely macrophages), but in the tumours the exacerbated phenotype was associated with acquired H*ras* or *Kras* mutation in a majority (74%) of the

tumours. The reported incidence of *Ras* mutation in human HCCs is <10%, but the Ras/MAPK pathway is activated in 50-100% of cases (277-279). This is in concordance with previous reports of acquired *Ras* mutations in aging obese C3H mice (277), suggesting this is a pro-tumorigenic pathway of major importance in metabolic syndrome-associated cancer.

Chapter 4: The impact of interventions in the ALIOS C3H/He mouse model of NAFLD and HCC

4.1 Introduction

Despite the tremendous increase in the rate of NAFLD, to date there is no approved pharmacological treatment. Several compounds are being explored in clinical trials and generally the hope is that prevention of the progression of NAFLD to cirrhosis will also diminish the risk of HCC (243, 280). Treatments preventing the progression of NAFLD to cirrhosis would not necessarily prevent the development of HCC that arises in the absence of cirrhosis. While the risk of HCC is very much higher in cirrhotic individuals, the prevalence of obesity and earlier stages of NAFLD is so high, that even the much smaller risk associated with these stages translates into a significant number of patients. Reported evidence indicates that 20-50% of patients presenting with NAFLD-HCC develop it in the absence of cirrhosis (93, 263, 281) and the driving mechanisms are unclear. Roles for NASH and inflammation associated damage are suspected.

The model we developed was one associated with NAFLD progression to NASH and fibrosis but fell short of cirrhosis. The data presented in chapter 3 supports a potential role for inflammation and NASH, but also raises the potential contribution of steatosis itself, liver weight and lipogranulomas – arising in a background of elevated proliferation in these obese C3H/He mice.

In the hope of confirming HCC preventive strategies, we assessed two candidate interventions. Given the prevalence of DNA damage and its proposed role in the development of HCC, we firstly explored the role of Bucillamine, a drug with anti-oxidant properties that has been safely used for the treatment of rheumatoid arthritis in Japan for many years. Secondly, we studied the impact of a bile acid like drug, PX20606, which is a ligand and agonist for the Farsenoid X receptor (FXR). FXR promotes the conversion of cholesterol to bile acids in the liver and its excretion in bile, but also regulates lipid metabolism. Details and doses of the bucillamine and FXR agonist used are summarised in **Table** 4.1.

Table 4.1: design of the interventions used in the dietary animal model.

Diet plus + FXR agonist (PX20606) (Phenex Pharmaceutical)	Mice number	
	Control	ALIOS (HF)
FXRa 1 mg/kg/day (48 weeks)	12	12
FXRa 5 mg /kg/day (48 weeks)	8	8
Diet + Bucillamine (Santen Pharmaceutical)	**Mice number**	
	Control	ALIOS (HF)
Bucillamine 10 mg/kg/day (48 weeks)	11	11

4.2 Aims of the study in this chapter

- Explore the impact of antioxidant (Bucillamine) on NAFLD, NAFLD stage and HCC development.
- Explore the impact of FXR agonist (PX20606) on NAFLD, NAFLD stage and HCC development.
- Explore the impact of the interventions on hepatocyte DNA damage and proliferation.

4.3 The impact of bucillamine on the dietary animal model

4.3.1 Background

Bucillamine is an oral drug with an antioxidant activity and has been used as a first line treatment for Rheumatoid arthritis (RA) in Asia (Japan) (282, 283) for a number of years. It is also being assessed now in phase II clinical trials for the treatment of gout (284, 285), as well as for cysteinuria. Bucillamine (N-(2-mercapto-2-methylpropionyl)-L-cysteine) (**Figure** 4.1) is a cysteine derived compound and can pass into the cell rapidly via pathways involving the metabolism of the amino acid cysteine. These include the biosynthesis of glutathione (GSH). Intracellular reduced GSH acts as a major defence against oxidative stress, as it can be converted into the oxidised form GSSG and water by glutathione peroxidase, in the presence of free radicals and hydrogen peroxide (286-289). Bucillamine possesses two thiol groups that can be donated to replenish GSH. Bucillamine metabolites also have antioxidant activity through a single thiol group. Additionally, bucillamine may have an immunomodifying effect through inhibition of interleukin-6 (287, 290).

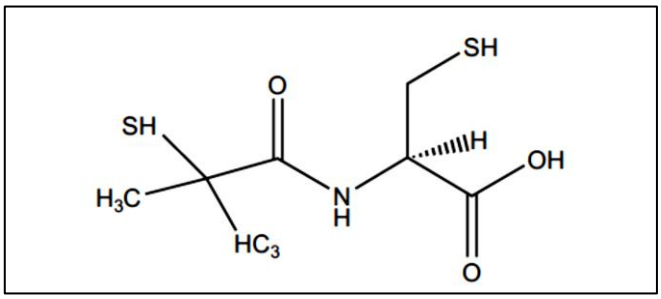

Figure 4.1: Chemical structure of bucillamine(287).

To explore the effect of bucillamine in our dietary animal model, it was mixed into food pellets to deliver an estimated dose of 10 mg/kg/day. The dose was estimated according to the average daily food intake of the animals. A control group (n=11) and an ALIOS diet (**H**igh **F**at **H**igh **F**ructose (**HF**)) group (n=11) were supplemented with bucillamine from the age of 24 weeks until 48 weeks, prior to cull as described in methods section 2.2.

4.3.2 The impact of bucillamine on body and liver weight

In the presence of bucillamine, the increase in body weight induced by the ALIOS (HF) diet was less marked. In this smaller group of animals (n=11 per group), the difference failed to reach statistical significance. The effect of the ALIOS diet on liver weight persisted, however, with a highly significant increase in either absence or presence of bucillamine (**Figure** 4.2**; A and B**).

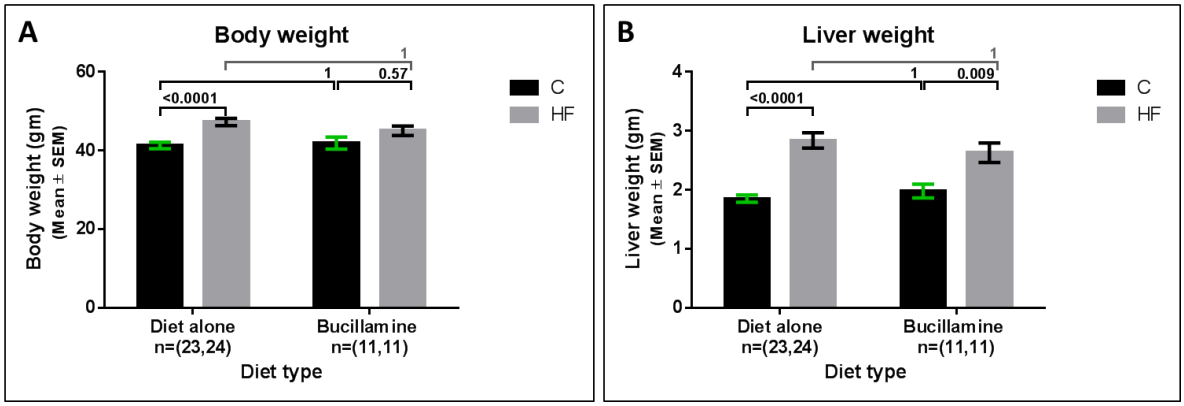

Figure 4.2: The effect of bucillamine on body and liver weight compared to the effect of ALIOS diet. The p value was determined by one-way ANOVA with multiple comparison correction (A=<0.001, B=<0.001). There was no significant effect of bucillamine on neither the body weight (A) nor the liver weight (B) compared to the diet alone groups.

4.3.3 The effect of bucillamine on the lipid profile and liver function

Bucillamine did not affect the levels of total serum cholesterol (**Figure** 4.3**; A**) but a quite marked and significant decrease in the serum triglyceride levels in the bucillamine treated ALIOS (HF) group was noted (**Figure** 4.3**; B**). Liver enzymes also showed some effects, with modest increases in alanine aminotransferase (ALT) in both of the bucillamine treated groups, and an overall increase in aspartate aminotransferase (AST) in the bucillamine treated control diet group. Alkaline phosphatase (ALP) levels, which were increased by the ALIOS diet, were further significantly increased in both dietary groups in the presence of bucillamine (**Figure** 4.3**; E**).

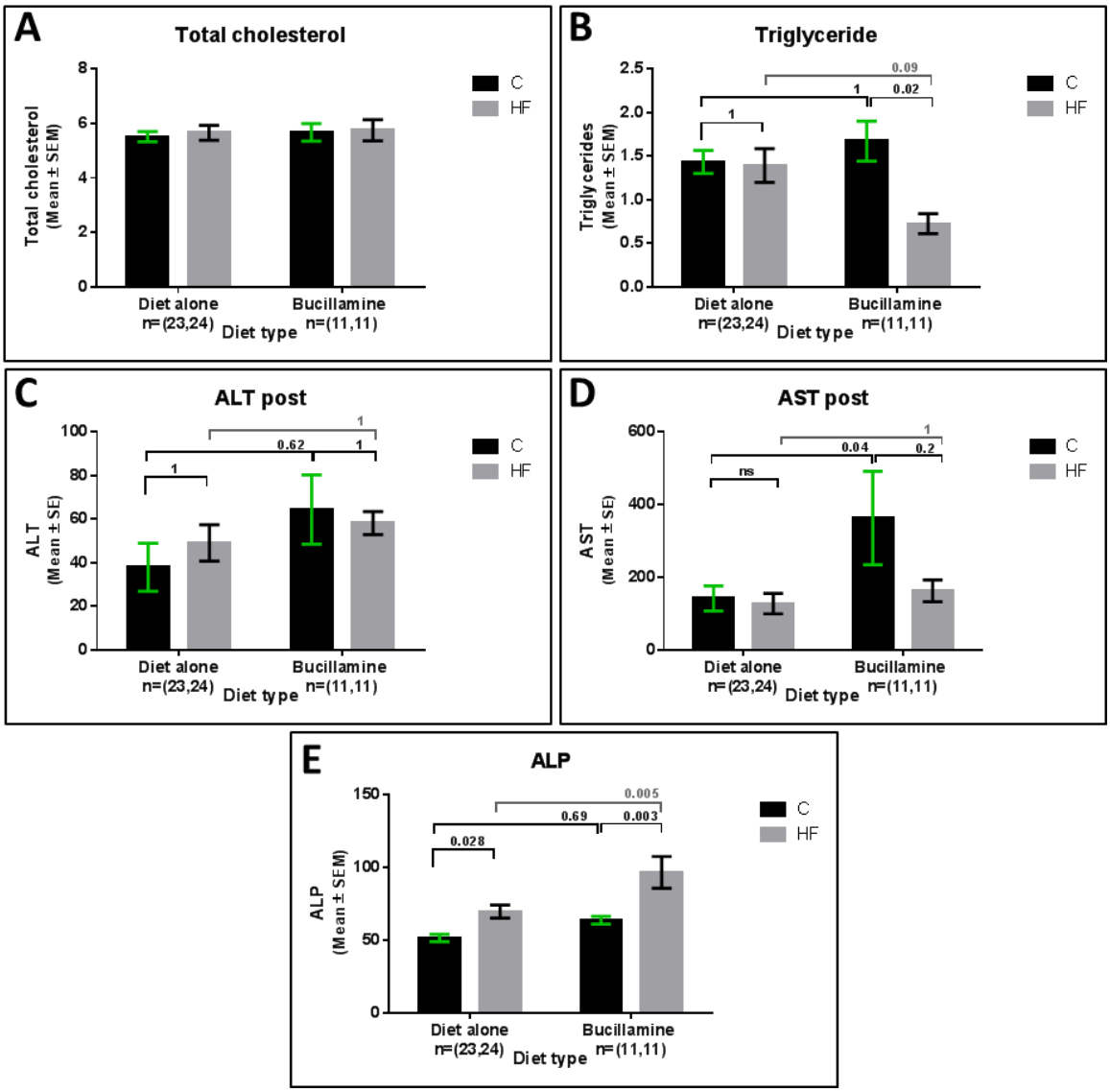

Figure 4.3: The effect of bucillamine on lipid profile and liver enzymes. Lipid profile represented by total cholesterol (A) and triglycerides (B). Liver enzymes tested were ALT-Alanine aminotransferase (C), AST-Aspartate aminotransferase (D) and ALP-Alkaline phosphatase (E). ns=not significant. Y axis values represent Mean ± SE of the mean. The p value was determined by one-way ANOVA with multiple comparison correction (A=0.94, B=0.019, C=0.39, D=0.025, E=<0.001).

4.3.4 The effect of bucillamine on NAFLD histopathology

The impact of bucillamine on NAFLD histopathology is summarised in **Table** 4.2 with categorical data sets and Chi^2 tests. The trends are also demonstrated graphically in **Figure** 4.4**.** There was a significant reduction of steatosis grade in the control diet group, although this was not evident in the ALIOS. The most remarkable effect of bucillamine on the histological parameters was the disappearance of hepatocellular ballooning and Mallory Denk bodies in both the control and the ALIOS groups respectively compared to diet alone groups. There was also a reduction in pigmented Kupffer cells in both bucillamine treated groups. Low level lobular inflammation was modestly increased in the bucillamine control diet group, but there was no impact on the higher starting baseline in the bucillamine ALIOS fed group. Fibrosis as a less subjective and more permanent biomarker of severity was also impacted and reduced by bucillamine. Consequent to these changes in the component parts, both the NAS and SAF combination scoring systems confirmed marked and highly significant reductions in the presence of bucillamine (**Figure** 4.5). Notably, there was little impact of bucillamine on lipogranulomas, megamitochondria, or portal inflammation.

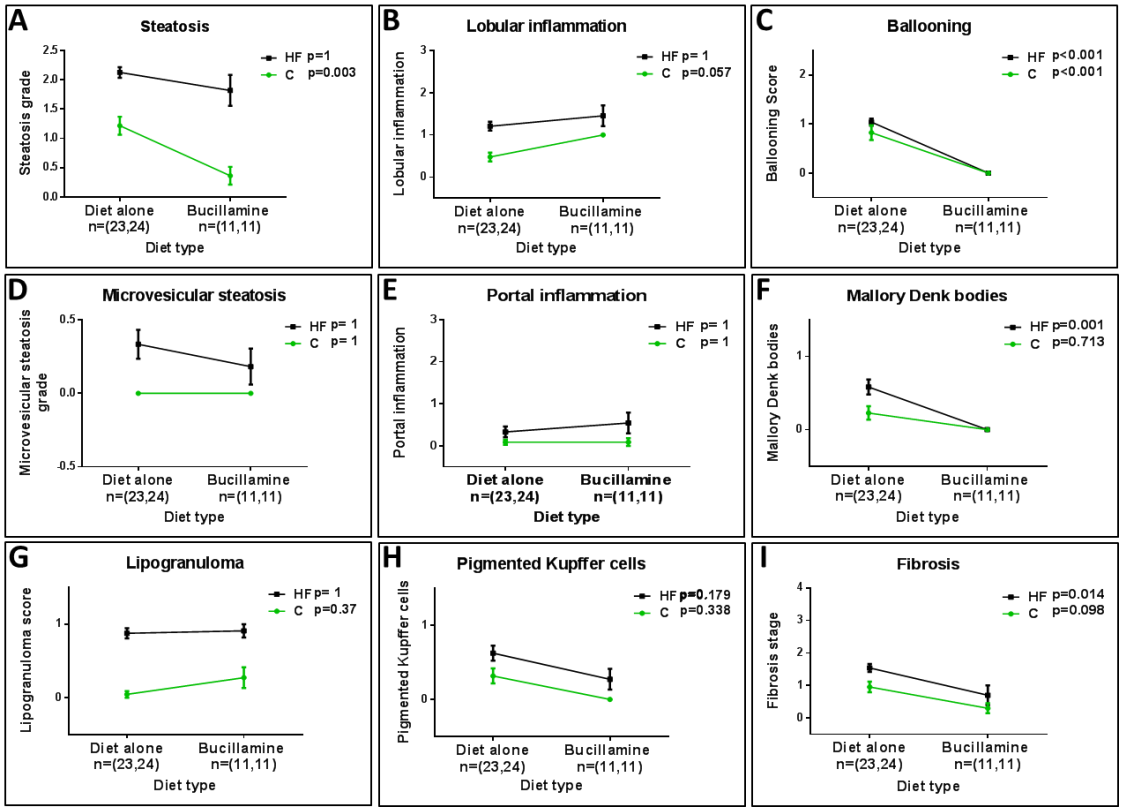

Figure 4.4: Effect of bucillamine on the histological parameters of NAFLD. Bucillamine significantly reduced steatosis (A), ballooning (C) and fibrosis (I) in the control group and reduced ballooning (C), Mallory Denk bodies (F) and fibrosis stage (I) in the ALIOS (HF) group. It caused increase in the lobular inflammation (B) in the control group. Y axis values represent Mean ± SE of the mean; the p value was determined by one-way ANOVA with multiple comparison correction.

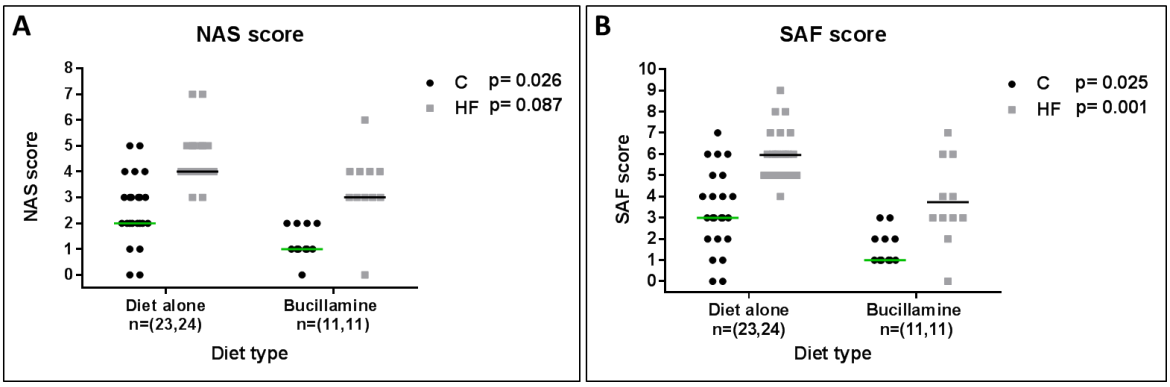

Figure 4.5: the effect of bucillamine on the histological scoring systems. Bucillamine reduced NAS score (A) (p=0.026, 0.087) and SAF score (B) (p=0.025, 0.001) in both the control and high fat groups. Y axis values represent individual values + the median; the p value was determined by one-way ANOVA with multiple comparison correction (A=<0.001, B <0.001).

Table 4.2: The impact of bucillamine on the histological parameters.

Histological parameters	Chi ^{2}					
	Bucillamine control group compared to control diet group			Bucillamine HF group compared to HF diet group		
	Diet alone C	Bucillamine C	p value	Diet alone HF	Bucillamine HF	p value
Steatosis grade (0/1/2/3)	4/10/9/0	7/4/0/0	**0.007**	0/1/19/4	1/2/6/2	0.213
Microvesicular Steatosis grade (0/1)	23/11	11/0	-	16/8	9/2	0.357
Hepatocellular ballooning score (0/1/2)	8/11/4	11/0/0	**0.001**	1/21/2	11/0/0	<**0.0001**
Mallory Denk bodies (None/present)	17/5	11/0	0.086	10/14	11/0	**0.001**
Megamitochondria (None/present)	19/3	11/0	0.199	14/10	9/2	0.174
Lipogranuloma (None/present)	21/1	8/3	0.059	3/21	1/10	0.769
Lobular Inflammation score (0/1/2/3)	12/11/0/0	0/11/0/0	**0.003**	1/17/6/0	1/5/4/1	0.32
Portal Inflammation score (0/1/2)	21/2/0	10/1/0	0.97	18/4/2	7/2/2	0.84
Pigmented Kupffer cells (None/present)	15/7	11/0	**0.035**	9/15	8/3	0.053
Apoptotic cells (None/present)	19/3	10/1	0.706	18/6	9/2	0.656
Perisinusoidal fibrosis score(0/1)	7/16	7/3	**0.035**	0/24	6/4	<**0.0001**
Periportal fibrosis score (0/1/2)	17/6/0	10/0/0	0.074	12/11/1	7/3/0	0.62
Fibrosis stage (0/1/2/3)	7/10/6/0	7/3/0/0	0.063	0/12/11/1	6/1/3/0	<**0.0001**
NAS score (<3, ≥3)	12/11	11/0	**0.005**	0/24	1/10	0.134
SAF activity (<2 either LI or B/>2 both LI & B)	15/8	11/0	**0.025**	2/22	11/0	<**0.001**

4.3.5 Quantification of DNA damage in the bucillamine treated group

Bucillamine treatment resulted in a highly significant reduction in the percentage of γ-H2AX positive nuclei (DNA damage), in both the bucillamine control and ALIOS (HF) groups ($p<0.0001$) supporting the hypothesis that the DNA damage resulted from oxidative free radical processes (**Figure** 4.6). Although markedly reduced in number, significant correlations between γ-H2AX positive nuclei and liver weight ($p<0.0001$), steatosis ($p<0.0001$), lipogranuloma ($p<0.0001$), lobular inflammation ($p=0.008$) and the histological scoring NAS ($p<0.0001$) and SAF ($p<0.0001$) persisted (**Table** 4.3).

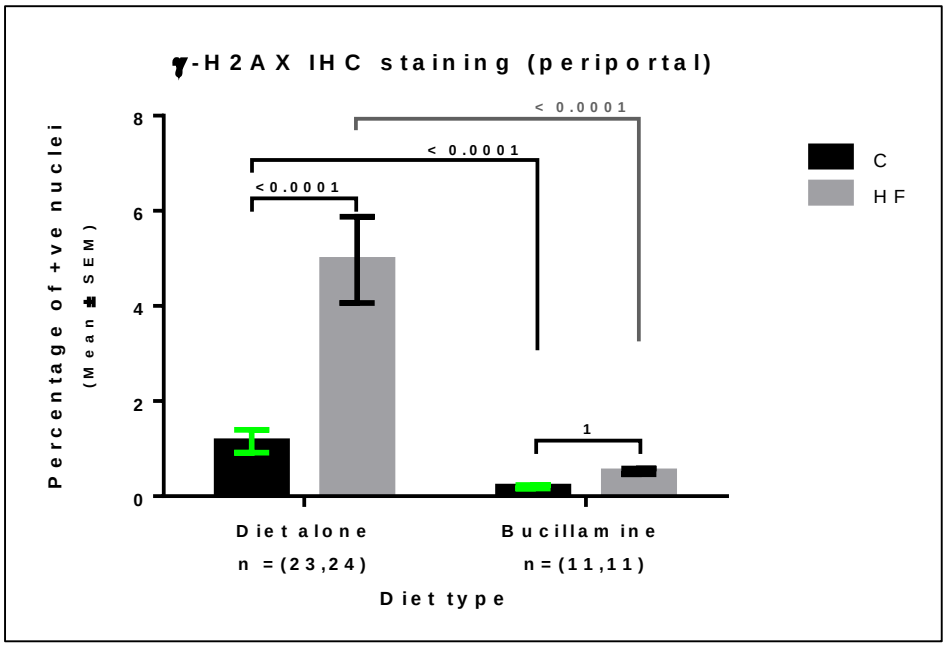

Figure 4.6: γ-H2AX immunohistochemical staining of the periportal area in the diet alone and the bucillamine treated groups. Y axis values represent Mean ± SE of the mean. The p value was determined by one-way ANOVA with multiple comparison correction ($p=<0.001$).

Table 4.3: Associations of γ-H2AX immunohistochemical staining of the periportal area with the phenotypic parameters, liver histopathology and tumours in bucillamine treated groups.

	γ-H2AX (% positive hepatocyte nuclei)(periportal)				
	Chi^2			Spearman rho	
	<0.36%	≥0.36%	P value	correlation	p value
Gross Phenotype Parameters					
Body weight (Continuous variable)				0.517	**0.014**
Liver weight (Continuous variable)				0.7	**<0.001**
Visceral Adipose Tissue				0.537	**0.012**
Histopathology Parameters					
Steatosis grade (0/1/2/3)	7/4/0/0	1/2/6/2	**0.003**	0.79	**<0.001**
Microvesicular Steatosis grade (0/1)	11/0	9/2	0.138	0.22	0.31
Hepatocellular ballooning score (0/1/2)	11/0/0	11/0/0	-	-	-
Mallory Denk bodies (None/present)	11/0	11/0	-	-	-
Megamitochondria (None/present)	11/0	9/2	0.138	0.224	0.31
Lipogranuloma (None/present)	8/3	1/10	**0.002**	0.685	**<0.001**
Lobular Inflammation score (0/1/2)	1/10/0/0	0/6/4/1	0.06	0.547	**0.008**
Portal Inflammation score (0/1/2)	9/2/0	8/1/2	0.58	0.189	0.4
Pigmented Kupffer cells (None/present)	11/0	8/3	0.062	0.324	0.14
Apoptotic cells (None/present)	10/1	9/2	0.534	0.094	0.67
Perisinusoidal fibrosis score(0/1)	8/2	5/5	0.16	0.309	0.18
Periportal fibrosis score (0/1/2)	10/0	7/3	0.06	0.389	0.09
Fibrosis stage (0/1/2/3)	8/2/0	5/2/3	0.277	0.357	0.12
NAS score (<3, ≥3)	11/0	1/10	**<0.001**	0.842	**<0.001**
SAF activity (<2 either LI or B/>2 both LI & B)	11/0	11/0	-	0.748	**<0.001**
Tumour development, progression and grade					
Tumour (absent/present)	5/6	3/8	0.375	0.253	0.255
Tumour number (continuous)				0.298	0.178
Tumour Number (1/ >1; n=14)	2/4	2/6	0.733	0.309	0.162
Tumour size (continuous)				0.253	0.256
Tumour size (<5mm/≥5mm); n=14	4/2	5/3	0.872	0.259	0.244
Tumour grade (1/2/3/4)	0/5/0/0	1/1/2/0	**0.045**	0.12	0.759

4.3.6 Proliferative status in the bucillamine treated group

In contrast to the bucillamine associated reduction in γ-H2AX-positive hepatocyte nuclei, there was no significant effect of bucillamine treatment on the number of Ki67-positive hepatocyte nuclei detected by IHC in either control or ALIOS (HF) diet bucillamine treated animals (**Figure** 4.7). The numbers of Ki67-positive nuclei, reflecting levels of proliferation, remained highly significantly associated with steatosis ($p<0.0001$), presence of lipogranuloma ($p<0.0001$), lobular inflammation ($p=0.037$), and γ-H2AX-positive nuclei ($p<0.0001$) (**Table** 4.4).

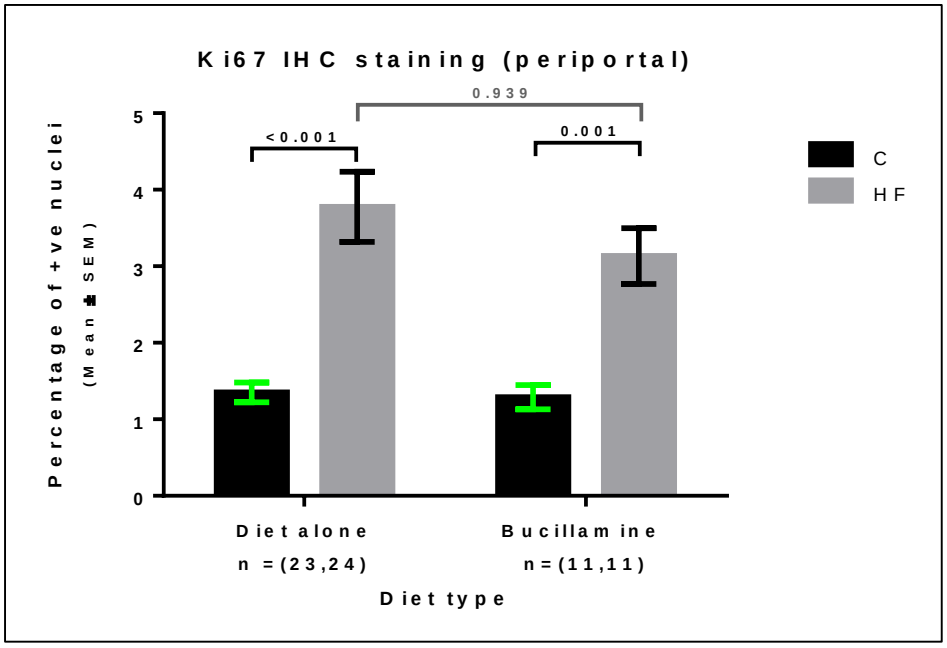

Figure 4.7: Ki67 immunohistochemical staining of the periportal area in the diet alone and the bucillamine treated groups. Y axis values represent Mean ± SE of the mean. The p value was determined by one-way ANOVA with multiple comparison correction ($p=<0.001$).

Table 4.4: Associations of Ki67 immunohistochemical staining of the periportal area with the phenotypic parameters, liver histopathology and γ-H2AX in bucillamine treated groups.

	Ki67 (% positive hepatocyte nuclei)(periportal)				
	Chi^2			Spearman rho	
	<2.015%	≥2.015%	P value	correlation	p value
Gross Phenotype Parameters					
Body weight (Continuous variable)				0.446	**0.037**
Liver weight (Continuous variable)				0.787	**<0.001**
Visceral Adipose Tissue				0.540	**0.012**
Histopathology Parameters					
Steatosis grade (0/1/2/3)	7/4/0/0	1/2/6/2	**0.002**	0.731	**<0.001**
Microvesicular Steatosis grade (0/1)	11/0	9/2	0.138	0.274	0.21
Hepatocellular ballooning score (0/1/2)	11/0/0	11/0/0	-	-	-
Mallory Denk bodies (None/present)	11/0	11/0	-	-	-
Megamitochondria (None/present)	11/0	9/2	0.138	0.274	0.21
Lipogranuloma (None/present)	8/3	1/10	**0.002**	0.722	**<0.001**
Lobular Inflammation score (0/1/2)	0/11/0/0	1/5/4/1	**0.013**	0.447	**0.037**
Portal Inflammation score (0/1/2)	10/1/0	7/2/2	0.375	0.154	0.493
Pigmented Kupffer cells (None/present)	11/0	8/3	0.062	0.178	0.429
Apoptotic cells (None/present)	10/1	9/2	0.534	0.031	0.89
Perisinusoidal fibrosis score(0/1)	7/3	6/4	0.639	0.173	0.466
Periportal fibrosis score (0/1/2)	10/0	7/3	0.06	0.231	0.328
Fibrosis stage (0/1/2/3)	7/3/0	6/1/3	0.19	0.203	0.391
NAS score (<3, ≥3)	11/0	1/10	**<0.001**	0.82	**<0.001**
SAF activity (<2 either LI or B/>2 both LI & B)	11/0	11/0	-	0.677	**0.001**
Tumour development, progression and grade					
Tumour (absent/present)	6/5	2/9	0.076	0.231	0.301
Tumour number (continuous)				0.327	0.138
Tumour Number (1/ >1; n=14)	2/3	2/7	0.480	0.315	0.154
Tumour size (continuous)				0.325	0.140
Tumour size (<5mm/≥5mm); n=14	4/1	5/4	0.360	0.350	0.111
Tumour grade (1/2/3/4)	0/4/0/0	1/2/2/0	0.286	0.558	0.119
Immunohistochemical markers					
γ-H2AX % positive (above/below median)	10/1	1/10	**<0.001**	0.781	**<0.001**

4.3.7 Association of bucillamine with HCC

Notably, despite the abrogation of NASH and dramatic reductions in DNA damage assessed by γ-H2AX positive nuclei, there was no reduction in either the development of tumours, numbers of tumours or size of tumours in the bucillamine treated animals (**Figure** 4.8**; A and B**). In the bucillamine groups alone, numbers were relatively small (n=22) and correlations between tumour development, tumour number or tumour size, with either physical parameters or histological features, were not significant (**Table** 4.5 and **Table** 4.6).

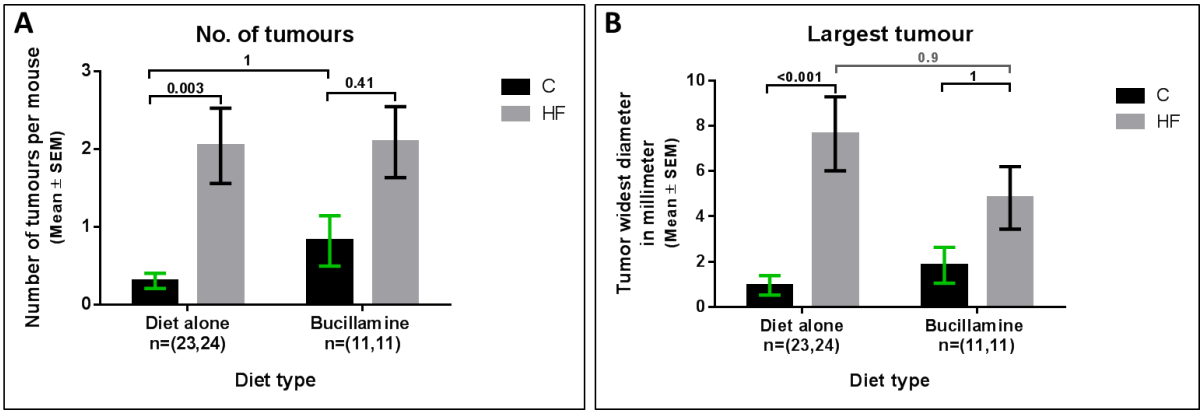

Figure 4.8: The effect of bucillamine treatment on tumour development in the murine dietary animal model. Y axis values represent Mean ± SE of the mean. The p value was determined by one-way ANOVA with multiple comparison correction (A=0.001, B=<0.001).

Table 4.5: Effect of bucillamine on HCC development in C3H/He mice.

	Tumour		Chi ^{2}	Spearman rho	
	No	Yes		Correlation	p value
Gross Phenotype Parameters					
Body weight				0.335	0.127
Liver weight				0.277	0212
Liver/body weight ratio				0.268	0.228
Visceral adipose tissue weight				0.138	0.551
Histological Parameters					
Steatosis grade (0/1/2/3)	4/4/4/0	4/4/4/2	0.619	0.249	0.263
Microvesicular Steatosis grade (0/1)	8/0	12/2	0.262	0.239	0.284
Hepatocellular ballooning score (B)(0/1/2)	8/0/0	14/0/0	-	-	-
Mallory Denk bodies (None/present)	8/0	14/0	-	-	-
Megamitochondria (None/present)	8/0	12/2	0.262	0.239	0.284
Lipogranuloma (None/present)	5/3	4/10	0.119	0.332	0.131
Lobular Inflammation score (LI) (0/1/2/3)	0/7/1/0	1/9/3/1	0.847	0.114	0.612
Portal Inflammation score (0/1/2)	8/0/0	9/3/2	0.233	0.407	0.06
Pigmented Kupffer cells (None/present)	8/0	11/3	0.159	0.3	0.174
Apoptotic cells (None/present)	7/1	12/2	0.907	0.025	0.912
Perisinusoidal fibrosis score(0/1)	5/2	8/5	0.658	0.099	0.678
Periportal fibrosis score (0/1/2)	7/0/0	10/3/0	0.168	0.308	0.186
Fibrosis stage (0/1/2/3)	5/2/0/0	8/2/3/0	0.524	0.161	0.497
NAS score (sum)				0.221	0.324
NAS score (<3/≥3)	3/2	6/8	0.145	0.311	0.16
SAF score (sum)				0.183	0.415
SAF activity (<2 either LI or B/>2 both LI & B)	8/0	14/0	-	-	-

Table 4.6: Effect of bucillamine on tumour size in C3H/He mice.

	Tumour		Chi ^{2}	Spearman rho	
	<5mm	≥5mm		correlation	p value
	n=9	n=5			
Gross Phenotype Parameters					
Body weight				-0.204	0.485
Liver weight				0.337	0.239
Liver/body weight ratio				0.611	**0.02**
Visceral adipose tissue weight				-0.149	0.628
Histopathology Parameters					
Steatosis grade (0/1/2/3)	3/2/2/2	1/2/2/0	0.705	-0.038	0.897
Microvesicular Steatosis grade (0/1)	7/2	5/0	0.255	-0.304	0.290
Hepatocellular ballooning score (0/1/2)	9/0/0	5/0/0	-	-	-
Mallory Denk bodies (None/present)	9/0	5/0	-	-	-
Megamitochondria (None/present)	7/2	5/0	0.255	-0.304	0.290
Lipogranuloma (None/present)	3/6	1/4	0.597	0.141	0.630
Lobular Inflammation score (0/1/2/3)	0/7/1/1	1/2/2/0	0.44	-0.022	0.941
Portal Inflammation score (0/1/2)	6/1/2	3/2/0	0.316	-0.022	0.941
Pigmented Kupffer cells (None/present)	6/3	5/0	0.145	-0.389	0.169
Apoptotic cells (None/present)	7/2	5/0	0.255	-0.304	0.290
Perisinusoidal fibrosis score(0/1)	5/3	3/2	0.928	0.025	0.935
Periportal fibrosis score (0/1/2)	6/2/0	4/1/0	0.835	-0.058	0.851
Fibrosis stage (0/1/2/3)	5/1/2/0	3/1/1/0	0.928	0.001	1
NAS score (sum)				0.075	0.798
NAS score (<3/≥3)	4/5	2/3	0.872	0.293	0.186
SAF score (sum)				-0.056	0.848
SAF activity (<2 either LI or B/>2 both LI & B)	9/0	5/0	-	-	-

There was no significant difference between the histological grade of the tumours in the bucillamine-treated animals compared to no bucillamine and the majority (6/9) were grade 2 hepatocellular carcinomas.

4.3.8 Quantification of p53 in the bucillamine treated group

Bucillamine treatment resulted in a significant reduction in the percentages of p53 IHC stained nuclei in the bucillamine ALIOS group compared to the diet alone ALIOS group ($p<0.001$) (**Figure** 4.9). As before, p53 IHC positive nuclei correlated significantly with the number of tumours ($p=0.001$), size of tumours ($p<0.0001$), steatosis grade ($p=0.019$), lipogranuloma ($p=0.003$) and the histological scoring systems NAS ($p=0.008$) and SAF ($p=0.043$), in addition to the correlation with γ-H2AX ($p=0.004$) and Ki67 ($p=0.005$) (**Table** 4.7).

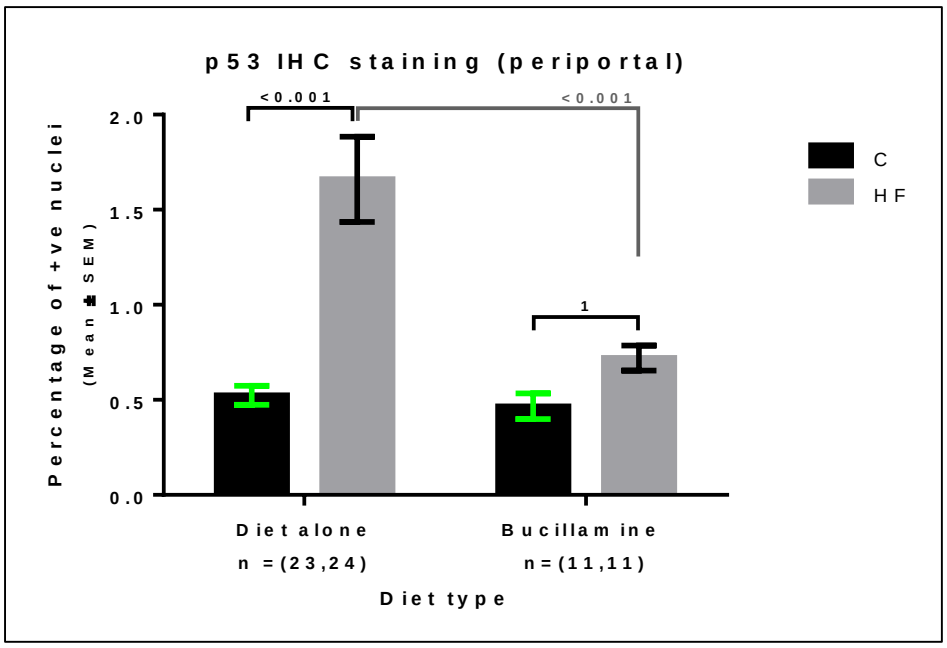

Figure 4.9: p53 immunohistochemical staining of the periportal area in the diet alone and the bucillamine treated groups. Y axis values represent Mean ± SE of the mean. The p value was determined by one-way ANOVA with multiple comparison correction (p=<0.001).

Table 4.7: Associations of p53 immunohistochemical staining of the periportal area with the phenotypic parameters, liver histopathology, tumours and immunohistochemical markers in the bucillamine treated groups.

	p53 IHC (% positive hepatocyte nuclei)(periportal)				
	Chi2			Spearman rho	
	<0.6%	≥0.6%	P value	correlation	P value
Gross Phenotype Parameters					
Body weight (Continuous variable)				0.573	**0.005**
Liver weight (Continuous variable)				0.672	**0.001**
Visceral Adipose Tissue				0.270	0.273
Histopathology Parameters					
Steatosis grade (0/1/2/3)	6/2/1/2	2/4/5/0	0.08	0.494	**0.019**
Microvesicular Steatosis grade (0/1)	10/1	10/1	1	0.224	0.315
Hepatocellular ballooning score (0/1/2)	11/0/0	11/0/0	-	-	-
Mallory Denk bodies (None/present)	11/0	11/0	-	-	-
Megamitochondria (None/present)	10/1	10/1	1	0.224	0.315
Lipogranuloma (None/present)	7/4	2/9	**0.03**	0.598	**0.003**
Lobular Inflammation score (0/1/2/3)	1/9/0/1	0/7/4/0	0.09	0.386	0.076
Portal Inflammation score (0/1/2)	8/1/2	9/2/0	0.58	0.077	0.733
Pigmented Kupffer cells (None/present)	9/2	10/1	0.534	0.063	0.782
Apoptotic cells (None/present)	8/3	11/0	0.062	-0.261	0.24
Perisinusoidal fibrosis score(0/1)	6/4	7/3	0.639	0.009	0.97
Periportal fibrosis score (0/1/2)	8/2	9/1	0.531	0.14	0.54
Fibrosis stage (0/1/2/3)	6/2/2	7/2/1	0.81	0.045	0.851
NAS score (<3, ≥3)	8/3	4/7	0.087	0.59	**0.008**
SAF activity (<2 either LI or B/>2 both LI & B)	11/0	11/0	-	0.436	**0.043**
Immunohistochemical markers					
γ-H2AX IHC periportal (median)	7/4	4/7	0.201	0.480	**0.024**
γ-H2AX IHC periportal (continuous)				0.588	**0.004**
Ki67 IHC periportal (median)	7/4	4/7	0.201	0.523	**0.012**
Ki67 IHC periportal (continuous)				0.573	**0.005**
Tumour development, progression and grade					
Tumour (no,yes)	7/4	1/10	**0.008**	0.701	**<0.001**
Tumour number (continuous)				0.659	**0.001**
Tumour Number (1/ >1; n=14)	1/3	3/7	0.852	0.666	**0.001**
Tumour size (continuous)				0.693	**<0.001**
Tumour size (5mm/ ≥5mm); n=14	3/1	6/4	0.597	0.716	**<0.001**
Tumour grade (1/2/3/4)	1/2/0/0	0/4/2/0	0.405	0.697	**0.037**

4.4 The impact of FXR agonist PX20606 on the dietary animal model

4.4.1 Background

FXR is a type II nuclear receptor that is a member of a subfamily of 7 nuclear receptor families (291). It is expressed in several organs like the liver, intestine, kidney, adipose tissue and muscle. It controls bile acid synthesis and plays a role in carbohydrate and lipid metabolism, and insulin sensitivity (292, 293).

The type II nuclear receptors usually bind to ligands, that are lipophilic and can pass through the nuclear pores, derived from either endogenous nutrients (e.g. fatty acids (FAs), bile acids (BA), oxysterols) or from exogenous chemicals. These nuclear receptors bind to and form a heterodimer with the Retinoid X receptor (RXR) to perform its function as a transcriptional factor (291).

Bile acid (which acts as FXR ligand) is synthesized and secreted by the hepatocytes and then stored in the gall bladder to be released into the intestine after meals, aiding the emulsification and absorption of fat (293). Most secreted bile acids are re-absorbed from the bowel (terminal ileum) (~ 95%) into the portal circulation, returning to the liver in what is called the enterohepatic circulation (294) (**Figure** 4.10).

According to the "energy vector" concept proposed by Evans and Mangelsdorf (291), lipolysis of triacylglycerol (TAG) in white adipose tissue (WAT) during fasting results in the release of fatty acids (FAs) into the circulation for use as an energy source by different tissues. When FAs reach the liver, they activate PPARα and stimulate FA catabolism. In the fed state, FXR acts as a BA regulator and BAs activate FXR receptors in the intestine, where they promote nutrient absorption and stimulate FGF19 production. In the fed state, liver FXR stimulates TAG-lipoprotein clearance (292) and represses cholesterol 7α hydroxylase (CYP7A1), the rate limiting step of BA synthesis, via two routes – namely the upregulation of small heterodimer partner (SHP) that inhibits CYP7A1 (294), and through the upregulation of FGF19 – that also inhibits CYP7A1. Cholesterol reverse transport is also activated through FXR-upregulated FGF19, aiding the depletion of excess cholesterol (**Figure** 4.10). FGF19 also stimulates glycogenesis in the liver and excess nutrients are consumed by the muscles or stored in WAT under the effect of PPARβ/δ and PPARα respectively (295). In addition to its effect on inhibition of bile acid synthesis, regulation of lipid metabolism, FXR also reportedly regulates intestinal inflammation, inhibits bacterial translocation into the liver, and influences liver proliferation and its regenerative capability (293, 296) (**Figure** 4.10).

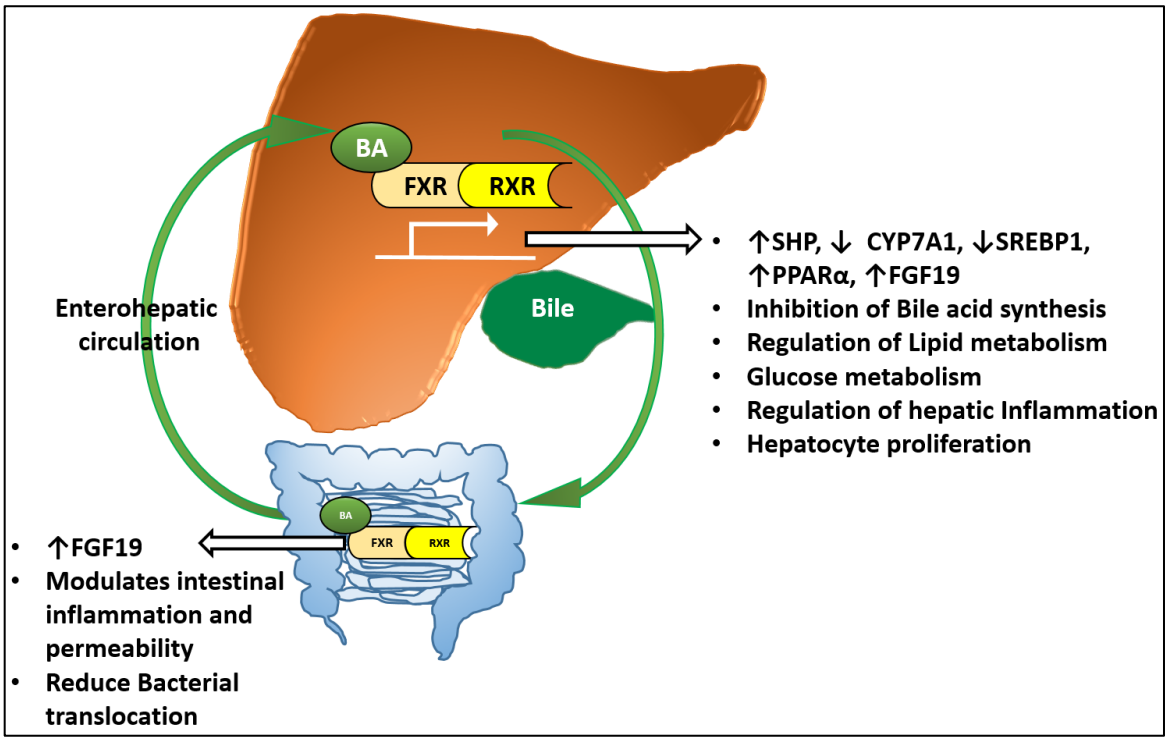

Figure 4.10: Schematic representation of FXR function.

It has been proposed that hepatic steatosis may be attenuated by FXR activation in rodents and humans. In an animal model, hepatic steatosis was more evident in *Fxr*-null mice fed a high-fat diet compared to WT mice (297). Hepatic levels of FXR are reportedly low in NAFLD patients (298).

Several FXR agonist compounds have been developed, the first reaching clinical trials being obeticholic acid (OCA), originating from the University of Perugia and GSK scientists in 2002 (299). Several other FXR agonists have followed, one of which is the compound used in our project (PX20606), developed by Phenex pharmaceuticals. PX20606 was reported to have a higher liver exposure and more FXR transcriptional activity compared to OCA (300, 301) . Its chemical structure is shown in (**Figure** 4.11).

This compound was mixed with the food pellets and given to the mice in the dietary model with an estimated daily dose of 1mg /kg/day (n=12,12 mice) or 5 mg/kg/day (n=8,8 mice) from the age of 24 weeks until 48 weeks. Doses were estimated based on average daily food consumption per cage.

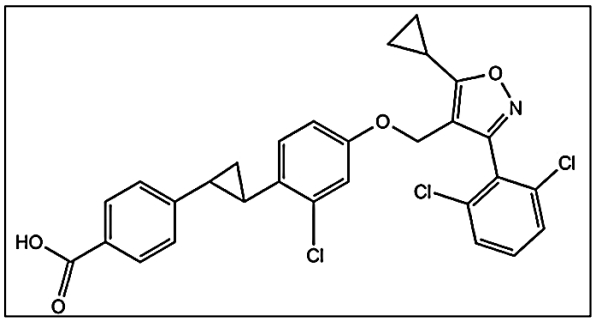

Figure 4.11: chemical structure of PX20606 FXR agonist(300).

4.4.2 The effect of PX20606 on body and liver weight

P20606 treatment did not show any effect on the body weight in the ALIOS (**H**igh **F**at **H**igh **F**ructose (**HF**)) fed animals (**Figure** 4.12**; A**). Liver weight on the other hand showed marked and highly significant changes. In the control diet animals, liver weight increased stepwise with 1 mg and 5 mg PX20606 doses (**Figure** 4.12**; B**). In ALIOS fed mice – compared to a higher starting baseline there were significant increases in both PX20606 dose groups, although a plateau was reached without further increase between doses (**Figure** 4.12**, B**).

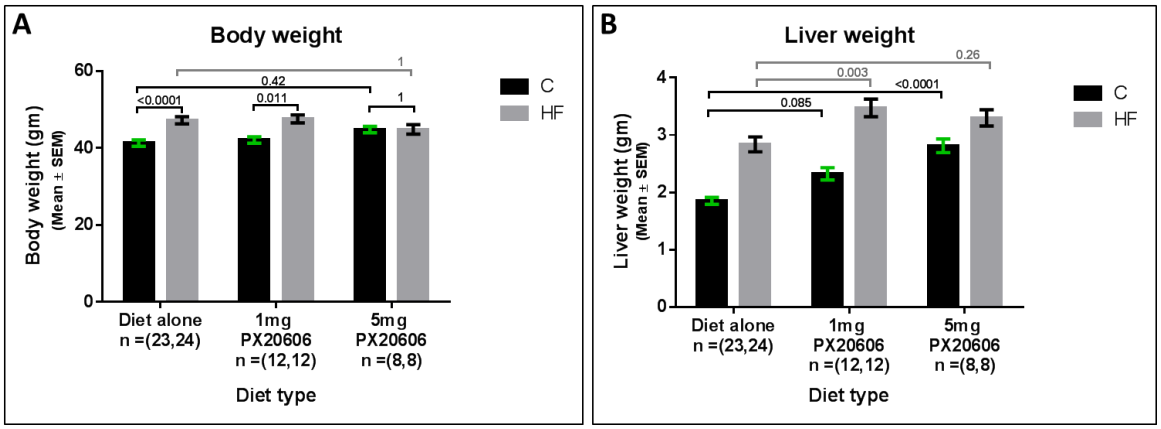

Figure 4.12: The effect of PX20606 on body and liver weight compared to the effect of ALIOS diet. (A) Shows no significant effect of both 1mg and 5 mg PX20606 on the body weight neither in the control nor in the HF fed groups. (B) There was a highly significant increase in liver weight in both PX20606 treated control groups compared to the control group in diet alone, with significant increase in the liver weight in PX20606 treated ALIOS (HF) groups compared to the diet alone HF group. All groups are 48-week-old. Y axis values represent Mean ± SE of the mean. The p value was determined by one-way ANOVA with multiple comparison correction (A<0.001, B<0.001).

4.4.3 The effect of PX20606 on lipid profile and liver function

PX20606 reduced cholesterol levels in both dietary groups at the higher 5mg dose but it was not statistically significant (**Figure** 4.13**; A**). There was also a marked reduction in triglyceride level in the 5 mg dose treated ALIOS (HF) group but was not statistically significant (**Figure** 4.13**; B**).

Rather than reductions, there were some increases in liver enzymes in the PX20606 treated animals, often more so in the control groups where the baseline untreated level was lower. In the animals receiving 1mg PX20606, the ALP was raised in the ALIOS (HF) group (**Figure** 4.13**; E**). Aminotransferases and ALP levels were increased in both control and ALIOS groups in the mice receiving 5mg PX20606 (**Figure** 4.13**; C, D and E**).

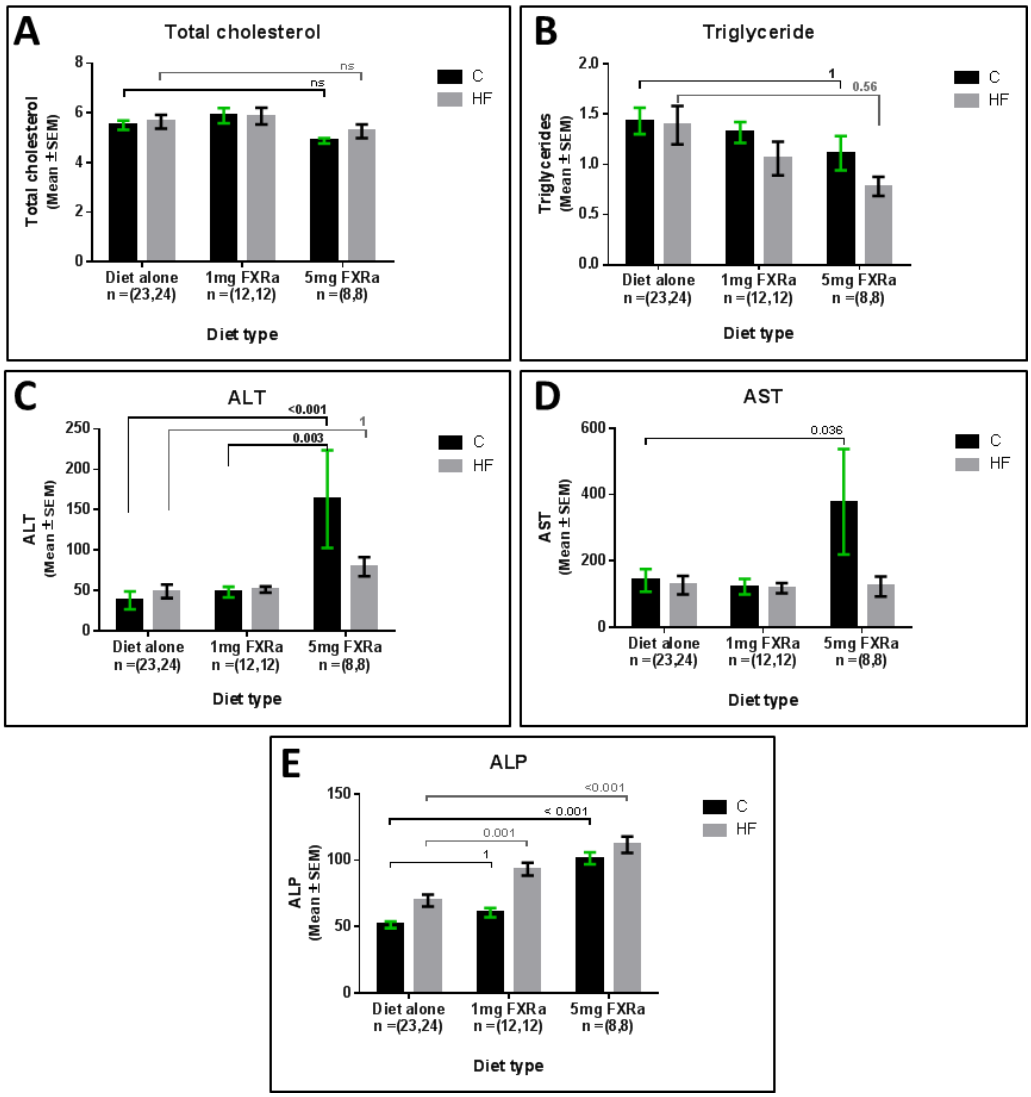

Figure 4.13: The effect of PX20606 on lipid profile and liver enzymes. Lipid profile represented by total cholesterol (A) and triglycerides (B). Liver enzymes are ALT-Alanine aminotransferase (C), AST-Aspartate aminotransferase (D) and ALP-Alkaline phosphatase (E). Y axis values represent Mean ± SE of the mean. ns = not significant, p value was determined by one-way ANOVA with multiple comparison correction (A=0.25, B=0.18, C<0.001, D=0.023, E<0.001).

4.4.4 Histological assessment of the impact of PX20606

Despite some relatively encouraging improvements in cholesterol and triglyceride levels, the PX20606 treatment did not improve histological parameters. In some instances histological parameters were worsened – particularly in the control diet group. The trends are shown in **Figure** 4.14, with categorical datasets and Chi2 tests in (**Table** 4.8**, Table** 4.9**)**. Although some of the changes in these relatively small groups of mice were not particularly marked, and there were not increases in inflammatory scores, there was a significant and more convincing stepwise dose associated increase in fibrosis stage, in both control and ALIOS (HF) diet mice.

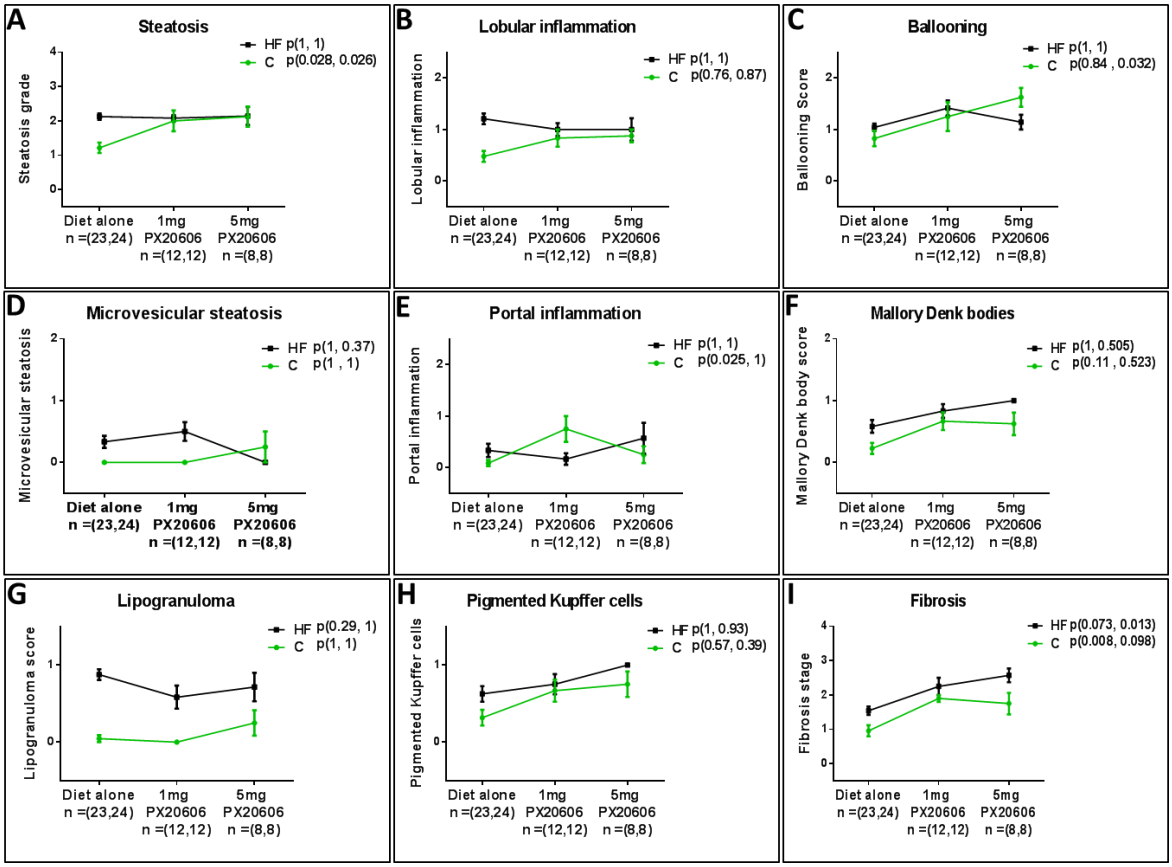

Figure 4.14: Effect of PX20606 on the histological parameters of NAFLD. PX20606 did not improve the steatosis grade in the ALIOS treated group; however, it had a clear effect on the control groups showing a significant increase in the steatosis grade with the dose (p=0.028, 0.026 respectively). Ballooning was also increased with PX20606 dose in the control groups (p=0.84, 0.032 respectively). PX20606 had a clear effect on worsening of fibrosis stage whether in the control (p=0.008, 0.098) or ALIOS treated group (0.073, 0.013). It caused increased portal inflammation in the 1mg PX20606 treated control group (p=0.025) but not in the 5mg PX20606 treated control group (p=1). Y axis values represent Mean ± SE of the mean; p-value was determined by one-way ANOVA with multiple comparison correction.

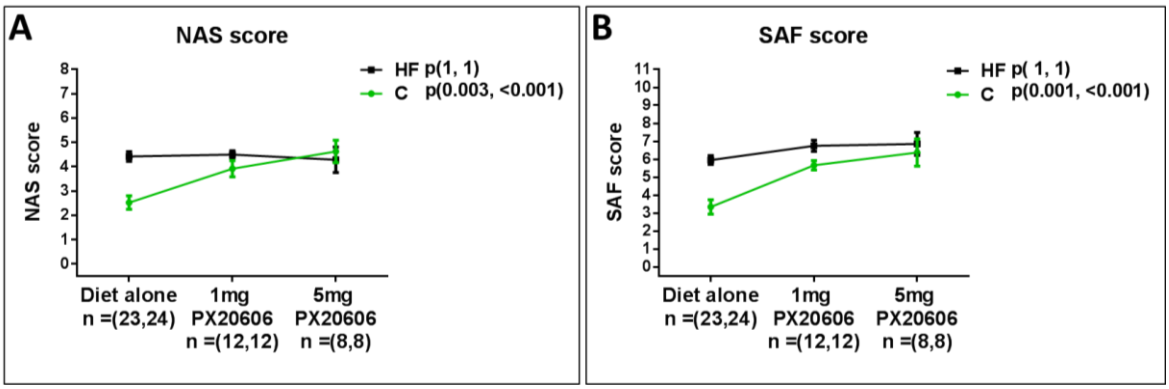

Figure 4.15: The effect of PX20606 on the histological scoring system. Y axis values represent Mean ± SE of the mean; p-value was determined by one-way ANOVA with multiple comparison correction (A<0.001, B<0.001).

Table 4.8: The impact of PX20606 on the histological parameters in the control treated groups (Chi^2).

Histological parameters	Chi ^{2}				
	PX206096 control groups compared to control diet group				
	Diet alone C	1mg PX20606 C	p value	5mg PX20606 C	p value
Steatosis grade (0/1/2/3)	4/10/9/0	0/6/0/6	**<0.0001**	0/2/3/3	**0.019**
Microvesicular Steatosis grade (0/1)	23/0	12/0	-	7/1	0.085
Hepatocellular ballooning score (0/1/2)	8/11/4	4/1/7	**0.024**	0/3/5	**0.035**
Mallory Denk bodies (None/present)	17/5	4/8	**0.012**	3/5	**0.041**
Megamitochondria (None/present)	19/3	8/4	0.175	5/3	0.148
Lipogranuloma (None/present)	21/1	12/0	0.453	6/2	0.099
Lobular Inflammation score (0/1/2/3)	12/11	3/8/1	0.143	1/7	0.05
Portal Inflammation score (0/1/2)	21/2	6/3/3	**0.005**	6/2	0.236
Pigmented Kupffer cells (None/present)	15/7	4/8	0.051	2/6	**0.035**
Apoptotic cells (None/present)	19/3	7/5	0.066	4/4	**0.037**
Perisinusoidal fibrosis score(0/1)	7/16	0/10	**0.049**	0/8	0.076
Periportal fibrosis score (0/1/2)	17/6	1/9	**0.001**	4/4	0.213
Fibrosis stage (0/1/2/3)	7/10/6/0	0/1/9/0	**0.002**	0/4/2/2	**0.046**
NAS score (<3, ≥3)	12/11	1/11	**0.011**	0/8	**0.009**
SAF activity (<2 either LI or B/>2 both LI & B)	15/8	6/6	0.383	1/7	**0.01**

Table 4.9: The impact of PX20606 on the histological parameters in the ALIOS (HF) treated groups (Chi^2).

Histological parameters	Chi ^{2}				
	PX20606 HF groups compared to HF diet group				
	Diet alone HF	1mg PX20606 HF	p value	5mg PX20606 HF	p value
Steatosis grade (0/1/2/3)	1/19/4/0	0/11/1/0	0.762	1/4/2/0	0.418
Microvesicular Steatosis grade (0/1)	16/8	6/6	0.334	7/0	0.076
Hepatocellular ballooning score (0/1/2)	1/21/2	0/7/5	**0.046**	0/6/1	0.78
Mallory Denk bodies (None/present)	10/14	2/10	0.134	0/7	**0.038**
Megamitochondria (None/present)	14/10	5/7	0.345	6/1	0.183
Lipogranuloma (None/present)	3/21	5/7	**0.047**	2/5	0.309
Lobular Inflammation score (0/1/2/3)	1/17/6/0	1/10/1/0	0.446	1/5/1	0.784
Portal Inflammation score (0/1/2)	18/4/2	10/2/0	0.839	4/2/1	0.816
Pigmented Kupffer cells (None/present)	9/15	3/9	0.453	0/7	0.054
Apoptotic cells (None/present)	18/6	11/1	0.234	3/4	0.109
Perisinusoidal fibrosis score(0/1)	0/24	0/12	-	0/7	-
Periportal fibrosis score (0/1/2)	12/11/1	3/9/0	0.261	0/6/1	0.08
Fibrosis stage (0/1/2/3)	0/12/11/1	3/3/6/0	**0.006**	0/3/4	**0.002**
NAS score (<3, ≥3)	0/24	0/12	-	0/7	-
SAF activity (<2 either LI or B/>2 both LI & B)	2/22	1/11	1	1/6	0.639

4.4.5 Quantification of hepatocyte DNA damage in PX20606 treated animals

DNA damage quantification was assessed by measuring the percentage of γ-H2AX positive nuclei in the periportal area. There was no statistically significant effect of PX20606 on γ-H2AX levels in the treated animals (**Figure** 4.16). As previously, γ-H2AX staining correlated significantly with lipogranuloma (0.017), fibrosis (0.006) and SAF score (0.005) (**Table** 4.10), supporting the association of DNA damage with worsening of NAFLD stage.

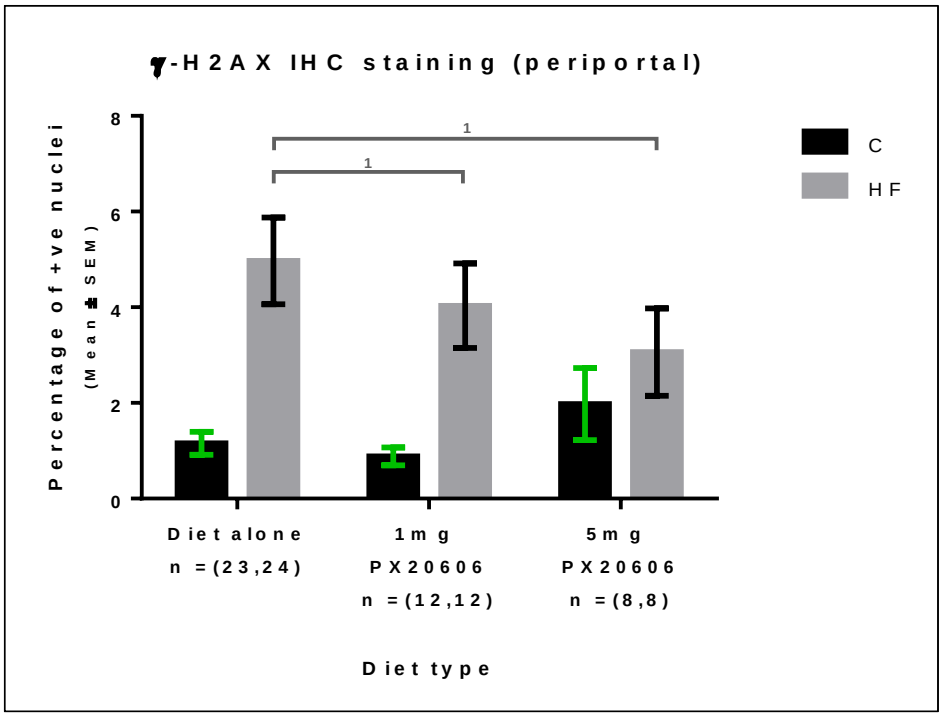

Figure 4.16: γ-H2AX immunohistochemical staining of the periportal area in the diet alone and the PX20606 treated groups. Y axis values represent Mean ± SE of the mean. The p value was determined by one-way ANOVA with multiple comparison correction.

Table 4.10: Associations of γ-H2AX immunohistochemical staining of the periportal area with the phenotypic parameters, liver histopathology and tumours in PX20606 treated groups.

	γ-H2AX (% positive hepatocyte nuclei)(periportal)				
	Chi^2			Spearman rho	
	<1.48%	≥1.48%	P value	correlation	p value
Gross Phenotype Parameters					
Body weight (Continuous variable)				0.606	**<0.001**
Liver weight (Continuous variable)				0.469	**0.003**
Visceral Adipose Tissue				0.493	**0.001**
Histopathology Parameters					
Steatosis grade (0/1/2/3)	0/7/6/6	0/2/12/6	0.101	0.164	0.32
Microvesicular Steatosis grade (0/1)	17/2	15/5	0.239	0.255	0.117
Hepatocellular ballooning score (0/1/2)	4/6/9	0/11/9	0.073	0.088	0.595
Mallory Denk bodies (None/present)	8/11	1/19	**0.006**	0.265	0.103
Megamitochondria (None/present)	13/6	11/9	0.389	0.201	0.219
Lipogranuloma (None/present)	15/4	10/10	0.06	0.38	**0.017**
Lobular Inflammation score (0/1/2)	4/14/1	2/16/2	0.643	0.212	0.195
Portal Inflammation score (0/1/2)	11/6/2	15/3/2	0.495	-0.081	0.626
Pigmented Kupffer cells (None/present)	7/12	2/18	**0.047**	0.411	**0.009**
Apoptotic cells (None/present)	13/6	12/8	0.584	-0.052	0.752
Perisinusoidal fibrosis score(0/1)	0/18	0/19	_	_	_
Periportal fibrosis score (0/1/2)	5/13/0	3/15/1	0.569	0.198	0.239
Fibrosis stage (0/1/2/3)	0/5/11/2	0/3/6/10	**0.035**	0.442	**0.006**
NAS score (<3, ≥3)	1/18	0/20	0.299	0.289	0.066
SAF activity (<2 either LI or B/>2 both LI & B)	7/12	2/18	**0.047**	0.445	**0.005**
Tumour development, progression and grade					
Tumour (absent/present)	10/9	4/16	**0.034**	0.242	0.137
Tumour number (continuous)				0.222	0.175
Tumour Number (1/ >1; n=25)	2/7	5/11	0.629	0.175	0.286
Tumour size (continuous)				0.288	0.076
Tumour size (<5mm/≥5mm); n=25	3/6	6/10	0.835	0.173	0.292
Tumour grade (1/2/3/4)	1/2/2/0	1/9/1/0	0.282	-0.216	0.422

4.4.6 Proliferative status in PX20606 treated animals

In the control diet mice supplemented with PX20606, there was a dose dependent increase in proliferation as measured by Ki67 IHC in periportal areas. In the ALIOS (HF) mice, where the level was already elevated, there was no additional effect of PX20606 treatment on proliferation levels (**Figure** 4.17). As reported in chapter 3, Ki67 correlated significantly with steatosis (p=0.002), fibrosis stage (p=0.007), NAS score (0.026), SAF score (0.006) and γ-H2AX (p< 0.0001) (**Table** 4.11).

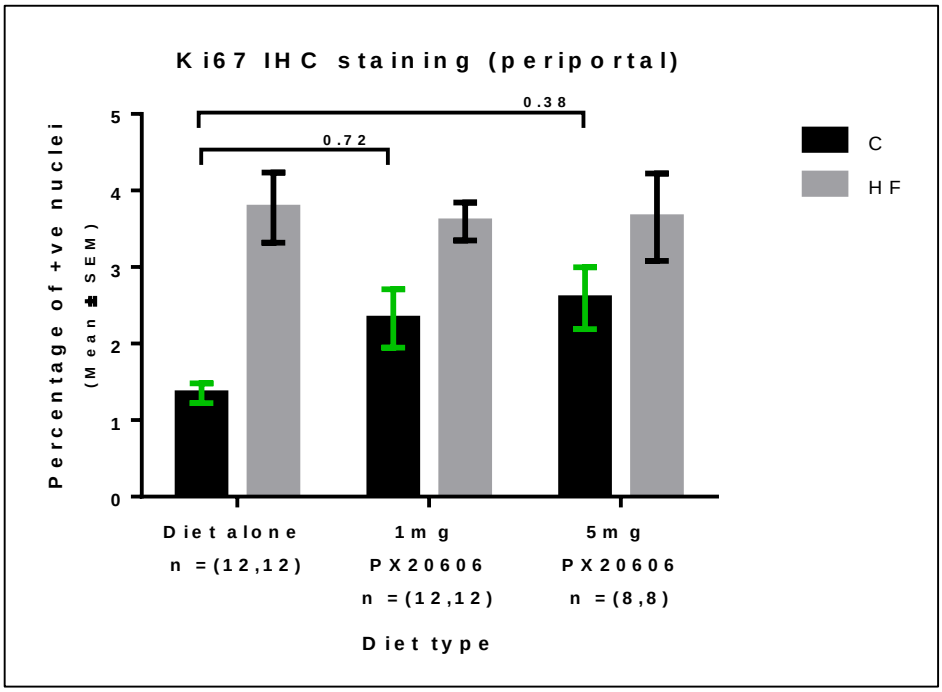

Figure 4.17: Ki67 immunohistochemical staining of the periportal area in the diet alone and the PX20606 treated groups. Y axis values represent Mean ± SE of the mean. The p value was determined by one-way ANOVA with multiple comparison correction.

Table 4.11: Associations of Ki67 immunohistochemical staining of the periportal area with the phenotypic parameters, liver histopathology, tumours and γ-H2AX in PX20606 treated groups.

	Ki67 (% positive hepatocyte nuclei)(periportal)				
	Chi^2			Spearman rho	
	<2.92%	≥2.92%	P value	correlation	p value
Gross Phenotype Parameters					
Body weight (Continuous variable)				0.649	**<0.001**
Liver weight (Continuous variable)				0.595	**<0.001**
Visceral Adipose Tissue				0.363	**0.023**
Histopathology Parameters					
Steatosis grade (0/1/2/3)	0/8/7/4	0/1/11/8	**0.028**	0.475	**0.002**
Microvesicular Steatosis grade (0/1)	18/1	14/6	**0.044**	0.413	**0.009**
Hepatocellular ballooning score (0/1/2)	2/7/10	2/10/8	0.811	-0.122	0.459
Mallory Denk bodies (None/present)	5/14	4/16	0.64	0.084	0.612
Megamitochondria (None/present)	14/5	10/10	0.129	0.094	0.571
Lipogranuloma (None/present)	14/5	11/9	0.224	0.216	0.186
Lobular Inflammation score (0/1/2)	3/15/1	3/15/2	0.857	0.154	0.351
Portal Inflammation score (0/1/2)	13/4/2	13/5/2	0.958	0.039	0.813
Pigmented Kupffer cells (None/present)	7/12	2/18	**0.047**	0.346	**0.031**
Apoptotic cells (None/present)	12/7	13/7	0.905	-0.017	0.92
Perisinusoidal fibrosis score(0/1)	0/18	0/19	-	-	-
Periportal fibrosis score (0/1/2)	5/13/0	3/15/1	0.569	0.242	0.149
Fibrosis stage (0/1/2/3)	5/10/3	3/7/9	0.142	0.435	**0.007**
NAS score (<3, ≥3)	0/19	1/19	0.323	0.356	**0.026**
SAF activity (<2 either LI or B/>2 both LI & B)	4/15	5/15	0.77	0.436	**0.006**
Tumour development, progression and grade					
Tumour (absent/present)	6/13	8/12	0.584	0.009	0.954
Tumour number (continuous)				-0.126	0.444
Tumour Number (1/ >1;n=25)	2/11	5/7	0.144	-0.118	0.476
Tumour size (continuous)				0.018	0.917
Tumour size (<5mm/≥5mm); n=25	5/8	4/8	0.790	0.067	0.684
Tumour grade (1/2/3/4)	1/6/2/0	1/5/1/0	0.915	0.169	0.531
Immunohistochemical markers					
γ-H2AX % positive (above/below median)	15/4	4/16	**<0.001**	0.649	**<0.001**

4.4.7 The impact of PX20606 on HCC in C3H/He mice

PX20606 treatment did not reduce tumour development, tumour number or tumour size. On the contrary, PX20606 treatment in the control diet group was associated with an increase in both the numbers and size of tumours (**Figure** 4.18).

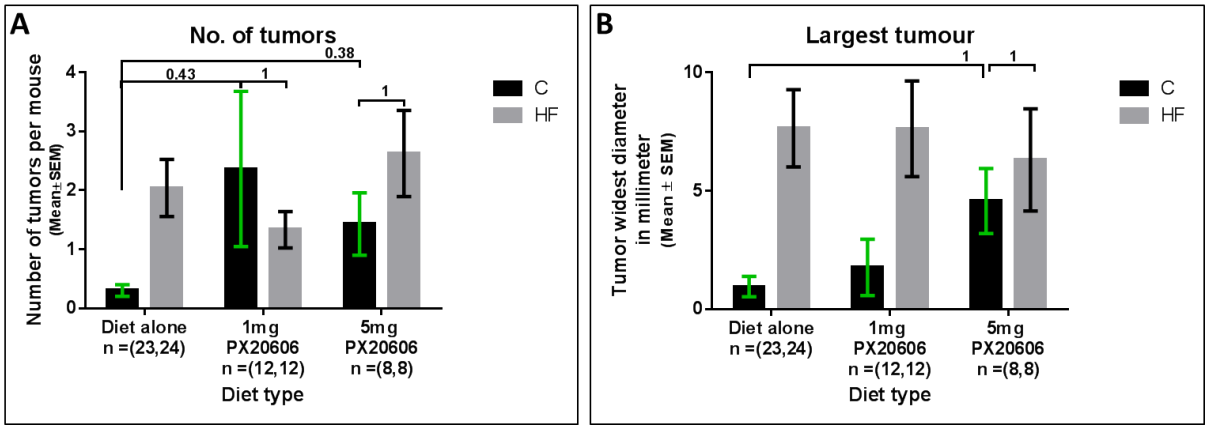

Figure 4.18: The effect of PX20606 treatment on tumour development in the murine dietary animal model. (A) PX20606 treatment did not decrease the number of tumours in the HF group but there was a significant increase in the number of tumours in the 5 mg PX20606 treated group compared to the control group of diet alone. (B) There was a significant increase in the size of tumours in the 5 mg PX20606 treated control compared to the diet alone control group. Y axis values represent Mean ± SE of the mean. The p value was determined by one-way ANOVA with multiple comparison correction.

As in the standard model without intervention, steatosis and lipogranuloma remained strongly associated with tumour development and size (**Table** 3.2, **Table** 3.4). In the PX20606 treated animals, there were also associations with hepatocellular ballooning (p= 0.017) and Mallory Denk bodies (0.028) (**Table** 4.12).

Table 4.12: Effect of PX20606 on tumour development in C3H/He mice

	Tumour		Chi ^{2}	Spearman rho	
	No	Yes		Correlation	p value
Gross Phenotype Parameters					
Body weight				0.116	0.477
Liver weight				0.410	**0.009**
Liver/body weight ratio				0.472	**0.002**
Visceral adipose tissue weight				0.337	**0.033**
Histological Parameters					
Steatosis grade (0/1/2/3)	0/3/3/8	0/6/15/4	**0.019**	-0.299	0.064
Microvesicular Steatosis grade (0/1)	12/2	20/5	0.656	-0.071	0.666
Hepatocellular ballooning score (B)(0/1/2)	4/4/6	0/13/12	**0.017**	0.184	0.263
Mallory Denk bodies (None/present)	6/8	3/22	**0.028**	0.351	**0.028**
Megamitochondria (None/present)	9/5	15/10	0.792	0.042	0.798
Lipogranuloma (None/present)	13/1	12,13	**0.005**	0.449	**0.004**
Lobular Inflammation score (LI) (0/1/2)	3/11/0	3/19/3	0.442	0.213	0.193
Portal Inflammation score (0/1/2)	8/4/2	18/5/2	0.679	-0.154	0.348
Pigmented Kupffer cells (None/present)	2/12	7/18	0.33	-0.156	0.343
Apoptotic cells (None/present)	11/3	14/11	0.159	0.226	0.167
Perisinusoidal fibrosis score(0/1)	0/12	0/25	-	-	-
Periportal fibrosis score (0/1/2)	2/10/0	6/18/1	0.792	-0.043	0.798
Fibrosis stage (0/1/2/3)	0/2/7/3	0/6/10/9	0.656	0.032	0.850
NAS score (sum)				0.040	0.809
NAS score (<3/≥3)	1/13	0/25	0.167	0.217	0.185
SAF score (sum)				0.139	0.399
SAF activity (<2 either LI or B/>2 both LI & B)	6/8	3/22	**0.028**	0.351	**0.028**

Table 4.13: Effect of PX20606 on HCC size in C3H/He mice

	Tumour		Chi ^{2}	Spearman rho	
	<5mm n=9	≥5mm n=16		correlation	p value
Gross Phenotype Parameters					
Body weight				0.016	0.939
Liver weight				0.508	**0.008**
Liver/body weight ratio				0.654	**<0.001**
Visceral adipose tissue weight				0.069	0.739
Histopathology Parameters					
Steatosis grade (0/1/2/3)	0/4/3/2	0,2,12,2	0.149	0.185	0.377
Microvesicular Steatosis grade (0/1)	8/1	12/4	0.405	0.167	0.426
Hepatocellular ballooning score (0/1/2)	0/4/5	0/9/7	0.571	-0.113	0.589
Mallory Denk bodies (None/present)	1/8	2/14	0.918	-0.021	0.922
Megamitochondria (None/present)	5/4	10/6	0.734	-0.068	0.747
Lipogranuloma (None/present)	5/4	7/9	0.571	0.113	0.589
Lobular Inflammation score (0/1/2)	1/6/2	2/13/1	0.773	-0.17	0.416
Portal Inflammation score (0/1/2)	5/2/2	13/3/0	0.177	-0.316	0.124
Pigmented Kupffer cells (None/present)	4/5	3/13	0.170	0.275	0.184
Apoptotic cells (None/present)	5/4	9/7	0.973	-0.007	0.975
Perisinusoidal fibrosis score(0/1)	0/9	0/16	-	-	-
Periportal fibrosis score (0/1/2)	2/6/1	4/12/0	0.589	-0.118	0.574
Fibrosis stage (0/1/2/3)	2/5/2	4/5/7	0.505	0.13	0.537
NAS score (sum)				0.055	0.794
NAS score (<3/≥3)	0/9	0/16	-	-	-
SAF score (sum)				0.108	0.609
SAF activity (<2 either LI or B/>2 both LI & B)	1/8	2/14	0.918	-0.021	0.922

4.4.8 Quantification of hepatic p53 in the PX20606 treated animals

The expression of p53 was assessed by IHC in the periportal areas. In the control diet animals, there was an increase in p53 positive nuclei, in keeping with a similar pattern of increased DNA damage (γ-H2AX). In the mice fed the ALIOS diet, where baseline 'untreated' levels of p53 were much higher, PX20606 treatment significantly reduced the percentage of p53 positive nuclei (**Figure** 4.19). Hepatocyte % p53 positive nuclei did not correlate with any of the histological parameters nor with the other immunohistochemical markers (**Table** 4.14).

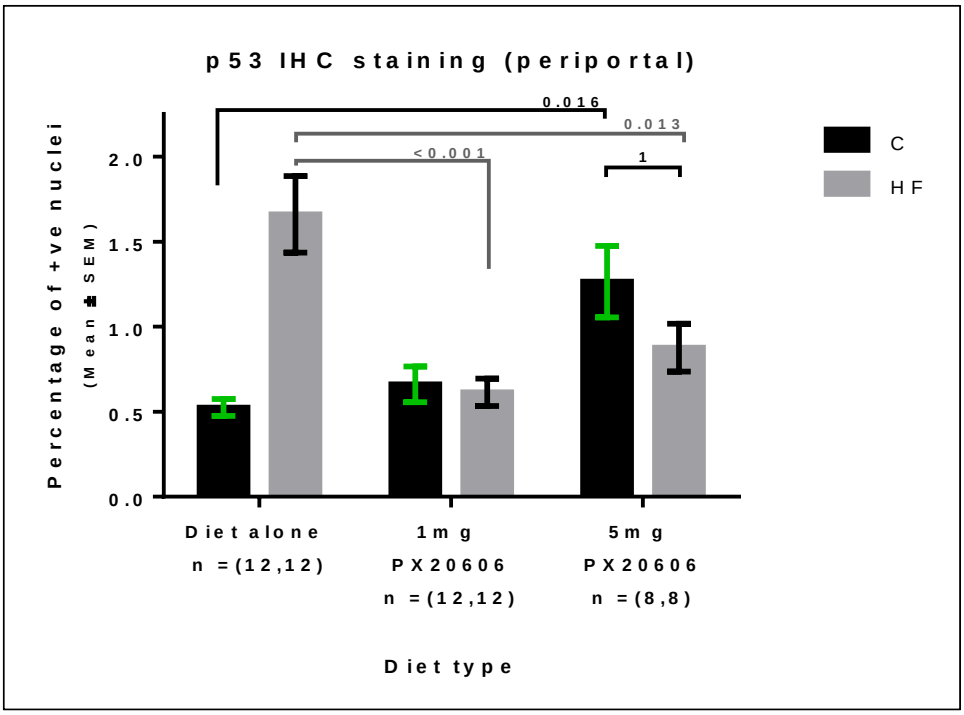

Figure 4.19: p53 immunohistochemical staining of the periportal area in the diet alone and the PX20606 treated groups. Y axis values represent Mean ± SE of the mean. The p value was determined by one-way ANOVA with multiple comparison correction.

Table 4.14: Associations of p53 immunohistochemical staining of the periportal area with the phenotypic parameters, liver histopathology, tumours and immunohistochemical markers in PX20606 treated groups.

	p53 IHC (% positive hepatocyte nuclei) (periportal)				
	Chi2			Spearman rho	
	<0.73%	≥0.73%	P value	correlation	P value
Gross Phenotype Parameters					
Body weight (Continuous variable)				-0.128	0.438
Liver weight (Continuous variable)				0.065	0.693
Visceral Adipose Tissue				0.004	0.980
Histopathology Parameters					
Steatosis grade (0/1/2/3)	4/8/7	5/10/5	0.767	0.008	0.692
Microvesicular Steatosis grade (0/1)	15/4	17/3	0.622	-0.166	0.312
Hepatocellular ballooning score (0/1/2)	4/7/8	0/10/10	0.127	0.012	0.943
Mallory Denk bodies (None/present)	7/12	2/18	**0.047**	0.103	0.534
Megamitochondria (None/present)	13/6	11/9	0.389	0.014	0.932
Lipogranuloma (None/present)	13/6	12/8	0.584	-0.038	0.818
Lobular Inflammation score (0/1/2/3)	2/16/1	4/14/2	0.640	-0.202	0.218
Portal Inflammation score (0/1/2)	11/5/3	15/4/1	0.436	-0.178	0.28
Pigmented Kupffer cells (None/present)	4/15	5/15	0.770	0.005	0.974
Apoptotic cells (None/present)	14/5	11/9	0.224	0.142	0.387
Perisinusoidal fibrosis score(0/1)	0/17	0/20	_	_	_
Periportal fibrosis score (0/1/2)	3/14/0	5/14/1	0.835	-0.072	0.673
Fibrosis stage (0/1/2/3)	0/3/7/7	0/5/10/5	0.695	-0.187	0.268
NAS score (<3, ≥3)	0/19	1/19	0.323	-0.173	0.292
SAF activity (<2 either LI or B/>2 both LI & B)	5/14	4/16	0.64	-0.13	0.431
Immunohistochemical markers					
γ-H2AX IHC periportal (median)	10/9	9/11	0.634	0.027	0.869
γ-H2AX IHC periportal (continuous)				-0.089	0.589
Ki67 IHC periportal (median)	10/9	9/11	0.634	0.046	0.783
Ki67 IHC periportal (continuous)				-0.047	0.775
Tumour development, progression and grade					
Tumour (no,yes)	9/10	5/15	0.146	0.133	0.420
Tumour number (continuous)				0.120	0.468
Tumour Number (1/ >1; n=25)	4/6	3/12	0.275	0.169	0.304
Tumour size (continuous)				0.139	0.406
Tumour size (<5mm/ ≥5mm) n=25	4/6	5/10	0.365	0.121	0.462
Tumour grade (1/2/3/4)	1/5/1/0	1/6/2/0	0.915	-0.059	0.827

4.5 Discussion

NAFLD and NAFLD derived HCC incidence is increasing around the world and a number of studies have and are being performed in an attempt to identify treatments that prevents the progression of NAFLD to NASH and fibrosis (280). The optimum treatment for NAFLD would be to lose weight and be less sedentary. However, the change in dietary habits and lifestyle around the world which have contributed to the increased prevalence of obesity are hard to change, with difficulty in compliance to lose weight and maintain weight loss. With major interest from the pharmaceutical industry, several compounds have been explored as treatments for NASH in phase II and III clinical trials (280). Our principal focus was to create a relevant pre-clinical animal model in which we could assess the impact of candidate therapies on NAFLD progression, but also on the development of HCC – albeit in a non-cirrhotic setting.

Inflammation and oxidative stress are both thought to be important in NAFLD progression. Vitamin E targets this axis, but its benefits were marginal in the clinical trial setting and its role limited because of its potential side effects. These include elevated cardiovascular risk as well as possibly an increased risk of developing other malignancies (prostatic cancer) (79, 280, 302, 303).

Bucillamine is a drug with antioxidant activity, with some immune modulating activity (289, 290), that is already used in clinical practice - for the treatment of rheumatoid arthritis in Japan. It is well tolerated and the side effects are already known (pruritus, mucocutaneous lesions and gastrointestinal symptoms) (287). Bucillamine is reported to have strong iron and copper chelating activity, which might partly explain its success in treating rheumatoid arthritis – where serum and synovial levels of iron and copper are reportedly high and contribute to tissue damage (288).

For these reasons – its modes of action and its safety - we selected it as an intervention to study in our model of NAFLD progression and HCC development. In chapter 3 data was presented showing that steatosis and NASH, associated with a significant increase in the DNA damage reflected by the increased γ-H2AX, were significantly correlated with HCC development. We hypothesised that bucillamine would inhibit oxidative stress-induced DNA damage, improve NASH, and prevent progression of fibrosis and the development of HCC.

In this chapter we have shown that bucillamine succeeded in improving the histological status of NAFLD in the treated animals – abolishing the cardinal feature of 'NASH', which is hepatocellular ballooning, as well as the presence of Mallory Denk bodies – which are also a

feature of steatohepatitis. Bucillamine also dramatically reduced both the % of hepatic nuclei positive for γ-H2AX and for p53, in keeping with it reducing DNA damage. These effects were consistent with previous reports of bucillamine effects in cardiovascular disease models (287). Also highly encouraging was that it significantly reduced liver fibrosis. Consequently both of the combination NAFLD scoring systems – the NAS and SAF scores – were significantly reduced by bucillamine treatment. These pre-clinical animal model data support bucillamine as a candidate treatment for NAFLD that would improve NASH and delay the development and progression of fibrosis.

Despite this remarkable effect, bucillamine did not succeed in preventing or reducing either the number or size of tumours in the treated mice. Notably, even though DNA damage was reduced, bucillamine treatment did not diminish lobular or portal inflammation. Neither did it impact the key features that were associated with HCC development – namely liver weight, grade of steatosis, the presence of lipogranulomas and hepatocyte proliferation. These data challenge the belief that it is inflammation-induced DNA damage that drives HCC development (273). DNA damage after bucillamine treatment was still evident, but at very low levels. An alternative hypothesis would be that steatosis related hepatocyte injury and a lipogranuloma centred inflammatory response creates a proliferative environment that encourages cancer development, even in the presence of minimal DNA damage. Further study of this model may provide new insight into the mechanisms underlying HCC development in NAFLD patients without cirrhosis. It also suggests that bucillamine – and possibly other antioxidants – would have little impact on the development of NAFLD related cancer in the absence of cirrhosis.

The other intervention studied was the FXR agonist, PX20606. The FXR bile acid axis is being explored as a NASH treatment strategy. Several FXR agonists are currently being assessed in clinical trials for NASH (82, 280). The FLINT study was a multicentre phase IIb clinical trial, in which treatment with obeticholic acid was seen to improve NASH (steatosis, lobular inflammation, fibrosis) scored histologically and this agent is now being assessed in a phase III clinical trial (82).

PX20606 is reportedly a more potent FXR agonist than obeticholic acid. In our study PX20606 was associated with an increase in the body weight of control animals, and increases in liver weight of both control and high fat fed animals. These observations were consistent with previous reports of increase in body weight (304) and therefore not unexpected in our PX20606

treated mice. Furthermore, there were encouraging reductions in serum triglycerides levels. Thereafter the data were not encouraging. There were some elevations in transaminases and ALP, suggesting damage to hepatocytes and biliary cells respectively. At a histological level, there was no improvement in any of the NAFLD criteria that were improved in human NAFLD in the FLINT study. On the contrary, there were increases in steatosis and inflammation. While numbers were small and some of these data were not consistent in control and ALIOS fed animals, there were also dose dependent increases in fibrosis stage, in both dietary groups, treated with PX20606. FXR is present in stellate cells in the liver and despite the previous studies that showed improvement of fibrosis after FXR activation (305), in our model activation of FXR was associated with cellular damage and increased fibrosis. The reasons for this are unknown, but given the contrary effects seen with other FXR agonists this should not necessarily be assumed to be a 'class effect'. Dosing in our animals was also uncertain, as PX20606 was administered in the diet rather than by gavage. It may be that the therapeutic window was small and liver injury was associated with overdose. Although the causes are uncertain, 19 deaths associated with incorrect dosing of obeticholic acid as a treatment for primary biliary cirrhosis (5mg per day rather than building up to a maximum does of 10mg twice weekly) have recently been reported in the USA (https://www.fda.gov/Drugs/DrugSafety/ucm576656.htm).

In regard to FXR and tumour development, our data were also disappointing. Previous studies have reported that Fxr-null mice developed spontaneous HCC by 12-16 months of age (306, 307). The hypothesis was that an FXR agonist would reduce cancer development. While there was no impact of PX20606 in the mice on the ALIOS diet, who nevertheless had greater numbers and size of tumours compared to controls, the PX20606 treated control animals actually developed more cancers. This effect in the control diet animals was also dose dependent and associated with some of the markers of increased injury, as well as being associated with increases in liver weight and proliferation, key features shown in Chapter 3 to be important indicators for the development of HCC in this dietary model.

Collectively, these data suggest that FXR agonists should be used cautiously in patients with NAFLD. PX20606 treatment not only worsened NASH, it also promoted cancer development in those animals with less severe disease.

In conclusion, while our interventional studies failed to prevent the development of HCC in our model, they have contributed to our mechanistic understanding. Furthermore, bucillamine may be worthy of exploration as a treatment to delay NAFLD progression to NASH and fibrosis.

Chapter 5: MDM2 inhibition for non-genotoxic activation of TP53 – a novel strategy for the treatment of liver cancer

5.1 Introduction

Hepatocellular carcinoma (HCC) is the 6th commonest cancer, and the second leading cause of cancer death worldwide (84). The cancer typically presents at an advanced stage when there are few therapeutic options (308). Coexistent chronic liver disease is present in the majority of patients and consequent to a combination of tumour resistance and liver dysfunction, cytotoxic therapies have a very limited role. The multikinase inhibitor sorafenib can prolong survival in carefully selected individuals, but only by a median of ten weeks (308, 309). Consequently the overall 5 year survival is less than 15% (310). There is a need to identify drivers of HCC progression which can be targeted safely in the liver microenvironment.

The *TP53* tumour suppressor gene, dubbed 'the guardian of the genome', is frequently inactivated in a wide range of common sporadic cancers. In its normal function it is a transcription factor that plays an important role in the cellular response to injury or DNA damage, regulating a host of downstream transcriptional targets that lead to cell cycle arrest and suppression of growth, facilitating repair or inducing apoptosis. *TP53* is one of the most commonly altered genes in HCC, mutated in about a third of cases according to The Cancer Genome Atlas (TCGA – accessed July 2017 (311, 312)). *TP53* mutation is often associated with aflatoxin B exposure and chronic viral infection with hepatitis-B (HBV) and hepatitis-C (HCV) (311, 312). The prevalence in the growing numbers of elderly patients with obesity associated non-alcoholic fatty liver disease (NAFLD) is uncertain, but possibly *TP53* mutation is less common (2/11 cases studied in TCGA) in this patient group. Notably, in many cases p53 may be dysfunctional owing to reduced expression or suppressed activity, rather than mutation. While attempts to restore p53 in the presence of mutation have as yet had little impact on cancer treatment, there is hope that in the large numbers of patients with dysfunctional wild type (WT) p53, restoring levels or function might have therapeutic benefit.

MDM2 is a transcriptional target of p53, responsible for regulating its effects via a negative feedback loop (174, 175, 313). MDM2 is an E3 ubiquitin ligase that binds to the N-terminal region of p53, prevents its activation and promotes its degradation. There is interest, therefore, in exploring the effects of restoring p53 activity and/or levels by inhibiting its negative regulation by MDM2. To date, a number of small molecule inhibitors of the p53-MDM2 interaction have been developed, which lead to stabilisation and release of p53 from the inhibitory effect of MDM2. As yet, none of these agents have entered clinical trials for patients with HCC. We have used three different MDM2 inhibitors to explore MDM2-p53 inhibition as a potential therapeutic strategy for patients with *TP53* WT HCC, namely, Nutlin-3 (216),

RG7388 (237) and HDM201 (238, 314-317), the last two of which are already in clinical trials in different cancer types.

5.2 Aims of the study in this chapter

To explore the effect of non-genotoxic activation of p53 through MDM2 inhibition by small molecule inhibitors in liver cancer cell lines.

5.3 Growth curves of different liver cancer cell lines

To select the optimum seeding densities of cells and the appropriate duration of treatment with the compounds of interest, growth curves were generated for a panel of liver cancer cell lines that were selected for different *TP53* status, since our interest was to examine specific p53-dependence. The *TP53* wild type ($p53^{WT}$) cell lines investigated were HepG2 and SK-Hep-1. The p53 defective cell lines used were Huh-7, Huh-1, SNU475 and SNU182 which are *TP53* mutant ($p53^{MUT}$) and Hep3B which is*TP53* null ($p53^{NULL}$) as shown in **Figure** 5.1and **Table** 5.1. The doubling time range for this panel was 30-48 hours apart from SNU475 and SNU182 with a longer doubling time of 60-72 hours. Accordingly the optimum length of treatment that aimed at covering at least two doubling times was 96 hours for all of the liver cancer cell lines apart from SNU182 and SNU475 that were treated for 120 hours, as they were growing slower than the rest of the cell lines.

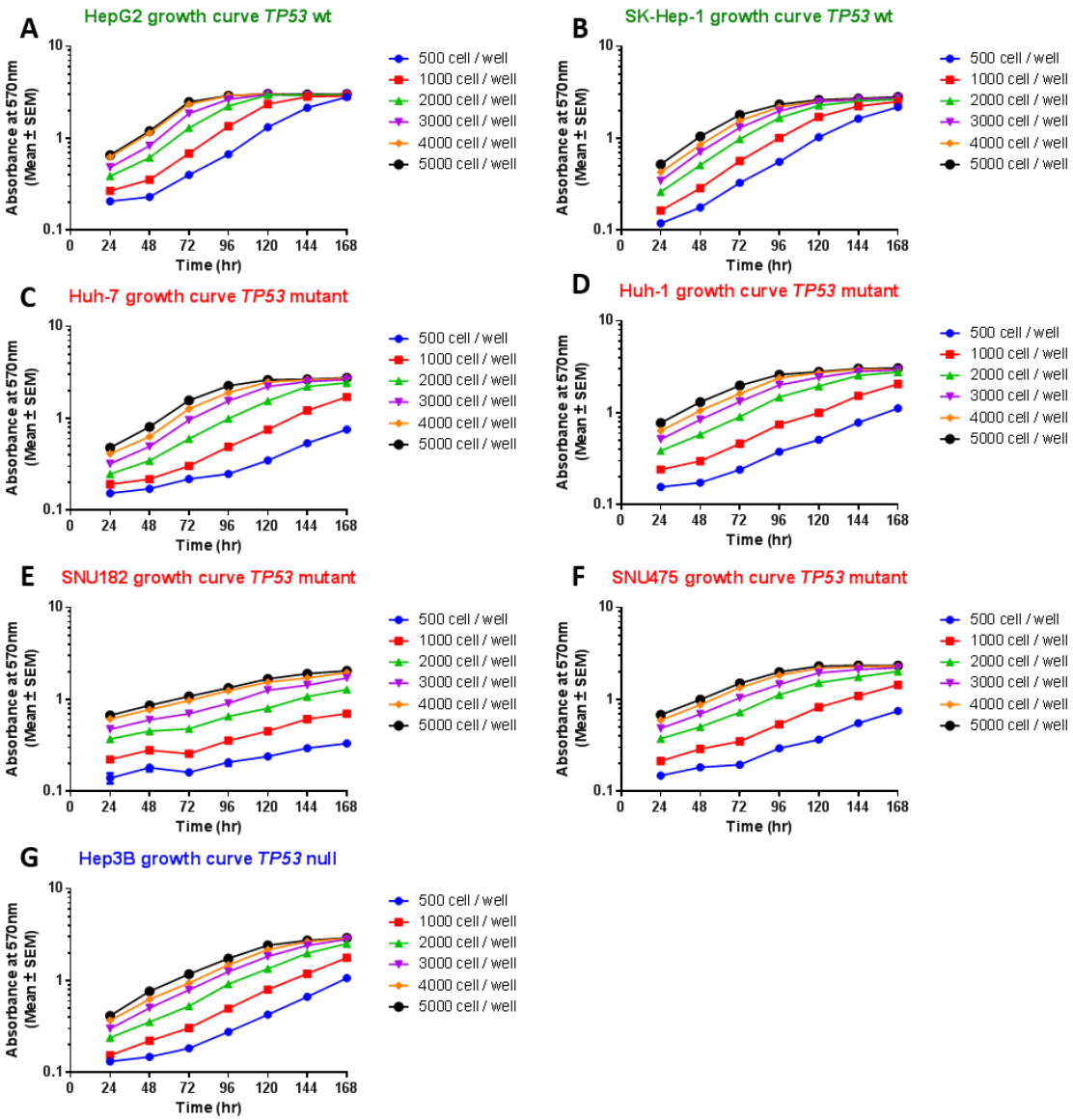

Figure 5.1: Growth curves of liver cancer cell lines with different *TP53* status. *TP53* WT cell lines (HepG2 (A) and SK-Hep-1 (B)), *TP53* Mutant (Huh-7 (C), Huh-1 (D), SNU182 (E), SNU475 (F) and *TP53* Null (Hep3B (G)). Six different densities (500 to 5000 cells per well) were seeded in 96 well plates for 7 days and then an SRB assay was carried out for each time point to monitor the culture growth.

5.4 MDM2 inhibitors repressed the proliferation and colony formation of liver cancer cell lines in a p53-dependent manner

5.4.1 Growth inhibition of $p53^{WT}$ liver cancer cell lines by MDM2 inhibitors

Cells were exposed to different concentrations (1nM to 10µM) of three structurally different small molecule inhibitors of MDM2, namely nutlin-3, RG7388 and HDM201. The effects on SRB assay determined growth are summarised in **Table** 5.1. Nutlin-3 was the least potent of the three MDM2 inhibitors with a GI_{50} of ~2µM; while RG7388 and HDM201 were more potent inhibitors compared to nutlin-3, with GI_{50} values in $p53^{WT}$ cell lines which were at the Nano molar range (≤ 30 nM for HepG2 and ≤ 60 nM for SK-Hep-1). HDM201 showed greater specificity at high doses – as evidenced by the absence of growth inhibition in cells with mutant or null *TP53* background. The impact of increasing doses of the three MDM2 inhibitors on proliferation for the different cell lines is shown in **Figure** 5.2, where no effect of HDM201 on *TP53* mutant or null cells were evident at doses up to 10 µM. The growth curves for determination of GI_{50} doses in HepG2 and SK-Hep-1 $p53^{WT}$ cells are shown in (**Figure** 5.2**; F and G**), with HDM201 GI_{50} doses of 30.7±0.2 nM in HepG2 cells and 60.1±1.5 nM for SK-Hep-1 cells (**Table** 5.1).

Table 5.1: GI_{50} concentrations of HDM201, RG7388 and Nutlin-3 for the panel of liver cancer cell lines of varying *TP53* status

Cell line	*TP53* status	HDM201 (nM)	RG7388 (nM)	Nutlin-3 (µM)
HepG2	**Wild type**	**30.7** ± 0.2	**18.2** ± 2.1	**1.99** ± 0.17
SK-Hep-1	**Wild type**	**60.1** ± 1.5	**27.1** ± 5.7	**2.25** ± 0.12
Huh-7	**Mutant** (Homozygous) c.659A>G; p.Y220C	**>10000**	**4770** ± 547	**21.1** ± 2.1
Hep3B	**Null** c.(del)	**>10000**	**5300** ± 890	**26.87** ± 1.4
SNU475	**Mutant** (Heterozygous) c.785G>A; p.G262D c.715A>G; p.N239D	**>10000**	**8462** ± 93	**>30**
SNU182	**Mutant** (Homozygous) c.644G>T; p.S215I	**>10000**	**5424** ± 241	**>30**
Huh-1	**Mutant** (Homozygous) c.329G>T; p.R110L	**>10000**	**8229** ± 220	**>30**

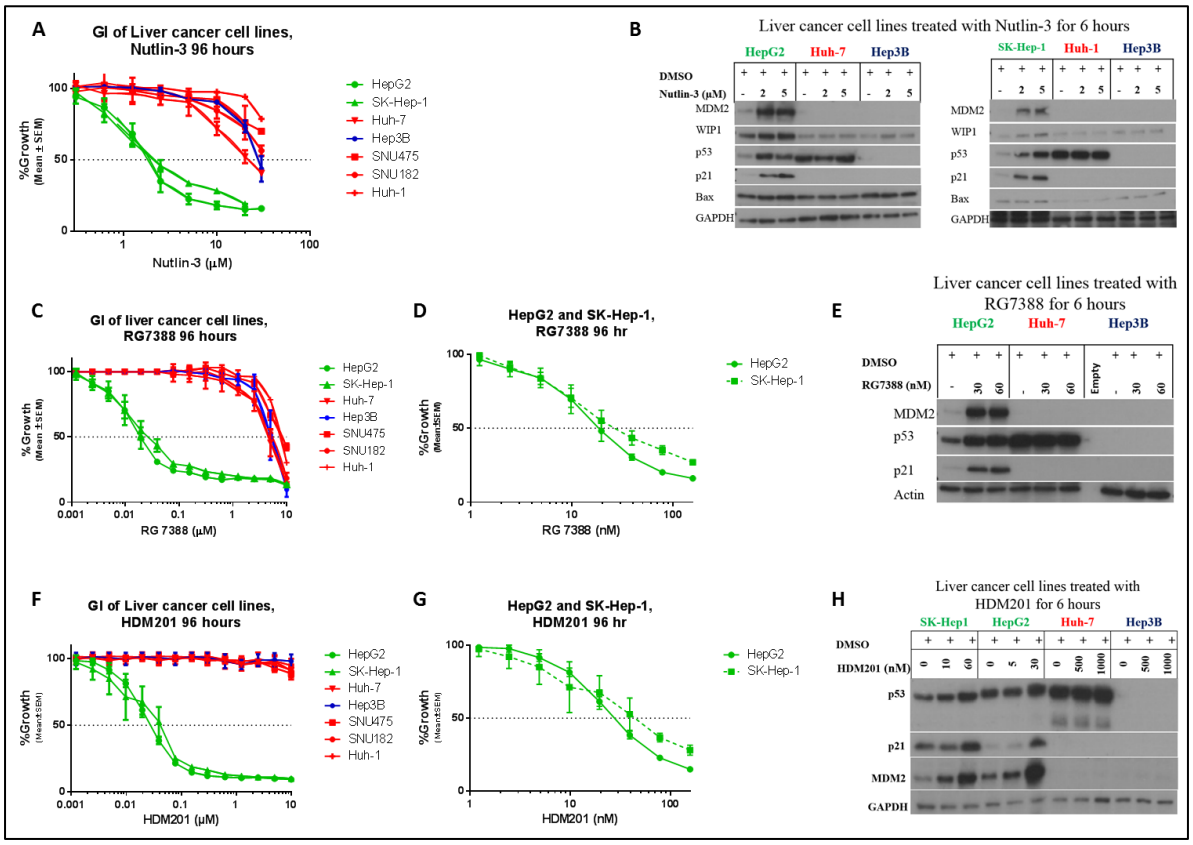

Figure 5.2: The effect of three MDM2 inhibitors on the growth of liver cancer cell lines. (A) SRB growth inhibition assay and (B) Immunoblotting of liver cancer cell lines with different *TP53* status with the effect at the protein level measured by western blotting after incubating with two different concentrations of Nutlin-3 (2 and 5 μM) for 6 hours. (C) and (D) shows the growth inhibitory effect of RG7388 on liver cancer cell lines with (D) showing the potent effect on $p53^{WT}$ cell lines (HepG2 and SK-Hep-1) treated with RG7388 at nanomolar concentrations (SRB); with the effect at the protein level measured by western blotting after incubating with 30 and 60 nM shown in (E). The growth inhibitory effect of HDM201 in shown in (F) and (G) and at the protein level by western blot (H). All the western blots show stabilization of p53 and induction of its downstream targets (p21 and MDM2) in $p53^{WT}$ cell lines but not in $p53^{MUT/NULL}$ cell lines. Green colour is used for $p53^{WT}$ cell lines, while red is used for $p53^{MUT}$ and blue for $p53^{NULL}$ cell lines. Error bars represent standard error of the mean of three independent repeats. GAPDH and β-Actin were used as loading controls in immunoblotting.

5.4.2 The effect of MDM2 inhibitors on p53 protein levels and of its downstream targets

The protein expression of p53 and of its downstream transcriptional targets in liver cancer cell lines was assessed by immunoblotting (**Figure** 5.2). In $p53^{WT}$ cell lines exposed to the three MDM2 inhibitors at their GI_{50} dose, stabilisation of p53 was clearly evident, associated with increase in the downstream transcriptional targets MDM2 and p21 after 6 hours (**Figure** 5.2**; B, E and H)**. In contrast, there were no changes in p53 levels nor of its downstream targets in either Huh-7 or Hep3B cells, even after exposure to 1000 nM of HDM201 (**Figure** 5.2**; H).**

Time course exposure of $p53^{WT}$ cell lines to increasing doses of MDM2 inhibitors over 24 hours showed a dose dependent stabilisation and increase in p53, manifested by the increase in level of both total p53 and p53 phosphorylated at the Serine 15 site ($pp53^{Ser15}$) (**Figure** 5.3) that was evident as early as two hours of exposure to the three MDM2 inhibitors; this increase was maintained at 6 and 24 hour time points.

A dose dependent increase of p53 downstream transcriptional targets (MDM2 and p21) by MDM2 inhibitors was observed and was most prominent after 6 hours (**Figure** 5.3). Interestingly, there was no evidence of cleaved PARP nor a change in PARP levels even after 24 hours in either of the $p53^{WT}$ cell lines (**Figure** 5.3**; C**).

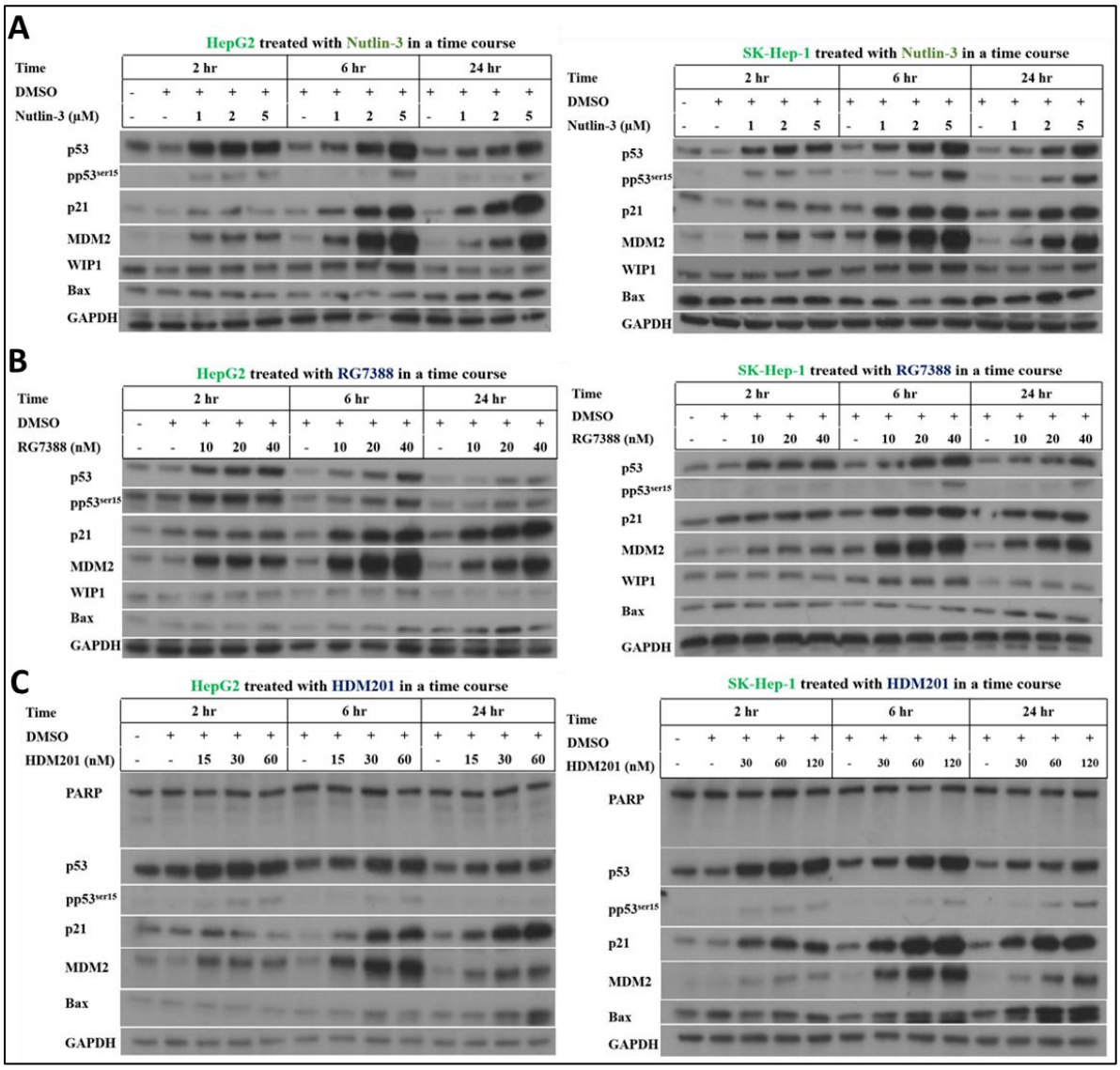

Figure 5.3: Time course treatment of p53^{WT} cell lines with ~ 0.5, 1 and 2X GI$_{50}$ doses of three different MDM2 inhibitors for 2, 6 and 24 hours. All MDM2 inhibitors (A) Nutlin-3, (B) RG7388 and (C) HDM201 showed a similar effect, represented by a dose-dependent stabilisation of p53 as early as 2 hours, that increased over 6 hours and subsequently decreased by 24 hours. The p53 downstream transcriptional target gene products (p21, MDM2 and WIP1) showed a similar dose-dependent increase that was most prominent after 6 hours. GAPDH was used as loading control.

5.4.3 Inhibition of colony formation ability of p53WT cell lines by MDM2 inhibitors

The Colony formation ability of a selected group of liver cancer cell lines (HepG2 and SK-hep-1 $p53^{WT}$, Huh-7-$p53^{MUT}$ and Hep3B-$p53^{NULL}$) was tested in response to a wide dose range of the three MDM2 inhibitors. Nutlin-3 (0.007- 5µM), RG7388 (1-80 nM) and HDM201 (5-300 nM) (**Figure** 5.4).

All the three tested MDM2 inhibitors showed inhibition of the ability of the $p53^{WT}$ cell lines to form colonies. The 50% clonogenic survival (LC_{50}) doses for Nutlin-3 were 0.96±0.1 µM and 2.32±0.05 µM for HepG2 & SK-Hep-1 respectively (**Figure** 5.4**; A**). The RG7388 LC_{50} doses were 8.59±0.38 nM and 37.15±9.43 nM for HepG2 & SK-Hep-1 respectively (**Figure** 5.4**; B**). HDM201 LC_{50} doses were 11.14±1.32 nM and 54.06±5.22 nM for HepG2 & SK-Hep-1 respectively (**Figure** 5.4**; C**). While there was no detectable reduction in colony forming ability for the $p53^{MUT/NULL}$ cell lines (Huh-7 and Hep3B) (**Figure** 5.4).

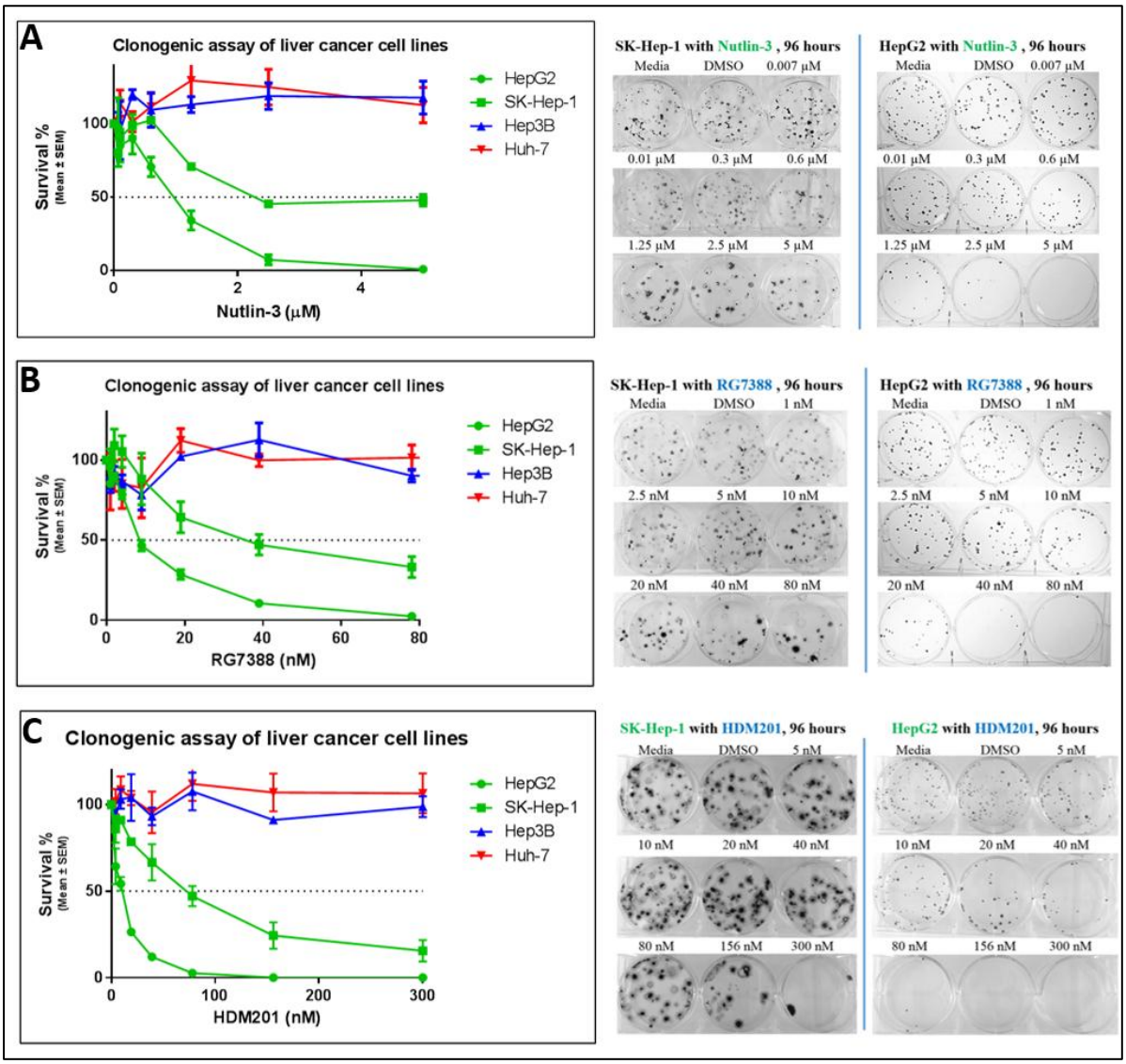

Figure 5.4: Clonogenic survival of liver cancer cell lines treated with three different MDM2 inhibitors for 96 hours. (A) nutlin-3 dose range (0.007- 5μM), (B) RG7388 (1-80 nM) and (C) HDM201 (5-300 nM) with representative pictures of the colonies to the right of each corresponding figure. Error bars represent the standard error of the mean of three independent repeats.

5.5 The effect of HDM201 on cell cycle distribution in liver cancer cell lines

Of the three MDM2 inhibitors, HDM201, in addition to being potent was more specific and showed growth inhibition of only $p53^{WT}$ cell lines with no detectable effect on $p53^{MUT/NULL}$ cell lines even at high doses (1 µM). This contrasted with RG7388, which had a growth inhibitory effect on $p53^{MUT/NULL}$ cell lines at high doses and could be the result of off-target effects. We therefore chose to take HDM201 forward for further characterisation of efficacy against liver cancer cell lines.

The growth and clonogenic inhibition properties of HDM201 were explored at a cell cycle level using FACS analysis, as shown for 24, 48 and 72-hour treatments in **Figure** 5.5. GI_{50} and 10 times the GI_{50} doses were used to study the effects of low and high doses of HDM201 compared to DMSO controls. In HepG2 cells there was a significant dose dependent increase in G0/G1 phase cells ($p=0.049$, for GI_{50} and $p=0.009$ for 10X GI_{50}), associated with similar stepwise decreases in S phase cells ($p=0.01$) **(Figure** 5.5**; A**). With SK-Hep-1 cells, an increase in G0/G1 was similarly evident at the lower GI_{50} dose ($p=0.07$), but at the higher dose there was a prominent and significant increase in cells at G2/M ($p=0.02$), with fewer cells at G0/G1 ($p=0.01$) and S phases ($p=0.04$) (**Figure** 5.5**; B**). The cell line and dose dependent changes observed at 24 hours persisted at 72 hours (**Figure** 5.5). There were no HDM201 induced cell cycle changes in p53 mutant or null cell lines (**Figure** 5.5**; C and D**).

Notably, there was no detectable Sub-G1 fraction induced by treatment with HDM201, suggesting no apoptotic cell death or disintegration for either cell line, even after 72 hours treatment (**Figure** 5.5).

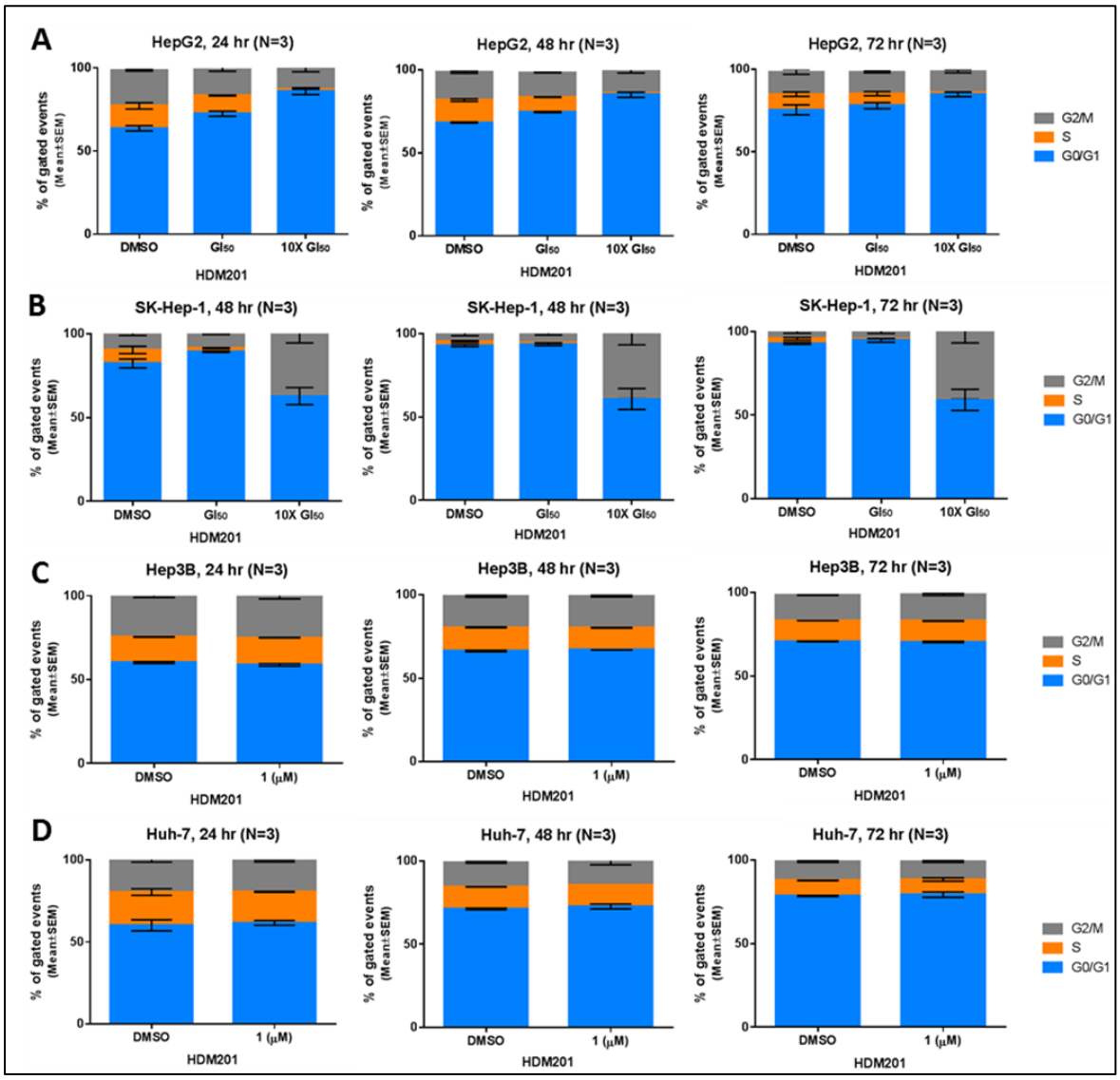

Figure 5.5: The effect of HDM201 on cell cycle distribution over 72 hours of treatment. (A) HepG2 cell cycle distribution, showing a dose dependent increase in G0/G1 phase with reduction in S phase. (B) SK-Hep-1 cell cycle distribution showing an increase in G0/G1 phase at the GI_{50} level but G0/G1 decreases and G2/M phase increases at 10X GI_{50}. (C) and (D) showing the cell cycle distribution of Huh-7 and Hep3B cells, with no obvious change in their cell cycle distribution, even at a high dose (1μM). Data represent mean ± standard error of the mean (SEM) of three independent repeats.

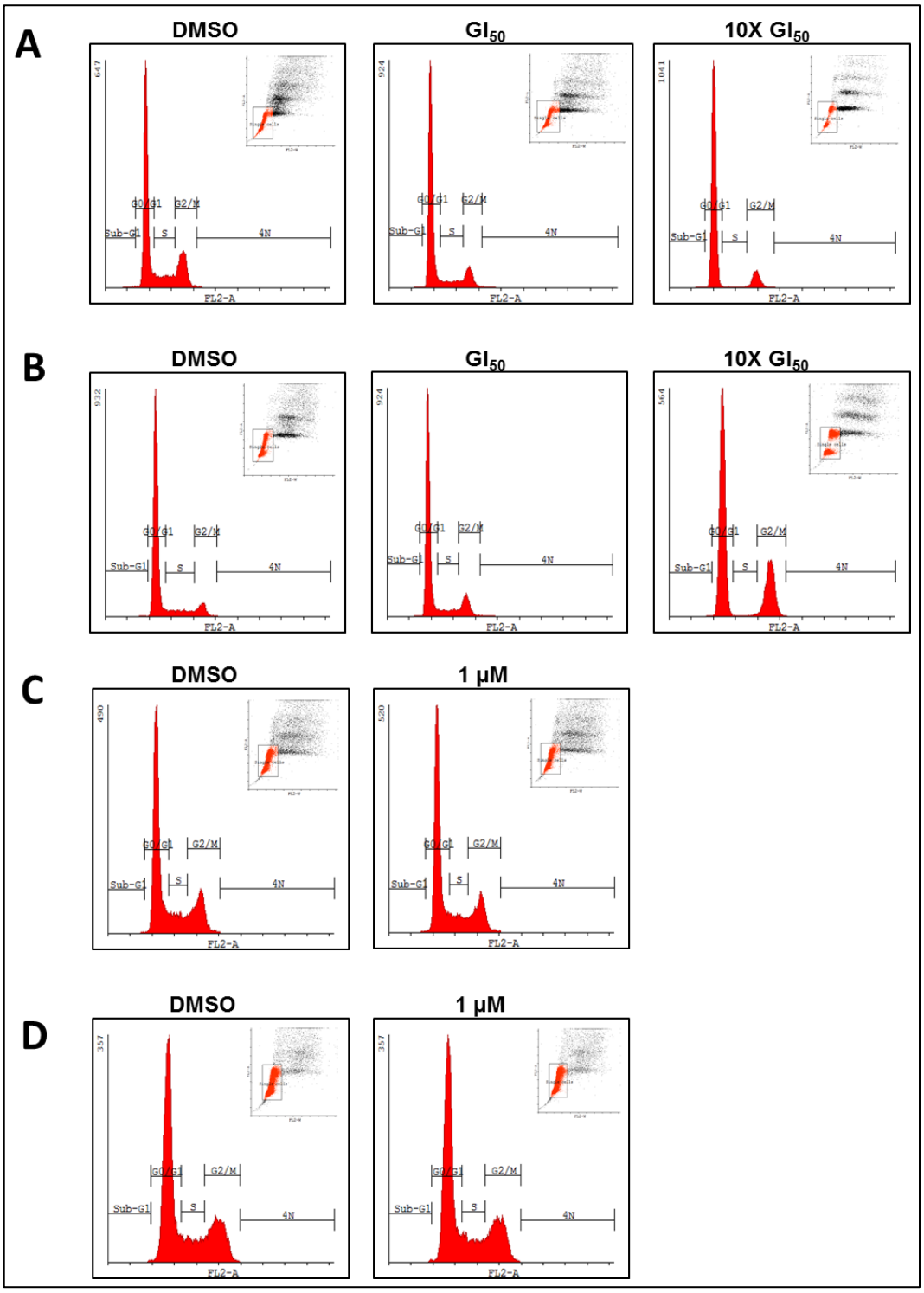

Figure 5.6: Cell cycle profile showing the effect of HDM201 on cell cycle distribution in liver cancer cell lines. (A) HepG2 cell cycle distribution, showing a dose-dependent increase in G0/G1 phase with reduction in S phase. (B) SK-Hep-1 cell cycle distribution showing an increase in G0/G1 phase at the GI_{50} level but G0/G1 decreases and G2/M phase increases at 10X GI_{50}. (C) and (D) showing the cell cycle distribution of Huh-7 and Hep3B cells, with no obvious change in their cell cycle distribution, even at a high dose (1µM).

5.6 HDM201 inhibits growth without inducing apoptosis and does not inhibit the metabolic activity in p53 ^{WT} liver cancer cell lines

It has been reported that MDM2 inhibitors induce apoptosis in $p53^{WT}$ cell lines *in vitro* and *in vivo* (318, 319). The absence of detectable change in sub-G1 phase on FACS and the lack of PARP cleavage on western blotting (**Figure** 5.3**; C**) argued against HDM201 induced apoptosis contributing to the reduced cell numbers and colonies. A caspase 3/7 assay following treatment with HDM201 supported this further, as neither $p53^{WT}$ nor $p53^{MUT/NULL}$ showed any detectable increase in caspase activity in HDM201 treated cells compared to the DMSO control even at high doses up to 10X the GI50 for $p53^{WT}$ cell lines and up to 1µM for $p53^{MUT/NULL}$ cell lines (**Figure** 5.7).

Furthermore, an XTT assay, assessing mitochondrial enzymatic activity, confirmed that the cells were still metabolically active. Even at high doses of HDM201 inducing growth suppression, the metabolic activity of treated cells was higher than that before starting treatment (**Figure** 5.8**; A and B**). The overall reductions in measured metabolic activities for different HDM201 concentrations can be explained by the growth inhibitory effect of the drug with induction of cell cycle arrest and hence fewer number of cells, but the reduced number of cells still retain metabolic activity.

$p53^{MUT/NULL}$ cells showed no detectable difference in the metabolic activity between any of the treatment conditions (**Figure** 5.8**; C and D**).

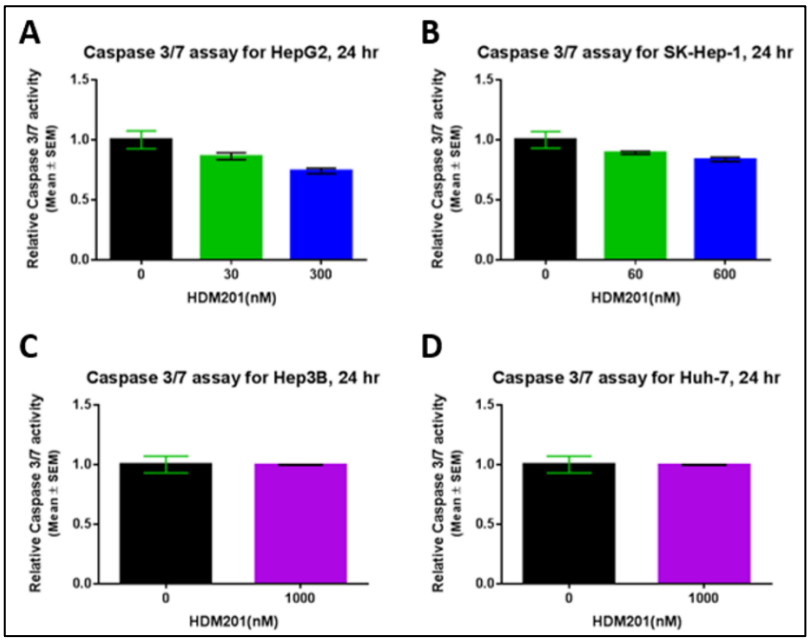

Figure 5.7: Apoptotic (caspase 3/7) activity after treatment with HDM201. There was no increase in the caspase 3/7 activity in $p53^{WT}$ cell lines treated with GI_{50} and 10X GI_{50} for 24hrs (A) and (B); nor in the $p53^{MUT/NULL}$ treated with a high dose (1µM) for 24 hours (C) and (D).

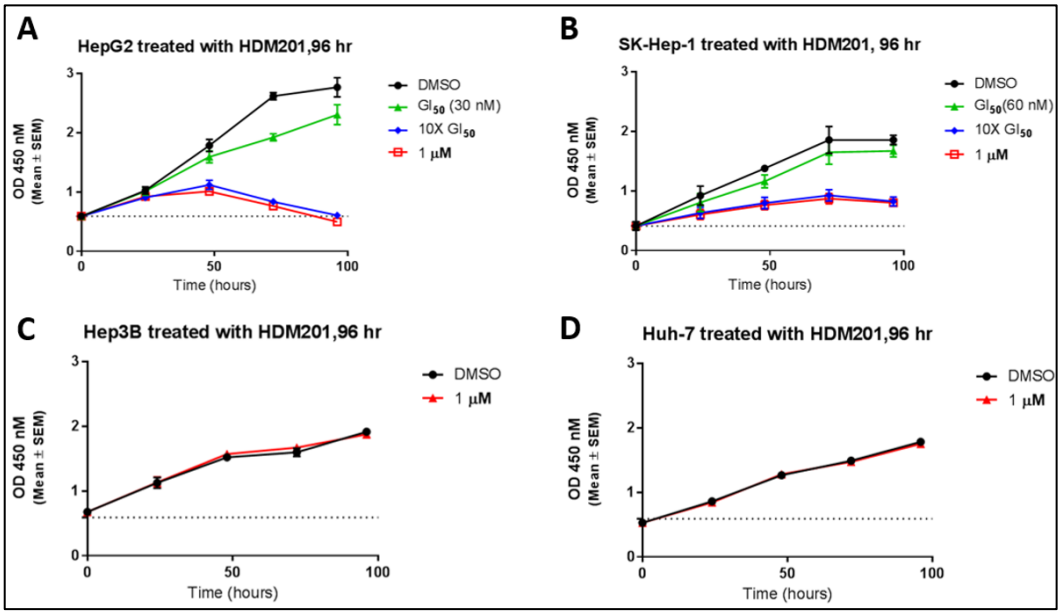

Figure 5.8: Metabolic activity measured by XTT assay in liver cancer cell lines after treatment with HDM201 for 96 hours. (A) and (B) HepG2 and SK-hep-1 $p53^{WT}$ cell lines treated with GI_{50} and 10X GI_{50} showed reduction in overall metabolic activity, reflecting the growth inhibition by treatment with HDM201, but the growth inhibited cells remained metabolically active during and at the end of the treatment period. (C) and (D) $p53^{MUT/NULL}$ treated with a high dose (1µM) for 96 hours and the treatment did not have any effect on either proliferation or the metabolic activity in those two cell lines. Y-axis represent the optical density (OD) at 450 nanometre wavelength. Data represent mean± standard error of the mean (SEM) of three independent repeats.

5.7 HDM201 increases the transcription of p53 downstream transcriptional targets

Having confirmed HDM201 stabilisation of p53, with increases in its protein level and that of downstream transcriptional target gene protein products by western blot, we explored the regulation of a broader panel of transcriptionally regulated p53 target genes at the mRNA level by qRT-PCR, as shown in **Figure** 5.9. The genes included negative regulators of p53 (*PPM1D* and *MDM2*), cell cycle arrest genes (*CDKN1A* and *GADD45A*) and pro-apoptotic genes involved in both the intrinsic (*BAX* and *PUMA* (*BBC3*)) and extrinsic pathways (*FAS* and *TNFBSF10B*).

In $p53^{WT}$ cell lines there was a significant dose dependent increase in expression of all the downstream transcriptional targets of p53 at 6 hours, apart from *BAX* in HepG2. Notably, the highest increases (~ 4 fold for the GI_{50} and ~ 10 folds for $10XGI_{50}$) were for *CDKN1A* and *MDM2* at 6 hours (p= 0.01, 0.008 respectively for HepG2; p= <0.0001, 0.002 respectively for SK-Hep-1) (**Figure** 5.9**; A and B**). The HDM201 induced changes in expression of pro-apoptotic genes were much more modest than those involved in negative feedback control and cell cycle arrest. The patterns of expression were similar after 24 hours, although increases in the expression of *CDKN1A* and *MDM2* were even more marked (~4 fold for the GI_{50} and >20 folds for $10XGI_{50}$) (**Figure** 5.9**; A and B**). There were no effects on expression of these target genes in $p53^{MUT/NULL}$ cell lines, even after exposure to very high doses of HDM201 (**Figure** 5.9**; C and D**).

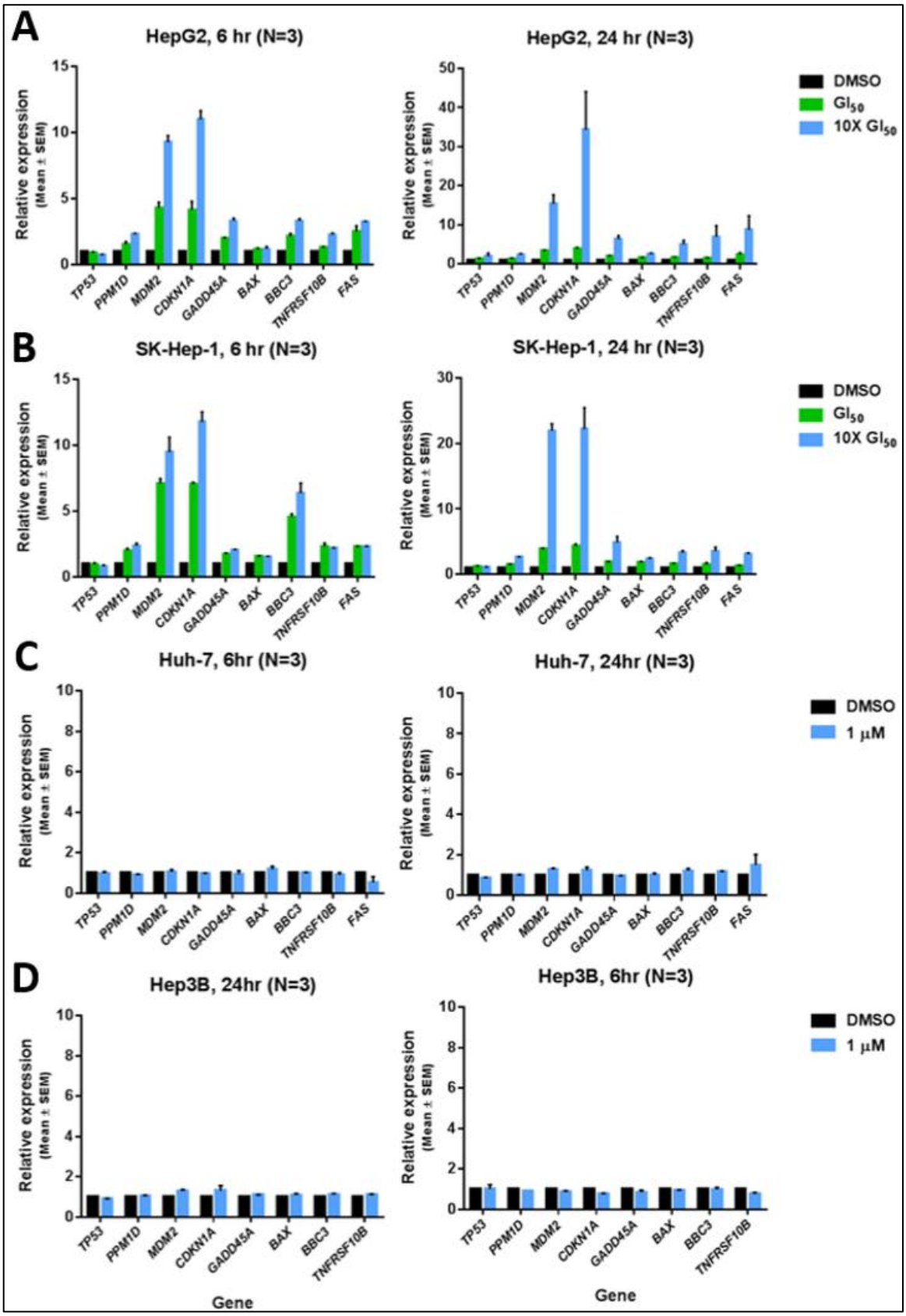

Figure 5.9: qRT-PCR measurement of mRNA expression for *TP53* and downstream transcriptional targets of p53 in response to HDM201. Different doses of HDM201 were used (GI_{50} and 10X GI_{50} for $p53^{WT}$ and 1µM for $p53^{MUT/NULL}$) for 6 and 24 hour time points. The expression was relative to DMSO control and *GAPDH* reference gene in (A) HepG2, (B) SK-Hep-1, (C) Huh-7 and (D) Hep3B. Data represent mean± standard error of the mean (SEM) of three independent repeats.

5.8 HDM201 induced cell cycle arrest was associated with induction of senescence

Although there was no evidence for HDM201 inducing apoptosis, and cellular metabolic activity was retained, the arrested state of treated cells was not always reversible, particularly at 10X GI_{50} dose, as shown by the time lapse images in **Figure** 5.10. Although confluency was reached 12 days after drug removal at the $G1_{50}$ dose, at the higher dose scant recovery was evident, with many cells viable but not dividing (**Figure** 5.10**; A**). In SK-Hep-1 the cells underwent morphological changes with a several-fold increase in size compared to the DMSO control. Although at the GI_{50} dose, confluency was reached 12 days after drug removal, at the higher dose the morphological changes persisted, resulting in the formation of giant cells (**Figure** 5.10**; B**). We therefore investigated the possible induction of senescence. $p53^{WT}$ cells incubated with HDM201 at GI_{50} and 10X GI_{50} for 96 hours were subsequently stained with SA-β-Gal, which reports β-Galactosidase accumulation as a green-blue cytoplasmic staining and is a widely used marker of cellular senescence (320, 321). Both $p53^{WT}$ cell lines showed positive staining for SA-β-Gal and the intensity of staining and the number of positively stained cells was proportionate to the dose of the HDM201 (**Figure** 5.11).

Cellular senescence can occur during both G1 and G2 arrest (185, 322, 323). In the $p53^{WT}$ liver cancer cell studied, as reported above, G1 or G2 arrest after 96 hours was associated with marked induction of p21, a p53 downstream target linked with both cell cycle arrest and the induction of senescence.

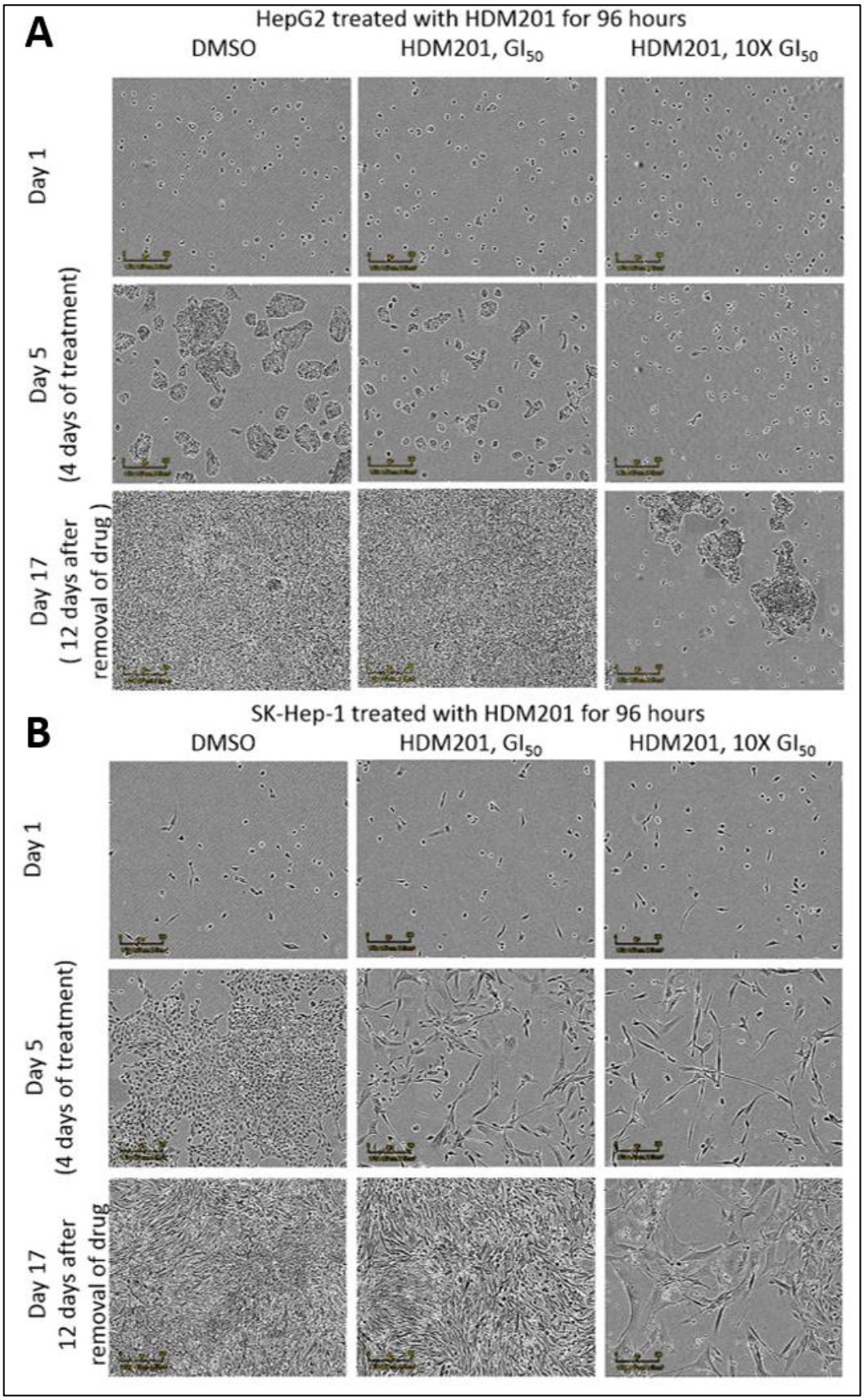

Figure 5.10: Incucyte experiment showing the effect of HDM201 on the cell morphology of p53^{WT} cell lines (HepG2 and SK-Hep-1) after treatment with HDM201 for 96 hours. The drug was removed after 96hrs and replaced with media and the cells left to grow. Sequential images of the cultures were taken every 6 hours. (A) HepG2 and (B) SK-Hep-1. Magnification power 10X, Scale bar = 300 µM.

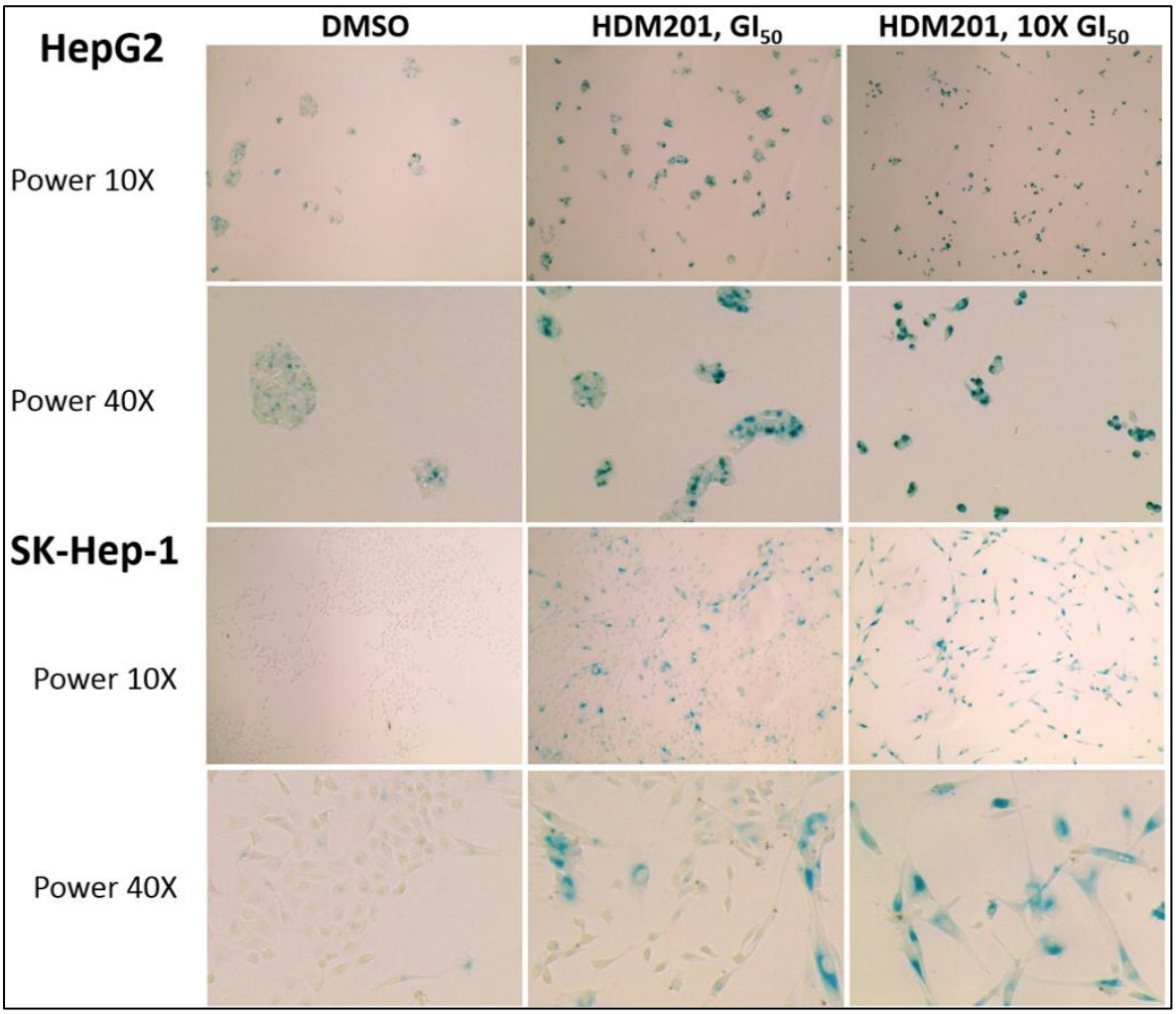

Figure 5.11: HDM201 induces senescence in p53^{WT} liver cancer cell lines. SA-β-Gal staining of HepG2 and SK-Hep-1 after treatment with DMSO control, or GI_{50} and 10X GI_{50} of HDM201 for 96 hours, imaged at low power (10X) and high power (40X). Positive cytoplasmic staining (blue-green) is evident in a few cells in the DMSO control, but the number of positive stained cells and the intensity of staining increases with the dose of HDM201 to include nearly all the cells that are treated with the high dose. SK-Hep-1, in addition to blue-green staining, showed a change in the morphology of cells at high dose of HDM201, with cells becoming larger in size compared to DMSO control.

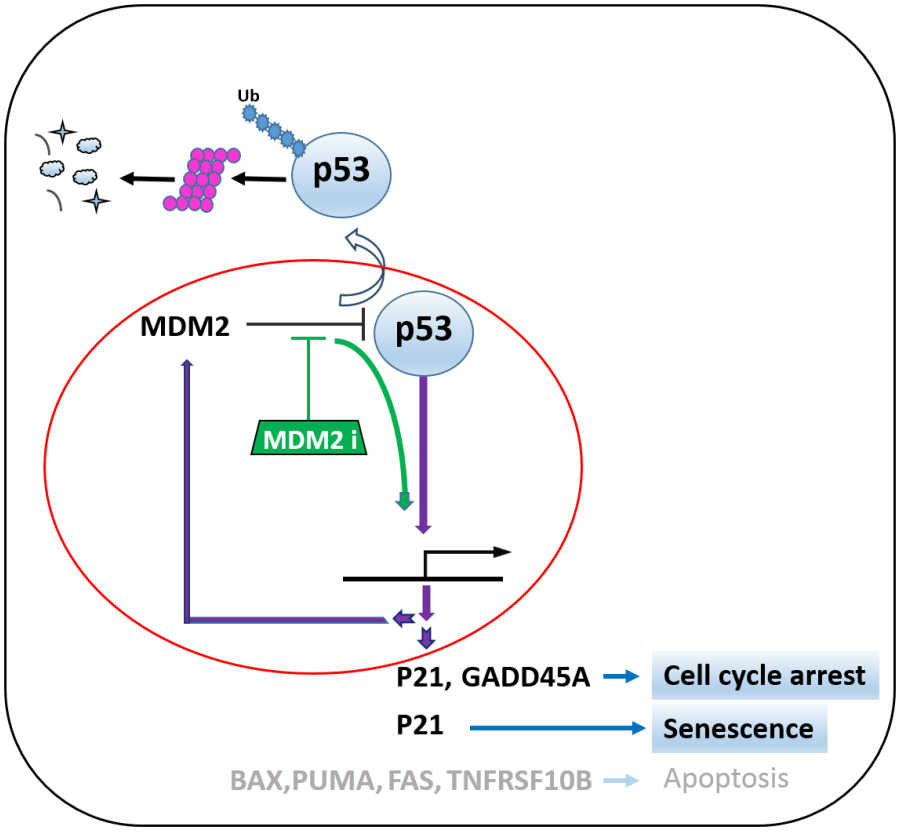

Figure 5.12: Schematic summary representing the p53 pathway and the effect of MDM2 inhibition, linking p53 activation to downstream transcriptional targets that induce the dominant response of cell cycle arrest and senescence, and minimal activation of pro-apoptotic genes.

5.9 HDM201 inhibits the growth of liver cancer xenografts *in vivo*

After confirming that HDM201 induced growth inhibition, cell cycle arrest and senescence of $p53^{WT}$ cell lines (HepG2 and SK-Hep-1), we moved on to test whether this growth inhibitory effect can be replicated *in vivo*. Bioware® Brite HepG2-Red-Fluc (HepG2-Luc) luciferase transfected cells were purchased from (Perkin Elmer, USA) to be used in an *in vivo* xenograft model. In principle, using this cell line provided the ability to estimate the xenograft tumour size by two methods, the standard tumour measurement using Vernier calipers and the use of an IVIS imaging system.

5.9.1 HepG2-Luc responds to MDM2 inhibitors in the same pattern as HepG2

The parental cell line that HepG2-Luc was derived from is a HepG2 cell line that was purchased from ATCC (HB8065). Parental HepG2 was stably transfected with firefly luciferin gene from *Luciola Italica* (Red-Fluc) using the Red-FLuc-Puro third generation lentivirus vehicle in order to express luciferase enzyme and hence generate luminescence in the presence of D-Luciferin as a substrate.

Before starting the xenograft study, we had to ensure that HepG2-Luc cells responded to HDM201 compound in the same way that the parental HepG2 cell line; therefore, we challenged this cell line with the three MDM2 inhibitors in parallel with the parental HepG2 cell line. The HepG2-Luc cells responded to all three MDM2 inhibitors in the same way as the parental HepG2 cell line (**Figure** 5.13). Colony formation was inhibited by HDM201 as for the HepG2 cell line (**Figure** 5.13**; D**). The GI_{50} and LC_{50} doses for HepG2-Luc compared to the parental HepG2 are shown in **Table** 5.2.

Further to this, the caspase 3/7 activity and the mitochondrial activity were assessed in HepG2-Luc in parallel to the parental HepG2 cell line, and again the results were very similar to the parental cell line (**Figure** 5.14). The same transcriptional profile changes were also shown by qRT-PCR assays (**Figure** 5.15).

Table 5.2: The GI_{50} and LC_{50} for HepG2-Luc versus parental HepG2 cell lines for the three MDM2 inhibitors

	GI_{50}			LC_{50}
Cell line	**Nutlin-3 (µM)**	**RG7388 (µM)**	**HDM201 (µM)**	**HDM201 (µM)**
HepG2	**1.71**± 0.08	**0.015** ± 0.001	**0.029** ± 0.001	**0.010**± 0.001
HepG2-Luc	**1.44**± 0.07	**0.012** ± 0.001	**0.027** ± 0.002	**0.009**± 0.001

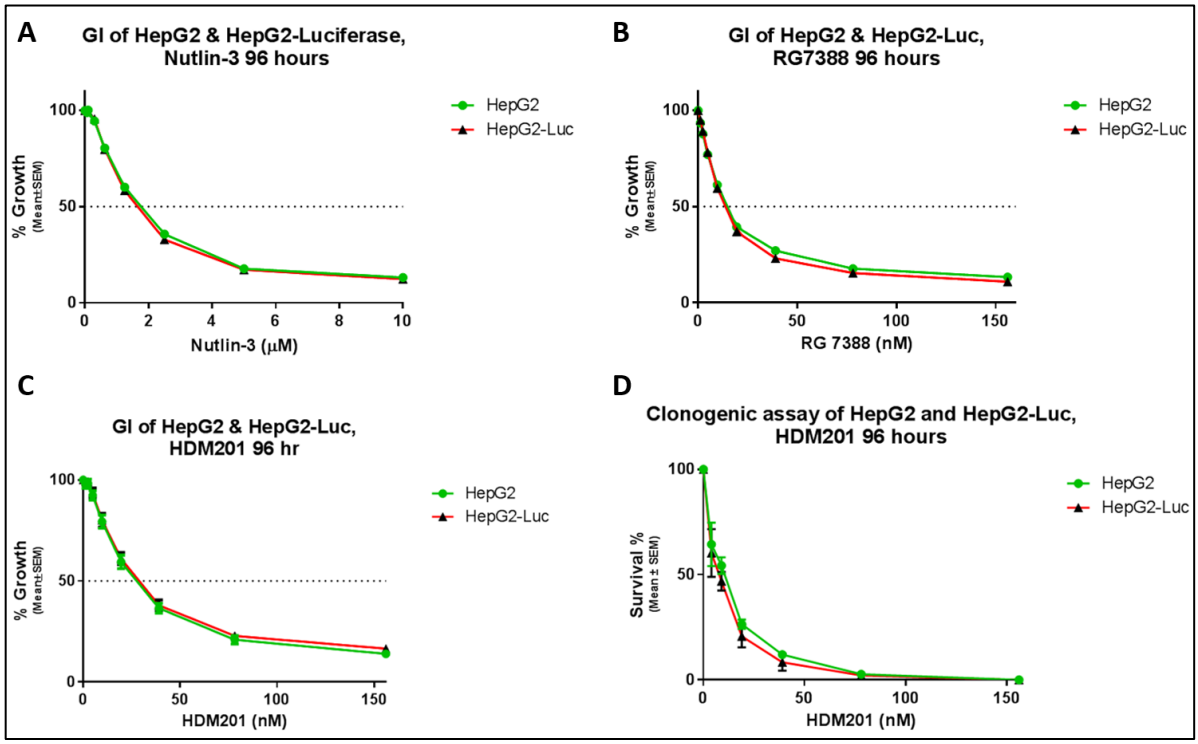

Figure 5.13: Growth inhibition and clonogenic survival of HepG2 and HepG2-Luc cell lines. (A), (B) and (C) are SRB growth inhibition assay results for HepG2 versus HepG2-Luc after treatment with Nutlin-3, RG7388 and HDM201 respectively for 96 hours. (D) Clonogenic survival of HepG2 and HepG2-Luc with a dose range of 5-300 nM of HDM201 treatment for 96 hours. Error bars represent standard error of the mean of three independent repeats.

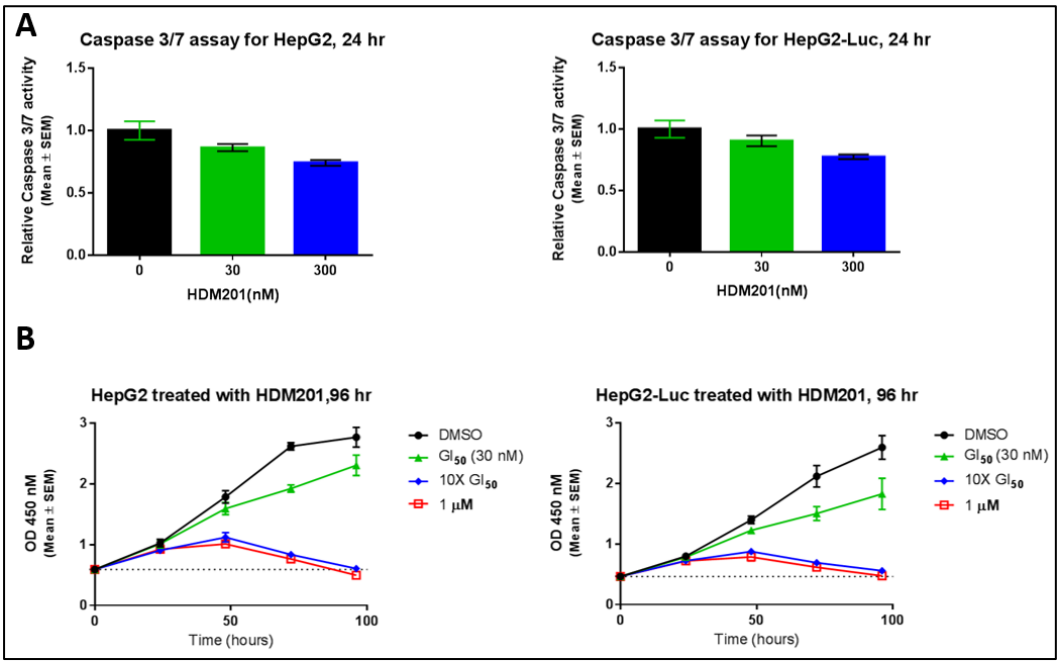

Figure 5.14: Caspase 3/7 activity and XTT assay for HepG2 and HepG2-Luc cells. (A) Caspase 3/7 assay of HepG2 (left) and HepG2-Luc (right) after exposure to GI_{50} and 10X GI_{50} of HDM201 for 24 hours. (B) XTT assay measuring the mitochondrial metabolic activity of HepG2 (left) and HepG2-Luc (right) after exposure to GI_{50} and 10X GI_{50} and 1µM of HDM201 for 96 hours. Error bars represent standard error of the mean of three independent repeats.

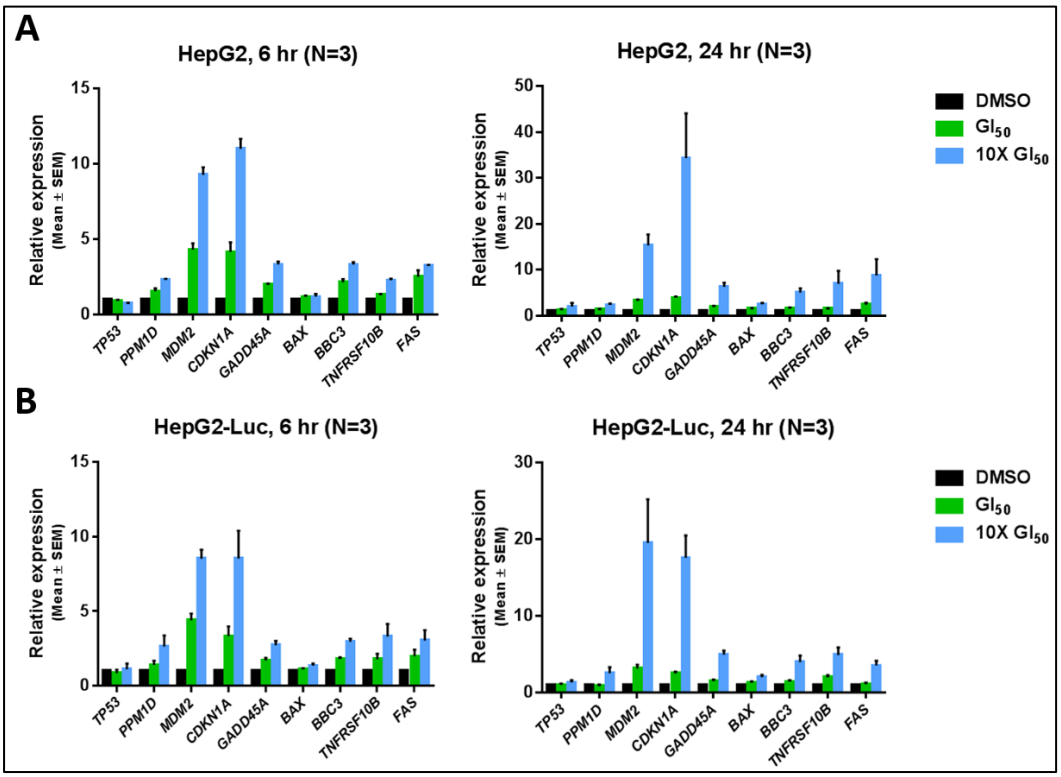

Figure 5.15: mRNA expression of *TP53* and p53 downstream transcriptional targets by qRT-PCR in HepG2 and HepG2-Luc in response to HDM201. HepG2 (A) and HepG2-Luc (B) were exposed to HDM201 at a GI_{50} and 10X GI_{50} for 6 and 24-hour time points to compare the changes in levels of expression between the parental cell line (HepG2) and HepG2-Luc. The expression was relative to DMSO control and *GAPDH* used as a reference gene. Error bars represent standard error of the mean of three independent repeats.

5.9.2 Establishing a xenograft model with HepG2-Luc in immunocompromised mice

Preliminary studies done by other PhD students showed that there was variability in HepG2 xenograft growth in CD1 nude mice. Therefore, we decided to test the growth of HepG2-Luc xenografts in two different strains of immunocompromised mice, NOD SCID gamma (NSG) (Bred in house) and CD1 nude mice (Charles River, UK). CD1 nude mice were developed from the transfer of the nude gene from Crl:NU-Foxn1^{nu} to a CD-1 mouse through a series of crosses and backcrosses at Charles River laboratories in 1979. They lack a thymus gland and hence are unable to produce T-cells. They therefore exhibit T-cell immunodeficiency. NOD SCID gamma mice (NSG) mice are further immunocompromised by lacking T, B and natural killer (NK) cells (324).

After injecting HepG2-Luc cells in the right flank of each mouse of both mice strains (female), they were left to grow and monitored closely. Tumour volume was determined by standard external calliper measurement of the greatest longitudinal diameter (length) and the greatest transverse diameter (width). Then tumour volume was calculated based on calliper measurements by the following modified ellipsoidal formula (325, 326):

$$Tumour\ volume = ½\ (Length \times Width^2)$$

Growth of HepG2-Luc xenografts NSG was observed in all the 5 injected mice compared to only two out of five xenografts in CD-1 nude mice, and these two tumours grew much more slowly (**Figure** 5.16). Therefore we decided to use the NSG mice to test the effect of HDM201 on HepG2-Luc *in vivo*.

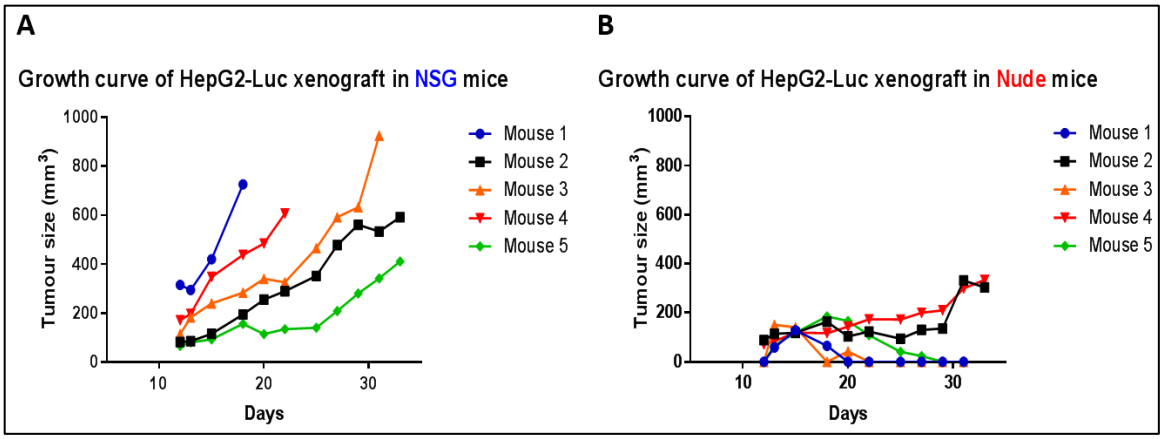

Figure 5.16: Growth curve of HepG2-Luc xenografts in NSG and CD1 nude mice. (A) NSG mice (n=5) showing growth of HepG2-Luc xenografts in all the injected mice. (B) CD1 nude mice showing failure of growth of the HepG2-Luc xenografts in 3 out of 5 injected mice.

5.9.3 The effect of HDM201 at a dose of 25 mg/kg/day for 7 days on HepG2-Luc xenografts

When the HepG2-Luc xenografts reached dimensions of 5x5 mm on the flanks of NSG mice, the mice were alternately allocated into one of two groups of (10) control and (10) treated. Each group consisted of two cages with 5 mice per cage. The treated group received HDM201 once a day by oral gavage at a dose of 25 mg/kg/day for 7 days, while the control group received the control vehicle by the same route (5% ethanol alcohol in 1% HydroxyPropyl Methyl Cellulose (HPMC)) (**Figure** 5.17**; A**). This dose frequency was similar to Regimen 2C used in phase I clinical trials for different tumours (single daily dose for one week in a 4 week cycle) (314). The drug was well tolerated with no signs of toxicity or appreciable body weight loss (**Figure** 5.17**; B**).

HDM201 at 25mg/kg/day resulted in a significant inhibition of tumour growth, which was most prominent on day 12 (p=0.0004) (**Figure** 5.17**; A, C, D and E**). The survival time was defined by the time in days that the tumour took to reach 4 times the starting volume, which was increased from 8.4 days in the control group to 15.26 days in the treated group (p=0.0078) (**Figure** 5.17**; F**).

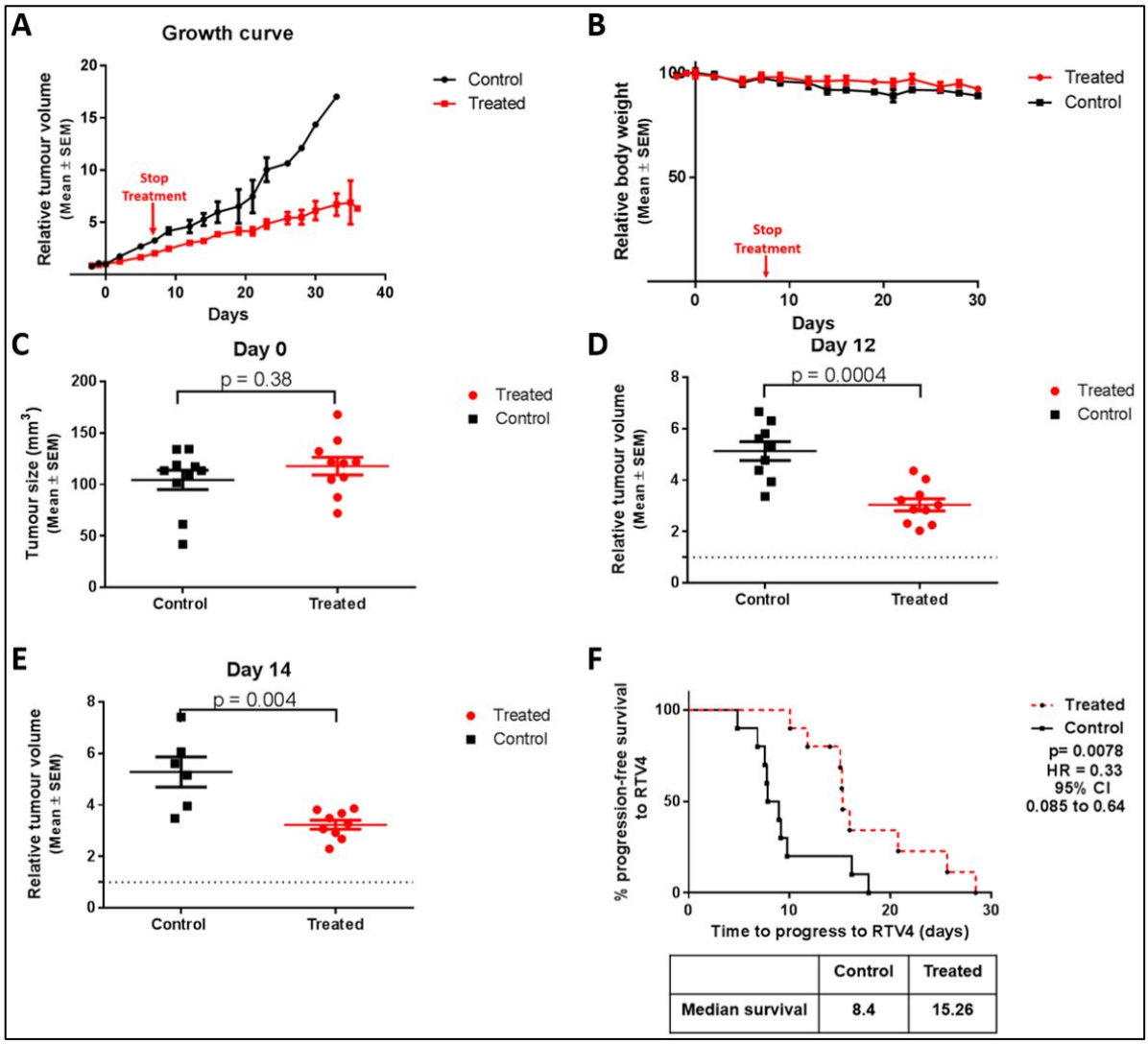

Figure 5.17: The effect of oral 25 mg/kg/day HDM201 (single daily dose) on HepG2-Luc xenografts in NSG mice. (A) the growth curve of the xenografts is represented by the mean of the relative tumour volume (RTV) of each tumour to its starting volume before commencing treatment on day 0 and stopping it on day 7 (red arrow). (B) The effect of oral HDM201 on the body weight of NSG mice bearing the HepG2-Luc xenografts. (C) The volume of xenograft tumours (mm^3) in both groups (control and treated) on day 0 before starting treatment with HDM201. (D) and (E) represent the RTV difference between the control and treated groups on day 12 and day 14 with p values on each graph. (F) Survival reflected by the time taken by each xenograft to reach 4 times the starting volume with the median survival of each group in a table below the graph. The p value was calculated by Log-Rank test, HR = hazard ratio, CI= confidence interval. Error bars represent the standard error of the mean.

In vivo bioluminescence imaging by IVIS scanning was carried out in parallel as an additional method of monitoring tumour growth and estimating response to the intervention (327-329). Bioluminescence imaging is based on detection of light emitted from mice and this light is generated from luciferase-luciferin reaction in the cells; in our study it was the HepG2-Luc xenograft cells, and it has been used in different animal models for neoplasia. Unfortunately the IVIS data obtained did not match the caliper measurements data (**Figure** 5.19**; A and B**) and some of the tumours despite clearly and visibly growing exponentially did not produce a bioluminescence signal (**Figure** 5.19**; A**) and there was fluctuation of the detected signals over several time points that led to a zigzag pattern of the plotted data that did not match the growth of the tumours obtained by caliper measurement (**Figure** 5.19**; A and B**). Similar problems with bioluminescence imaging signals by IVIS scanning have been previously reported (330, 331); this can be due to several factors including improper absorption of luciferin intraperitoneally, improper delivery of luciferin into tumour cells due to variability in the blood supply to the xenograft and intratumoural haemorrhage and necrosis. These issues cast doubt on the usefulness of the IVIS imaging and we decided to stop further use of the IVIS scanning in this experiment and the experiment to follow.

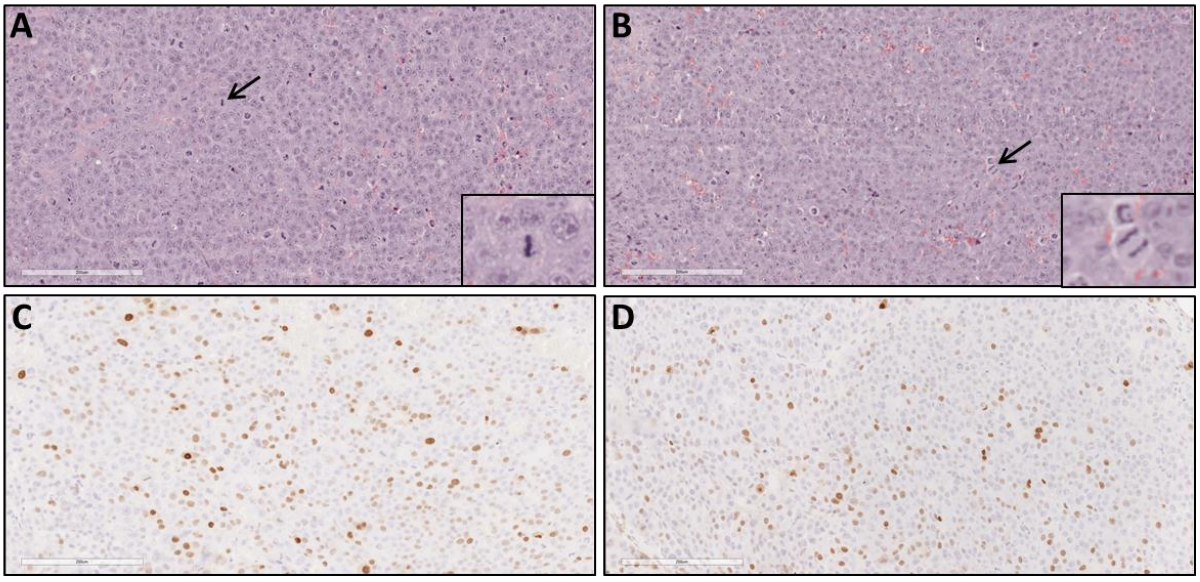

Figure 5.18: HepG2-Luc xenografts tissue sections with H&E and p21 immunohistochemical staining. (A) and (B) are H&E stained sections of a control and treated mice xenografts respectively and both are showing mitotic index (arrow and zoomed image). Immunohistochemical staining for p21 in the xenografts is shown in (C) control and (D) treated with no significant difference in the number of p21-positively stained nuclei due to the fact that these were end-point xenografts and were not taken after stopping the treatment.

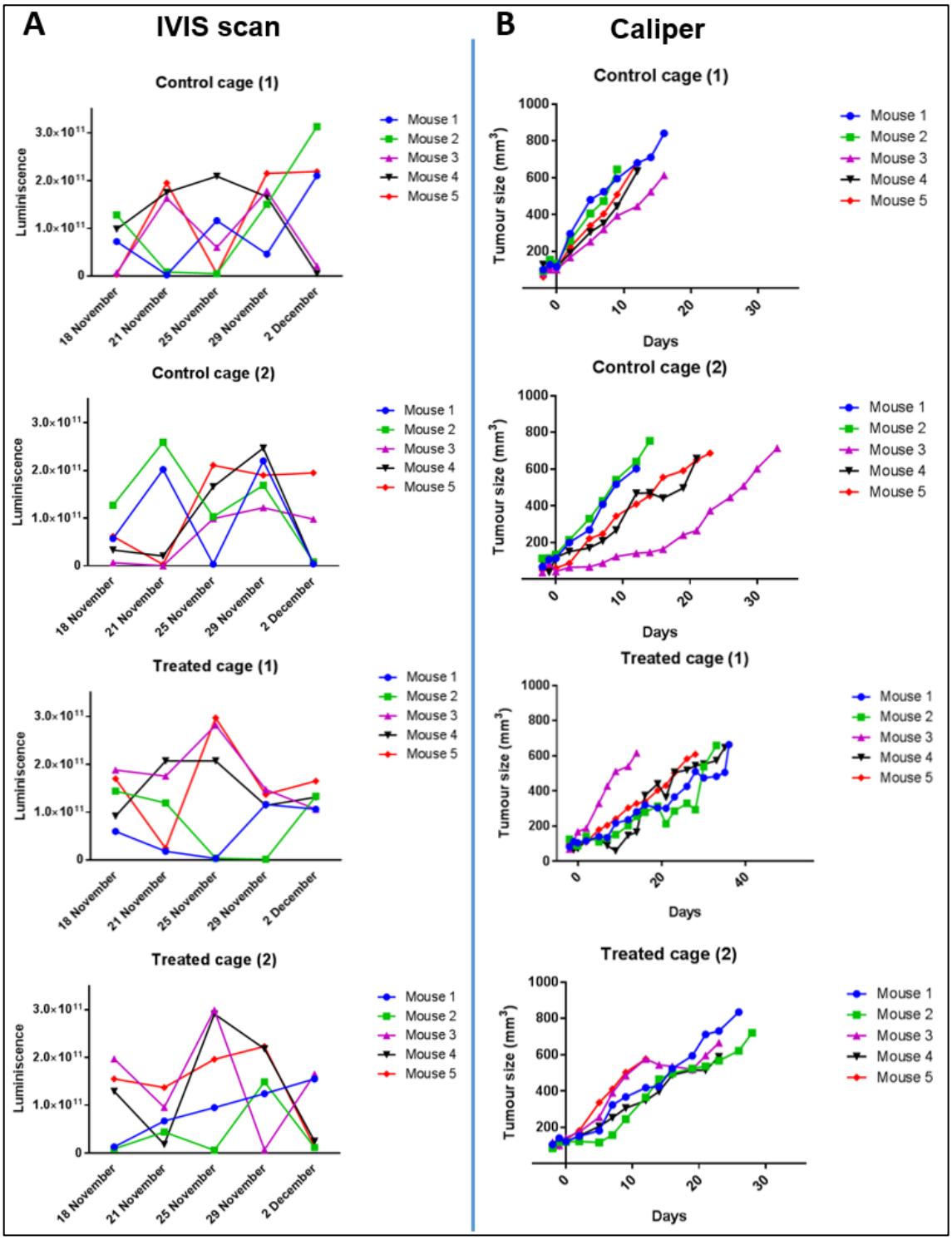

Figure 5.19: IVIS scan compared to the standard tumour measurement by caliper. (A) IVIS scan data of each individual HepG2-Luc xenograft in each cage in the control and treated groups obtained by injecting the NSG mice with D-Luciferin intraperitoneally 10 minutes before scanning. (B) Standard caliper measurements data of HepG2-Luc xenograft tumours of each individual xenograft in each cage of the control and treated groups.

5.9.4 The effect of HDM201 100 mg/kg/day for 10 days on HepG2-Luc xenografts

To explore the effects of a higher dose of HDM201 on HepG2 xenografts, the experiment was repeated with tumour bearing mice allocated alternately to receive control vehicle by oral gavage (n=9 mice) or HDM201 100 mg/kg/day for 10 days (n=9 mice). This dose frequency and duration was planned to be partly similar to regimen 2A in a phase I clinical trial for different tumours (single daily dose for two weeks in a 4 week cycle) (314); however, treatment was discontinued at day 10 as the mice showed signs of toxicity, reflected by loss of body weight (range 4%-12%) (**Figure** 5.20**; A and B**). Body weight was subsequently regained (**Figure** 5.20**; B**). At the higher dose, significant growth inhibition was again observed, as shown at day 12 (p=0.03) (**Figure** 5.20**; D**) and day 21 (p=0.001) (**Figure** 5.20**; E**). A plateau in tumour volume was maintained for approximately 20 days after discontinuation of the drug, (**Figure** 5.20**; A**) (**Figure** 5.21), with survival differences of 19.91 days for control vehicle only treated mice compared to 41.74 days post treatment with HDM201 (p=0.0017) (**Figure** 5.20**; F**).

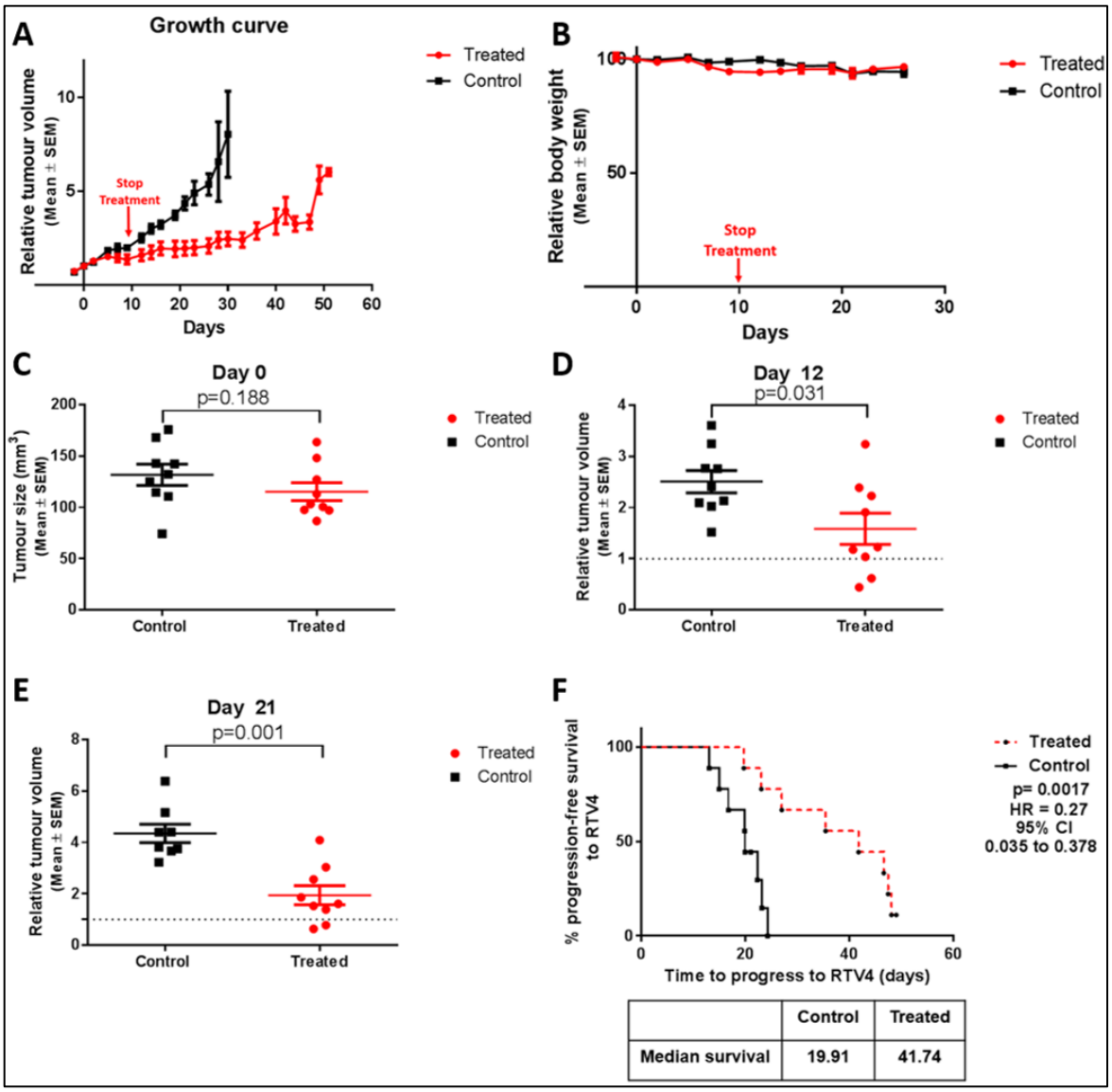

Figure 5.20: The effect of oral 100 mg/kg/day HDM201 (single daily dose) on HepG2-Luc xenografts in NSG mice. (A) the growth curve of the xenografts represented by the mean of the relative tumour volume (RTV) of each tumour to its starting volume before commencing treatment on day 0 and stopping it on day 10 (red arrow). (B) The effect of oral HDM201 on the body weight of NSG mice bearing the Hepg2-Luc xenografts. (C) The volume of xenograft tumours (mm^3) in both groups (control and treated) on day 0 before starting treatment with HDM201. (D) and (E) represent the relative tumour volume difference between the control and treated groups on day 12 and day 21 with p-values on each graph (t-test). (F) Survival reflected by the time taken by each xenograft to reach 4 times the starting volume with the median survival of each group in a table below the graph. The p value calculated by Log-Rank test, HR = hazard ratio, CI= confidence interval. Error bars represent the standard error of the mean.

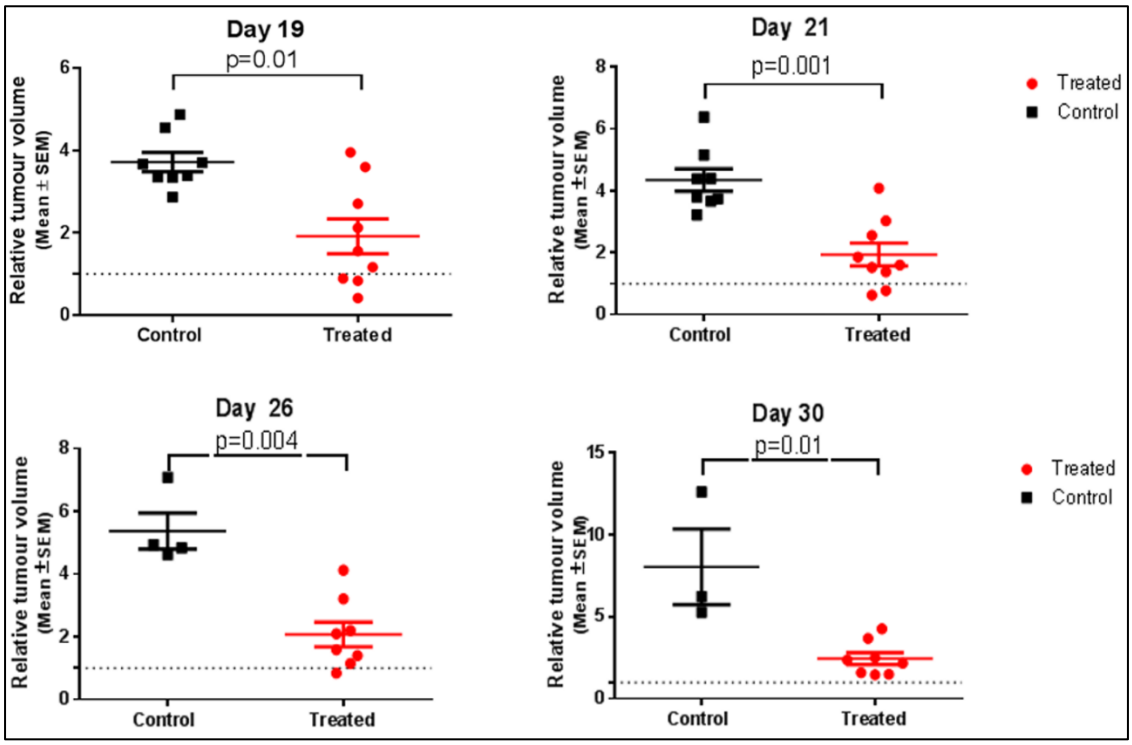

Figure 5.21: the effect of oral HDM201 100 mg/kg/day (single daily dose) on HeG2-Luc xenografts in NSG mice. Shows that the effect of 100mg/kg/day HDM201 on slowing tumour growth continued to be statistically significant in the treated group compared to the control and the statistical significance increased and maintained from day 19 till day 30. Error bars represent standard error of the mean (SEM).

5.10 Discussion

Treatment options for patients with advanced primary liver cancers are limited, with barriers to progress well recognised and recently reviewed (156). Although the MDM2-p53 pathway is frequently dysfunctional in liver cancer (332), TCGA and the Catalogue Of Somatic Mutations In Cancer (COSMIC) (199) data indicates that *TP53* is directly mutated in only a minority of patients. There is hope, therefore, that activating levels of WT p53 may be of benefit and relevant for a substantial proportion of patients – especially if a sustained impact on tumour growth can be achieved, in the absence of either systemic or liver related toxicities. Small molecule MDM2-p53 binding antagonists are already in clinical trials, largely as dose finding studies in leukaemias, in addition to phase 1 clinical trials for advanced solid tumours and lymphomas (https://clinicaltrials.gov/).

Of the reported MDM2 small molecule inhibitors, only the early tool compound nutlin-3 has been previously tested with liver cancer cell lines and reported to cause inhibition of growth regardless of the *TP53* status of the cells at high doses - possibly an off-target effect mediated through p73 (333). The effects of more potent, specific and clinically relevant inhibitors such as RG7388 and HDM201 have not been reported in liver cancer cell lines. Therefore, we explored all three compounds in liver cancer cell lines with different *TP53* status.

Each of the three compounds induced growth inhibition in $p53^{WT}$ liver cancer cells. The GI_{50} of nutlin-3 was approximately 2 µM for $p53^{WT}$ cell lines. As previously reported, nutlin-3 did induce growth inhibition at much higher doses (>20 µM) in two of the $p53^{MUT/NULL}$ cell lines, but these are off-target effects at doses outside the physiologically relevant range. Our focus was on more potent, specific and clinically relevant MDM2-p53 inhibitors. Both RG7388 and HDM201 demonstrated pronounced growth inhibition, with doses in the nanomolar range for $p53^{WT}$cell lines. Off target growth inhibition of $p53^{MUT/NULL}$ cell line was detectable for RG7388, but only after exceeding 150 times the GI_{50} dose seen with the $p53^{WT}$ cell lines. HDM201 was notable not only for its low GI_{50} doses with the $p53^{WT}$ cells (30, 60 nM respectively for HepG2 and SK-Hep-1), but also because it had no detectable off target effects on growth inhibition of $p53^{MUT/NULL}$ liver cancer cell lines, even at a dose as high as 10 µM (> 300 times the GI_{50} for HepG2 and >150 times the GI_{50} for SK-Hep-1). Our subsequent and more detailed characterisations of specific and potent MDM2 inhibition in these liver cancer cells lines focused on HDM201. Similar to the growth inhibition studies, clonogenic survival assays showed that the HDM201 inhibition of colony formation was also limited to $p53^{WT}$ cell lines.

Exploring additional *in vitro* effects of HDM201 confirmed increased protein levels of MDM2, alongside prominent protein stabilisation of p53 in $p53^{WT}$ cells. As expected, there was no transcriptional increase in *TP53* mRNA, but increased levels of p53 protein was followed by transcriptional and translational increases in MDM2. At the same time, there were marked and sustained transcriptional increases in *CDKN1A*, followed by pronounced increases in the translated p21 protein product. These effects were specific to $p53^{WT}$ cells.

Although there were some relatively small transcriptional increases in pro-apoptotic genes, these were not as marked as the changes observed for *CDKN1A/p21*. Our analyses of apoptotic endpoints showed no evidence of PARP cleavage by western blot, no increases in caspase3/7 activity and a lack of subG1 signals when cells were analysed by FACS. These collective observations indicated that for the HDM201 treated liver cancer cells, increased apoptosis played no part in their response. However, the sustained growth inhibition in the presence of continued metabolic activity *in vitro* or cessation of treatment *in vivo* were indicative of senescence, which *in vitro* was supported by staining for β-galactosidase. Furthermore, we found that the increased levels of *CDKN1A*/p21 at mRNA and protein levels was associated with the observed cell cycle arrest and the induction of senescence. It has been reported previously that Nutlin-3a causes growth inhibition in $p53^{WT}$ T-cell leukaemia cell lines by inducing senescence through induction of p21 protein levels (320), but it has not been previously reported that MDM2 inhibition induces senescence in HCC.

Senescent cells express various secretory proteins, collectively referred to as the senescence associated secretory phenotype (SASP), that includes cytokines, chemokines, growth factors and matrix-remodelling associated proteases (334). Among these secreted molecules, interleukins like IL-1 alpha, IL-6 and IL-8 have an effect in promoting the elimination of senescent cells by the immune system. Also, it has been reported that through their secreted SASP peptides, senescent fibroblasts and hepatocytes play a role in the differentiation of circulating immune cells and their recruitment to tumour sites, thus contributing to tumour immune surveillance (210, 335, 336).

While a treatment that induces cancer cell death may be more attractive at first consideration, the restoration of WT p53 in a transgenic inducible animal model was reported to eliminate liver cancer, by inducing senescence and triggering an innate anti-tumour response (210, 337). Whether this might translate in the human setting is as yet unknown, but the potential is exciting.

We have extended previous tumour xenograft studies of MDM2-p53 small molecule inhibitors (318) to the liver cancer cell line, HepG2. The growth inhibitory effect of HDM201 was reproduced *in vivo*, with the drug significantly suppressing the rate of tumour growth in a dose-dependent fashion. At the higher dose, the suppression of growth was impressively sustained for two to three weeks following discontinuation of treatment, before resuming. These observations are in keeping with the induction of growth arrest and senescence. The response to repeated treatment is worthy of further exploration, as this may have relevance for clinical translation. Furthermore, the impact of immune clearance of senescent cells is not well modelled in immunocompromised mice. Immune clearance of cancer cells, achieving sustained anti-tumour responses following treatment with MDM2-p53 inhibitors may have translational relevance for liver cancer as well as other solid tumours and should be further explored.

In conclusion, we have demonstrated promising results with highly significant growth inhibitory effects *in vitro* and *in vivo* in $p53^{WT}$ liver cancer cell lines induced by small molecule MDM2-p53 binding antagonists. Our study shows that targeting this pathway is worthy of further exploration for patients with liver cancer.

Chapter 6: Results - The effect of WIP1 inhibitor GSK2830371 as a single agent and in combination with MDM2 inhibitors on liver cancer cell lines

6.1 Introduction

One of the downstream transcriptional targets of p53 is *PPM1D* which encodes a wild type-p53 induced phosphatase (WIP1). It is a member of the PPM family of Ser/Thr phosphatases, WIP1 functions by dephosphorylating several key DNA damage and stress response proteins (ATM, ATR, Chk1, Chk2, H2AX, MDM2 and p53) (230, 338-342). Being a downstream target of p53 and at the same time acting on p53 makes it part of an auto-regulatory negative feedback loop that plays an important role in regulating the function of p53 by dephosphorylating p53 at the Ser15 site. Therefore, inhibition of this phosphatase will lead to stabilisation of phosphorylated p53. Overexpression of WIP1 is believed to promote tumorigenesis and the inhibition of apoptosis and senescence (343, 344). It has been reported that WIP1 is overexpressed at the mRNA and protein levels in several solid tumours (e.g breast, ovarian, neuroblastoma, medulloblastoma, gastric and pancreatic tumours) and was associated with poor prognosis (228, 229, 232). PPM1D is amplified in ~ 5% of HCC (TCGA accessed July 2017) (311, 312) and is rarely mutated in HCC (1 out of 921 cases) according to the COSMIC data base (199). However, it was found to be overexpressed in HCC at the mRNA and protein levels in 65% and 59% of cases respectively, and was associated with poor prognosis, larger tumour size and advanced stage (228, 229, 232).

GSK2830371 is a small molecule inhibitor of WIP1 (WIP1i). It binds to it and allosterically inhibits WIP1 function through binding to a structural flap sub-domain that is unique to WIP1 and in addition causes ubiquitination of WIP1 which leads to its degradation (239). Several studies have reported the growth inhibitory effect of GSK2830371 on several types of cancer, whether alone or in combination with MDM2 inhibitors (339, 345, 346) but its effect has not previously been tested in liver cancer. Our aim was to test the WIP1i effect as a single agent and in combination with MDM2 inhibitors on liver cancer cell lines subsequent to establishing the growth inhibitory effect of MDM2 inhibitors on $p53^{WT}$ liver cancer *in vitro* and *in vivo* in chapter 5.

6.2 Aims of the study in this chapter

To explore the effect of a small molecule inhibitor of WIP1 (GSK2830371), as a single agent and in combination with small molecule MDM2 inhibitors, on liver cancer cell lines.

6.3 GSK2830371 has no or minimal effect on liver cancer cell lines when used alone at low micromolar doses

6.3.1 GSK2830371 effect on the proliferation of liver cancer cell lines

The effect of WIP1i (GSK2830371) was tested on a panel of liver cancer cell lines with different *TP53* status, the same panel that was used to test the effect of MDM2 inhibitors in chapter 5. Cells were exposed to different concentrations of WIP1i (0.07-10 µM) for 96hours and an SRB assay was used to determine the effect of the drug on cell proliferation (**Figure** 6.1**)**. WIP1i as a single agent did not have any growth inhibitory effect on $p53^{MUT/NULL}$ cell lines; but had a mild growth inhibitory effect on $p53^{WT}$ cells. For HepG2 ($p53^{WT}$) a dose of 2.5 µM GSK2830371 inhibited proliferation by ~ 23% and this growth inhibitory effect did not exceed 35% even with the maximum dose used (10 µM). In the other $p53^{WT}$ cell line (SK-Hep-1), 2.5 µM GSK2830371 had ~15% growth inhibitory effect and at higher doses showed a growth inhibitory effect of up to 69.6% at 10 µM, with a GI_{50} value of 7.49±0.51 µM (**Figure** 6.1) (**Table** 6.1).

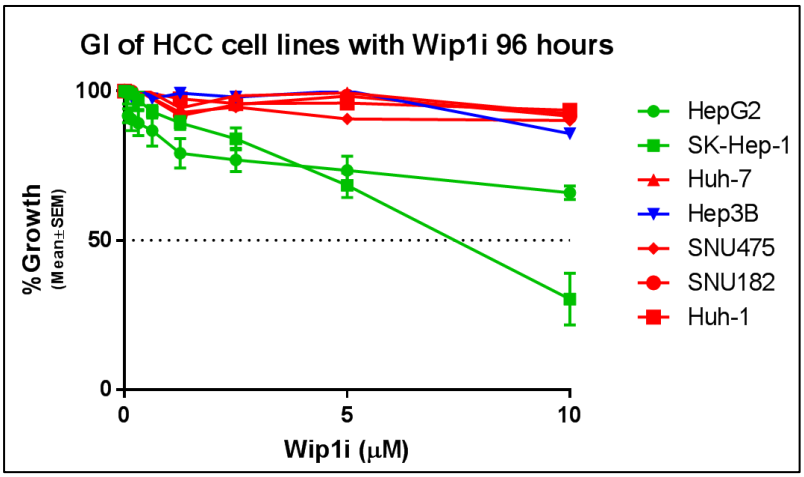

Figure 6.1: growth inhibition assay of liver cancer cell lines with different *TP53* status with WIP1i for 96 hours (SRB assay). $p53^{WT}$ cell lines (Green), $p53^{MUT}$ (Red) and $p53^{NULL}$ (blue). Error bars represent the standard error of the mean for three independent repeats.

6.3.2 The effect of GSK2830371 at the protein level in p53^{WT} cell lines

To investigate the effect of WIP1 inhibition at the protein level in p53^{WT} cell lines (HepG2 & SK-Hep-1), cells were seeded in 6 well plates at a density of 3x10^5 cells/well for 48 hours and then treated with a wide range of WIP1i (0.07-10 µM) for 6 hours before collection of cell lysates for western blot analysis.

In addition to a direct inhibitory effect on WIP1 phosphatase activity, GSK2830371 had been reported to promote the degradation of WIP1 protein (239) and our western blot results showed that this was also evident with HepG2 and SK-Hep-1 cells. Even at very low dose of GSK2830371 there was a marked reduction in WIP1 protein level in both of these p53^{WT} cell lines (**Figure** 6.2). Also, there was prominent dose dependent increase in p53 phosphorylated at serine 15 (pp53^{Ser15}) which confirmed the inhibitory effect of GSK2830371 on the ability of WIP1 to dephosphorylate pp53^{Ser15}. Despite this increased pp53^{Ser15}, the total p53 level did not change nor did that of other p53 downstream transcriptional targets, namely MDM2, p21 and BAX (**Figure** 6.2).

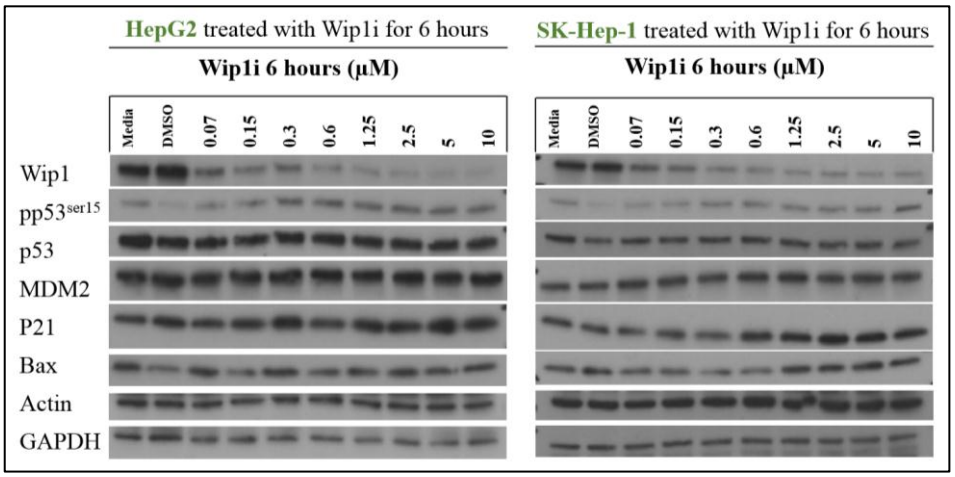

Figure 6.2: Immunoblot of HepG2 and SK-Hep-1 cell lines treated with different concentrations of GSK2830371 WIP1i (0.07-10 µM) for 6 hours. GAPDH and β-actin were used as loading controls.

6.4 GSK2830371 potentiates the effect of MDM2 inhibitors on repressing the growth of liver cancer cell lines through the p53 pathway

To assess the effect of WIP1 inhibition on the response to MDM2 inhibitors in liver cancer cell lines, GSK2830371 (2.5 µM) was combined with a wide range of MDM2 inhibitors. This dose did not have any effect on $p53^{MUT/NULL}$ cells and only a minimal effect on $p53^{WT}$ cell lines when used alone (as mentioned above (6.3.1)).

GSK2830371 potentiated the growth inhibitory response of all the three MDM2 inhibitors in a p53 dependent manner. A reduction in the GI_{50} value was observed for all three MDM2 inhibitors tested (Nutlin-3, RG7388 and HDM201) in the presence of GSK2830371 (2.5 µM) with both $p53^{WT}$ cell lines (HepG2 & SK-Hep-1) as summarised in **Table** 6.1. For the HepG2 cell line, the fold reduction in the GI_{50} was 1.48 for Nutlin-3 (p=0.008), 1.29 for RG7388 (p=0.01), and 1.79 for HDM201 (p=0.01). The reduction in the GI_{50} for SK-Hep-1 was more pronounced and was by 3.2 fold for Nutlin-3 (p=0.004), 2.84 fold for RG7388 (p=0.01), and 2.3 fold for HDM201 (p=0.0002) respectively (**Figure** 6.3) (**Table** 6.1). In contrast, there was no effect of the combination on the proliferation of the $p53^{MUT/NULL}$ cell lines (**Figure** 6.3).

Table 6.1: GI_{50} of MDM2 inhibitors alone and in combination with WIP1i (2.5 µM) in $p53^{WT}$ liver cancer cell lines

	GI_{50}						
Cell line	**Nutlin-3 (µM)**	**Nutlin-3 (µM)+ Wip1i (2.5 µM)**	**RG7388 (nM)**	**RG7388 (nM) + Wip1i (2.5 µM)**	**HDM201 (nM)**	**HDM201 (nM) + Wip1i (2.5 µM)**	**Wip1i (µM)**
HepG2	**1.71** ± 0.08	**1.16** ± 0.09	**15.34** ± 1.05	**11.94** ± 0.53	**29.22** ± 1.63	**16.3** ± 0.81	**> 10**
SK-Hep-1	**2.2** ± 0.17	**0.68** ± 0.04	**27.3** ± 5.47	**9.6** ± 3.41	**60.08** ± 1.49	**26.07** ± 1.81	**7.49** ± 0.51

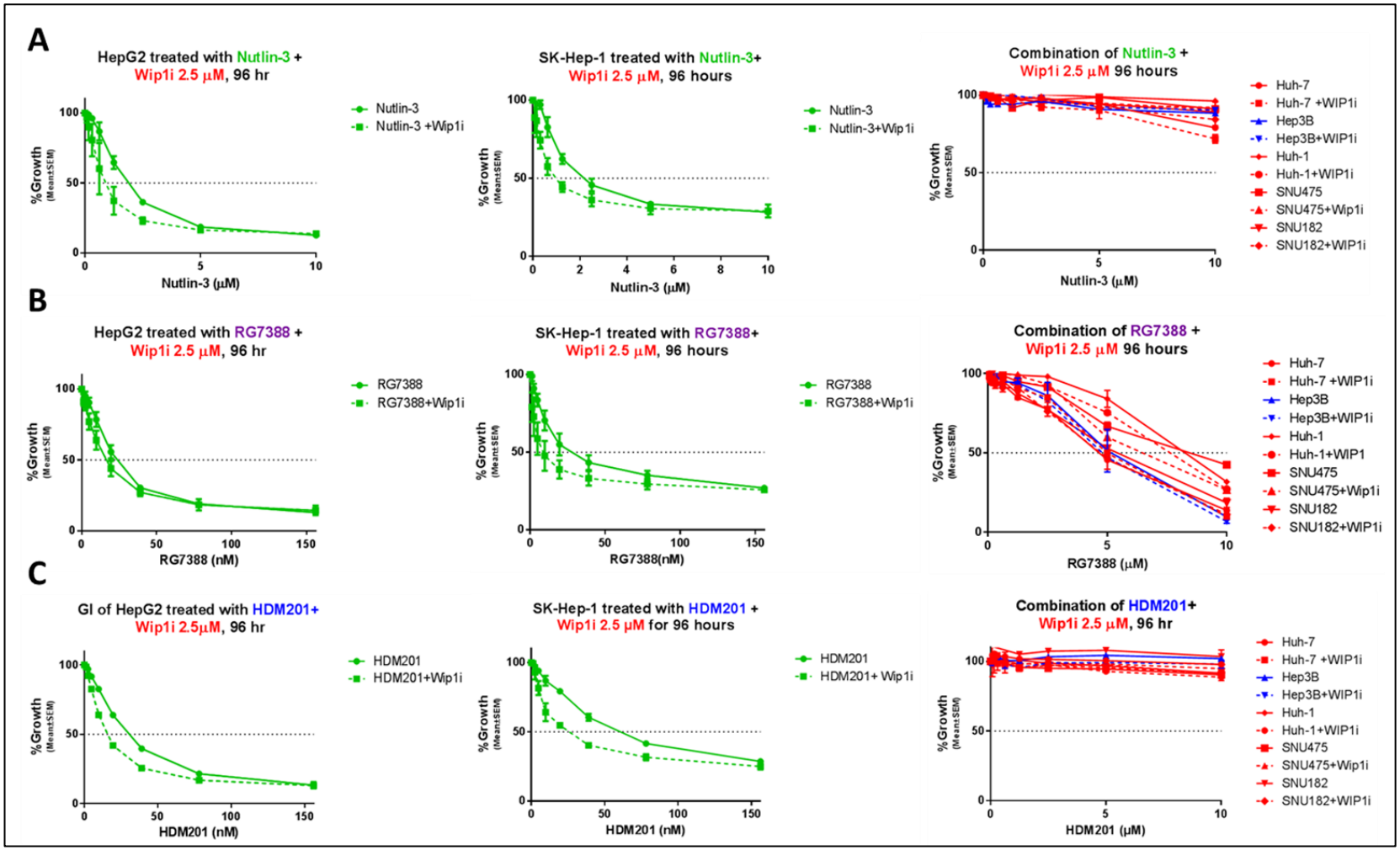

Figure 6.3: Combination effect of different MDM2 inhibitors with GSK2830371 WIP1i on liver cancer cell lines. (A) Nutlin-3, (B) RG7388 and (C) HDM201 alone and in combination with WIP1i 2.5 µM for 96 hours in $p53^{WT}$ cell lines (HepG2 and SK-Hep-1 green coloured) and $p53^{MUT}$ (red coloured) and $p53^{NULL}$ (blue coloured) cell lines. The continuous lines represent MDM2 inhibitors alone and the dotted line represents the combinations of MDM2i and WIP1i 2.5 µM. Error bars represent standard error of the mean of three independent repeats.

6.5 The effect of GSK2830371 as a single agent and in combination with HDM201 on protein levels in p53^{WT} liver cancer cell lines

The effects of single agent and combined treatments on the protein levels of p53, its downstream regulatory targets and PARP were assessed by immunoblotting (**Figure** 6.4). As HDM201 was the most potent and specific MDM2 inhibitor of the three tested, further combination treatments were performed with GSK2830371 WIP1i (2.5 µM) and HDM201.

GSK2830371 resulted in a prominent reduction of WIP1 protein levels when used alone or in combination with HDM201 in both p53^{WT} cell lines (HepG2 and SK-Hep-1) as early as 6 hours after treatment (**Figure** 6.4).

Stabilization of post-translationally modified p53 by GSK2830371 was clearly evident, reflected by phosphorylation at Ser15 and acetylation at Lysine 382, and was more prominent after combination of the same dose of WIP1i with HDM201 in both cell lines. The MDM2 and p21^{WAF1} downstream targets of p53 were induced by HDM201 and the induction was more prominent in combination treatment compared to HDM201 alone. For BAX the increased effect of combination treatment was more evident in SK-Hep-1 than HepG2. The detection of WIP1 protein levels was suppressed by the GSK2830371 treatment (**Figure** 6.4). There was no evidence of cleaved PARP nor a change in full-length PARP levels regardless of whether cells were exposed to single compounds or to combination.

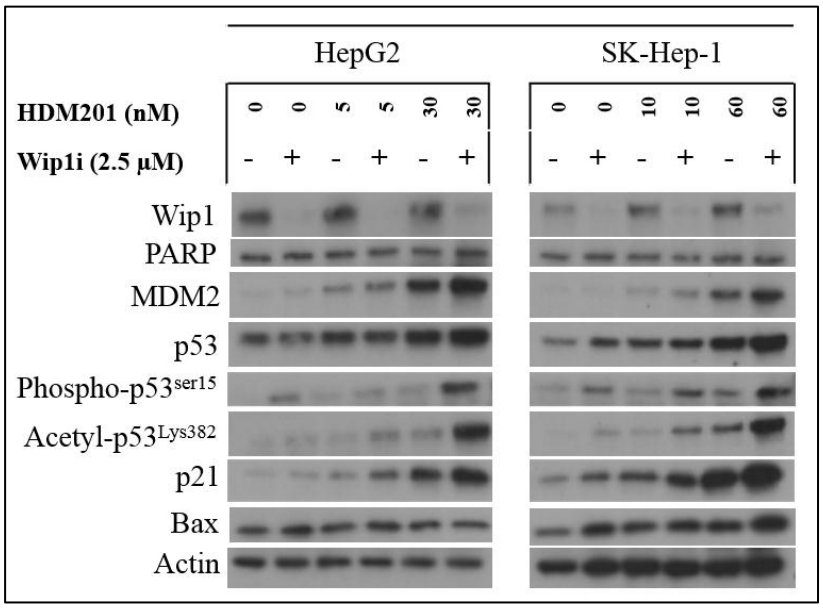

Figure 6.4: Immunoblot of HepG2 and SK-Hep-1 treated with HDM201 alone and in combination with WIP1i (GSK2830371) for 6 hours. The maximum dose of HDM201 used represents the approximate GI_{50} for that cell line (30 nM for HepG2 and 60nM for SK-Hep-1). β-Actin was used as a loading control.

6.6 The effect of GSK2830371 as a single agent and in combination with HDM201 on the clonogenic survival of liver cancer cell lines

HDM201 had an inhibitory effect on the colony forming ability of $p53^{WT}$ cell lines, as shown in chapter 5 (5.4.3). GSK2830371 (2.5µM) potentiated the effect of HDM201, reflected by the reduction of clonogenic survival LC_{50} values for $p53^{WT}$ cell lines. GSK2830371 (2.5µM) significantly reduced the LC_{50} for SK-Hep-1 by 63.1% (2.72 fold) (p=0.043), from (73.9±20.2) to (27.2±6.3) nM; while for HepG2 the LC_{50} was reduced by 28.3% (1.26 fold) (p=0.07) from (11.14±1.3) to (7.9±0.4) nM (**Figure** 6.5). There was no effect on the colony forming ability of $p53^{MUT/NULL}$ cells, whether after exposure to HDM201 alone or in combination with WIP1i.

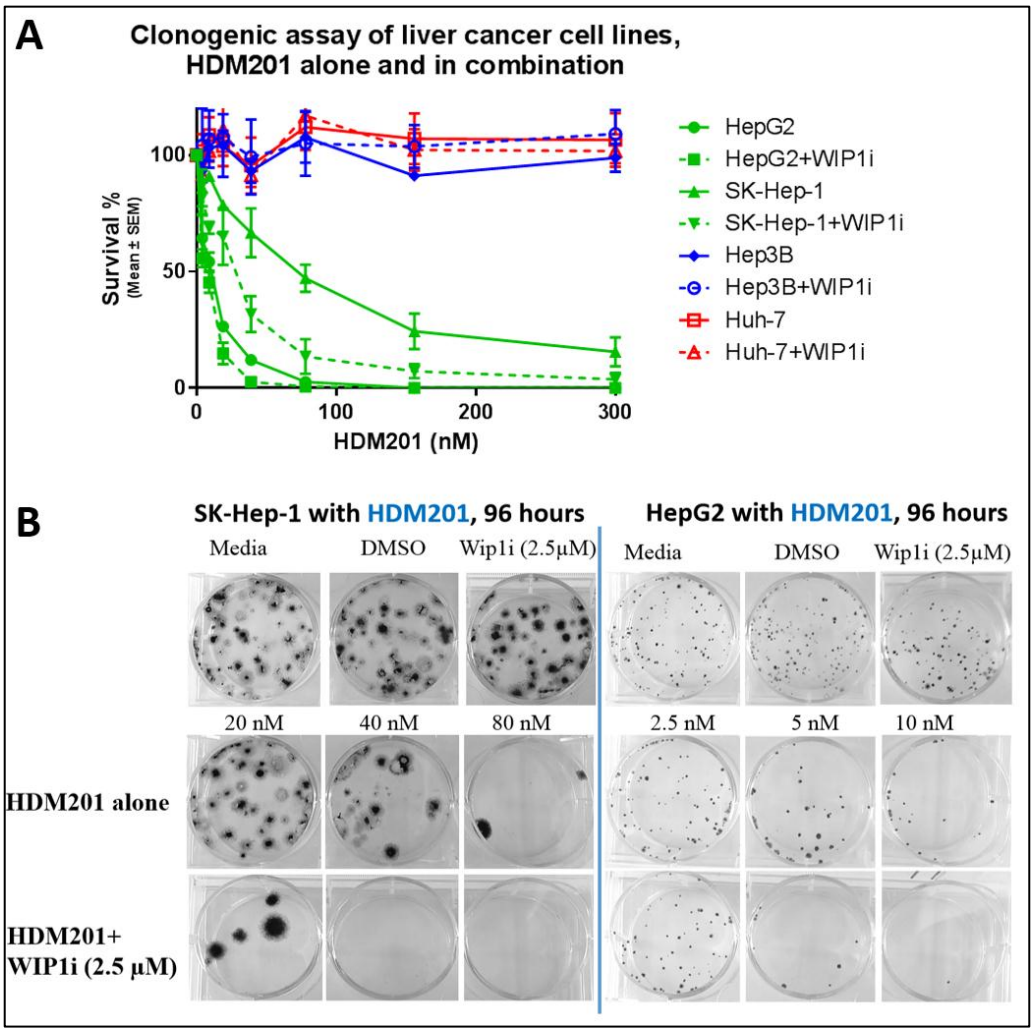

Figure 6.5: The effect of HDM201 alone and in combination with WIP1i (2.5 µM) on the cloning efficiency of liver cancer cell lines after treatment for 96 hours. (A) Clonogenic survival of $p53^{WT}$ (HepG2 and SK-Hep-1(green)) and $p53^{MUT/NULL}$ (Huh-7 (red) and Hep3B (blue)), the continuous lines represent the effect of HDM201 alone and the interrupted lines represent the combination treatment. A wide range of HDM201 was used (1, 2.5, 5, 10, 20, 40, 80, 156 and 300 nM) alone and in combination with GSK2830371 (2.5µM) WIP1i for 96 hours. (B) Selected images of the colonies of both $p53^{WT}$ cell lines (HepG2 and SK-Hep-1) showing the media, DMSO control and GSK2830371 (2.5µM) WIP1i alone and three doses of HDM201

alone and combination with WIP1i. Error bars represent the mean and the SEM of three independent repeats.

6.7 The effect of GSK2830371 on cell cycle distribution when used as a single agent and in combination with HDM201

The GSK2830371 (2.5µM) WIP1i potentiation of the growth and clonogenic inhibitory activities of HDM201 (that was shown in 6.4 and 6.6) were explored at a cell cycle level using FACS analysis after 24, 48 and 72 hours treatment as shown in **Figure** 6.6. Compared to DMSO control, WIP1i (2.5 µM) on its own did not have any effect on the cell cycle distribution of the liver cancer cell lines (**Figure** 6.6). When GSK2830371 (2.5µM) was combined with the GI_{50} and 10X GI_{50} of HDM201 the cell cycle distribution of the $p53^{WT}$ cell lines was markedly affected.

With HepG2 cells, compared to HDM201 alone, when GSK2830371 WIP1i (2.5 µM) was combined with the GI_{50} of HDM201 it resulted in a significant increase in the number of cells in G0/G1 phase (p=0.001), a decrease in S phase (p=0.01) and G2/M (p=0.01). But when WIP1i was combined with 10X GI_{50} of HDM201 the effect was different, as it resulted in a reduction in G0/G1 phase (p=0.002) and an increase in G2/M phase (p=0.002) with no difference in S phase (p=0.2). These early changes at 24 hours persisted at 72 hours (**Figure** 6.6**; A**).

For SK-Hep-1, GSK2830371 (2.5µM) WIP1i potentiated the effect of HDM201 whether at the GI_{50} or 10X GI_{50}, resulting in a significant reduction in G0/G1 phase (p=0.02) and S phase (p=0.003), and a significant increase in G2/M phase (p=0.02) (**Figure** 6.6**; B**). This effect was evident as early as 24 hours and persisted at 72 hours. With the $p53^{MUT/NULL}$ cell lines, on the other hand, WIP1i did not have any effect on the cell cycle distribution, whether alone or in combination with 1 µM HDM201 (**Figure** 6.6**; C and D**); indicating that the observed changes and potentiation effects by GSK2830371 were p53-dependent.

There were no detectable increases in Sub-G1 signals on the FACS histograms either after HDM201 treatment or after the combination with WIP1i, showing no evidence of apoptosis.

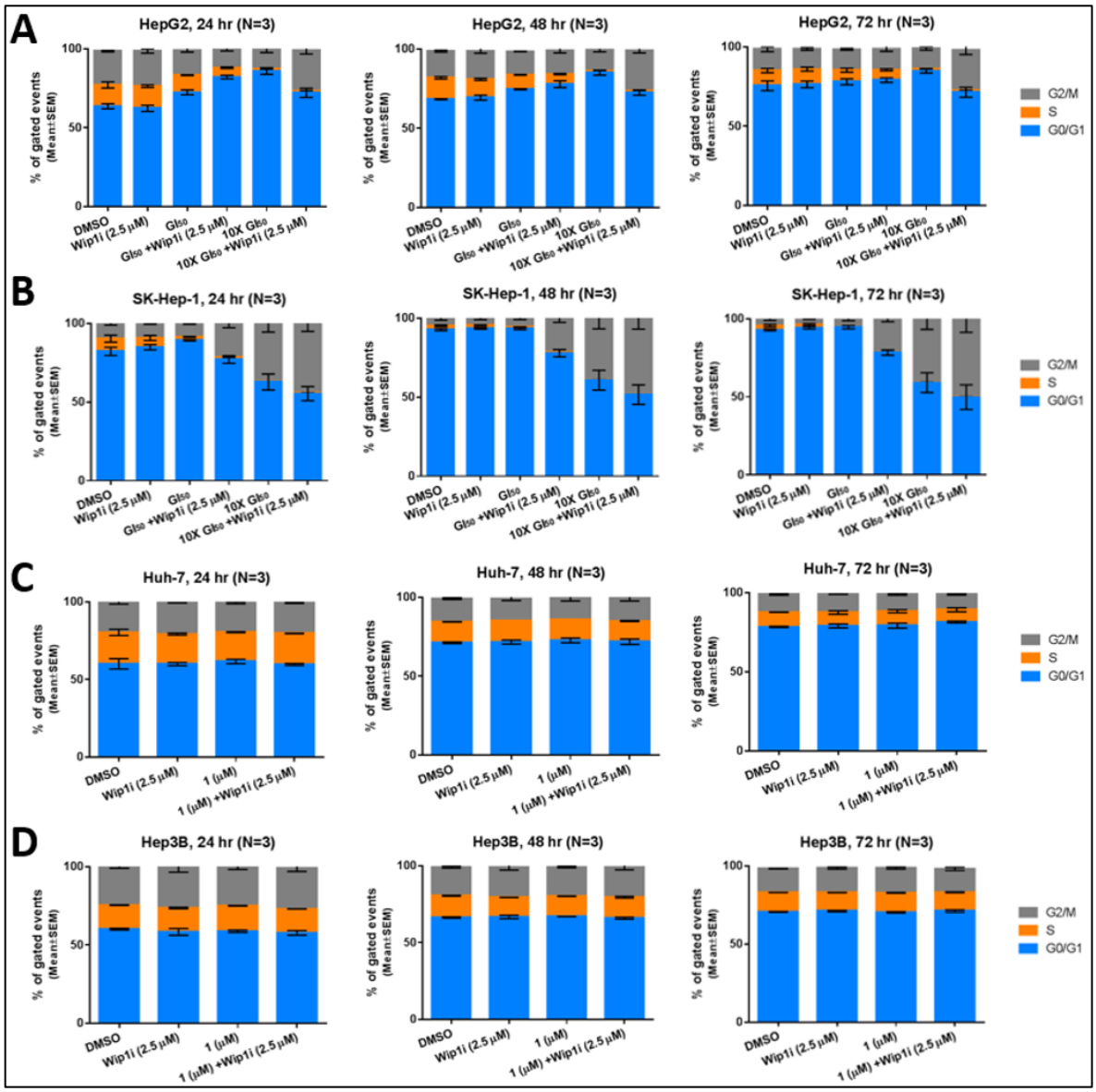

Figure 6.6: Cell cycle analysis showing the effect of GSK2830371 (2.5μM) WIP1i on the cell cycle distribution when combined with HDM201. Liver cancer cell lines with different *TP53* status was treated with HDM201 alone and in combination with WIP1i for 24, 48 and 72 hours. For $p53^{WT}$ cell lines the GI_{50} (30 nM for HepG2 and 60 nM for SK-Hep-1) and 10 times the GI50 of HDM201 was used alone and in combination with WIP1i 2.5 μM, while one high dose (1 μM) was used alone and in combination with WIP1i 2.5 μM in $p53^{MUT/NULL}$ cell lines. (A) HepG2, (B) SK-Hep-1, (C) Huh-7 and (D) Hep3B. Error bars represent standard error of the mean of three independent repeats.

6.8 GSK2830371 as a single agent or in combination with HDM201 does not induce apoptosis and does not inhibit the metabolic activity in liver cancer cell lines

GSK2830371 WIP1i (2.5 µM) potentiated the growth inhibitory effect of HDM201 and induced changes in cell cycle distribution in $p53^{WT}$ cells but, despite reducing the clonogenic cell survival, did not cause an increase in Sub-G1 on FACS analysis and there was no evidence of PARP cleavage in western blotting (**Figure** 6.4). This means that although WIP1i is potentiating the effects of HDM201 through the p53 pathway, it is still not inducing any apoptosis in these cell lines. This lack of apoptosis was further supported by a caspase 3/7 activity assay that showed no detectable increase in the caspase activity in the treated cells whether they were treated with WIP1i alone, HDM201 alone or in combination. Furthermore, this applied for both $p53^{WT}$ and $p53^{MUT/NULL}$ cells (**Figure** 6.7).

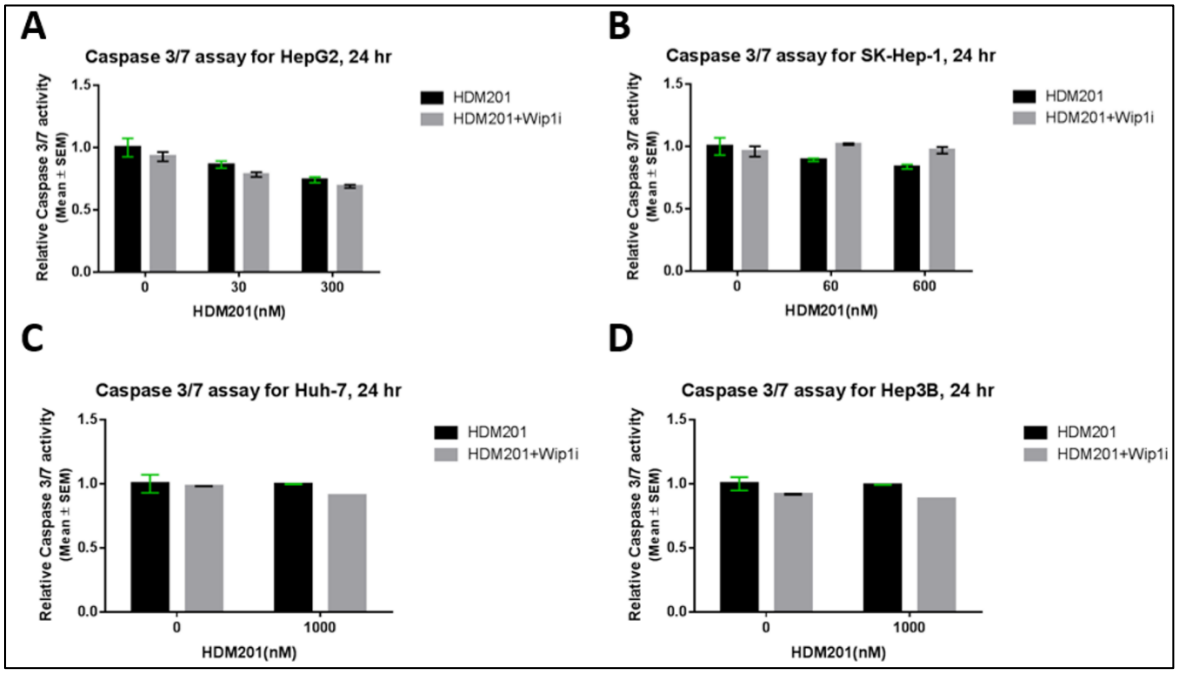

Figure 6.7: Caspase 3/7 activity in liver cancer cell lines after treatment with HDM201 alone and in combination with GSK2830371 (2.5µM) WIP1i. Liver cancer cell lines with different *TP53* status were treated with HDM201 alone and in combination with WIP1i 2.5 µM for 24 hours. For $p53^{WT}$ cell lines the GI_{50} (30 nM for HepG2 and 60 nM for SK-Hep-1) and 10 times the GI_{50} of HDM201 was used alone and in combination with WIP1i 2.5 µM, while one high dose (1 µM) was used alone and in combination with WIP1i 2.5 µM in $p53^{MUT/NULL}$ cell lines. (A) HepG2, (B) SK-Hep-1, (C) Huh-7 and (D) Hep3B. No detectable increase in caspase activity was evident, whether for HDM201 alone or in combination treatment. Error bars represent standard error of the mean of three independent repeats.

The XTT assay that assesses the mitochondrial enzymatic activity and confirmed the cells were still metabolically active after HDM201 treatment in chapter 5, once again confirmed that WIP1i (2.5 µM) on its own did not affect the metabolic activity of the cells (**Figure** 6.8). Even after combination with HDM201 and despite the growth inhibition, the cells were still metabolically active and generally their metabolic activity was maintained after 96hours treatment (**Figure** 6.8**; A and B**). $P53^{MUT/NULL}$ cells showed no detectable difference in the metabolic activity between any of the treatment conditions (**Figure** 6.8**; C and D**).

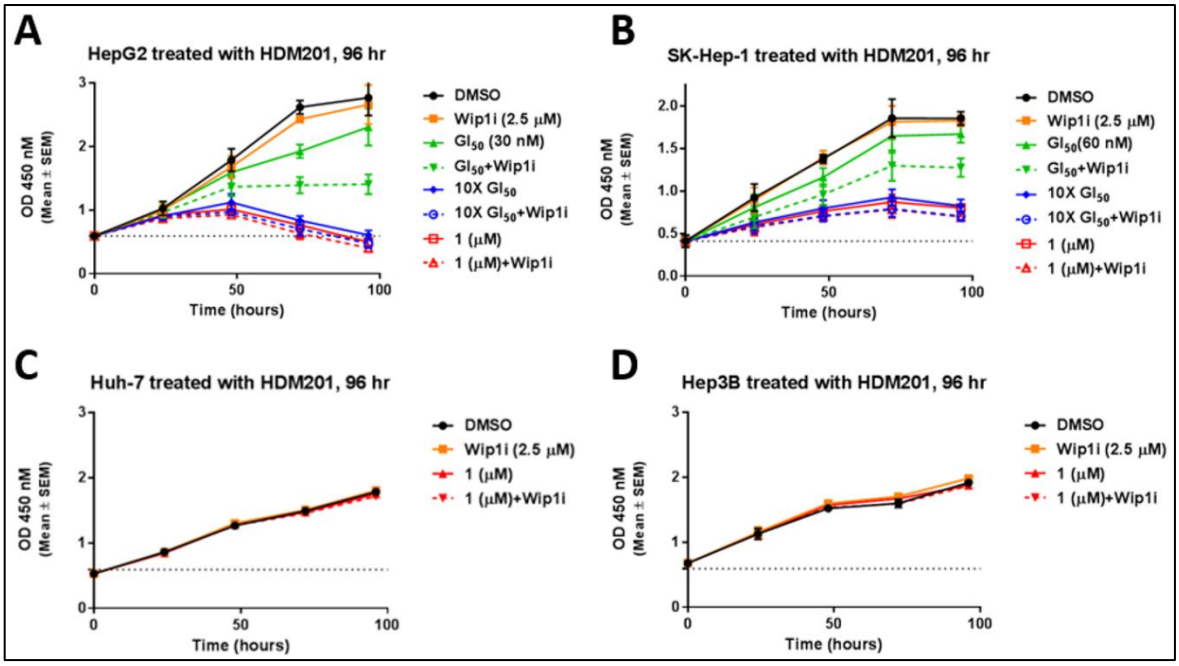

Figure 6.8: XTT assay measuring the metabolic activity in liver cancer cell lines in response to HDM201 alone and in combination with GSK2830371 (2.5µM) WIP1i. Liver cancer cell lines with different *TP53* status were treated with HDM201 alone and in combination with WIP1i 2.5 µM for 96 hours. For $p53^{WT}$ cell lines the GI_{50} (30 nM for HepG2 and 60 nM for SK-Hep-1), 10 times the GI_{50} of HDM201 and a high dose of (1 µM) was used alone and in combination with WIP1i (2.5 µM), while for $p53^{MUT/NULL}$ cell lines only the high dose (1 µM) was used alone and in combination with WIP1i (2.5 µM). (A) HepG2, (B) SK-Hep-1, (C) Huh-7 and (D) Hep3B. Y-axis represent the optical density (OD) at 450 nanometre wavelength. Data represent mean± standard error of the mean (SEM) of three independent repeats.

6.9 The effects of WIP1i as a single agent and in combination with HDM201 on the level of expression of p53 and its downstream transcriptional target genes in liver cancer cell lines

The GSK2830371 WIP1i potentiated the effect of HDM201 in terms of growth inhibition, clonogenic cell survival, cell cycle arrest, stabilization of p53 and increased expression of p53 downstream transcriptional targets at the protein level. We also investigated the effect of the inhibitor combination at the mRNA level of gene expression (**Figure** 6.9). Cell lines were treated with each compound alone and in combination for two time-points (6 and 24 hours) and RNA was extracted. A qRT-PCR assay was used to determine the compound-induced changes in the levels of expression of selected genes that represent different pathways activated by p53, but all are p53 downstream transcriptional targets. This set of genes includes the negative regulators of p53 (*PPM1D* and *MDM2*), cell cycle arrest genes (*CDKN1A (p21WAF1)* and *GADD45A*) and pro apoptotic genes governing both the intrinsic pathway (*BAX* and *BBC3* (*PUMA*)) and extrinsic pathway (*FAS* and *TNFRSF10B (DR5)*).

In $p53^{WT}$ cells, the combination of WIP1i (2.5 µM) and HDM201 showed a prominent potentiation of the effects of HDM201 at the transcriptional level for both time points (6 and 24 hours). In HepG2 the combination showed a significant increase in the transcript levels of the growth arrest genes *CDKN1A* (*p21WAF1*) (p=0.005) and *GADD45A* (p=0.005), in addition to *MDM2* (p=0.04), *BAX* (p=0.01) and *FAS* (0.02) transcripts at 6 hours. After 24 hours the potentiating effect on the GI_{50} dose was still significant for *CDKN1A* (*p21WAF1*) (p=0.02), *GADD45A* (p=0.007) and *BBC3* (*PUMA*) (p=0.02) (**Figure** 6.9**; A**).

The effect was more prominent in SK-Hep-1 cell line at both the GI_{50} and the 10X GI_{50} with a significant increase in the transcriptional levels of *MDM2* (p=0.01), *CDKN1A (p21WAF1)* (0.001) and *GADD45A* (p=0.01), and *PUMA* (p=0.04, 0.003 for GI_{50} and 10X GI_{50} respectively) at 6 hours. After 24 hours the potentiating effect on the GI_{50} dose of HDM201 was still statistically significant for *MDM2* (p=0.01), *GADD45A* (p=0.03) and *CDKN1A* (*p21WAF1*) (p=0.008) (**Figure** 6.9**; B**).

There was no significant change at the transcriptional level in any of the investigated genes in $p53^{MUT/NULL}$ cell lines (Huh-7/Hep3B) despite using a very high dose (1µM) alone and in combination with GSK2830371 WIP1i (**Figure** 6.9**; C and D**).

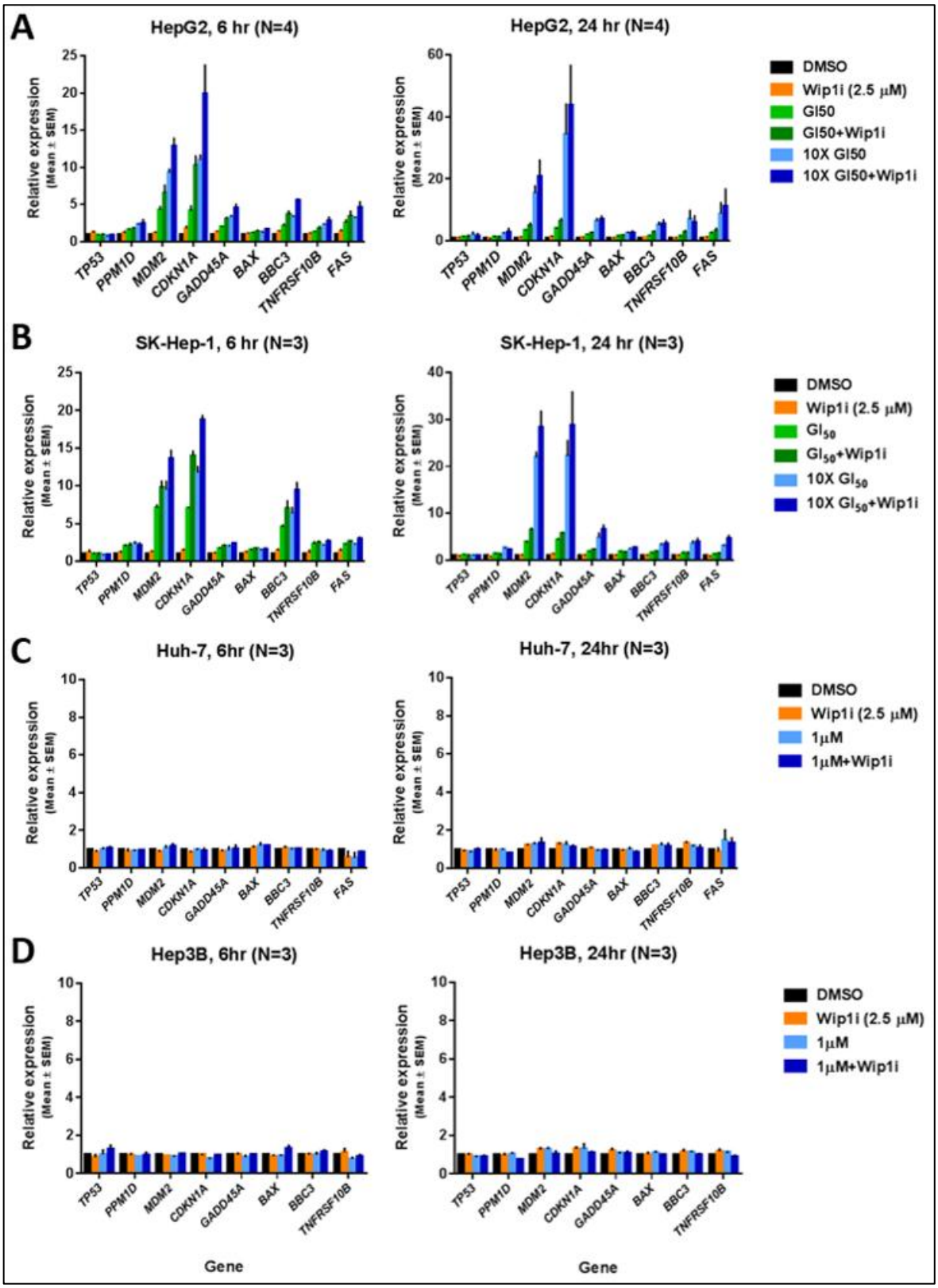

Figure 6.9: The expression of *TP53* and its downstream transcriptional targets by qRT-PCR in response to HDM201 alone and in combination with GSK2830371 WIP1i in liver cancer cell lines. Different doses of HDM201 were used (GI_{50} and 10X GI_{50} for $p53^{WT}$ and 1μM for $p53^{MUT/NULL}$) alone and in combination with WIP1i (2.5 μM) for 6 and 24-hour time points. The expression was relative to DMSO control and *GAPDH* was used as an internal reference gene (A) HepG2, (B) SK-Hep-1, (C) Huh-7 and (D) Hep3B. Data represent mean ± SEM of three independent repeats.

6.10 GSK2830371 potentiate the HDM201 induced senescence in $p53^{WT}$ cell lines

In Chapter 5 it was shown that HDM201 induced cell cycle arrest and senescence in $p53^{WT}$ HepG2 and SK-Hep-1 cells, particularly at high dose (5.5). Combination treatment with the GSK2830371 WIP1i (2.5 µM) potentiated this effect and on Incucyte time lapse imaging, the number of cells that recovered from growth inhibition was much lower than for the corresponding HDM201 only treated cells (**Figure** 6.10; **Figure** 6.11).

These results were further supported by SA-β-Gal staining for senescence, which showed potentiation of the effect of HDM201 by WIP1i, reflected by the increased percentage and intensity of positively stained cells (green-blue) for the combination treatment (**Figure** 6.12; **Figure** 6.13). This potentiation was statistically significant with p values of (0.01, 0.001) for WIP1i + 0.5 GI_{50} and (0.01, 0.026) for the WIP1i + GI_{50} of HDM201 in both SK-Hep-1 and HepG2 respectively (**Figure** 6.14).

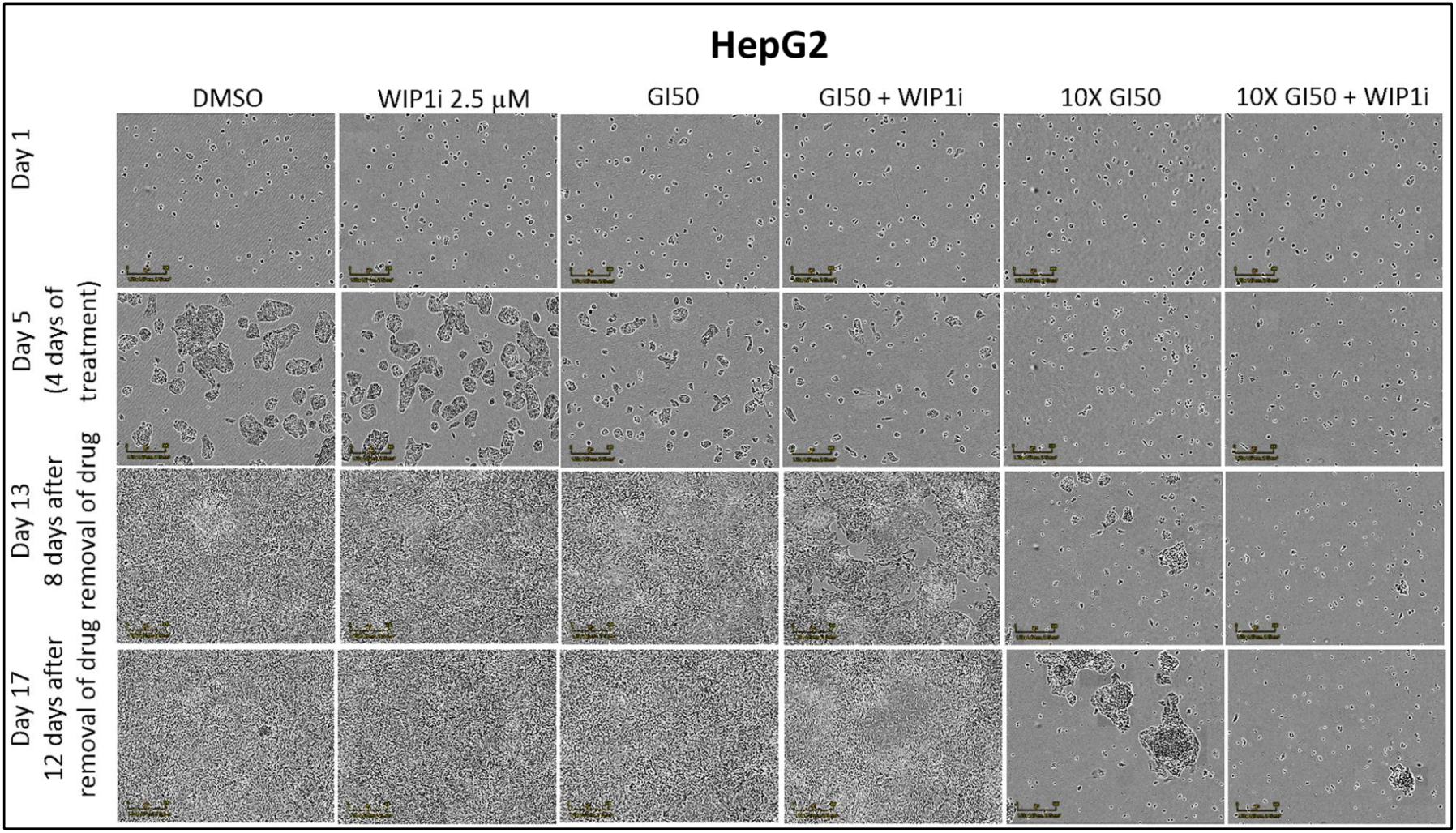

Figure 6.10: Incucyte experiment showing the effect of HDM201 alone and in combination with GSK2830371 WIP1i on HepG2 p53^{WT} liver cancer cell line. Cells were treated with the GI_{50} and 10X GI_{50} of HDM201 alone and in combination with WIP1i 2.5 µM for 96 hours. The compounds were removed by replacing the media and the cells were left to grow. Sequential pictures were taken every 6 hours. Magnification power 10X, Scale bar = 300 µM.

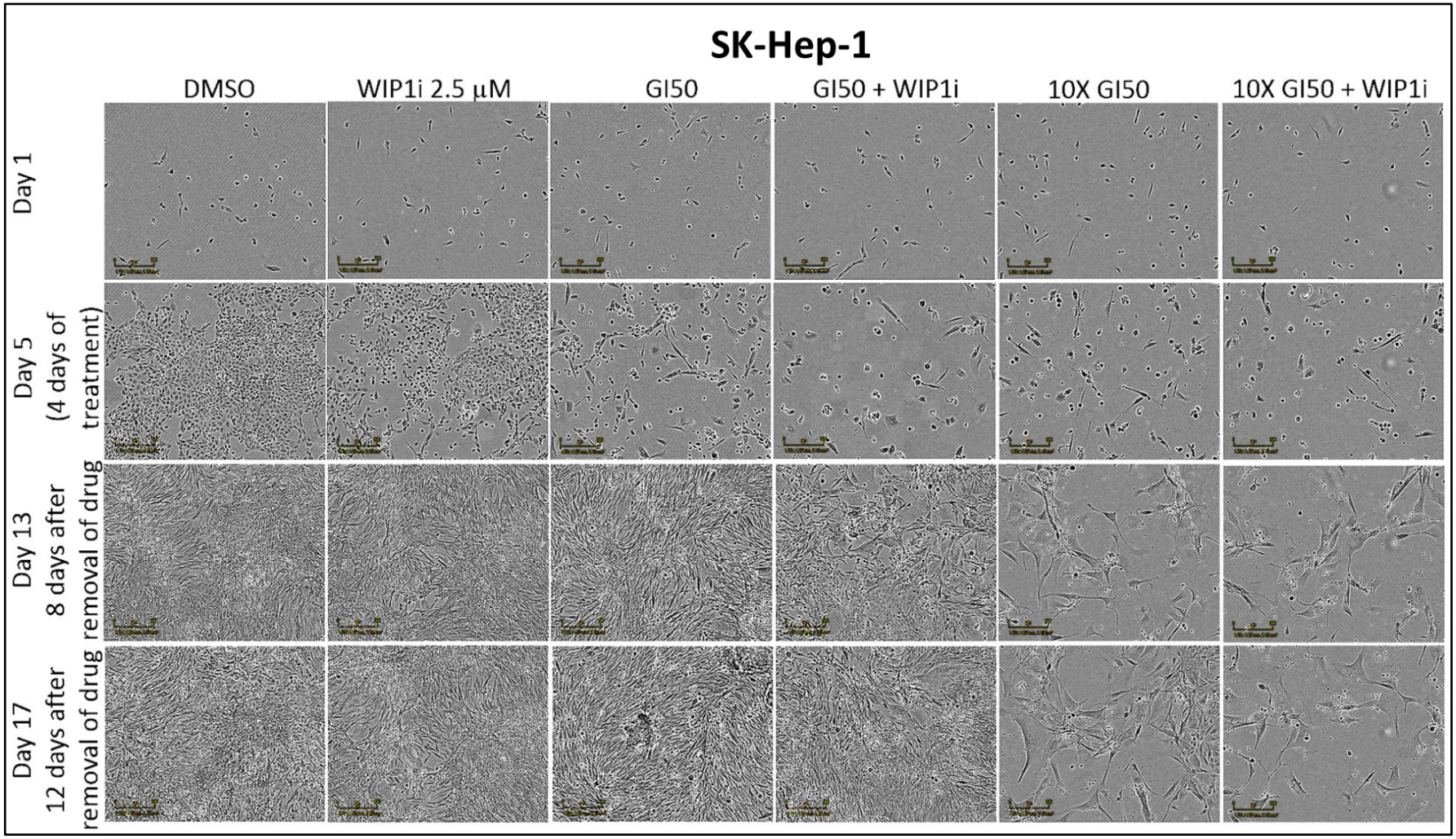

Figure 6.11: Incucyte experiment showing the effect of HDM201 alone and in combination with GSK2830371 WIP1i on SK-Hep-1 p53^{WT} liver cancer cell line. Cells were treated with the GI_{50} and 10X GI_{50} of HDM201 alone and in combination with WIP1i 2.5 µM for 96 hours. The compounds were removed by replacing the media and the cells were left to grow. Sequential pictures were taken every 6 hours. Magnification power 10X, Scale bar = 300 µM.

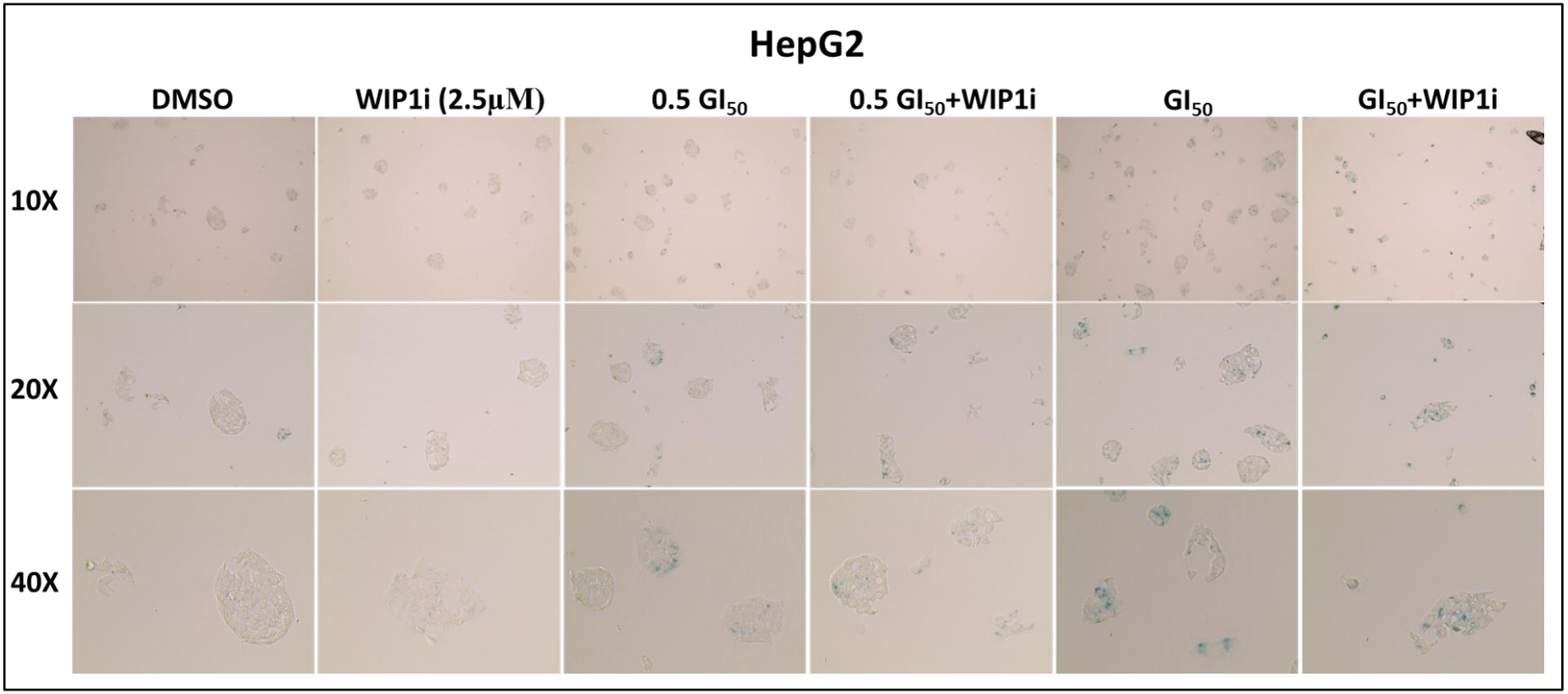

Figure 6.12: GSK2830371 WIP1i potentiates HDM201 induced senescence in HepG2 p53^{WT} liver cancer cell line. SA-β-Gal staining of HepG2 after treatment with DMSO, 0.5 GI_{50} and GI_{50} of HDM201 alone and in combination with WIP1i (2.5 µM) for 96 hours at 10X, 20X and 40X magnification power. Positive cytoplasmic staining (blue-green) is shown in a few cells in the DMSO control but the number of positive stained cells and the intensity of staining increases with the dose of HDM201 and this was further potentiated after combining HDM201 with WIP1i to include most of the cells that are treated with the combination.

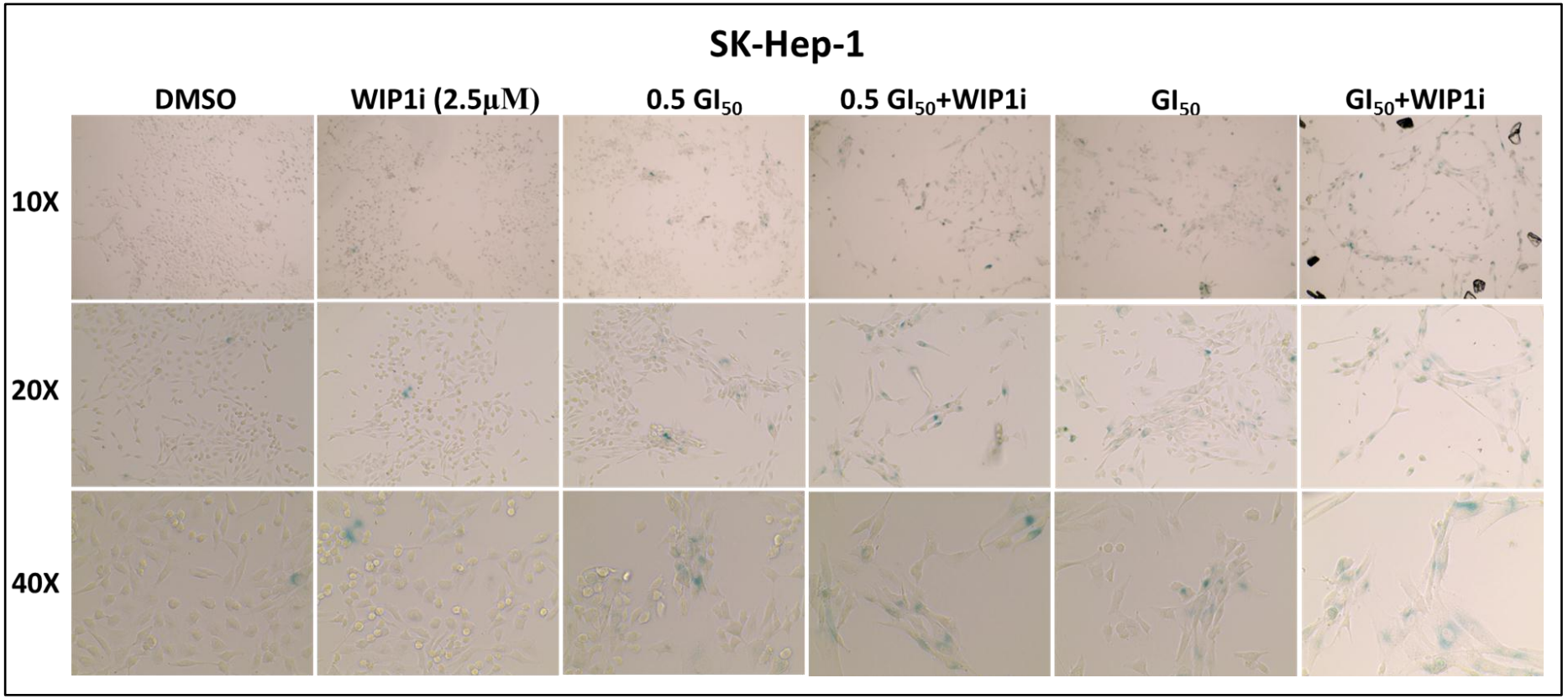

Figure 6.13: GSK2830371 WIP1i potentiates HDM201 induced senescence in SK-Hep-1 p53^{WT} liver cancer cell lines. SA-β-Gal staining of SK-Hep-1 after treatment with DMSO, 0.5 GI_{50} and GI_{50} of HDM201 alone and in combination with WIP1i (2.5 µM) for 96 hours at 10X, 20X and 40X magnification power. Positive cytoplasmic staining (blue-green) is shown in a few cells in the DMSO control but the number of positive stained cells and the intensity of staining increases with the dose of HDM201 and this was further potentiated after combining HDM201 with WIP1i to include most of the cells that are treated with the combination. SK-Hep-1 cells also showed a change in morphology, becoming larger in size compared to DMSO control.

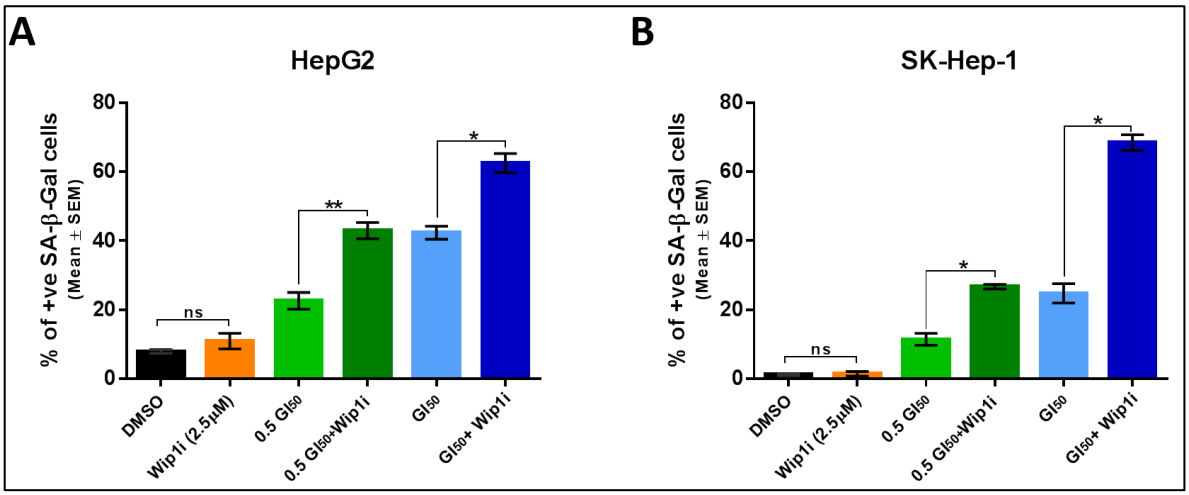

Figure 6.14: GSK2830371 WIP1i potentiation of HDM201 induced senescence in p53^{WT} liver cancer cell lines. While there was no significant difference between the DMSO control and WIP1i (2.5 μM), both p53^{WT} cell lines, HepG2 (A) and SK-Hep-1 (B) showed significant potentiation of senescence by WIP1i for both 0.5 GI_{50} (p=0.001, 0.01) and the GI_{50} doses of HDM201 (0.026, 0.01) respectively. ns= not significant. Data represent mean ± SEM of three independent repeats.

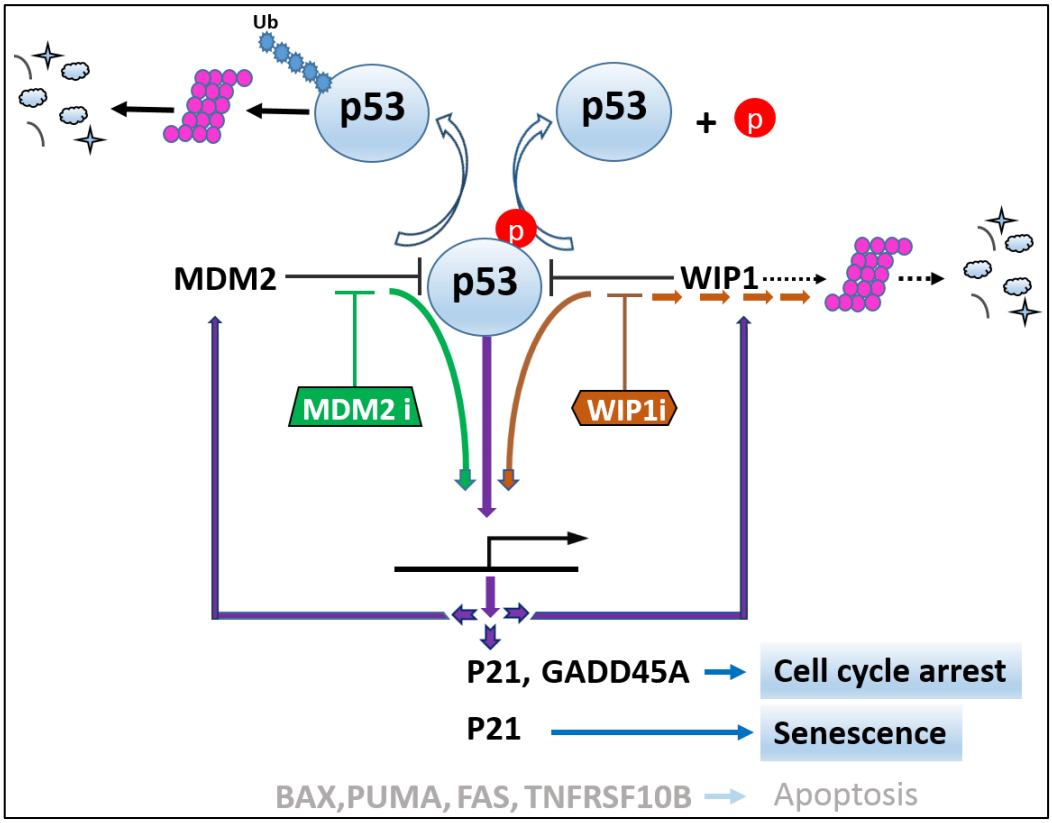

Figure 6.15: Schematic summary representing the p53 pathway and the effect of MDM2 and WIP1 inhibition. Linking p53 activation to downstream transcriptional targets that induce the dominant response of cell cycle arrest and senescence by MDM2 inhibition in HepG2 and SK-Hep-1 cells, which is potentiated by WIP1 inhibition.

6.11 The effect of GSK2830371 as a single agent and in combination with HDM201 on HepG2-Luc

Because of the potential for *in vivo* xenograft imaging, a large number of experiments was carried out to test whether the luciferase transfected HepG2-Luc cell line retained its $p53^{WT}$ status and behaves in the same way as the parental HepG2 cell line. These experiments confirmed that HepG2-Luc response to GSK2830371 as a single agent and in combination with HDM201 was the same as HepG2, in terms of growth inhibition (**Figure** 6.16**; A**), clonogenic survival (**Figure** 6.16**;B**), caspase 3/7 activity (**Figure** 6.16**; C and D**), or metabolic activity (**Figure** 6.16**; E and F**), cell cycle changes (**Figure** 6.17**; A and B**) and mRNA expression of p53 transcriptional target genes (**Figure** 6.17**; C and D**).

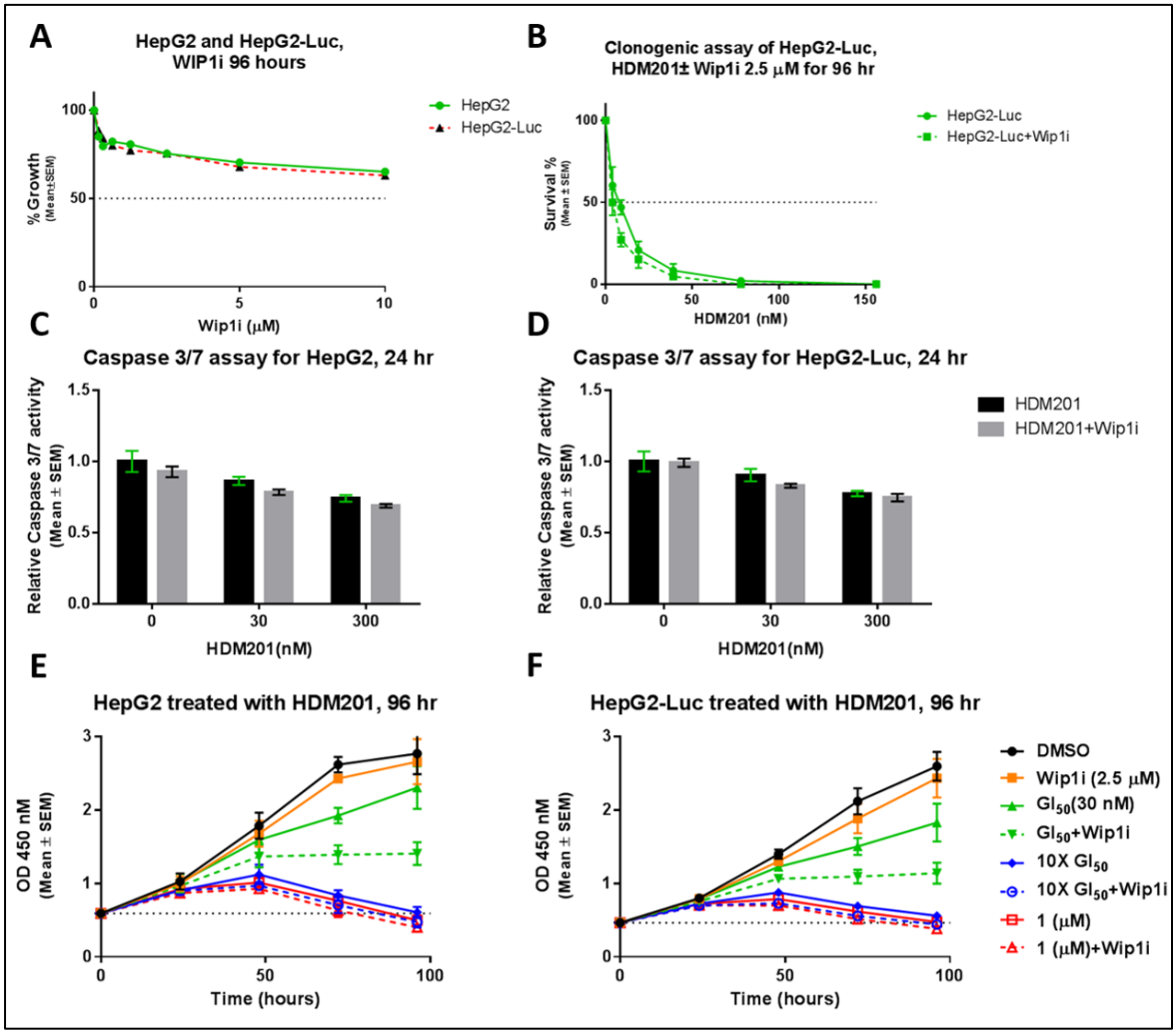

Figure 6.16: Comparison of the effect of GSK2830371 WIP1i alone and in combination with HDM201 on HepG2 and HepG2-Luc. (A) Growth inhibition assay (SRB) of HepG2 and HepG2-Luc after exposure to WIP1i (0.07-10 µM) for 96 hours. (B) Clonogenic survival assay of HepG2-Luc after exposure to HDM201 (1-156 nM) alone and in combination with WIP1i (2.5 µM) for 96 hours. (C) and (D) Caspase 3/7 assay of HepG2 and HepG2-Luc respectively after exposure to WIP1i (2.5 µM) alone and in combination with the GI_{50} and 10X GI_{50} of HDM201 for 24 hours. (E) and (F) XTT assay measuring the mitochondrial metabolic activity

of HepG2 and HepG2-Luc respectively after exposure to WIP1i (2.5 µM) alone and in combination with GI_{50} and 10X GI_{50} and 1µM of HDM201 for 96 hours. Error bars represent the standard error of the mean of three independent repeats.

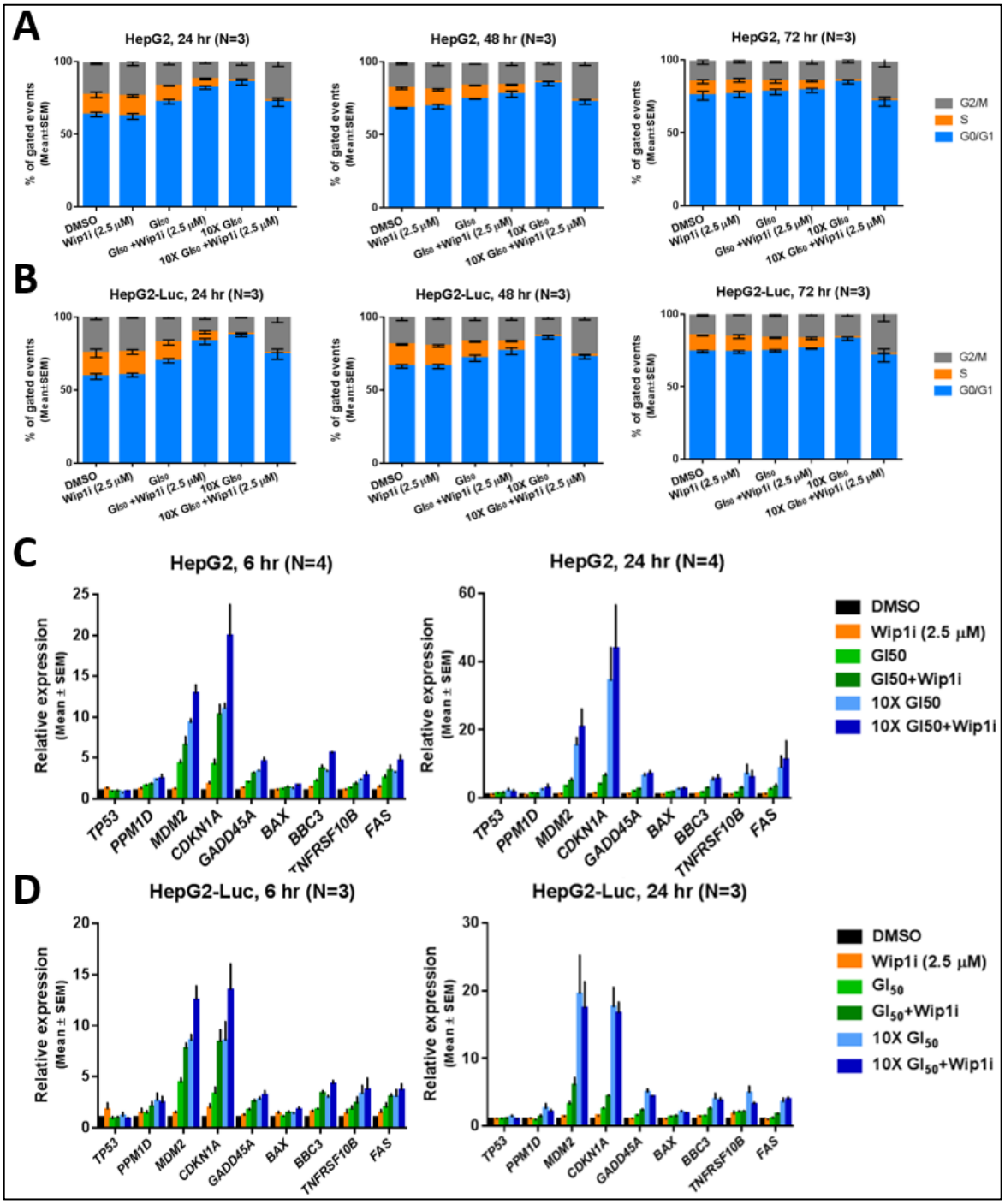

Figure 6.17: Cell cycle analysis and mRNA expression of p53 transcriptional target genes in HepG2 and HepG2-Luc. (A) and (B) FACS analysis of the cell cycle in HepG2 and HepG2-Luc respectively in response to WIP1i (2.5 µM) alone and in combination with GI_{50} and 10X GI_{50} doses of HDM201 for 24, 48 and 72 hour time points. (C) and (D) represent the expression of *TP53* and its downstream transcriptional targets by qRT-PCR in HepG2 and HepG2-Luc respectively in response to GSK2830371 WIP1i (2.5 µM) alone and in combination with GI_{50} and 10X GI_{50} doses of HDM201 for 6 and 24 hour time points. The expression was relative to DMSO control and *GAPDH* housekeeping gene was used as an internal reference. Error bars represent ±SEM for three independent repeats.

6.12 Discussion

The inhibitory effect of GSK2830371 on WIP1 phosphatase (239) was confirmed by Western blot analysis of $p53^{ser15}$ phosphorylation status and WIP1 protein levels. Even at low doses of GSK2830371 as a single agent there was a prominent reduction in WIP1 protein level with an increase in the phosphorylation of $p53^{ser15}$ and concomitant increased $p53^{Lys382}$ acetylation, in addition to a mild induction of p21 in immunoblotting of $p53^{WT}$ HepG2 and SK-Hep-1 liver cancer cell lines. This is consistent with previous reports in other types of cancer cell lines (239, 345, 346). The mild induction of p21 explains the small growth inhibitory effect of GSK2830371 alone at high doses in $p53^{WT}$ cell lines.

Recent studies including those by our own group have reported that GSK2830371 can potentiate the p53-dependent effects of Nutlin-3 and our own group extended these observations to the clinically relevant RG7388 (Idasanutlin) MDM2 inhibitor (339, 345, 346). The work described in this thesis extends these studies to liver cancer cell lines and includes the more potent and specific HDM201 inhibitor. A low dose of GSK2830371 (2.5 µM) which had minimal effect on its own was shown to significantly potentiate the growth inhibitory effect of all the three tested MDM2 inhibitors and reduced their GI_{50} by 2-3-fold and also significantly reduced the clonogenic survival (LC_{50}) of $p53^{WT}$ liver cancer cell lines.

Other studies have reported that potentiation of the effect of MDM2 inhibitors by combination with GSK2830371 and MDM2 inhibitors includes the induction of apoptosis (345, 346); but a major difference with the tested $p53^{WT}$ liver cancer cell lines was absence of the induction of apoptosis, as evidenced by no change in Sub-G1 in FACS based cell cycle analysis, no increase in the caspase 3/7 catalytic activity, no evidence of PARP cleavage by western blot and continued evidence of mitochondrial metabolic activity despite sustained inhibition of proliferation. At the protein level there was marked stabilization of p53 and increase in the levels of the phosphorylated p53 and acetylated p53 in addition to prominent increases in p53 downstream transcriptional targets MDM2 and p21.

GSK2830371 potentiated the effect of HDM201 on the induction of senescence, manifested by increased SA-β-Gal staining, as well as the increased number of cells not recovering from growth inhibition and not dividing even 12 days after removal of the drug combination. The lack of an apoptotic response and potentiation of MDM2i induced senescence by WIP1 inhibition may be a feature of some liver cancers, which should be explored further. This was supported by the observed arrest of the cells in G1 and G2 phases, together with pronounced increases in *CDKN1A* (*p21WAF1*) transcript and $p21^{WAF1}$ protein expression, which has been

reported to be necessary for senescence (347, 348). This is in accord with recent reports that combination of GSK2830371 treatment with Nutlin-3 can induce senescence in some breast and colon cancer cell lines (339, 345).

Despite the fact that PPM1D was not mutated or amplified in either of the tested $p53^{WT}$ liver cancer cell lines, chemical inhibition of WIP1 nevertheless potentiated the sensitivity of these cell lines to MDM2 inhibitors, which opens the possibility for future use of this combination in the treatment of patients with liver cancers that warrants further exploration.

In clinical trials, one of the reported dose-limiting main side effects of MDM2 inhibitors, including HDM201, is haematological (thrombocytopenia and neutropenia) (217, 314); by using combinations of HDM201 + WIP1i it may be possible to reduce the required dose of MDM2 inhibitors to induce tumour regression and growth inhibition without potentiating the side effects of using MDM2 inhibitors on their own. This could allow patients to benefit from non-genotoxic activation of p53 with minimal side effects. However, for systemic treatment this would depend on the absence of a potentiating effect on the haematological toxicity, which would have to be explored first.

Chapter 7: Summary, Conclusions and Future Directions

The incidence of HCC is increasing in many parts of the world. Despite the advances in treatment options for different types of cancers that have led to a decrease in the mortality rate over the last two decades, HCC stands out with a dramatic increase in the mortality rate. This reflects incidence, but is also attributable to typically late diagnosis due to the lack of clinical manifestations in the earlier stages, and the lack of effective treatment for advanced cases (308). NAFLD is the commonest chronic liver disease in western populations and several studies have confirmed that NAFLD is a risk factor for HCC development. NAFLD is estimated to affect 25% of the global population, and even though only 3-5% of those affected develop NASH, this still represents a huge number of people at risk of developing cirrhosis and cirrhosis related HCC (16). Recent reports also indicate that many NAFLD-HCC cases occur without cirrhosis (93). In combination, these reports suggest that the rising HCC mortality is partly attributable to NAFLD-HCC and highlight the urgent need to have a better understanding of this disease and to find a treatment for NAFLD, which would prevent the development of HCC in those patients.

It has been reported that NAFLD related HCC patients have a shorter survival by 5 months compared to other causes of HCC like hepatitis (349). This has been attributed to the fact that viral hepatitis patients more often undergo frequent screening, and also that in obese NAFLD patients who are having surveillance, early stage HCC is more difficult to detect by abdominal ultrasound scanning – the standard technique used. Furthermore, NAFLD is part of a metabolic syndrome in which other comorbidities and risk factors like cardiovascular disease that increase mortality can limit patient treatment options like surgical resection and liver transplantation. Collectively all these factors can make NAFLD–HCC a sub-category of HCC with poorer prognosis (349).

We have succeeded in our attempt to mimic the development of NAFLD and to have a better understanding of the course and progression of the disease, including the development of HCC in NAFLD. By feeding C3H/He mice the ALIOS diet (rich in trans-fatty acids and fructose sweetened water) for up to 1 year, we have created an animal model that recapitulates what happens in the general population. The mice developed obesity and NAFLD, with many of the histological features characteristic of NASH, as well as liver tumour development (shown in chapter 3). We explored two candidate interventions in an attempt to prevent HCC development in NAFLD, namely the antioxidant bucillamine and an FXR agonist (PX20606). Our hypotheses were that the use of antioxidant drug will prevent DNA damage induced by free fatty acid generated ROS, improve NASH and prevent HCC development, while the use of

FXR agonist would similarly alleviate steatosis and improve NASH through effects on the regulation of lipid metabolism.

In the dietary animal model without interventions, the mouse livers showed increases in liver weight and steatosis and increased DNA damage manifested by the elevated levels of γ-H2AX positive nuclei and increased levels of p53. Notably, liver weight increased in the aging mice, which was attributed partly to accumulation of fat, but also to an elevation in hepatocyte proliferation manifested by the elevated levels of Ki67 positive nuclei in the ALIOS fed animals. Both DNA damage and Ki67 positive hepatocytes were most prominent around the portal tracts where the fat had accumulated (periportal steatosis), in keeping with a relationship with chronic liver injury.

The main predictors of tumour development in the dietary animal model were the liver weight itself, steatosis, proliferation (Ki67) and lipogranuloma. As lipogranulomas are defined as fat surrounded by macrophages, we hypothesize that steatosis and macrophages are the main drivers of HCC development in our model, alongside the creation of a fatty liver disease induced proliferative environment.

In chapter 4 we explored the impact of dietary supplementation with bucillamine and despite showing a highly significant reduction in the DNA damage levels (γ-H2AX), and despite showing a significant effect on improvement of the NASH score, through abolition of Ballooning and improvement of fibrosis, mice nevertheless still developed tumours. Bucillamine treatment did not result in any improvement of liver weight, steatosis nor lipogranuloma – supporting further our belief that these were the key predictors of tumour development in our dietary animal model. Additionally, bucillamine did not have any effect on the proliferative environment in ALIOS animal livers, as measured by Ki67.

Presently, the mechanisms underlying the proliferative environment that promotes tumour development in this NAFLD model remain to be established. Activation of the Hedgehog pathway offers one potential candidate mechanism worthy of consideration. The Hedgehog (HH) signalling pathway got its name from the abnormal hedgehog-like protrusions on the fly larva that had mutation in this pathway. This pathway has a role in embryonic liver development. It also controls cell proliferation, migration, differentiation and survival (350-352). It consists of seven components which comprise the HH ligands, transmembrane Patched receptor (PTCH) which continuously represses the HH pathway, the transmembrane receptor smoothened (SMO) and Glioma associated oncoprotein (GLI). The pathway is repressed by

binding of PTCH to SMO in the absence of the ligand. In the presence of the ligand, the inhibitory effect of PTCH is abolished and SMO is activated, leading to re-localisation of the GLI transcription factors into the nucleus to induce transcription of several targets that controls cellular proliferation, differentiation and survival (350, 352, 353). These pathway components have been found to be mutated in different types of cancers (liver cancer, prostatic, ovarian and neuroblastoma) and contribute to their progression and development (114). Previous studies reported the expression levels of HH components to be higher than adjacent liver tissues in 65-72% of HCC cases (354).

In normal liver the HH pathway is inactivated but it has been found to be activated in chronic liver injury and responsible for hepatic progenitor cell fate - and the regeneration and development of hepatocytes. Activation of HH in hepatic stellate cells is also partly responsible for the transformation of hepatic stellate cells into myofibroblast-like cells which promote liver fibrosis (350, 351). During NAFLD there is continuous state of injury and healing therefore there is continual activation of the HH pathway, which may contribute to hepatocarcinogenesis. HH expression is reported to be increased in NAFLD liver and in ballooned hepatocytes and to correlate with the severity of NAFLD (355). Furthermore, interestingly, HH activation was found to be associated with macrophage recruitment into the liver through osteopontin production as a downstream transcriptional target of HH. Osteopontin is an extracellular matrix protein that plays a role in macrophage recruitment and activation, together with the secretion of pro-inflammatory cytokines (IL-1β, IL-6, TNF-α and monocyte chemotactic protein 1 (MCP1)) (**Figure** 7.1) (350, 355).

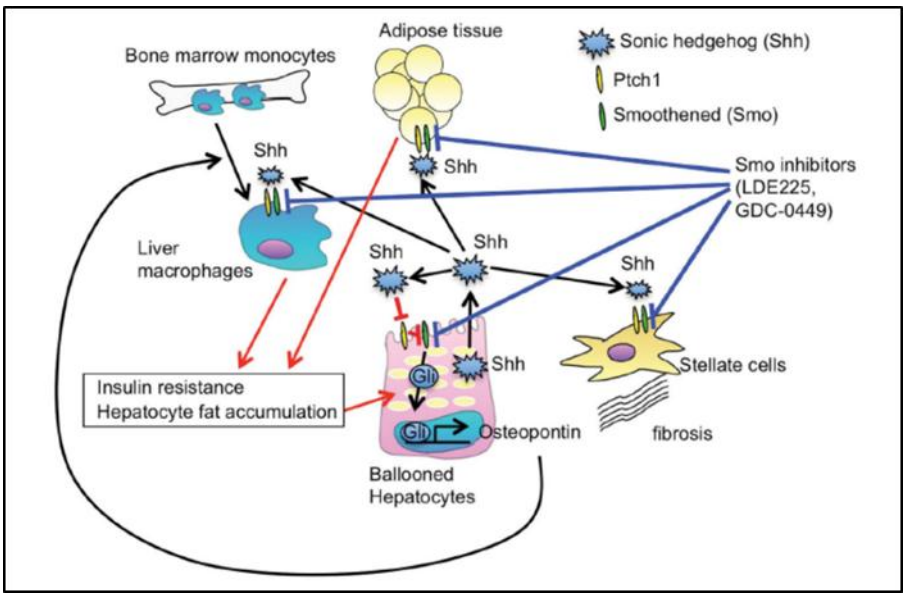

Figure 7.1: Hedgehog signalling pathway in NAFLD adapted from Seki 2016 (350). In the absence of ligand, the PTCH binds to SMO and inhibits the HH signalling. In the presence of ligand (Shh), which binds to PTCH, the inhibitory effect of PTCH on SMO is relieved. This results in activation of the HH pathway. As a result, GLI (transcriptional factor) translocate to the nucleus and induces transcription of several targets. One of the transcriptional targets is osteopontin that is produced by ballooned hepatocytes. Osteopontin induces liver accumulation of macrophages that secrete chemokines and lead to progression of NAFLD. Additionally, ballooned hepatocytes activate HH in other cell types through a paracrine effect; in the stellate cells this leads to fibrosis, in the adipocytes it leads to insulin resistance, and via the macrophages to the progression of NAFLD. The use of a SMO inhibitor suppresses HH signalling and consequently helps to prevent NAFLD progression and insulin resistance.

The second intervention in our animal model, was the FXR agonist (PX20606) (Chapter 4). Despite the previous reports that showed a beneficial effect of FXR agonist treatment in NASH, our FXR agonist PX20606 did not show a similar effect. PX20606 caused an increase in steatosis and inflammation and a significant increase in liver fibrosis. Liver enzymes were also increased. These changes were more prominent in the control diet animals. Furthermore, PX20606 did not prevent tumour development - on the contrary it caused more tumours in the control diet groups. We have been unable to pursue further mechanistic studies with PX20606. It is worth noting, however, that the effects of PX20606 in the control animals was dose related. Ideally, an agent which may have a relatively narrow therapeutic window, or where this is not defined, should be given by gavage in a more controlled fashion, rather than as a supplement in the diet. It is unlikely that the observed toxicity was a result of a 'class effect', as similar effects have not been seen with similar agents in either animal of human studies. The other point to note, was the further increase seen in Ki67 induced proliferation. FXR agonists can contribute directly to liver regeneration and in our model this may have been exacerbated as a consequence of liver injury. While this may be of benefit in the context of chronic liver injury, the association

between Ki67 and tumour formation was clear in our model. While this may be a cause for caution, the elevated risk was in control animals. While theoretically one might be concerned about a potential increase in non-cirrhotic HCC if FXR agonists are widely used, this concern should be academic only, as patients with mild NAFLD (less than F2 fibrosis in current clinical practice), should not be treated with agents to delay progression. Ideally, the research community and Pharma should openly discuss these issues and how to manage them going forward.

After our success in creating the animal model, in which we failed to prevent the development of HCC, with either intervention studied, we directed our interest to p53, and its potential role in the treatment of HCC. The incidence of *TP53* mutation in liver cancer is in less than 30% of HCC cases and additional mechanisms of its inactivation are suspected. RNA sequencing analysis of the HCC in the tumours from our animal model confirmed an absence of mutation in p53. Overall though, although the p53 pathway appeared intact, it was ineffective in our model. In the ALIOS mice, the immunohistochemical staining for p53 showed increases in the percentage of positively stained nuclei in the areas of fat accumulation and DNA damage (γ-H2AX) (periportal). The p53 protein showed a positive correlation with *Cdkn1a* (*p21*) mRNA, suggesting it was functional. Additionally, the percentage of p53 positive nuclei was higher in tumours compared to the peritumoural area. In addition, the p53 downstream target *Cdkn1a* (*p21*) showed a striking increase at the mRNA level in tumours compared to non-tumours. Despite the increase in p53 and the 14 fold increase in *Cdkn1a* (*p21*), a large number of tumours did not express p21 protein and this increase in p53 was not sufficient to stop tumour development and proliferation.

Focused subsequently on p53, we hypothesised that exploiting the p53 pathway through non-genotoxic activation of p53 would cause growth inhibition of $p53^{WT}$ liver cancer cell lines and could be of use in treating $p53^{WT}$ HCC.

In chapter 5 we showed that small molecule inhibitors of MDM2 cause growth inhibition of $p53^{WT}$ liver cancer cell lines (HepG2 and SK-Hep-1) and that this can be achieved by nanomolar range doses of the clinically relevant MDM2 inhibitor, HDM201. This was shown by SRB growth inhibition and clonogenic cell survival assays. Supporting evidence of mechanism was provided by the prominent stabilisation of p53 and the increase in *TP53* downstream transcriptional targets (*CDKN1A* (p21) and *MDM2*) by qRT-PCR and Western blotting analysis (Chapter 5). But notably, the growth inhibition by HDM201 was not accompanied by any signs of apoptosis; there was no increase in caspase 3/7 activity nor of the apoptotic markers on

Western blot analysis. Furthermore, the cells maintained their mitochondrial activity (measured by XTT assay) despite prolonged growth inhibition following MDM2 inhibition. This prompted us to further hypothesise that non genotoxic activation of p53 through MDM2-p53 inhibition will induce senescence in p53WT liver cancer cell lines.

Leonard Hayflick and Paul Moorhead reported senescence more than 50 years ago (356). Senescence (which describes a permanent cell cycle arrest) is a potent tumour suppressor mechanism (357). Several reports indicated that activation of p53 in tumour cells, even if it was transient, can induce tumour regression, and this regression is tumour type dependent. It has been reported that activation of p53 induces apoptosis in some cells types but in the absence of apoptosis can produce reversible growth arrest, or induce senescence in other cell types, e.g. apoptosis in lymphoid cells and senescence in HCC and some types of sarcoma (357). The role of p53 and induction of senescence in liver cancer has been reported for KrasV12 transduced embryonic hepatoblasts injected subcutaneously or into the livers of mice, which then develop tumours. The mice in that study had doxycycline-inducible p53, and upon doxycycline treatment, even for 2 days, there was p53 activation which induced senescence shown by SA-β-Gal positive staining and p16 and p15 positivity (210, 337). The tumours not only showed senescence, they showed regression. The regression was through recruitment of inflammatory cells (macrophages, neutrophils and natural killer cells) that caused the involution of tumours by immune clearance. This was achieved through the chemokines secreted by the senescent tumour cells, like monocyte chemoattractant protein1 (MCP1) that recruits macrophages. Neutrophil activating protein 3 or CXCL1 that attracts neutrophils was elevated, as was IL15 that induces activation and proliferation of natural killer cells (210). This tumour regression was absent in tumours grown in immunocompromised NSG mice, confirming the role of innate immunity in tumour clearance (210, 337).

In (chapter 5) and through our *in vitro* work and *in vivo* HepG2 xenograft model we confirmed our hypothesis. We showed for the first time that non-genotoxic activation of p53 through inhibition of MDM2-p53 caused p53-dependent growth inhibition resulting from the induction of senescence in $p53^{WT}$ liver cancer cell lines (HepG2 and SK-Hep-1). For this we used the small molecule inhibitor of MDM2, HDM201. This was evidenced by the significant increase in *CDKN1A* at both the mRNA level and the protein level, which was associated with cell cycle arrest and positive staining for the senescence marker, SA-β-Gal. In addition, Incucyte experiments showed through time-lapse image capture that the $p53^{WT}$ liver cancer cells failed to proliferate after removal of HDM201.

In the *in vivo* study, treatment of the NSG mice with HDM201 at a dose of 100 mg/kg/day for 10 days caused sustained tumour growth delay after treatment was stopped. This was most probably through induction of senescence. However, due to the experiment planning and the need to use severely immunocompromised NSG mice that lack natural killer, B and T lymphocytes, we could not investigate the presence of senescence in our treated xenografts, nor study the effect of senescence induced immune clearance of tumour cells.

After the encouraging results with MDM2 inhibitors described in chapter 5, we decided to take a step further and explore the effect of GSK2830371, a small molecule inhibitor of WIP1, another downstream target of p53. WIP1 is part of an additional negative autoregulatory feedback loop, which in this case downregulates p53 function through dephosphorylation of p53 protein. From the literature it has been reported that WIP1 is overexpressed in approximately 59-65% of HCC cases and is associated with poor prognosis (229, 232). As it is a negative regulator of p53 function, we hypothesised that inhibition of WIP1 would help to maintain p53 in its active phosphorylated state and accentuate the effect of p53 release by MDM2 inhibitors, thereby potentiating growth inhibition by MDM2 inhibitors in $p53^{WT}$ HCC cell lines. In chapter 6 we showed that GSK2830371 (WIP1i) on its own did not have a big inhibitory effect on the growth of liver cancer cell lines. There was a mild growth inhibitory effect, but it did not exceed 23% at a dose of 2.5 μM in $p53^{WT}$ liver cancer cell lines, which was chosen for subsequent combination studies with MDM2 inhibitors.

Combined targeting of both the PPM1D/WIP1 and MDM2 negative feedback suppressors of p53 in *TP53* wild-type human liver cancer cells was confirmed to potentiate the growth inhibitory effects of these compounds. This was shown *in vitro* with a dose of GSK2830371 (WIP1i), which had minimal effect on its own, producing several-fold reductions in the doses of MDM2 inhibitors to achieve GI_{50} and LC_{50} levels of growth inhibition and clonogenic survival for $p53^{WT}$ liver cancer cell lines (HepG2 and SK-Hep-1). The combination with GSK2830371 increased stabilisation of total and phosphorylated p53 and the expression of p53 downstream targets (p21 and MDM2) at the mRNA and protein level compared to MDM2 inhibitors alone. GSK2830371 also potentiated the effect of HDM201 on arresting the cell cycle and on the induction of senescence, shown by increased numbers of SA-β-Gal positively stained liver cancer cell lines in the presence of combined GSK2830371 and HDM201 treatment.

In summary,

- Using a combination of C3H/He mice and the ALIOS diet, an animal model of the metabolic syndrome associated with NAFLD, NAFLD progression to NASH and fibrosis, and development of HCC was created.
- DNA damage (γ-H2AX) was increased upon feeding ALIOS diet and DNA damage response (p53) was increased and both correlated with NAFLD progression.
- Age, as well as steatosis contributed to the creation of a proliferative environment (Ki67) that associated with tumour development.
- Liver weight, steatosis grade, lipogranuloma were independent predictors of tumour development
- The Bucillamine intervention reduced DNA damage and reduced ballooning and fibrosis but did not reduce liver weight, steatosis, lipogranuloma nor Ki67 and did not prevent tumour development.
- The FXR agonist (PX20606) did not improve NAFLD in ALIOS fed animals and caused worsening of NAFLD in the control diet animals, in association with an increase in the number of tumours in the control animals.
- All NAFLD-HCC were of p53 wild type status.
- p53 was not adequately functional as a tumour suppressor, despite its wild type status and despite elevated *Cdkn1a*(p21) expression.
- We nevertheless showed the p53 pathway could be exploited through non-genotoxic activation of p53 by MDM2-p53 binding antagonists that caused growth inhibition of $p53^{WT}$ liver cancer cell lines *in vitro* and *in vivo* through induction of senescence. This may be relevant for the future treatment of patients with $p53^{WT}$ HCC.
- Combined targeting of the PPM1D/WIP1 and MDM2 negative feedback suppressors of p53 in *TP53* wild-type human liver cancer cells was demonstrated through the use of GSK2830371 (WIP1 inhibitor) which potentiated the effect of the MDM2 inhibitor (HDM201) on the induction of senescence in $p53^{WT}$ liver cancer cell lines.

Future directions:

1)- Detailed comparative analysis of the RNAseq data from the dietary animal model liver samples, between samples from the control and ALIOS treated mice and in the tumour samples will enable us to have a better understanding of the changes induced by the ALIOS diet and the changes that accompanied and led to hepatocarcinogenesis.

2)- Immunophenotyping of the liver and HCC FFPE tissue section to have a better understanding of the role of immunity in NAFLD progression and tumour development - in light of our data showing steatosis and lipogranuloma (macrophages) to be the independent predictors of tumour development. Several markers of inflammatory cells are suggested for characterisation (F4/80, CD4, CD8, Ly6C and neutrophil elastase).

3)- Exploring the expression of Hedgehog pathway components in our animal model.

4)- To further support the evidence of MDM2 inhibition induced senescence in $p53^{WT}$ cell lines and xenografts, staining for Ki67 can be helpful, as the absence of Ki67 staining should help to recognise senescent cells. Additional markers of senescence that can be tested and probed for include p16 and p15 cyclin dependent kinase inhibitors, transforming growth factor-β (TGFβ), plasminogen activator inhibitor 1 (PAI1), insulin-like growth factor 1 (IGF1)-binding proteins, DEC1 (also known as TNFRSF10C) and decoy receptor 2 (DCR2; also known as TNFRSF10D) (356).

4)- To further support that p21 is the main factor responsible for MDM2 inhibitor induced-senescence, knocking down p21 expression in $p53^{WT}$ liver cancer cell lines (HepG2 and SK-Hep-1) followed by treatment with MDM2 inhibitors for the same duration (96 hours), and then testing for markers of senescence, like SA-β-Gal staining, will clarify whether this senescence induction was p21 mediated and dependent.

5)- The *in vivo* effects need further work. To clearly show that MDM2 inhibitor treatment activated p53 and lead to increase in *TP53* downstream transcriptional targets in HepG2 xenografts, we suggest repeating the xenograft model with the same dose but culling the animals immediately after stopping treatment. This would facilitate assessment of p53 reactivation and evidence of its downstream targets p21 and MDM2 in the xenograft tumours at the protein level (IHC and Western blot) as well as detection at the RNA level, using real time PCR. Evidence of senescence could be tested using other markers of senescence, like SA-β-Gal staining of the xenografts or other markers like p16 and p15.

6)- Loco regional delivery of MDM2 inhibitors as a treatment option for HCC. The main systemic side effects of MDM2 inhibitors are haematological, to reduce these side effects loco regional delivery of the MDM2 inhibitors to HCC may be useful to avoid or minimise these side effects. This can be achieved through TACE, but instead of loading the beads with doxorubicin that is commonly used in TACE, MDM2 inhibitors can be loaded onto the beads and in this way patients with HCC of $p53^{WT}$ status should benefit from the effect of p53 activation through MDM2 inhibitors in their tumours without having to expose all the body tissues to the effect of these drugs.

7)- Combining MDM2 inhibitors and other drugs in the treatment of HCC. The only first line systemic FDA approved treatment for HCC is the multikinase inhibitor sorafenib (308). We showed that the use of MDM2 inhibitors have a significant growth inhibitory effect on $p53^{WT}$ liver cancer *in vitro* and *in vivo* in chapter 5. Both drugs (HDM201 and sorafenib) are known to have side effects, sorafenib associated with the hand-foot syndrome and gastrointestinal disturbances, while HDM201/MDM2 inhibitors have dose dependent myelosuppression. The use of combination treatment of more than one compound aims at reducing the required dose and have a synergistic effect on inhibiting tumour growth. Several reports in acute myeloid leukemia and renal cell carcinoma indicated that the combined treatment of MDM2 inhibitors and sorafenib is synergistic, with increased growth inhibition and apoptosis and decreased migration of cancer cells (358, 359). Based on our initial *in vitro* data, another suggested combination worth pursuing is the combination of MDM2 inhibitors with a WIP1 inhibitor.

Limitations of our work:

One of the main limitations of the dietary animal model and the interventions used was delivering accurate doses. Because of the large number of animals and the long duration of the study, delivering accurate doses of bucillamine and PX20606 through oral gavage was a big challenge, therefore we used an estimate method of delivering the drugs through calculating the weekly average consumption of food by mice and accordingly integrated the drug of choice with the food pellet, but having several mice per cage (4) made delivering accurate doses challenging. Assessing whether the drugs were reaching therapeutic levels in the treated animals after this method of drug delivery can be assessed. This can be achieved directly through checking drug levels in the collected blood samples from the treated mice or indirectly through assessing the expression of FXR-target genes (e.g. FGF19) at the protein level through IHC or western blotting.

The second limitation was the difficulty in getting specific antibodies for immunohistochemical staining and Western blotting due to the fact that the vast majority of the specific and sensitive antibodies are mouse monoclonal antibodies designed against human versions of the protein targets. Our study was in mice, therefore it was not practically possible to use mouse antibodies and we had to search for antibodies from different species that were mostly polyclonal and less specific than the mouse monoclonal antibodies.

Another limitation of the *in vitro* work was the lack of a p53 wild type hepatocellular carcinoma cell line, as both p53WT cell lines used were of Hepatoblastoma origin (HepG2) and cholangiocarcinoma (SK-Hep-1). The vast majority if not all the available HCC cell lines were of $p53^{MUT}$ and those that were supposed to be $p53^{WT}$ HCC cell lines, after thorough search at the time of the study appeared to be not HCC but other types of liver tumours e.g Huh-6 clone 5 which is supposed to be p53 wild type was another hepatoblastoma cell line. To overcome this obstacle we tried to grow our own primary liver cancer cell line using surgical biopsy tumour sample taken from patient with HCC. Unfortunately, after few passages the cells stopped growing and underwent senescence manifested by morphological changes. This was probably mediated by p53, which might explain the rarity of $p53^{WT}$ HCC cell lines and that our two $p53^{WT}$ liver cancer cell lines were harbouring Ras mutations that probably enabled them to overcome this and continue to proliferate in cell culture.

References

1. Vinay Kumar, Abul K. Abbas, Fausto. N. Robbins & Cotran's Pathologic Basis of Disease. Seventh edition. Philadelphia, PA : Elsevier/Saunders; 2004.

2. Pocock G, Richards CD, Richards DA. Human physiology. Fourth edition. Oxford : Oxford University Press; 2012.

3. Angulo P, Lindor KD. Non-alcoholic fatty liver disease. Journal of Gastroenterology and Hepatology. 2002;17 Suppl:S186-90.

4. Cao G, Yi T, Liu Q, Wang M, Tang S. Alcohol consumption and risk of fatty liver disease: a meta-analysis. Peer J. 2016;4:e2633.

5. Wesolowski SR, Kasmi KC, Jonscher KR, Friedman JE. Developmental origins of NAFLD: a womb with a clue. Nature Reviews Gastroenterology & Hepatology. 2017;14(2):81-96.

6. Rafiq N, Bai C, Fang Y, Srishord M, McCullough A, Gramlich T, et al. Long-term follow-up of patients with nonalcoholic fatty liver. Clinical Gastroenterology and Hepatology. 2009;7(2):234-8.

7. Smith BW, Adams LA. Non-alcoholic fatty liver disease. Critical Reviews in Clinical Laboratory Sciences. 2011;48(3):97-113.

8. Ballestri S, Nascimbeni F, Baldelli E, Marrazzo A, Romagnoli D, Lonardo A. NAFLD as a sexual dimorphic disease: role of gender and reproductive status in the development and progression of nonalcoholic fatty liver disease and inherent cardiovascular risk. Advances in Therapy. 2017;34(6):1291-326.

9. Shaw JE, Sicree RA, Zimmet PZ. Global estimates of the prevalence of diabetes for 2010 and 2030. Diabetes Research and Clinical Practice. 2010;87(1):4-14.

10. Dommermuth R, Ewing K. Metabolic syndrome: systems thinking in heart disease. Primary Care. 2018;45(1):109-29.

11. Yu J, Shen J, Sun TT, Zhang X, Wong N. Obesity, insulin resistance, NASH and hepatocellular carcinoma. Seminars in Cancer Biology. 2013;23(6 Pt B):483-91.

12. Temple JL, Cordero P, Li J, Nguyen V, Oben JA. A guide to non-alcoholic fatty liver disease in childhood and adolescence. International Journal of Molecular Sciences. 2016;17(6).

13. Engin A. The Definition and Prevalence of Obesity and Metabolic Syndrome. Advances in Experimental Medicine and Biology. 2017;960:1-17.

14. Chen CL, Yang HI, Yang WS, Liu CJ, Chen PJ, You SL, et al. Metabolic factors and risk of hepatocellular carcinoma by chronic hepatitis B/C infection: a follow-up study in Taiwan. Gastroenterology. 2008;135(1):111-21.

15. Polesel J, Zucchetto A, Montella M, Dal Maso L, Crispo A, La Vecchia C, et al. The impact of obesity and diabetes mellitus on the risk of hepatocellular carcinoma. Annals of Oncology. 2009;20(2):353-7.

16. Younossi ZM, Koenig AB, Abdelatif D, Fazel Y, Henry L, Wymer M. Global epidemiology of nonalcoholic fatty liver disease-Meta-analytic assessment of prevalence, incidence, and outcomes. Hepatology. 2016;64(1):73-84.

17. Williams CD, Stengel J, Asike MI, Torres DM, Shaw J, Contreras M, et al. Prevalence of nonalcoholic fatty liver disease and nonalcoholic steatohepatitis among a largely middle-aged population utilizing ultrasound and liver biopsy: a prospective study. Gastroenterology. 2011;140(1):124-31.

18. Calle EE, Rodriguez C, Walker-Thurmond K, Thun MJ. Overweight, obesity, and mortality from cancer in a prospectively studied cohort of U.S. adults. The New England Journal of Medicine. 2003;348(17):1625-38.

19. Vernon G, Baranova A, Younossi ZM. Systematic review: the epidemiology and natural history of non-alcoholic fatty liver disease and non-alcoholic steatohepatitis in adults. Alimentary Pharmacology & Therapeutics. 2011;34(3):274-85.

20. Ogden CL, Carroll MD, Lawman HG, Fryar CD, Kruszon-Moran D, Kit BK, et al. Trends in obesity prevalence among children and adolescents in the United States, 1988-1994 through 2013-2014. JAMA. 2016;315(21):2292-9.

21. Ferreira DM, Simao AL, Rodrigues CM, Castro RE. Revisiting the metabolic syndrome and paving the way for microRNAs in non-alcoholic fatty liver disease. The FEBS Journal. 2014;281(11):2503-24.

22. Hubscher SG. Histological assessment of non-alcoholic fatty liver disease. Histopathology. 2006;49(5):450-65.

23. Lavine JE, Schwimmer JB. Nonalcoholic fatty liver disease in the pediatric population. Clinics in Liver Disease. 2004;8(3):549-58, viii-ix.

24. Schwimmer JB, Deutsch R, Kahen T, Lavine JE, Stanley C, Behling C. Prevalence of fatty liver in children and adolescents. Pediatrics. 2006;118(4):1388-93.

25. Fan JG, Zhu J, Li XJ, Chen L, Li L, Dai F, et al. Prevalence of and risk factors for fatty liver in a general population of Shanghai, China. Journal of Hepatology. 2005;43(3):508-14.

26. Shen L, Fan JG, Shao Y, Zeng MD, Wang JR, Luo GH, et al. Prevalence of nonalcoholic fatty liver among administrative officers in Shanghai: an epidemiological survey. World Journal of Gastroenterology. 2003;9(5):1106-10.

27. Agopian VG, Kaldas FM, Hong JC, Whittaker M, Holt C, Rana A, et al. Liver transplantation for nonalcoholic steatohepatitis: the new epidemic. Annals of Surgery. 2012;256(4):624-33.

28. Renehan AG, Tyson M, Egger M, Heller RF, Zwahlen M. Body-mass index and incidence of cancer: a systematic review and meta-analysis of prospective observational studies. Lancet. 2008;371(9612):569-78.

29. Abdelmalek MF, Suzuki A, Guy C, Unalp-Arida A, Colvin R, Johnson RJ, et al. Increased fructose consumption is associated with fibrosis severity in patients with nonalcoholic fatty liver disease. Hepatology. 2010;51(6):1961-71.

30. Stanhope KL, Schwarz JM, Keim NL, Griffen SC, Bremer AA, Graham JL, et al. Consuming fructose-sweetened, not glucose-sweetened, beverages increases visceral adiposity and lipids and decreases insulin sensitivity in overweight/obese humans. The Journal of Clinical Investigation. 2009;119(5):1322-34.

31. Wolk A, Gridley G, Svensson M, Nyren O, McLaughlin JK, Fraumeni JF, et al. A prospective study of obesity and cancer risk (Sweden). Cancer Causes & Control. 2001;12(1):13-21.

32. Day CP, James OF. Steatohepatitis: a tale of two "hits"? Gastroenterology. 1998;114(4):842-5.

33. Tilg H, Moschen AR. Evolution of inflammation in nonalcoholic fatty liver disease: the multiple parallel hits hypothesis. Hepatology. 2010;52(5):1836-46.

34. Saltiel AR, Kahn CR. Insulin signalling and the regulation of glucose and lipid metabolism. Nature. 2001;414(6865):799-806.

35. Perez-Carreras M, Del Hoyo P, Martin MA, Rubio JC, Martin A, Castellano G, et al. Defective hepatic mitochondrial respiratory chain in patients with nonalcoholic steatohepatitis. Hepatology. 2003;38(4):999-1007.

36. Hirosumi J, Tuncman G, Chang L, Gorgun CZ, Uysal KT, Maeda K, et al. A central role for JNK in obesity and insulin resistance. Nature. 2002;420(6913):333-6.

37. Schultz A, Neil D, Aguila MB, Mandarim-de-Lacerda CA. Hepatic adverse effects of fructose consumption independent of overweight/obesity. International Journal of Molecular Sciences. 2013;14(11):21873-86.

38. Browning JD, Horton JD. Molecular mediators of hepatic steatosis and liver injury. The Journal of Clinical Investigation. 2004;114(2):147-52.

39. Walker AK, Yang F, Jiang K, Ji JY, Watts JL, Purushotham A, et al. Conserved role of SIRT1 orthologs in fasting-dependent inhibition of the lipid/cholesterol regulator SREBP. Genes & Development. 2010;24(13):1403-17.

40. Choi SE, Kemper JK. Regulation of SIRT1 by microRNAs. Molecules and Cells. 2013;36(5):385-92.

41. Lee J, Padhye A, Sharma A, Song G, Miao J, Mo YY, et al. A pathway involving farnesoid X receptor and small heterodimer partner positively regulates hepatic sirtuin 1 levels via microRNA-34a inhibition. The Journal of Biological Chemistry. 2010;285(17):12604-11.

42. Purushotham A, Schug TT, Xu Q, Surapureddi S, Guo X, Li X. Hepatocyte-specific deletion of SIRT1 alters fatty acid metabolism and results in hepatic steatosis and inflammation. Cell Metabolism. 2009;9(4):327-38.

43. Fulop P, Derdak Z, Sheets A, Sabo E, Berthiaume EP, Resnick MB, et al. Lack of UCP2 reduces Fas-mediated liver injury in ob/ob mice and reveals importance of cell-specific UCP2 expression. Hepatology. 2006;44(3):592-601.

44. Pogribny IP, Starlard-Davenport A, Tryndyak VP, Han T, Ross SA, Rusyn I, et al. Difference in expression of hepatic microRNAs miR-29c, miR-34a, miR-155, and miR-200b is associated with strain-specific susceptibility to dietary nonalcoholic steatohepatitis in mice. Laboratory Investigation. 2010;90(10):1437-46.

45. Farrell GC, Larter CZ, Hou JY, Zhang RH, Yeh MM, Williams J, et al. Apoptosis in experimental NASH is associated with p53 activation and TRAIL receptor expression. Journal of Gastroenterology and Hepatology. 2009;24(3):443-52.

46. Cazanave SC, Mott JL, Elmi NA, Bronk SF, Werneburg NW, Akazawa Y, et al. JNK1-dependent PUMA expression contributes to hepatocyte lipoapoptosis. The Journal of Biological Chemistry. 2009;284(39):26591-602.

47. Wang Y, Ausman LM, Russell RM, Greenberg AS, Wang XD. Increased apoptosis in high-fat diet-induced nonalcoholic steatohepatitis in rats is associated with c-Jun NH2-terminal kinase activation and elevated proapoptotic Bax. The Journal of Nutrition. 2008;138(10):1866-71.

48. Hirsova P, Ibrahim SH, Krishnan A, Verma VK, Bronk SF, Werneburg NW, et al. Lipid-induced signaling causes release of inflammatory extracellular vesicles from hepatocytes. Gastroenterology. 2016;150(4):956-67.

49. Ibrahim SH, Hirsova P, Gores GJ. Non-alcoholic steatohepatitis pathogenesis: sublethal hepatocyte injury as a driver of liver inflammation. Gut. 2018.

50. Hirsova P, Gores GJ. Ballooned hepatocytes, undead cells, sonic hedgehog, and vitamin E: therapeutic implications for nonalcoholic steatohepatitis. Hepatology. 2015;61(1):15-7.

51. Ibrahim SH, Hirsova P, Tomita K, Bronk SF, Werneburg NW, Harrison SA, et al. Mixed lineage kinase 3 mediates release of C-X-C motif ligand 10-bearing chemotactic extracellular vesicles from lipotoxic hepatocytes. Hepatology. 2016;63(3):731-44.

52. Povero D, Panera N, Eguchi A, Johnson CD, Papouchado BG, de Araujo Horcel L, et al. Lipid-induced hepatocyte-derived extracellular vesicles regulate hepatic stellate cell via microRNAs targeting PPAR-gamma. Cellular and Molecular Gastroenterology and Hepatology. 2015;1(6):646-63.e4.

53. Povero D, Eguchi A, Niesman IR, Andronikou N, de Mollerat du Jeu X, Mulya A, et al. Lipid-induced toxicity stimulates hepatocytes to release angiogenic microparticles that require Vanin-1 for uptake by endothelial cells. Science Signaling. 2013;6(296):ra88.

54. Garcia-Martinez I, Santoro N, Chen Y, Hoque R, Ouyang X, Caprio S, et al. Hepatocyte mitochondrial DNA drives nonalcoholic steatohepatitis by activation of TLR9. The Journal of Clinical Investigation. 2016;126(3):859-64.

55. Ma J, Zhou Q, Li H. Gut microbiota and nonalcoholic fatty liver disease: Insights on mechanisms and therapy. Nutrients. 2017;9(10).

56. Backhed F, Ding H, Wang T, Hooper LV, Koh GY, Nagy A, et al. The gut microbiota as an environmental factor that regulates fat storage. Proceedings of the National Academy of Sciences of the United States of America. 2004;101(44):15718-23.

57. Caesar R, Reigstad CS, Backhed HK, Reinhardt C, Ketonen M, Lunden GO, et al. Gut-derived lipopolysaccharide augments adipose macrophage accumulation but is not essential for impaired glucose or insulin tolerance in mice. Gut. 2012;61(12):1701-7.

58. Cani PD, Amar J, Iglesias MA, Poggi M, Knauf C, Bastelica D, et al. Metabolic endotoxemia initiates obesity and insulin resistance. Diabetes. 2007;56(7):1761-72.

59. Wang Z, Klipfell E, Bennett BJ, Koeth R, Levison BS, Dugar B, et al. Gut flora metabolism of phosphatidylcholine promotes cardiovascular disease. Nature. 2011;472(7341):57-63.

60. Corbin KD, Zeisel SH. Choline metabolism provides novel insights into nonalcoholic fatty liver disease and its progression. Current Opinion in Gastroenterology. 2012;28(2):159-65.

61. Lim JS, Mietus-Snyder M, Valente A, Schwarz JM, Lustig RH. The role of fructose in the pathogenesis of NAFLD and the metabolic syndrome. Nature Reviews Gastroenterology & Hepatology. 2010;7(5):251-64.

62. Delarue J, Normand S, Couet C, Pachiaudi C, Urbain C, Lamisse F, et al. Effects of free fatty acids on the metabolic response to oral fructose in lean healthy humans. International Journal of Obesity and Related Metabolic Disorders. 1996;20(2):130-6.

63. McGarry JD. Malonyl-CoA and carnitine palmitoyltransferase I: an expanding partnership. Biochemical Society Transactions. 1995;23(3):481-5.

64. Magee N, Zou A, Zhang Y. Pathogenesis of nonalcoholic steatohepatitis: Interactions between liver parenchymal and nonparenchymal cells. BioMed Research International. 2016;2016:5170402.
65. Caligiuri A, Gentilini A, Marra F. Molecular pathogenesis of NASH. International Journal of Molecular Sciences. 2016;17(9).
66. Feldman A, Eder SK, Felder TK, Kedenko L, Paulweber B, Stadlmayr A, et al. Clinical and metabolic characterization of lean caucasian subjects with non-alcoholic fatty liver. The American Journal of Gastroenterology. 2017;112(1):102-10.
67. Benedict M, Zhang X. Non-alcoholic fatty liver disease: An expanded review. World Journal of Hepatology. 2017;9(16):715-32.
68. Bedossa P, Poitou C, Veyrie N, Bouillot JL, Basdevant A, Paradis V, et al. Histopathological algorithm and scoring system for evaluation of liver lesions in morbidly obese patients. Hepatology. 2012;56(5):1751-9.
69. Kleiner DE, Makhlouf HR. Histology of nonalcoholic fatty liver disease and nonalcoholic steatohepatitis in adults and children. Clinics in Liver Disease. 2016;20(2):293-312.
70. Brunt EM, Janney CG, Di Bisceglie AM, Neuschwander-Tetri BA, Bacon BR. Nonalcoholic steatohepatitis: a proposal for grading and staging the histological lesions. The American Journal of Gastroenterology. 1999;94(9):2467-74.
71. Kleiner DE, Brunt EM, Van Natta M, Behling C, Contos MJ, Cummings OW, et al. Design and validation of a histological scoring system for nonalcoholic fatty liver disease. Hepatology. 2005;41(6):1313-21.
72. Chalasani N, Szabo G (Eds.). Alcoholic and Non-Alcoholic Fatty Liver Disease- Bench to Benchside.: Springer International Publishing Switzerland; 2016.
73. Rinella ME, Sanyal AJ. Management of NAFLD: a stage-based approach. Nature Reviews Gastroenterology & Hepatology. 2016;13(4):196-205.
74. Wong VW, Chan RS, Wong GL, Cheung BH, Chu WC, Yeung DK, et al. Community-based lifestyle modification programme for non-alcoholic fatty liver disease: a randomized controlled trial. Journal of Hepatology. 2013;59(3):536-42.
75. Browning JD, Baker JA, Rogers T, Davis J, Satapati S, Burgess SC. Short-term weight loss and hepatic triglyceride reduction: evidence of a metabolic advantage with dietary carbohydrate restriction. The American Journal of Clinical Nutrition. 2011;93(5):1048-52.
76. Caiazzo R, Lassailly G, Leteurtre E, Baud G, Verkindt H, Raverdy V, et al. Roux-en-Y gastric bypass versus adjustable gastric banding to reduce nonalcoholic fatty liver disease: a 5-year controlled longitudinal study. Annals of Surgery. 2014;260(5):893-8; discussion 8-9.

77. Puzziferri N, Roshek TB, 3rd, Mayo HG, Gallagher R, Belle SH, Livingston EH. Long-term follow-up after bariatric surgery: a systematic review. JAMA. 2014;312(9):934-42.
78. Dulai PS, Singh S, Patel J, Soni M, Prokop LJ, Younossi Z, et al. Increased risk of mortality by fibrosis stage in nonalcoholic fatty liver disease: systematic review and meta-analysis. Hepatology. 2017;65(5):1557-65.
79. Sanyal AJ, Chalasani N, Kowdley KV, McCullough A, Diehl AM, Bass NM, et al. Pioglitazone, vitamin E, or placebo for nonalcoholic steatohepatitis. New England Journal of Medicine. 2010;362(18):1675-85.
80. Lavine JE, Schwimmer JB, Van Natta ML, Molleston JP, Murray KF, Rosenthal P, et al. Effect of vitamin E or metformin for treatment of nonalcoholic fatty liver disease in children and adolescents: the TONIC randomized controlled trial. JAMA. 2011;305(16):1659-68.
81. Boettcher E, Csako G, Pucino F, Wesley R, Loomba R. Meta-analysis: pioglitazone improves liver histology and fibrosis in patients with non-alcoholic steatohepatitis. Alimentary Pharmacology & Therapeutics. 2012;35(1):66-75.
82. Neuschwander-Tetri BA, Loomba R, Sanyal AJ, Lavine JE, Van Natta ML, Abdelmalek MF, et al. Farnesoid X nuclear receptor ligand obeticholic acid for non-cirrhotic, non-alcoholic steatohepatitis (FLINT): a multicentre, randomised, placebo-controlled trial. Lancet. 2015;385(9972):956-65.
83. Zein CO, Lopez R, Fu X, Kirwan JP, Yerian LM, McCullough AJ, et al. Pentoxifylline decreases oxidized lipid products in nonalcoholic steatohepatitis: new evidence on the potential therapeutic mechanism. Hepatology. 2012;56(4):1291-9.
84. International Agency for Research on Cancer. World Cancer Report. World Health Organisation. 2014.
85. Ryerson AB, Eheman CR, Altekruse SF, Ward JW, Jemal A, Sherman RL, et al. Annual Report to the Nation on the Status of Cancer, 1975-2012, featuring the increasing incidence of liver cancer. Cancer. 2016;122(9):1312-37.
86. Yasui K, Hashimoto E, Komorizono Y, Koike K, Arii S, Imai Y, et al. Characteristics of patients with nonalcoholic steatohepatitis who develop hepatocellular carcinoma. Clinical Gastroenterology and Hepatology. 2011;9(5):428-33; quiz e50.
87. Baffy G, Brunt EM, Caldwell SH. Hepatocellular carcinoma in non-alcoholic fatty liver disease: an emerging menace. Journal of Hepatology. 2012;56(6):1384-91.
88. Michelotti GA, Machado MV, Diehl AM. NAFLD, NASH and liver cancer. Nature Reviews Gastroenterology & Hepatology. 2013;10(11):656-65.
89. El-Serag HB, Rudolph KL. Hepatocellular carcinoma: epidemiology and molecular carcinogenesis. Gastroenterology. 2007;132(7):2557-76.

90. Poon D, Anderson BO, Chen LT, Tanaka K, Lau WY, Van Cutsem E, et al. Management of hepatocellular carcinoma in Asia: consensus statement from the Asian Oncology Summit 2009. The Lancet Oncology. 2009;10(11):1111-8.

91. Montalto G, Cervello M, Giannitrapani L, Dantona F, Terranova A, Castagnetta LA. Epidemiology, risk factors, and natural history of hepatocellular carcinoma. Annals of the New York Academy of Sciences. 2002;963:13-20.

92. Sanyal AJ, Yoon SK, Lencioni R. The etiology of hepatocellular carcinoma and consequences for treatment. The Oncologist. 2010;15 Suppl 4:14-22.

93. Wong CR, Nguyen MH, Lim JK. Hepatocellular carcinoma in patients with non-alcoholic fatty liver disease. World Journal of Gastroenterology. 2016;22(37):8294-303.

94. Gurtsevitch VE. Human oncogenic viruses: hepatitis B and hepatitis C viruses and their role in hepatocarcinogenesis. Biochemistry Biokhimiia. 2008;73(5):504-13.

95. Sheikh MY, Choi J, Qadri I, Friedman JE, Sanyal AJ. Hepatitis C virus infection: molecular pathways to metabolic syndrome. Hepatology. 2008;47(6):2127-33.

96. Villanueva A, Hoshida Y. Depicting the role of TP53 in hepatocellular carcinoma progression. Journal of Hepatology. 2011;55(3):724-5.

97. Harrison SA. Liver disease in patients with diabetes mellitus. Journal of Clinical Gastroenterology. 2006;40(1):68-76.

98. El-Serag HB, Hampel H, Javadi F. The association between diabetes and hepatocellular carcinoma: a systematic review of epidemiologic evidence. Clinical Gastroenterology and Hepatology. 2006;4(3):369-80.

99. Teoh NC, Fan JG. Diabetes mellitus and prognosis after curative therapy for hepatocellular carcinoma: alas, still grave for those who are hyperglycemic. Journal of Gastroenterology and Hepatology. 2008;23(11):1633-4.

100. Makarova-Rusher OV, Altekruse SF, McNeel TS, Ulahannan S, Duffy AG, Graubard BI, et al. Population attributable fractions of risk factors for hepatocellular carcinoma in the United States. Cancer. 2016;122(11):1757-65.

101. Nordenstedt H, White DL, El-Serag HB. The changing pattern of epidemiology in hepatocellular carcinoma. Digestive and Liver Disease. 2010;42 Suppl 3:S206-14.

102. Berentzen TL, Gamborg M, Holst C, Sorensen TI, Baker JL. Body mass index in childhood and adult risk of primary liver cancer. Journal of Hepatology. 2014;60(2):325-30.

103. Stickel F, Hellerbrand C. Non-alcoholic fatty liver disease as a risk factor for hepatocellular carcinoma: mechanisms and implications. Gut. 2010;59(10):1303-7.

104. Hashimoto E, Tokushige K. Hepatocellular carcinoma in non-alcoholic steatohepatitis: growing evidence of an epidemic? Hepatology Research. 2012;42(1):1-14.

105. Ng L. molecular pathogenesis of hepatocellular carcinoma. Hong Kong J Radiol. 2012;15:23.

106. Dhanasekaran R, Bandoh S, Roberts LR. Molecular pathogenesis of hepatocellular carcinoma and impact of therapeutic advances. F1000Research. 2016;5.

107. Wang Z, Li Z, Ye Y, Xie L, Li W. Oxidative stress and liver cancer: etiology and therapeutic targets. Oxidative Medicine and Cellular Longevity. 2016;2016:7891574.

108. Malhi H, Bronk SF, Werneburg NW, Gores GJ. Free fatty acids induce JNK-dependent hepatocyte lipoapoptosis. The Journal of Biological Chemistry. 2006;281(17):12093-101.

109. Wei Y, Wang D, Topczewski F, Pagliassotti MJ. Saturated fatty acids induce endoplasmic reticulum stress and apoptosis independently of ceramide in liver cells. American Journal of Physiology Endocrinology and Metabolism. 2006;291(2):E275-81.

110. Ma C, Kesarwala AH, Eggert T, Medina-Echeverz J, Kleiner DE, Jin P, et al. NAFLD causes selective CD4(+) T lymphocyte loss and promotes hepatocarcinogenesis. Nature. 2016;531(7593):253-7.

111. Shalapour S, Lin XJ, Bastian IN, Brain J, Burt AD, Aksenov AA, et al. Inflammation-induced IgA+ cells dismantle anti-liver cancer immunity. Nature. 2017;551(7680):340-5.

112. Hou XJ, Ye F, Li XY, Liu WT, Jing YY, Han ZP, et al. Immune response involved in liver damage and the activation of hepatic progenitor cells during liver tumorigenesis. Cellular Immunology. 2017.

113. Machado MV, Diehl AM. Pathogenesis of nonalcoholic steatohepatitis. Gastroenterology. 2016;150(8):1769-77.

114. Zheng X, Zeng W, Gai X, Xu Q, Li C, Liang Z, et al. Role of the Hedgehog pathway in hepatocellular carcinoma (review). Oncology Reports. 2013;30(5):2020-6.

115. Hotamisligil GS. Inflammation and metabolic disorders. Nature. 2006;444(7121):860-7.

116. Marra F, Bertolani C. Adipokines in liver diseases. Hepatology. 2009;50(3):957-69.

117. Kong L, Zhou Y, Bu H, Lv T, Shi Y, Yang J. Deletion of interleukin-6 in monocytes/macrophages suppresses the initiation of hepatocellular carcinoma in mice. Journal of Experimental & Clinical Cancer Research. 2016;35(1):131.

118. Aubrey BJ, Kelly GL, Janic A, Herold MJ, Strasser A. How does p53 induce apoptosis and how does this relate to p53-mediated tumour suppression? Cell Death and Differentiation. 2017.

119. Adolph TE, Grander C, Grabherr F, Tilg H. Adipokines and non-alcoholic fatty liver disease: multiple Interactions. International Journal of Molecular Sciences. 2017;18(8).

120. Kaser S, Moschen A, Cayon A, Kaser A, Crespo J, Pons-Romero F, et al. Adiponectin and its receptors in non-alcoholic steatohepatitis. Gut. 2005;54(1):117-21.

121. Kadowaki T, Yamauchi T, Kubota N, Hara K, Ueki K, Tobe K. Adiponectin and adiponectin receptors in insulin resistance, diabetes, and the metabolic syndrome. The Journal of Clinical Investigation. 2006;116(7):1784-92.

122. Thakur V, Pritchard MT, McMullen MR, Nagy LE. Adiponectin normalizes LPS-stimulated TNF-alpha production by rat Kupffer cells after chronic ethanol feeding. American Journal of Physiology Gastrointestinal and Liver Physiology. 2006;290(5):G998-1007.

123. Park EJ, Lee JH, Yu GY, He G, Ali SR, Holzer RG, et al. Dietary and genetic obesity promote liver inflammation and tumorigenesis by enhancing IL-6 and TNF expression. Cell. 2010;140(2):197-208.

124. Angulo P, Alba LM, Petrovic LM, Adams LA, Lindor KD, Jensen MD. Leptin, insulin resistance, and liver fibrosis in human nonalcoholic fatty liver disease. Journal of Hepatology. 2004;41(6):943-9.

125. Shen J, Sakaida I, Uchida K, Terai S, Okita K. Leptin enhances TNF-alpha production via p38 and JNK MAPK in LPS-stimulated Kupffer cells. Life Sciences. 2005;77(13):1502-15.

126. Aleffi S, Petrai I, Bertolani C, Parola M, Colombatto S, Novo E, et al. Upregulation of proinflammatory and proangiogenic cytokines by leptin in human hepatic stellate cells. Hepatology. 2005;42(6):1339-48.

127. Ikejima K, Okumura K, Kon K, Takei Y, Sato N. Role of adipocytokines in hepatic fibrogenesis. Journal of Gastroenterology and Hepatology. 2007;22 Suppl 1:S87-92.

128. Stefanou N, Papanikolaou V, Furukawa Y, Nakamura Y, Tsezou A. Leptin as a critical regulator of hepatocellular carcinoma development through modulation of human telomerase reverse transcriptase. BMC Cancer. 2010;10:442.

129. Biddinger SB, Kahn CR. From mice to men: insights into the insulin resistance syndromes. Annual Review of Physiology. 2006;68:123-58.

130. Gallagher EJ, LeRoith D. Minireview: IGF, Insulin, and Cancer. Endocrinology. 2011;152(7):2546-51.

131. Bugianesi E. Non-alcoholic steatohepatitis and cancer. Clinics in Liver Disease. 2007;11(1):191-207, x-xi.

132. Ohlsson C, Mohan S, Sjogren K, Tivesten A, Isgaard J, Isaksson O, et al. The role of liver-derived insulin-like growth factor-I. Endocrine Reviews. 2009;30(5):494-535.

133. Martinez-Lopez N, Varela-Rey M, Fernandez-Ramos D, Woodhoo A, Vazquez-Chantada M, Embade N, et al. Activation of LKB1-Akt pathway independent of

phosphoinositide 3-kinase plays a critical role in the proliferation of hepatocellular carcinoma from nonalcoholic steatohepatitis. Hepatology. 2010;52(5):1621-31.

134. Stickel F, Hellerbrand C. Non-alcoholic fatty liver disease as a risk factor for hepatocellular carcinoma mechanisms and implications. Gut and Liver. 2010;59(10):1303-7.

135. Burt AD, Ferrell LD, Hübscher S. MacSween's pathology of the liver. Seventh edition. ed: Philadelphia, PA : Elsevier; 2018.

136. Schlageter M, Terracciano LM, D'Angelo S, Sorrentino P. Histopathology of hepatocellular carcinoma. World Journal of Gastroenterology. 2014;20(43):15955-64.

137. Edmondson HA, Steiner PE. Primary carcinoma of the liver: a study of 100 cases among 48,900 necropsies. Cancer. 1954;7(3):462-503.

138. Kojiro M. Pathology of hepatocellular carcinoma.: Blackwell Publishing Ltd.; 2009. 1–184 p.

139. Salomao M, Yu WM, Brown RS, Jr., Emond JC, Lefkowitch JH. Steatohepatitic hepatocellular carcinoma (SH-HCC): a distinctive histological variant of HCC in hepatitis C virus-related cirrhosis with associated NAFLD/NASH. The American Journal of Surgical Pathology. 2010;34(11):1630-6.

140. Goldblum. JR, Lamps. LW, McKenney. JK, Myers. JL. Rosai and Acherman's surgical pathology. Eleventh edition. Philadelphia, PA: Elsevier; 2017.

141. Park HS, Jang KY, Kim YK, Cho BH, Moon WS. Hepatocellular carcinoma with massive lymphoid infiltration: a regressing phenomenon?. Pathology Research and Practice. 2009;205(9):648-52.

142. Brierley DJ, Gospodarowicz MK, Wittekind C (Eds). TNM classification of malignant tumours. Eighth edition.: Wiley-Blackwell; 2017.

143. Llovet JM, Bru C, Bruix J. Prognosis of hepatocellular carcinoma: the BCLC staging classification. Seminars in Liver Disease. 1999;19(3):329-38.

144. Cillo U, Vitale A, Grigoletto F, Farinati F, Brolese A, Zanus G, et al. Prospective validation of the Barcelona Clinic Liver Cancer staging system. Journal of Hepatology. 2006;44(4):723-31.

145. Tabrizian P, Roayaie S, Schwartz ME. Current management of hepatocellular carcinoma. World Journal of Gastroenterology. 2014;20(30):10223-37.

146. Wang H, Liu H, Chen K, Xiao J, He K, Zhang J, et al. SIRT1 promotes tumorigenesis of hepatocellular carcinoma through PI3K/PTEN/AKT signaling. Oncology Reports. 2012;28(1):311-8.

147. Llovet JM, Fuster J, Bruix J. Intention-to-treat analysis of surgical treatment for early hepatocellular carcinoma: resection versus transplantation. Hepatology. 1999;30(6):1434-40.

148. Fong Y, Sun RL, Jarnagin W, Blumgart LH. An analysis of 412 cases of hepatocellular carcinoma at a Western center. Annals of Surgery. 1999;229(6):790-9; discussion 9-800.

149. Bruix J, Sherman M. Management of hepatocellular carcinoma. Hepatology. 2005;42(5):1208-36.

150. Mazzaferro V, Regalia E, Doci R, Andreola S, Pulvirenti A, Bozzetti F, et al. Liver transplantation for the treatment of small hepatocellular carcinomas in patients with cirrhosis. The New England Journal of Medicine. 1996;334(11):693-9.

151. Llovet JM, Ricci S, Mazzaferro V, Hilgard P, Gane E, Blanc JF, et al. Sorafenib in advanced hepatocellular carcinoma. The New England Journal of Medicine. 2008;359(4):378-90.

152. EASL-EORTC clinical practice guidelines: management of hepatocellular carcinoma. Journal of Hepatology. 2012;56(4):908-43.

153. Shibata T, Iimuro Y, Yamamoto Y, Maetani Y, Ametani F, Itoh K, et al. Small hepatocellular carcinoma: comparison of radio-frequency ablation and percutaneous microwave coagulation therapy. Radiology. 2002;223(2):331-7.

154. Llovet JM, Real MI, Montana X, Planas R, Coll S, Aponte J, et al. Arterial embolisation or chemoembolisation versus symptomatic treatment in patients with unresectable hepatocellular carcinoma: a randomised controlled trial. Lancet. 2002;359(9319):1734-9.

155. Lo CM, Ngan H, Tso WK, Liu CL, Lam CM, Poon RT, et al. Randomized controlled trial of transarterial lipiodol chemoembolization for unresectable hepatocellular carcinoma. Hepatology. 2002;35(5):1164-71.

156. Llovet JM, Zucman-Rossi J, Pikarsky E, Sangro B, Schwartz M, Sherman M, et al. Hepatocellular carcinoma. Nature Reviews Disease Primers. 2016;2:16018.

157. Nicolini D, Svegliati-Baroni G, Candelari R, Mincarelli C, Mandolesi A, Bearzi I, et al. Doxorubicin-eluting bead vs conventional transcatheter arterial chemoembolization for hepatocellular carcinoma before liver transplantation. World Journal of Gastroenterology. 2013;19(34):5622-32.

158. Kulik LM, Atassi B, van Holsbeeck L, Souman T, Lewandowski RJ, Mulcahy MF, et al. Yttrium-90 microspheres (TheraSphere) treatment of unresectable hepatocellular carcinoma: downstaging to resection, RFA and bridge to transplantation. Journal of Surgical Oncology. 2006;94(7):572-86.

159. Kwon JH, Bae SH, Kim JY, Choi BO, Jang HS, Jang JW, et al. Long-term effect of stereotactic body radiation therapy for primary hepatocellular carcinoma ineligible for local ablation therapy or surgical resection. Stereotactic radiotherapy for liver cancer. BMC Cancer. 2010;10:475.

160. Cheng AL, Kang YK, Chen Z, Tsao CJ, Qin S, Kim JS, et al. Efficacy and safety of sorafenib in patients in the Asia-Pacific region with advanced hepatocellular carcinoma: a phase III randomised, double-blind, placebo-controlled trial. The Lancet Oncology. 2009;10(1):25-34.

161. Bruix J, Qin S, Merle P, Granito A, Huang YH, Bodoky G, et al. Regorafenib for patients with hepatocellular carcinoma who progressed on sorafenib treatment (RESORCE): a randomised, double-blind, placebo-controlled, phase 3 trial. Lancet. 2017;389(10064):56-66.

162. Lau JK, Zhang X, Yu J. Animal models of non-alcoholic fatty liver disease: current perspectives and recent advances. The Journal of Pathology. 2017;241(1):36-44.

163. Eccleston HB, Andringa KK, Betancourt AM, King AL, Mantena SK, Swain TM, et al. Chronic exposure to a high-fat diet induces hepatic steatosis, impairs nitric oxide bioavailability, and modifies the mitochondrial proteome in mice. Antioxidants & Redox Signaling. 2011;15(2):447-59.

164. Lieber CS, Leo MA, Mak KM, Xu Y, Cao Q, Ren C, et al. Model of nonalcoholic steatohepatitis. The American Journal of Clinical Nutrition. 2004;79(3):502-9.

165. Trak-Smayra V, Paradis V, Massart J, Nasser S, Jebara V, Fromenty B. Pathology of the liver in obese and diabetic ob/ob and db/db mice fed a standard or high-calorie diet. International Journal of Experimental Pathology. 2011;92(6):413-21.

166. Leclercq IA, Farrell GC, Schriemer R, Robertson GR. Leptin is essential for the hepatic fibrogenic response to chronic liver injury. Journal of Hepatology. 2002;37(2):206-13.

167. Yamada T, Obata A, Kashiwagi Y, Rokugawa T, Matsushima S, Hamada T, et al. Gd-EOB-DTPA-enhanced-MR imaging in the inflammation stage of nonalcoholic steatohepatitis (NASH) in mice. Magnetic Resonance Imaging. 2016;34(6):724-9.

168. Anstee QM, Goldin RD. Mouse models in non-alcoholic fatty liver disease and steatohepatitis research. International Journal of Experimental Pathology. 2006;87(1):1-16.

169. Kohli R, Kirby M, Xanthakos SA, Softic S, Feldstein AE, Saxena V, et al. High-fructose, medium chain trans fat diet induces liver fibrosis and elevates plasma coenzyme Q9 in a novel murine model of obesity and nonalcoholic steatohepatitis. Hepatology. 2010;52(3):934-44.

170. Dragani TA, Manenti G, Gariboldi M, De Gregorio L, Pierotti MA. Genetics of liver tumor susceptibility in mice. Toxicology Letters. 1995;82-83:613-9.

171. Oren M, Levine AJ. Molecular cloning of a cDNA specific for the murine p53 cellular tumor antigen. Proceedings of the National Academy of Sciences of the United States of America. 1983;80(1):56-9.

172. Shangary S, Wang S. Targeting the MDM2-p53 interaction for cancer therapy. Clinical Cancer Research. 2008;14(17):5318-24.

173. Meek DW. Regulation of the p53 response and its relationship to cancer. The Biochemical Journal. 2015;469(3):325-46.

174. Momand J, Zambetti GP, Olson DC, George D, Levine AJ. The mdm-2 oncogene product forms a complex with the p53 protein and inhibits p53-mediated transactivation. Cell. 1992;69(7):1237-45.

175. Chen J, Marechal V, Levine AJ. Mapping of the p53 and mdm-2 interaction domains. Molecular and Cellular Biology. 1993;13(7):4107-14.

176. Freedman DA, Levine AJ. Nuclear export is required for degradation of endogenous p53 by MDM2 and human papillomavirus E6. Molecular and Cellular Biology. 1998;18(12):7288-93.

177. Haupt Y, Maya R, Kazaz A, Oren M. Mdm2 promotes the rapid degradation of p53. Nature. 1997;387(6630):296-9.

178. Jones SN, Roe AE, Donehower LA, Bradley A. Rescue of embryonic lethality in Mdm2-deficient mice by absence of p53. Nature. 1995;378(6553):206-8.

179. Montes de Oca Luna R, Wagner DS, Lozano G. Rescue of early embryonic lethality in mdm2-deficient mice by deletion of p53. Nature. 1995;378(6553):203-6.

180. Loughery J, Meek D. Switching on p53: an essential role for protein phosphorylation? Biodiscovery. 2013(8).

181. Zhao Y, Aguilar A, Bernard D, Wang S. Small-molecule inhibitors of the MDM2-p53 protein-protein interaction (MDM2 Inhibitors) in clinical trials for cancer treatment. Journal of Medicinal Chemistry. 2015;58(3):1038-52.

182. Vogelstein B, Lane D, Levine AJ. Surfing the p53 network. Nature. 2000;408(6810):307-10.

183. Liu J, Zhang C, Feng Z. Tumor suppressor p53 and its gain-of-function mutants in cancer. Acta Biochimica et Biophysica Sinica. 2014;46(3):170-9.

184. Green DR, Kroemer G. Cytoplasmic functions of the tumour suppressor p53. Nature. 2009;458(7242):1127-30.

185. Gire V, Dulic V. Senescence from G2 arrest, revisited. Cell Cycle. 2015;14(3):297-304.

186. Goldstein I, Ezra O, Rivlin N, Molchadsky A, Madar S, Goldfinger N, et al. p53, a novel regulator of lipid metabolism pathways. Journal of Hepatology. 2012;56(3):656-62.

187. Parrales A, Iwakuma T. p53 as a Regulator of Lipid Metabolism in Cancer. International Journal of Molecular Sciences. 2016;17(12).

188. Feki A, Irminger-Finger I. Mutational spectrum of p53 mutations in primary breast and ovarian tumors. Critical Reviews in Oncology/Hematology. 2004;52(2):103-16.
189. Yue X, Zhao Y, Xu Y, Zheng M, Feng Z, Hu W. Mutant p53 in cancer: accumulation, gain-of-function, and therapy. Journal of Molecular Biology. 2017;429(11):1595-606.
190. Freed-Pastor WA, Prives C. Mutant p53: one name, many proteins. Genes & Development. 2012;26(12):1268-86.
191. Stindt MH, Muller PA, Ludwig RL, Kehrloesser S, Dotsch V, Vousden KH. Functional interplay between MDM2, p63/p73 and mutant p53. Oncogene. 2015;34(33):4300-10.
192. Pfister NT, Fomin V, Regunath K, Zhou JY, Zhou W, Silwal-Pandit L, et al. Mutant p53 cooperates with the SWI/SNF chromatin remodeling complex to regulate VEGFR2 in breast cancer cells. Genes & Development. 2015;29(12):1298-315.
193. Zhao Y, Zhang C, Yue X, Li X, Liu J, Yu H, et al. Pontin, a new mutant p53-binding protein, promotes gain-of-function of mutant p53. Cell Death and Differentiation. 2015;22(11):1824-36.
194. Zhang C, Liu J, Liang Y, Wu R, Zhao Y, Hong X, et al. Tumour-associated mutant p53 drives the Warburg effect. Nature Communications. 2013;4:2935.
195. Tomita K, Teratani T, Suzuki T, Oshikawa T, Yokoyama H, Shimamura K, et al. p53/p66Shc-mediated signaling contributes to the progression of non-alcoholic steatohepatitis in humans and mice. Journal of Hepatology. 2012;57(4):837-43.
196. Derdak Z, Villegas KA, Harb R, Wu AM, Sousa A, Wands JR. Inhibition of p53 attenuates steatosis and liver injury in a mouse model of non-alcoholic fatty liver disease. Journal of Hepatology. 2013;58(4):785-91.
197. Cheung O, Puri P, Eicken C, Contos MJ, Mirshahi F, Maher JW, et al. Nonalcoholic steatohepatitis is associated with altered hepatic MicroRNA expression. Hepatology. 2008;48(6):1810-20.
198. Vousden KH, Lu X. Live or let die: the cell's response to p53. Nature Reviews Cancer. 2002;2(8):594-604.
199. Forbes SA, Beare D, Boutselakis H, Bamford S, Bindal N, Tate J, et al. COSMIC: somatic cancer genetics at high-resolution. Nucleic Acids Research. 2017;45(D1):D777-D83.
200. Teufel A, Staib F, Kanzler S, Weinmann A, Schulze-Bergkamen H, Galle PR. Genetics of hepatocellular carcinoma. World Journal of Gastroenterology. 2007;13(16):2271-82.
201. Vermeulen K, Van Bockstaele DR, Berneman ZN. The cell cycle: a review of regulation, deregulation and therapeutic targets in cancer. Cell Proliferation. 2003;36(3):131-49.

202. Sherr CJ, Roberts JM. Inhibitors of mammalian G1 cyclin-dependent kinases. Genes & Development. 1995;9(10):1149-63.

203. Jin S, Tong T, Fan W, Fan F, Antinore MJ, Zhu X, et al. GADD45-induced cell cycle G2-M arrest associates with altered subcellular distribution of cyclin B1 and is independent of p38 kinase activity. Oncogene. 2002;21:8696.

204. Sobecki M, Mrouj K, Colinge J, Gerbe F, Jay P, Krasinska L, et al. Cell-cycle regulation accounts for variability in Ki-67 expression levels. Cancer Research. 2017;77(10):2722-34.

205. Yang C, Zhang J, Ding M, Xu K, Li L, Mao L, et al. Ki67 targeted strategies for cancer therapy. Clinical & Translational Oncology. 2017.

206. Esfandiari A. Modulation of p53 signalling and response to MDM2-p53 binding antagonists [PhD thesis]. Newcastle University, Faculty of Medical Sciences, 2015.

207. Rufini A, Tucci P, Celardo I, Melino G. Senescence and aging: the critical roles of p53. Oncogene. 2013;32(43):5129-43.

208. Chakradeo S, Elmore LW, Gewirtz DA. Is Senescence Reversible? Current Drug Targets. 2016;17(4):460-6.

209. Ventura A, Kirsch DG, McLaughlin ME, Tuveson DA, Grimm J, Lintault L, et al. Restoration of p53 function leads to tumour regression in vivo. Nature. 2007;445:661.

210. Xue W, Zender L, Miething C, Dickins RA, Hernando E, Krizhanovsky V, et al. Senescence and tumour clearance is triggered by p53 restoration in murine liver carcinomas. Nature. 2007;445(7128):656-60.

211. Dashzeveg N, Yoshida K. Cell death decision by p53 via control of the mitochondrial membrane. Cancer Letters. 2015;367(2):108-12.

212. Yu J, Zhang L. The transcriptional targets of p53 in apoptosis control. Biochemical and Biophysical Research Communications. 2005;331(3):851-8.

213. Siddiqui WA, Ahad A, Ahsan H. The mystery of BCL2 family: Bcl-2 proteins and apoptosis: an update. Archives of Toxicology. 2015;89(3):289-317.

214. Burgess A, Chia KM, Haupt S, Thomas D, Haupt Y, Lim E. Clinical overview of MDM2/X-targeted therapies. Frontiers in Oncology. 2016;6:7.

215. Wasylyk C, Salvi R, Argentini M, Dureuil C, Delumeau I, Abecassis J, et al. p53 mediated death of cells overexpressing MDM2 by an inhibitor of MDM2 interaction with p53. Oncogene. 1999;18(11):1921-34.

216. Vassilev LT, Vu BT, Graves B, Carvajal D, Podlaski F, Filipovic Z, et al. In vivo activation of the p53 pathway by small-molecule antagonists of MDM2. Science. 2004;303(5659):844-8.

217. Tisato V, Voltan R, Gonelli A, Secchiero P, Zauli G. MDM2/X inhibitors under clinical evaluation: perspectives for the management of hematological malignancies and pediatric cancer. Journal of Hematology & Oncology. 2017;10:133.

218. Laurie NA, Donovan SL, Shih CS, Zhang J, Mills N, Fuller C, et al. Inactivation of the p53 pathway in retinoblastoma. Nature. 2006;444(7115):61-6.

219. Abbas HA, Maccio DR, Coskun S, Jackson JG, Hazen AL, Sills TM, et al. Mdm2 is required for survival of hematopoietic stem cells/progenitors via dampening of ROS-induced p53 activity. Cell Stem Cell. 2010;7(5):606-17.

220. Mahfoudhi E, Lordier L, Marty C, Pan J, Roy A, Roy L, et al. P53 activation inhibits all types of hematopoietic progenitors and all stages of megakaryopoiesis. Oncotarget. 2016;7(22):31980-92.

221. Hyman DM, Chatterjee M, Vos Fd, Lin C-C, Suárez C, Tai D, et al. Abstract CT150: Optimizing the therapeutic index of HDM2 inhibition: Results from a dose- and regimen-finding Phase I study of NVP-HDM201 in pts with TP53wt advanced tumors. Cancer Research. 2017;77(13 Supplement):CT150-CT.

222. ClinicalTrials .gov. https://clinicaltrials.gov/ct2/results?cond=&term=HDM201&cntry1=&state1=&recrs= Accessed December 2017.

223. Liu Y, Zhang Y, Bautista D, Tang S, Zhou J, Li C, et al. Trans-arterial p53-gene-embolization with gelatin sponge microparticles for hepatocellular carcinoma with BCLC stage B: single-center experience. Cell Biochemistry and Biophysics. 2015;71(1):99-104.

224. Peng Z. Current status of gendicine in China: recombinant human Ad-p53 agent for treatment of cancers. Human Gene Therapy. 2005;16(9):1016-27.

225. Atencio IA, Grace M, Bordens R, Fritz M, Horowitz JA, Hutchins B, et al. Biological activities of a recombinant adenovirus p53 (SCH 58500) administered by hepatic arterial infusion in a Phase 1 colorectal cancer trial. Cancer Gene Therapy. 2006;13(2):169-81.

226. Tian G, Liu J, Zhou JS, Chen W. Multiple hepatic arterial injections of recombinant adenovirus p53 and 5-fluorouracil after transcatheter arterial chemoembolization for unresectable hepatocellular carcinoma: a pilot phase II trial. Anti-Cancer Drugs. 2009;20(5):389-95.

227. Yu M, Chen W, Zhang J. p53 gene therapy for pulmonary metastasis tumor from hepatocellular carcinoma. Anti-Cancer Drugs. 2010;21(9):882-4.

228. Li GB, Zhang XL, Yuan L, Jiao QQ, Liu DJ, Liu J. Protein phosphatase magnesium-dependent 1delta (PPM1D) mRNA expression is a prognosis marker for hepatocellular carcinoma. PLOS ONE. 2013;8(3):e60775.

229. Xu Z, Cao C, Xia H, Shi S, Hong L, Wei X, et al. Protein phosphatase magnesium-dependent 1delta is a novel tumor marker and target in hepatocellular carcinoma. Frontiers of Medicine. 2016;10(1):52-60.

230. Lowe J, Cha H, Lee MO, Mazur SJ, Appella E, Fornace AJ, Jr. Regulation of the Wip1 phosphatase and its effects on the stress response. Frontiers in Bioscience (Landmark edition). 2012;17:1480-98.

231. Lu X, Nguyen TA, Moon SH, Darlington Y, Sommer M, Donehower LA. The type 2C phosphatase Wip1: an oncogenic regulator of tumor suppressor and DNA damage response pathways. Cancer Metastasis Reviews. 2008;27(2):123-35.

232. Scaggiante B, Kazemi M, Pozzato G, Dapas B, Farra R, Grassi M, et al. Novel hepatocellular carcinoma molecules with prognostic and therapeutic potentials. World Journal of Gastroenterology. 2014;20(5):1268-88.

233. William M. Bonner, Christophe E. Redon, Jennifer S. Dickey, Asako J. Nakamura, Olga A. Sedelnikova, Stéphanie Solier, et al. γH2AX and cancer. Nature Reviews Cancer. 2008;8.

234. Nims RW, Sykes G, Cottrill K, Ikonomi P, Elmore E. Short tandem repeat profiling: part of an overall strategy for reducing the frequency of cell misidentification. In vitro Cellular & Developmental Biology Animal. 2010;46(10):811-9.

235. Reid Y, Storts D, Riss T, Minor L. Authentication of Human Cell Lines by STR DNA Profiling Analysis. In: Sittampalam GS, Coussens NP, Brimacombe K, Grossman A, Arkin M, Auld D, et al., editors. Assay Guidance Manual. Bethesda (MD): Eli Lilly & Company and the National Center for Advancing Translational Sciences; 2004.

236. Skehan P, Storeng R, Scudiero D, Monks A, McMahon J, Vistica D, et al. New colorimetric cytotoxicity assay for anticancer-drug screening. Journal of the National Cancer Institute. 1990;82(13):1107-12.

237. Ding Q, Zhang Z, Liu JJ, Jiang N, Zhang J, Ross TM, et al. Discovery of RG7388, a potent and selective p53-MDM2 inhibitor in clinical development. Journal of Medicinal Chemistry. 2013;56(14):5979-83.

238. Furet P, Masuya K, Kallen J, Stachyra-Valat T, Ruetz S, Guagnano V, et al. Discovery of a novel class of highly potent inhibitors of the p53-MDM2 interaction by structure-based design starting from a conformational argument. Bioorganic & Medicinal Chemistry Letters. 2016;26(19):4837-41.

239. Gilmartin AG, Faitg TH, Richter M, Groy A, Seefeld MA, Darcy MG, et al. Allosteric Wip1 phosphatase inhibition through flap-subdomain interaction. Nature Chemical Biology. 2014;10(3):181-7.

240. Dimri GP, Lee X, Basile G, Acosta M, Scott G, Roskelley C, et al. A biomarker that identifies senescent human cells in culture and in aging skin in vivo. Proceedings of the National Academy of Sciences of the United States of America. 1995;92(20):9363-7.

241. Workman P, Aboagye EO, Balkwill F, Balmain A, Bruder G, Chaplin DJ, et al. Guidelines for the welfare and use of animals in cancer research. British Journal of Cancer. 2010;102(11):1555-77.

242. Torre LA, Bray F, Siegel RL, Ferlay J, Lortet-Tieulent J, Jemal A. Global cancer statistics, 2012. CA: a Cancer Journal for Clinicians. 2015;65(2):87-108.

243. Ferramosca A, Di Giacomo M, Zara V. Antioxidant dietary approach in treatment of fatty liver: New insights and updates. World Journal of Gastroenterology. 2017;23(23):4146-57.

244. Cobbina E, Akhlaghi F. Non-alcoholic fatty liver disease (NAFLD) - pathogenesis, classification, and effect on drug metabolizing enzymes and transporters. Drug Metabolism Reviews. 2017;49(2):197-211.

245. Van Herck MA, Vonghia L, Francque SM. Animal models of nonalcoholic fatty liver disease-A Starter's Guide. Nutrients. 2017;9(10).

246. Hussain SP, Schwank J, Staib F, Wang XW, Harris CC. TP53 mutations and hepatocellular carcinoma: insights into the etiology and pathogenesis of liver cancer. Oncogene. 2007;26(15):2166-76.

247. Rudnick DA, Davidson NO. Functional relationships between lipid metabolism and liver regeneration. International Journal of Hepatology. 2012;2012:549241.

248. Picard C, Lambotte L, Starkel P, Sempoux C, Saliez A, Van den Berge V, et al. Steatosis is not sufficient to cause an impaired regenerative response after partial hepatectomy in rats. Journal of Hepatology. 2002;36(5):645-52.

249. Rao MS, Papreddy K, Abecassis M, Hashimoto T. Regeneration of liver with marked fatty change following partial hepatectomy in rats. Digestive Diseases and Sciences. 2001;46(9):1821-6.

250. Kele PG, van der Jagt EJ, Gouw AS, Lisman T, Porte RJ, de Boer MT. The impact of hepatic steatosis on liver regeneration after partial hepatectomy. Liver International. 2013;33(3):469-75.

251. Tanoue S, Uto H, Kumamoto R, Arima S, Hashimoto S, Nasu Y, et al. Liver regeneration after partial hepatectomy in rat is more impaired in a steatotic liver induced by dietary fructose compared to dietary fat. Biochemical and Biophysical Research Communications. 2011/03/05 ed2011. p. 163-8.

252. Cho JY, Suh KS, Kwon CH, Yi NJ, Lee KU. Mild hepatic steatosis is not a major risk factor for hepatectomy and regenerative power is not impaired. Surgery. 2006;139(4):508-15.
253. Miele L, Beale G, Patman G, Nobili V, Leathart J, Grieco A, et al. The Kruppel-like factor 6 genotype is associated with fibrosis in nonalcoholic fatty liver disease. Gastroenterology. 2008;135(1):282-91.e1.
254. Tetri LH, Basaranoglu M, Brunt EM, Yerian LM, Neuschwander-Tetri BA. Severe NAFLD with hepatic necroinflammatory changes in mice fed trans fats and a high-fructose corn syrup equivalent. American Journal of Physiology Gastrointestinal and Liver Physiology. 2008;295(5):G987-95.
255. Charlton M, Krishnan A, Viker K, Sanderson S, Cazanave S, McConico A, et al. Fast food diet mouse: novel small animal model of NASH with ballooning, progressive fibrosis, and high physiological fidelity to the human condition. American Journal of Physiology Gastrointestinal and Liver Physiology. 2011;301(5):G825-34.
256. Yeh MM, Brunt EM. Pathological features of fatty liver disease. Gastroenterology. 2014;147(4):754-64.
257. Tiniakos DG, Vos MB, Brunt EM. Nonalcoholic fatty liver disease: pathology and pathogenesis. Annual Review of Pathology. 2010;5:145-71.
258. Dowman JK, Hopkins LJ, Reynolds GM, Nikolaou N, Armstrong MJ, Shaw JC, et al. Development of hepatocellular carcinoma in a murine model of nonalcoholic steatohepatitis induced by use of a high-fat/fructose diet and sedentary lifestyle. The American Journal of Pathology. 2014;184(5):1550-61.
259. Ganz M, Bukong TN, Csak T, Saha B, Park JK, Ambade A, et al. Progression of non-alcoholic steatosis to steatohepatitis and fibrosis parallels cumulative accumulation of danger signals that promote inflammation and liver tumors in a high fat-cholesterol-sugar diet model in mice. Journal of Translational Medicine. 2015;13:193.
260. Whitehead A, Ogle L, Patman GL, Anwar G, Tiniakos DG, Anstee QM, et al. P0267 : Ras and p-ERK in metabolic syndrome associated Hepatocellular Carcinoma (HCC). Journal of Hepatology. 2015;62(Supplement 2):S406.
261. Jain D, Nayak NC, Kumaran V, Saigal S. Steatohepatitic hepatocellular carcinoma, a morphologic indicator of associated metabolic risk factors: a study from India. Archives of Pathology & Laboratory Medicine. 2013;137(7):961-6.
262. Farges O, Ferreira N, Dokmak S, Belghiti J, Bedossa P, Paradis V. Changing trends in malignant transformation of hepatocellular adenoma. Gut. 2011;60(1):85-9.
263. Rinella ME. Nonalcoholic fatty liver disease: a systematic review. JAMA. 2015;313(22):2263-73.

264. Delladetsima JK, Horn T, Poulsen H. Portal tract lipogranulomas in liver biopsies. Liver. 1987;7(1):9-17.

265. Zhu H, Bodenheimer HC, Jr., Clain DJ, Min AD, Theise ND. Hepatic lipogranulomas in patients with chronic liver disease: association with hepatitis C and fatty liver disease. World Journal of Gastroenterology. 2010;16(40):5065-9.

266. Krenkel O, Tacke F. Liver macrophages in tissue homeostasis and disease. Nature Reviews Immunology. 2017;17(5):306-21.

267. Wan J, Benkdane M, Teixeira-Clerc F, Bonnafous S, Louvet A, Lafdil F, et al. M2 Kupffer cells promote M1 Kupffer cell apoptosis: a protective mechanism against alcoholic and nonalcoholic fatty liver disease. Hepatology. 2014;59(1):130-42.

268. Harmon RC, Tiniakos DG, Argo CK. Inflammation in nonalcoholic steatohepatitis. Expert Review of Gastroenterology & Hepatology. 2011;5(2):189-200.

269. Arango Duque G, Descoteaux A. Macrophage Cytokines: Involvement in Immunity and Infectious Diseases. Frontiers in Immunology. 2014;5(491).

270. Noy R, Pollard JW. Tumor-associated macrophages: from mechanisms to therapy. Immunity. 2014;41(1):49-61.

271. Yan W, Liu X, Ma H, Zhang H, Song X, Gao L, et al. Tim-3 fosters HCC development by enhancing TGF-beta-mediated alternative activation of macrophages. Gut. 2015;64(10):1593-604.

272. Wolf MJ, Adili A, Piotrowitz K, Abdullah Z, Boege Y, Stemmer K, et al. Metabolic activation of intrahepatic CD8+ T cells and NKT cells causes nonalcoholic steatohepatitis and liver cancer via cross-talk with hepatocytes. Cancer Cell. 2014;26(4):549-64.

273. Wilson CL, Jurk D, Fullard N, Banks P, Page A, Luli S, et al. NFkappaB1 is a suppressor of neutrophil-driven hepatocellular carcinoma. Nature Communications. 2015;6:6818.

274. Hatting M, Tacke F. From NAFLD to HCC: Is IL-17 the crucial link? Hepatology. 2017;65(2):739-41.

275. Wang C, Jurk D, Maddick M, Nelson G, Martin-Ruiz C, von Zglinicki T. DNA damage response and cellular senescence in tissues of aging mice. Aging Cell. 2009;8(3):311-23.

276. Begriche K, Massart J, Robin MA, Bonnet F, Fromenty B. Mitochondrial adaptations and dysfunctions in nonalcoholic fatty liver disease. Hepatology. 2013;58(4):1497-507.

277. Delire B, Starkel P. The Ras/MAPK pathway and hepatocarcinoma: pathogenesis and therapeutic implications. European Journal of Clinical Investigation. 2015;45(6):609-23.

278. Schmidt CM, McKillop IH, Cahill PA, Sitzmann JV. Increased MAPK expression and activity in primary human hepatocellular carcinoma. Biochemical and Biophysical Research Communications. 1997;236(1):54-8.

279. Calvisi DF, Ladu S, Gorden A, Farina M, Conner EA, Lee JS, et al. Ubiquitous activation of Ras and Jak/Stat pathways in human HCC. Gastroenterology. 2006;130(4):1117-28.

280. Townsend SA, Newsome PN. Review article: new treatments in non-alcoholic fatty liver disease. Alimentary Pharmacology & Therapeutics. 2017;46(5):494-507.

281. Gaddikeri S, McNeeley MF, Wang CL, Bhargava P, Dighe MK, Yeh MM, et al. Hepatocellular carcinoma in the noncirrhotic liver. American Journal of Roentgenology. 2014;203(1):W34-47.

282. Nanke Y, Iwatani M, Kobashigawa T, Yago T, Yamanaka H, Kotake S. Radiographic repair in three Japanese patients with rheumatoid arthritis treated with bucillamine. Modern Rheumatology. 2009;19(6):681-6.

283. Sekiguchi N, Kameda H, Amano K, Takeuchi T. Efficacy and safety of bucillamine, a D-penicillamine analogue, in patients with active rheumatoid arthritis. Modern Rheumatology. 2006;16(2):85-91.

284. Bucillamine for the treatment of acute gout flare in subjects with moderate to severe gout.Clinal Trials.Gov https://www.clinicaltrials.gov/ct2/show/study/NCT02330796. Accessed 28/08/2017.

285. Keenan RT, Schlesinger N. New and pipeline drugs for gout. Current Rheumatology Reports. 2016;18(6):32.

286. Ceconi C, Curello S, Cargnoni A, Ferrari R, Albertini A, Visioli O. The role of glutathione status in the protection against ischaemic and reperfusion damage: effects of N-acetyl cysteine. Journal of Molecular and Cellular Cardiology. 1988;20(1):5-13.

287. Horwitz LD. Bucillamine: a potent thiol donor with multiple clinical applications. Cardiovascular Drug Reviews. 2003;21(2):77-90.

288. Mazor D, Greenberg L, Shamir D, Meyerstein D, Meyerstein N. Antioxidant properties of bucillamine: possible mode of action. Biochemical and Biophysical Research Communications. 2006;349(3):1171-5.

289. Yeung JH. The effects of bucillamine on glutathione and glutathione-related enzymes in the mouse. Biochemical Pharmacology. 1991;42(4):847-52.

290. Matsuno H, Sugiyama E, Muraguchi A, Nezuka T, Kubo T, Matsuura K, et al. Pharmacological effects of SA96 (bucillamine) and its metabolites as immunomodulating drugs--the disulfide structure of SA-96 metabolites plays a critical role in the pharmacological action of the drug. International Journal of Immunopharmacology. 1998;20(6):295-304.

291. Evans RM, Mangelsdorf DJ. Nuclear Receptors, RXR, and the Big Bang. Cell. 2014;157(1):255-66.

292. Tanaka N, Aoyama T, Kimura S, Gonzalez FJ. Targeting nuclear receptors for the treatment of fatty liver disease. Pharmacology & Therapeutics. 2017.
293. Ali AH, Carey EJ, Lindor KD. Recent advances in the development of farnesoid X receptor agonists. Annals of Translational Medicine. 2015;3(1):5.
294. de Aguiar Vallim TQ, Tarling EJ, Edwards PA. Pleiotropic roles of bile acids in metabolism. Cell Metabolism. 2013;17(5):657-69.
295. de Boer JF, Schonewille M, Boesjes M, Wolters H, Bloks VW, Bos T, et al. Intestinal farnesoid X receptor controls transintestinal cholesterol excretion in mice. Gastroenterology. 2017;152(5):1126-38.e6.
296. Carr RM, Reid AE. FXR agonists as therapeutic agents for non-alcoholic fatty liver disease. Current Atherosclerosis Reports. 2015;17(4):500.
297. Li Y, Jadhav K, Zhang Y. Bile acid receptors in non-alcoholic fatty liver disease. Biochemical Pharmacology. 2013;86(11):1517-24.
298. Yang ZX, Shen W, Sun H. Effects of nuclear receptor FXR on the regulation of liver lipid metabolism in patients with non-alcoholic fatty liver disease. Hepatology International. 2010;4(4):741-8.
299. Pellicciari R, Fiorucci S, Camaioni E, Clerici C, Costantino G, Maloney PR, et al. 6alpha-ethyl-chenodeoxycholic acid (6-ECDCA), a potent and selective FXR agonist endowed with anticholestatic activity. Journal of Medicinal Chemistry. 2002;45(17):3569-72.
300. Hambruch E, Miyazaki-Anzai S, Hahn U, Matysik S, Boettcher A, Perovic-Ottstadt S, et al. Synthetic farnesoid X receptor agonists induce high-density lipoprotein-mediated transhepatic cholesterol efflux in mice and monkeys and prevent atherosclerosis in cholesteryl ester transfer protein transgenic low-density lipoprotein receptor (-/-) mice. The Journal of Pharmacology and Experimental Therapeutics. 2012;343(3):556-67.
301. Copeland RA. The drug-target residence time model: a 10-year retrospective. Nature Reviews Drug Discovery. 2016;15(2):87-95.
302. Lippman SM, Klein EA, Goodman PJ, Lucia MS, Thompson IM, Ford LG, et al. Effect of selenium and vitamin E on risk of prostate cancer and other cancers: the Selenium and vitamin E cancer prevention trial (SELECT). JAMA. 2009;301(1):39-51.
303. Saremi A, Arora R. Vitamin E and cardiovascular disease. American Journal of Therapeutics. 2010;17(3):e56-65.
304. Watanabe M, Horai Y, Houten SM, Morimoto K, Sugizaki T, Arita E, et al. Lowering bile acid pool size with a synthetic farnesoid X receptor (FXR) agonist induces obesity and diabetes through reduced energy expenditure. The Journal of Biological Chemistry. 2011;286(30):26913-20.

305. Fiorucci S, Antonelli E, Rizzo G, Renga B, Mencarelli A, Riccardi L, et al. The nuclear receptor SHP mediates inhibition of hepatic stellate cells by FXR and protects against liver fibrosis. Gastroenterology. 2004;127(5):1497-512.

306. Kim I, Morimura K, Shah Y, Yang Q, Ward JM, Gonzalez FJ. Spontaneous hepatocarcinogenesis in farnesoid X receptor-null mice. Carcinogenesis. 2007;28(5):940-6.

307. Yang F, Huang X, Yi T, Yen Y, Moore DD, Huang W. Spontaneous development of liver tumors in the absence of the bile acid receptor farnesoid X receptor. Cancer Research. 2007;67(3):863-7.

308. Llovet JM, Villanueva A, Lachenmayer A, Finn RS. Advances in targeted therapies for hepatocellular carcinoma in the genomic era. Nature Reviews Clinical Oncology. 2015;12(8):436.

309. EASL-EORTC Clinical Practice Guidelines: Management of hepatocellular carcinoma. European Journal of Cancer. 2012;48(5):599-641.

310. London WT MK, Liver cancer, In: Schottenfeld D, Fraumeni JF Jr, editors. Cancer Epidemiology and Prevention. Third edition. New York, NY: Oxford University Press; 2006. pp 763–786.

311. Cerami E, Gao J, Dogrusoz U, Gross BE, Sumer SO, Aksoy BA, et al. The cBio cancer genomics portal: an open platform for exploring multidimensional cancer genomics data. Cancer Discovery. 2012;2(5):401-4.

312. Gao J, Aksoy BA, Dogrusoz U, Dresdner G, Gross B, Sumer SO, et al. Integrative analysis of complex cancer genomics and clinical profiles using the cBioPortal. Science Signaling. 2013;6(269):pl1.

313. Wu X, Bayle JH, Olson D, Levine AJ. The p53-mdm-2 autoregulatory feedback loop. Genes & Development. 1993;7(7a):1126-32.

314. Hyman D, Chatterjee M, Langenberg MHG, Lin CC, Suárez C, Tai D, et al. Dose- and regimen-finding phase I study of NVP-HDM201 in patients (pts) with TP53 wild-type (wt) advanced tumors. European Journal of Cancer. 2016;69:S128-9.

315. Holzer P, Chène P, Ferretti S, Furet P, Gabriel T, Gruenenfelder B, et al. Abstract 4855: Discovery of NVP-HDM201 - first disclosure of a next-generation Mdm2 inhibitor with superior characteristics. Cancer Research. 2016;76(14 Supplement):4855.

316. Ferretti S, Rebmann R, Berger M, Santacroce F, Albrecht G, Pollehn K, et al. Abstract 1224: Insights into the mechanism of action of NVP-HDM201, a differentiated and versatile Next-Generation small-molecule inhibitor of Mdm2, under evaluation in phase I clinical trials. Cancer Research. 2016;76(14 Supplement):1224.

317. Stachyra-Valat T, Baysang F, D'Alessandro A-C, Dirk E, Furet P, Guagnano V, et al. Abstract 1239: NVP-HDM201: Biochemical and biophysical profile of a novel highly potent and selective PPI inhibitor of p53-Mdm2. Cancer Research. 2016;76(14 Supplement):1239.
318. Lakoma A, Barbieri E, Agarwal S, Jackson J, Chen Z, Kim Y, et al. The MDM2 small-molecule inhibitor RG7388 leads to potent tumor inhibition in p53 wild-type neuroblastoma. Cell Death Discovery. 2015;1.
319. Chen L, Rousseau RF, Middleton SA, Nichols GL, Newell DR, Lunec J, et al. Pre-clinical evaluation of the MDM2-p53 antagonist RG7388 alone and in combination with chemotherapy in neuroblastoma. Oncotarget. 2015;6(12):10207-21.
320. Hasegawa H, Yamada Y, Iha H, Tsukasaki K, Nagai K, Atogami S, et al. Activation of p53 by Nutlin-3a, an antagonist of MDM2, induces apoptosis and cellular senescence in adult T-cell leukemia cells. Leukemia. 2009;23(11):2090-101.
321. Kumar R, Gont A, Perkins TJ, Hanson JEL, Lorimer IAJ. Induction of senescence in primary glioblastoma cells by serum and TGFbeta. Scientific Reports. 2017;7(1):2156.
322. Mao Z, Ke Z, Gorbunova V, Seluanov A. Replicatively senescent cells are arrested in G1 and G2 phases. Aging (Albany NY). 2012;4(6):431-5.
323. Mombach JCM, Bugs CA, Chaouiya C. Modelling the onset of senescence at the G1/S cell cycle checkpoint. BMC Genomics. 2014;15(7):S7.
324. Shultz LD, Ishikawa F, Greiner DL. Humanized mice in translational biomedical research. Nature Reviews Immunology. 2007;7(2):118-30.
325. Euhus DM, Hudd C, LaRegina MC, Johnson FE. Tumor measurement in the nude mouse. Journal of Surgical Oncology. 1986;31(4):229-34.
326. Tomayko MM, Reynolds CP. Determination of subcutaneous tumor size in athymic (nude) mice. Cancer Chemotherapy and Pharmacology. 1989;24(3):148-54.
327. Edinger M, Cao YA, Hornig YS, Jenkins DE, Verneris MR, Bachmann MH, et al. Advancing animal models of neoplasia through in vivo bioluminescence imaging. European Journal of Cancer. 2002;38(16):2128-36.
328. Caceres G, Zankina R, Zhu X, Jiao JA, Wong H, Aller A, et al. Determination of chemotherapeutic activity in vivo by luminescent imaging of luciferase-transfected human tumors. Anti-Cancer Drugs. 2003;14(7):569-74.
329. Jenkins DE, Oei Y, Hornig YS, Yu SF, Dusich J, Purchio T, et al. Bioluminescent imaging (BLI) to improve and refine traditional murine models of tumor growth and metastasis. Clinical & Experimental Metastasis. 2003;20(8):733-44.
330. Christoph S, Schlegel J, Alvarez-Calderon F, Kim YM, Brandao LN, DeRyckere D, et al. Bioluminescence imaging of leukemia cell lines in vitro and in mouse xenografts: effects of

monoclonal and polyclonal cell populations on intensity and kinetics of photon emission. Journal of Hematology & Oncology. 2013;6:10.

331. Jost SC, Collins L, Travers S, Piwnica-Worms D, Garbow JR. Measuring brain tumor growth: combined bioluminescence imaging-magnetic resonance imaging strategy. Molecular Imaging. 2009;8(5):245-53.

332. Meng X, Franklin DA, Dong J, Zhang Y. MDM2-p53 pathway in hepatocellular carcinoma. Cancer Research. 2014;74(24):7161-7.

333. Wang J, Zheng T, Chen X, Song X, Meng X, Bhatta N, et al. MDM2 antagonist can inhibit tumor growth in hepatocellular carcinoma with different types of p53 in vitro. Journal of Gastroenterology and Hepatology. 2011;26(2):371-7.

334. Lee M, Lee JS. Exploiting tumor cell senescence in anticancer therapy. BMB Reports. 2014;47(2):51-9.

335. Kang TW, Yevsa T, Woller N, Hoenicke L, Wuestefeld T, Dauch D, et al. Senescence surveillance of pre-malignant hepatocytes limits liver cancer development. Nature. 2011;479(7374):547-51.

336. Sica A, Schioppa T, Mantovani A, Allavena P. Tumour-associated macrophages are a distinct M2 polarised population promoting tumour progression: potential targets of anti-cancer therapy. European Journal of Cancer. 2006;42(6):717-27.

337. Iannello A, Thompson TW, Ardolino M, Lowe SW, Raulet DH. p53-dependent chemokine production by senescent tumor cells supports NKG2D-dependent tumor elimination by natural killer cells. The Journal of Experimental Medicine. 2013;210(10):2057-69.

338. Lu X, Ma O, Nguyen TA, Jones SN, Oren M, Donehower LA. The Wip1 Phosphatase acts as a gatekeeper in the p53-Mdm2 autoregulatory loop. Cancer Cell. 2007;12(4):342-54.

339. Sriraman A, Radovanovic M, Wienken M, Najafova Z, Li Y, Dobbelstein M. Cooperation of Nutlin-3a and a Wip1 inhibitor to induce p53 activity. Oncotarget. 2016;7(22):31623-38.

340. Oliva-Trastoy M, Berthonaud V, Chevalier A, Ducrot C, Marsolier-Kergoat MC, Mann C, et al. The Wip1 phosphatase (PPM1D) antagonizes activation of the Chk2 tumour suppressor kinase. Oncogene. 2007;26(10):1449-58.

341. Lu X, Nannenga B, Donehower LA. PPM1D dephosphorylates Chk1 and p53 and abrogates cell cycle checkpoints. Genes & Development. 2005;19(10):1162-74.

342. Macurek L, Lindqvist A, Voets O, Kool J, Vos HR, Medema RH. Wip1 phosphatase is associated with chromatin and dephosphorylates gammaH2AX to promote checkpoint inhibition. Oncogene. 2010;29(15):2281-91.

343. Li J, Yang Y, Peng Y, Austin RJ, van Eyndhoven WG, Nguyen KC, et al. Oncogenic properties of PPM1D located within a breast cancer amplification epicenter at 17q23. Nature Genetics. 2002;31(2):133-4.

344. Hirasawa A, Saito-Ohara F, Inoue J, Aoki D, Susumu N, Yokoyama T, et al. Association of 17q21-q24 gain in ovarian clear cell adenocarcinomas with poor prognosis and identification of PPM1D and APPBP2 as likely amplification targets. Clinical Cancer Research. 2003;9(6):1995-2004.

345. Pechackova S, Burdova K, Benada J, Kleiblova P, Jenikova G, Macurek L. Inhibition of WIP1 phosphatase sensitizes breast cancer cells to genotoxic stress and to MDM2 antagonist nutlin-3. Oncotarget. 2016;7(12):14458-75.

346. Esfandiari A, Hawthorne TA, Nakjang S, Lunec J. Chemical Inhibition of Wild-Type p53-Induced Phosphatase 1 (WIP1/PPM1D) by GSK2830371 Potentiates the Sensitivity to MDM2 Inhibitors in a p53-Dependent Manner. Molecular Cancer Therapeutics. 2016;15(3):379-91.

347. Romanov VS, Abramova MV, Svetlikova SB, Bykova TV, Zubova SG, Aksenov ND, et al. p21(Waf1) is required for cellular senescence but not for cell cycle arrest induced by the HDAC inhibitor sodium butyrate. Cell Cycle. 2010;9(19):3945-55.

348. Kim YY, Jee HJ, Um JH, Kim YM, Bae SS, Yun J. Cooperation between p21 and Akt is required for p53-dependent cellular senescence. Aging Cell. 2017;16(5):1094-103.

349. Younossi ZM, Otgonsuren M, Henry L, Venkatesan C, Mishra A, Erario M, et al. Association of nonalcoholic fatty liver disease (NAFLD) with hepatocellular carcinoma (HCC) in the United States from 2004 to 2009. Hepatology. 2015;62(6):1723-30.

350. Seki E. Hedgehog Signal in hepatocytes mediates macrophage recruitment: a new mechanism and potential therapeutic target for fatty liver disease. Hepatology. 2016;63(4):1071-3.

351. Guillen-Sacoto MJ, Martinez AF, Abe Y, Kruszka P, Weiss K, Everson JL, et al. Human germline hedgehog pathway mutations predispose to fatty liver. Journal of Hepatology. 2017;67(4):809-17.

352. Briscoe J, Therond PP. The mechanisms of Hedgehog signalling and its roles in development and disease. Nature Reviews Molecular cell Biology. 2013;14(7):416-29.

353. Kwon H, Song K, Han C, Chen W, Wang Y, Dash S, et al. Inhibition of hedgehog signaling ameliorates hepatic inflammation in mice with nonalcoholic fatty liver disease. Hepatology. 2016;63(4):1155-69.

354. Della Corte CM, Viscardi G, Papaccio F, Esposito G, Martini G, Ciardiello D, et al. Implication of the Hedgehog pathway in hepatocellular carcinoma. World Journal of Gastroenterology. 2017;23(24):4330-40.

355. Matz-Soja M, Rennert C, Schonefeld K, Aleithe S, Boettger J, Schmidt-Heck W, et al. Hedgehog signaling is a potent regulator of liver lipid metabolism and reveals a GLI-code associated with steatosis. ELife. 2016;5.

356. Munoz-Espin D, Serrano M. Cellular senescence: from physiology to pathology. Nature Reviews Molecular Cell Biology. 2014;15(7):482-96.

357. Qian Y, Chen X. Senescence regulation by the p53 protein family. Methods of Molecular Biology. 2013;965:37-61.

358. Vatsyayan R, Singhal J, Nagaprashantha LD, Awasthi S, Singhal SS. Nutlin-3 enhances sorafenib efficacy in renal cell carcinoma. Molecular Carcinogenesis. 2013;52(1):39-48.

359. Zauli G, Celeghini C, Melloni E, Voltan R, Ongari M, Tiribelli M, et al. The sorafenib plus nutlin-3 combination promotes synergistic cytotoxicity in acute myeloid leukemic cells irrespectively of FLT3 and p53 status. Haematologica. 2012;97(11):1722-30.